Describing colloidal soft matter systems with microscopic continuum models

Mark J. Robbins

Submitted in partial fulfilment of the requirements for the award of
Doctor of Philosophy of Loughborough University

February 2012

Loughborough University

Certificate of originality

This is to certify that I am responsible for the work submitted in this thesis, that the original work is my own except as specified in acknowledgments or in footnotes, and that neither the thesis nor the original work contained therein has been submitted to this or any other institution for a degree.

Acknowledgements

First and foremost, I would like to thank my supervisor Andrew Archer for his constant guidance and support. His genuine enthusiasm for the various projects, has helped me to maintain the motivation and focus I needed. In the same vein, I would also like to thank Uwe Thiele for all of his help throughout my PhD and for providing me with great opportunities to attend various conferences across Europe. I would also like to acknowledge my colleagues and peers for useful discussions and for providing a good and enjoyable working atmosphere. I would like to thank my family and friends for all of their support, in particular my parents and my brother. Last, but by no means least, I would like to thank Kelly Wakefield for her help and support. She has been an invaluable proof reader to me, which also means that she is responsible for any spelling or grammar mistakes which remain.

Chapters 3 and 4 of this thesis are based on the publications:

U. Thiele, I. Vancea, A. J. Archer, M. J. Robbins, L. Frasitia, A. Stannard, E. Pauliac-Vaujour, C. P. Martin, M. O. Blunt and P. J. Moriarty, *Modelling approaches to the dewetting of evaporating thin films of nanoparticle suspensions*, J. Phys.: Condens. Matter **21**, 264016 (2009).

A. J. Archer, M. J. Robbins and U. Thiele *Dynamical density functional theory for the dewetting of evaporating thin films of nanoparticle suspensions exhibiting pattern formation*, Phys. Rev. E **81**, 021602 (2010).

M. J. Robbins, A. J. Archer and U. Thiele, *Modelling the evaporation of thin films of colloidal suspensions using Dynamical Density Functional Theory*, J. Phys.: Condens. Matter **23**, 415102 (2011).

Chapter 6 of this thesis is based on the publication:

M. J. Robbins, A. J. Archer, U. Thiele and E. Knobloch, *Modelling fluids and crystals using a two component modified phase filed crystal model*, submitted to New J. Phys. (2012).

Abstract

In this thesis we explore two different theories for modelling soft matter systems. We start by discussing density functional theory (DFT) and dynamical density functional theory (DDFT) and consider the thermodynamics underpinning these theories as well as showing how the main results may be derived from the microscopic properties of soft matter. We use this theory to set up a model for the evaporation of the solvent from a thin film of a colloidal suspension. The general background for such systems is discussed and we display some of the striking nanostructures which self-assemble during the evaporation process. We show that our theory successfully reproduces some of these patterns and deduce the various mechanisms and transport processes behind the formation of the different structures.

In the second part of this thesis we discuss results for a second model; the phase field crystal (PFC) model. The model equations are discussed, showing how they may be derived from DDFT as well as discussing the general background of PFC models. We present some results for the PFC model in its most commonly used form before going on to introduce a modified PFC model. We show how the changes in the model equations are reflected in the thermodynamics of the model. We then proceed by demonstrating how this modified PFC model may be used to qualitatively describe colloidal systems. A two component generalisation of the modified PFC model is introduced and used to investigate the transition between hexagonal and square ordering in crystalline structures. We conclude by discussing the similarities and connections between the two models presented in the thesis.

Contents

List of Figures

Chapter 1

Introduction

Colloidal solutions are comprised of relatively large particles or molecules dispersed evenly in a fluid medium. The inclusion of colloidal particles can radically alter the behaviour of fluids, leading to effects such as shear thinning or shear thickening etc. Colloidal suspensions may occur naturally (e.g. milk, smoke, clouds) and may also be constructed to form foams, emulsions, gels, aerosols, etc. and so they have many vital applications in day-to-day life. Therefore, as one would expect they are intensively studied, but unlike simple liquids, a lot of the complex behaviour of colloidal suspensions is not fully understood. Current theories tend to consider the various interaction forces between the colloids (e.g. Van der Waals forces, excluded volume repulsion, depletion interactions, etc. see for example Ref. [1]), while treating the fluid as a continuous medium. Having determined the effective interactions between the colloids, much of the machinery of the well-developed theory of simple liquids can be applied. An example of such a theory is density functional theory (DFT).

In chapter 2 we discuss DFT and dynamical density functional theory (DDFT) which is the underlying theory behind the two mathematical models presented in this thesis (in chapters 4 and 6). The theory is derived from the microscopic detail of a system, i.e. the coordinates of all of the particles/colloids. The resulting model equations are written down in terms of the one body density ρ which is calculated by taking ensemble averages over all possible microstates (microscopic configurations) of a system. As such, the individual motions of the particles/colloids are not described but the resulting approach retains enough information for the theories to predict some of the behaviour of the complex fluids. The theory is used directly in the formulation of a model for evaporating thin films of colloidal suspensions in chapter 4 and is applied with further assumptions and approximations as a generic model for fluids and crystals with defects in chapter 6.

The equilibrium and the full dynamic behaviour of different systems is a constantly recurring theme in this work. When examining the equilibrium behaviour of the system we wish to find the particular density (or order parameter) profile which minimises the free energy of the system. For the complex systems we study here, we often find various 'phases' in the different parameter ranges, where the equilibrium profile takes a certain form. We may obtain phase

diagrams for a system, which may be thought of as maps depicting where different phases occur in parameter space. These diagrams usually contain the limit of linear stability (referred to as the spinodal curve with respect to fluid systems) and the coexistence lines between the various phases (known as binodal curves in fluid systems). Understanding the states of the model in equilibrium gives great insight into the non-equilibrium behaviour of the system, as it allows us to determine the preferred state. However, sometimes the processes involved in the time-evolution of a system are important and to study the various transport and other processes that are involved we must solve the fully non-linear dynamic model. In the case of the two models presented here this means solving partial differential equations for the time evolution of the density (order parameter) field.

This thesis is structured as follows: first, in chapter 2, we present the DFT and DDFT which is used throughout the thesis. We describe how the two theories are derived and therefore give insight into the information which is contained and perhaps more importantly, the information which is excluded in the theories and the resulting models. The remainder of the thesis is then split into two case studies. In chapters 3–4 we present a DDFT model for evaporating thin films of colloidal suspensions. The general background and literature review for this case study is discussed in chapter 3 and then the model, the equilibrium behaviour and the fully non-linear dynamics of the model are presented in chapter 4. The second case study is presented in chapters 5–6 and involves using a modified phase field crystal (PFC) model to describe fluids and crystals with defects. In chapter 5 we discuss how the regular PFC model equations can be derived from the DDFT discussed in chapter 2, we give a general overview of the PFC literature and present some basic results for the regular PFC model in one and two dimensions. Then we move on to discuss the modified PFC model in chapter 6, where we investigate the equilibrium phase behaviour and the full dynamics of both a one component model (in 1D and 2D) and a two component model (in 2D). Finally, we conclude with a summary of the work and make some closing remarks which highlight the similarities between the two different models.

Chapter 2

Background and underlying theory

In the first case study presented in this thesis (chapter 4) we present a model of a nanoparticle suspension evaporating from a surface that is based on Dynamical Density Functional Theory (DDFT). The model consists of partial differential equations which describe the time evolution of two coupled density fields. In this chapter we present the background and underlying theory behind these model equations. In particular, in Sec. 2.1 we introduce Density Functional Theory (DFT) using an intuitive thermodynamic approach, following this, in Sec. 2.2, we briefly mention the more formal statistical mechanical derivation of DFT and then in Sec. 2.3 we discuss how the theory may be extended to describe the dynamics of fluid systems.

2.1 Thermodynamics of inhomogeneous liquids

We begin by recalling the thermodynamics relevant for describing homogeneous liquids. The first law of thermodynamics states that energy is conserved in macroscopic bodies, which leads to the identity [2]:

$$dU = \delta Q + \delta W, \tag{2.1}$$

where dU is a change in the internal energy brought about by a heat transfer δQ and work done δW (e.g. mechanical or magnetic work) on a system. We also have the following thermodynamic relations [2]:

$$\delta W \geq -P dV, \tag{2.2}$$

$$\delta Q \leq T dS, \tag{2.3}$$

where P is the pressure, dV is the change in volume, T is the temperature and dS is the change in entropy. The equalities/inequalities hold when the changes are reversible/irreversible.

One may develop the thermodynamics of a system by considering a number of different ensembles. We initially consider a homogeneous liquid contained within an isolated system where the internal energy U, the volume V and the number of particles N contained within the system are all fixed. This is known as a microcanonical ensemble. A diagram representing such a system is shown in Fig. 2.1 (a), where the hashed red lines indicate that the system is completely isolated

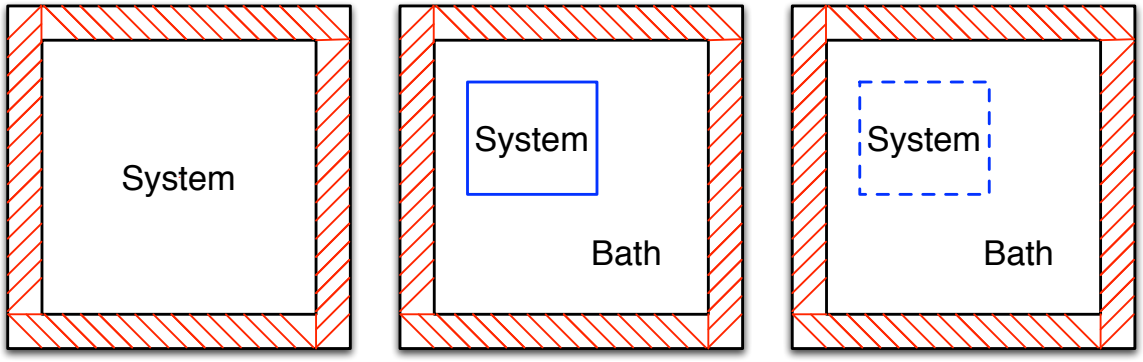

(a) Microcanonical ensemble **(b)** Canonical ensemble **(c)** Grand canonical ensemble

Figure 2.1: Two dimensional diagrammatic representations of three different thermodynamic ensembles are shown: (a) microcanonical ensemble where the internal energy U, volume V and the number of particles N are fixed, (b) canonical ensemble where the temperature T, volume V and the number of particles N are fixed and (c) grand canonical ensemble where the temperature T, volume V and the chemical potential μ are fixed.

from anything outside. From the definition of this ensemble we see that $dU = 0$ and $dV = 0$. There is no work done $\delta W = 0$, due to the constant volume of the system. Substituting these values into the conservation of energy law Eq. (2.1) we find that $\delta Q = 0$ and therefore, from the identity Eq. (2.3) we arrive at:

$$dS \geq 0. \tag{2.4}$$

This tells us that the equilibrium configuration of this system is the one which maximises the entropy S. This is a statement of the second law of thermodynamics; disorder increases monotonically as the system relaxes towards equilibrium. An alternative set up is the canonical ensemble, as shown in Fig. 2.1 (b), where the solid blue line represents a heat conducting boundary which particles cannot cross. Here we fix the volume V of the system and the number of particles N as before, but now we also fix the temperature T by coupling the system to a thermal bath and allow the internal energy U to fluctuate through the coupling to the bath. The constant volume means that there is no work done, i.e. $\delta W = 0$. Combining the two thermodynamic identities Eqs. (2.1) and (2.3) we arrive at the following expression:

$$dU - TdS \leq 0, \tag{2.5}$$

which can be re-written as:

$$dF \leq 0, \tag{2.6}$$

where $F = U - TS$ is the Helmholtz free energy [2] and dF is the change in the Helmholtz free energy. This therefore tells us that the equilibrium configuration of the system in the canonical ensemble corresponds to the minimum in the Helmholtz free energy. We can modify the canonical ensemble by retaining the fixed volume V and temperature T but now allowing particles to pass in and out of the system. Thus, the number of particles N in the system is no longer fixed, but is regulated by the chemical potential μ of the bath. The chemical potential defines the energy associated with adding or removing particles from the system and so it contributes to the conservation of energy identity Eq. (2.1) with the term μdN, where dN is the change in the number of particles. In Fig. 2.1 (c) we display a diagram which represents such systems, where the blue dashed line indicates that the particles can cross into and out of the system, i.e. the boundary need not be real. Following similar arguments to the previous case and including the μdN term to account for the change in energy when adding or removing a particle, we arrive at the following expression:

$$dU - TdS - \mu dN \leq 0, \tag{2.7}$$

which can be re-written as

$$d\Omega \leq 0, \tag{2.8}$$

where $\Omega = F - \mu N$ is the grand potential free energy [2] of the system and $d\Omega$ is the change in the grand potential. So in a similar manner to the canonical ensemble, a system in the grand canonical ensemble reaches equilibrium when the grand potential Ω is at a minimum. We introduce the number density of the system, which is the number of particles per unit volume $\rho = \frac{N}{V}$, which allows us to rewrite the grand potential as $\Omega = fV - \mu\rho V$, where f is the Helmholtz free energy per unit volume. Equivalently we may calculate these volumes as integrals over the system, leading to the following notation:

$$\Omega = \int_V d\mathbf{r} \;\; f - \int_V d\mathbf{r} \;\; \mu\rho, \tag{2.9}$$

where $\mathbf{r}$ is a continuous vector representing the coordinates of the system.

So far we have only considered homogeneous liquids, which are found in the bulk of the system where there are no spatial variations in any external fields influencing the system. The liquid becomes inhomogeneous when there is a spatially varying external field acting on the fluid such as that due to the wall of a container. In Fig. 2.2 (a) we display an example of a grand canonical system where there is a wall on one side and then in Fig. 2.2 (b) we show a sketch

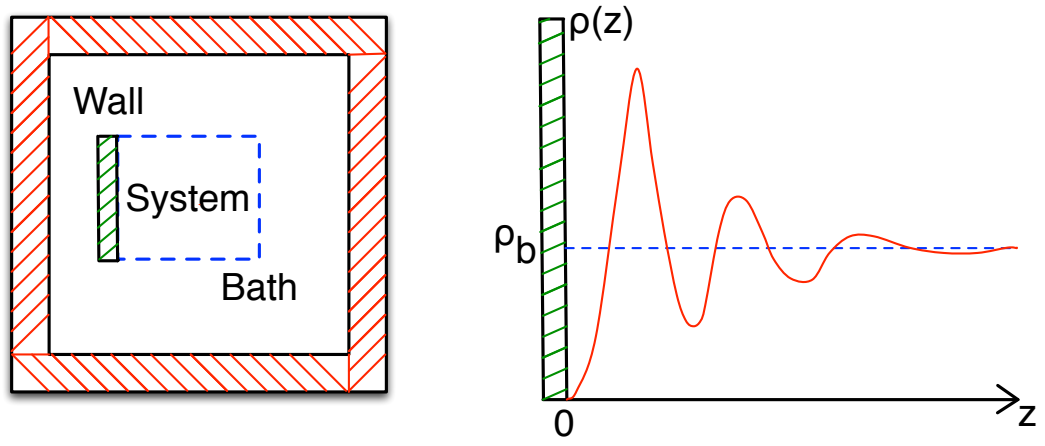

(a) Grand canonical ensemble with a wall

(b) Typical density profile near the wall

Figure 2.2: (a) Diagrammatic representation of a system treated in the grand canonical ensemble (like that shown in Fig. 2.1) having a wall on one side of the system which leads to inhomogeneity in the system. (b) A sketch showing the typical density profile of a fluid with bulk density ρ_b near the wall in such a system, where z is the perpendicular distance from the surface of the wall.

of the typical density profile of a fluid near the wall. The wall introduces inhomogeneity into the system causing the particles to pack into layers near the wall. As we are now considering an inhomogeneous liquid, we assume that the local density is a quantity which is a function of position $\mathbf{r}$ in the system, i.e. $\rho = \rho(\mathbf{r})$ and the Helmholtz free energy per unit volume and the grand potential become functionals of the density: $f[\rho(\mathbf{r})]$, $\Omega[\rho(\mathbf{r})]$, so Eq. (2.9) becomes:

$$\Omega[\rho(\mathbf{r})] = \int d\mathbf{r}\ \ f[\rho(\mathbf{r})] - \mu \int d\mathbf{r}\ \ \rho(\mathbf{r}). \tag{2.10}$$

As previously discussed, the equilibrium configuration corresponds to the minimum of the grand potential. Therefore we may state that the density profile $\rho^*(\mathbf{r})$ which minimises the functional $\Omega[\rho(\mathbf{r})]$ must be the equilibrium density profile; i.e. the equilibrium density profile satisfies the Euler-Lagrange equation:

$$\left.\frac{\delta\Omega[\rho(\mathbf{r})]}{\delta\rho(\mathbf{r})}\right|_{\rho(\mathbf{r})=\rho^*(\mathbf{r})} = 0. \tag{2.11}$$

Given a suitable approximation for the Helmholtz free energy term $F[\rho(\mathbf{r})] = \int d\mathbf{r}\ \ f[\rho(\mathbf{r})]$ in Eq. (2.10) we now have a formalism to enable us to describe the structure of the fluids under the influence of a given external potential. Using the minimisation principle Eq. (2.11), we can calculate the equilibrium density profile for a given external potential [1, 3]. For an ideal-gas,

i.e. a fluid composed of non-interacting particles, the Helmholtz free energy functional $F[\rho(\mathbf{r})]$ is known exactly [3]:

$$F[\rho(\mathbf{r})] = k_B T \int d\mathbf{r}\ \ \rho(\mathbf{r})[\ln(\Lambda^3 \rho(\mathbf{r})) - 1] + \int d\mathbf{r}\ \ V_{\text{ext}}(\mathbf{r})\rho(\mathbf{r}), \tag{2.12}$$

where k_B is the Boltzmann constant, Λ is the thermal de Broglie wavelength of the gas and V_{ext} is the external potential. Using the minimisation principle Eq. (2.11) for the ideal gas free energy in Eq. (2.12) we obtain:

$$k_B T \ln(\Lambda^3 \rho^*(\mathbf{r})) + V_{\text{ext}}(\mathbf{r}) - \mu = 0, \tag{2.13}$$

which can be solved for $\rho^*(\mathbf{r})$ to give:

$$\rho^*(\mathbf{r}) = \Lambda^{-3} e^{\beta\mu} e^{-\beta V_{\text{ext}}(\mathbf{r})}, \tag{2.14}$$

where $\beta = \frac{1}{k_B T}$. Thus, if we consider an ideal gas under the influence of an external potential that only varies in one direction, the density profile will only vary in that direction. An example of this is the external field above the surface of the Earth due to gravity (i.e. substitute $\mathbf{r} = h$ and $V_{\text{ext}} = mgh$ into Eq. (2.14)), then the resulting density profile abides by the Barometric law:

$$\rho(h) = \rho_0 e^{-\frac{mgh}{k_B T}}, \tag{2.15}$$

where $\rho_0 = \Lambda^{-3} e^{\beta\mu}$ is the density at $h = 0$.

Usually the interactions between the particles have a significant impact on the equilibrium density profiles and so one must add an additional term $\mathcal{F}_{ex}[\rho(\mathbf{r})]$ to the free energy which takes these interactions into consideration. Thus, the Helmholtz free energy in general is of the form:

$$F[\rho(\mathbf{r})] = \mathcal{F}_{\text{id}}[\rho(\mathbf{r})] + \mathcal{F}_{\text{ex}}[\rho(\mathbf{r})] + \int d\mathbf{r}\ \ V_{\text{ext}}(\mathbf{r})\rho(\mathbf{r}), \tag{2.16}$$

where $\mathcal{F}_{\text{id}}[\rho(\mathbf{r})] = k_B T \int d\mathbf{r}\, \rho(\mathbf{r})[\ln(\Lambda^3 \rho(\mathbf{r})) - 1]$ is the ideal gas contribution to the free energy. Applying the minimisation principle (2.11) we find that the equilibrium density profile takes the form:

$$\rho^*(\mathbf{r}) = \Lambda^{-3} e^{\beta\mu} e^{-\beta V_{\text{ext}}(\mathbf{r}) + c^{(1)}(\mathbf{r})}, \tag{2.17}$$

where the one body direct correlation function [3] is defined as:

$$c^{(1)}(\mathbf{r}) \equiv -\beta \frac{\delta \mathcal{F}_{\text{ex}}[\rho(\mathbf{r})]}{\delta \rho(\mathbf{r})}. \tag{2.18}$$

The external potential V_{ext} is a potential which acts on each particle of the system individually. However, if we were to consider an effective external potential $V_{\text{ext}}^{\text{eff}}$ which is the potential 'felt' by an individual particle we need to consider a contribution from the neighbouring particles in the system. It is clear from Eq. (2.17) that the effective external potential 'felt' by an individual particle is $V_{\text{ext}}^{\text{eff}}(\mathbf{r}) = V_{\text{ext}}(\mathbf{r}) - k_B T c^{(1)}(\mathbf{r})$ and so the one body direct correlation function can be thought of as a correction to the external potential V_{ext} to include the effective potential due to all the other particles in the system. Alternatively, one could consider the effective force acting on a particle located at position $\mathbf{r}$ in the system, due to the other particles in the system, which is simply given by the gradient of the one body direct correlation function $k_B T \nabla c^{(1)}(\mathbf{r})$ and so if we assume that the particles interact only via pair potentials $\nu(\mathbf{r}, \mathbf{r}')$ then the following sum-rule applies [3]:

$$-k_B T \rho(\mathbf{r}) \nabla c^{(1)}(\mathbf{r}) = \int d\mathbf{r}' \; \rho^{(2)}(\mathbf{r}, \mathbf{r}') \nabla \nu(\mathbf{r}, \mathbf{r}'), \tag{2.19}$$

where $\mathbf{r}'$ is another spatial coordinate and $\rho^{(2)}(\mathbf{r}, \mathbf{r}')$ is the two-body density distribution which gives the probability of there being a particle at $\mathbf{r}'$, given there is another particle at $\mathbf{r}$. Similar sum rules may be derived when the particles do not just interact via pair potentials, but there are also higher body potentials [4].

The excess free energy term $\mathcal{F}_{\text{ex}}[\rho(\mathbf{r})]$ is usually unknown. There are many different approximations which may be used, with some being more appropriate for certain models. In the low density limit the following is a good approximation for the excess free energy [1]:

$$\mathcal{F}_{\text{ex}}[\rho(\mathbf{r})] = \frac{1}{2} \int d\mathbf{r} \int d\mathbf{r}' \;\; f_m(|\mathbf{r} - \mathbf{r}'|) \rho(\mathbf{r}) \rho(\mathbf{r}') + O(\rho^3), \tag{2.20}$$

where $f_m(r) = e^{-\beta \nu(r)} - 1$ is the Mayer function and $\nu(r)$ is the (spherically symmetric) pair potential used to model the interactions between the particles in the liquid. There are many different approximations that can be used to take the particle interactions into account e.g. a gradient expansion, a Taylor series expansion or weighted density functionals[1]. For discussions on these and other approximations for the excess Helmholtz free energy, see Refs. [1, 3, 5].

[1] In Sec. 5.1 of chapter 5 we show how the free energy of the phase field crystal model may be derived by making a gradient expansion of the free energy.

2.2 Statistical mechanical derivation of DFT

Density functional theory may also be derived more formally from the statistical mechanics of fluids. Using statistical mechanics, thermodynamic quantities (such as those discussed above in Sec. 2.1; density ρ, chemical potential μ etc.) can be calculated by performing an ensemble average for the system. The resulting quantities (such as $\rho(\mathbf{r})$) are therefore statistical average quantities, and so do not depend on the degrees of freedom of the individual particles nor the form of the equations of motion, since the system is in equilibrium. As is clear from the previous section, once we have $\rho^*(\mathbf{r})$, this can be put into Eq. (2.10) to obtain Ω and all other thermodynamic quantities. Here we closely follow Evans' formalism [3] and omit some of the finer details and proofs. For a more rigorous derivation of DFT and a greater insight into its applications see Refs. [3, 5].

We begin by considering a system treated in the grand canonical ensemble, where the temperature T and volume V are fixed and the system can exchange particles with a reservoir with a fixed chemical potential μ (c.f. Fig. 2.1 (c) and discussion above in Sec. 2.1). The total energy for such a system is given by the Hamiltonian [1, 5]:

$$H_N = \sum_{i=1}^{N} \frac{\mathbf{p}_i^2}{2m} + \Phi(\mathbf{r}_1, \cdots, \mathbf{r}_N) + \sum_{i=1}^{N} V_{\text{ext}}(\mathbf{r}_i), \tag{2.21}$$

where N is the number of atoms, m is the mass of each atom, $\mathbf{p}_i$ is the momentum of atom i, Φ is the total interatomic potential energy and $V_{\text{ext}}(\mathbf{r})$ is the one-body external potential. The first term of the Hamiltonian H_N corresponds to the kinetic energy of the system.

The partition function is an important statistical mechanical object which allows us to obtain thermodynamic quantities from microscopic information. The partition function is a sum over all the possible microstates (microscopic configurations) and may be used to calculate the probability of the system being in a particular microstate. The particular form of the partition function depends on the ensemble being considered. The grand partition function which corresponds to the grand canonical ensemble is given by [3]:

$$\Xi = \text{Tr}(e^{-\beta(H_N - \mu N)}), \tag{2.22}$$

where Tr is the trace 'operator' [3] which essentially integrates over all possible microstates, incorporating the microscopic detail of the system:

$$\mathrm{Tr}(x) \equiv \sum_{N=0}^{\infty} \frac{1}{h^{3N} N!} \int\int x \, d\mathbf{r}_1 \cdots d\mathbf{r}_N \, d\mathbf{p}_1 \cdots d\mathbf{p}_N, \tag{2.23}$$

where h is Planck's constant and $\mathbf{r}_i$ denotes the position of atom i.

We now consider the probability density f, which gives us the probability of the system being in a given configuration. The equilibrium probability density f^* can be expressed using the Hamiltonian (2.21) and the partition function (2.22) in the following way:

$$f^* = \frac{e^{-\beta(H_N - \mu N)}}{\Xi}. \tag{2.24}$$

We consider the following functional of the probability density f [6]:

$$\Omega[f] = \mathrm{Tr}[f(H_N - \mu N + k_B T \ln(f))]. \tag{2.25}$$

By inserting the equilibrium probability density (2.24) into this functional (2.25) we obtain:

$$\begin{aligned} \Omega[f^*] &= \mathrm{Tr}\left\{ \frac{e^{-\beta(H_N-\mu N)}}{\Xi} \left[H_N - \mu N - k_B T(\beta(H_N - \mu N) + \ln(\Xi)) \right] \right\} \\ &= \frac{-k_B T \ln(\Xi)}{\Xi} \mathrm{Tr}\left\{ e^{-\beta(H_N-\mu N)} \right\} \\ &= -k_B T \ln(\Xi) \\ &\equiv \Omega, \end{aligned} \tag{2.26}$$

where Ω is the thermodynamic grand potential of the system [1]. Thus we see that at equilibrium, the functional Eq. (2.25) gives the thermodynamic grand potential of the system. Furthermore, using the result Eq. (2.26) and replacing $H_N - \mu N$ in Eq. (2.25) with an expression involving the equilibrium distribution function f^* from Eq. (2.24), we obtain:

$$\begin{aligned} \Omega[f] &= \mathrm{Tr}[f(-k_B T \ln(\Xi f^*) + k_B T \ln(f))] \\ &= \Omega + k_B T \mathrm{Tr}[f(\ln(f) - \ln(f^*))]. \end{aligned} \tag{2.27}$$

From a Gibbs' inequality, the quantity $\mathrm{Tr}[f(\ln(f) - \ln(f^*))]$ is always positive when $f \neq f^*$, hence, for non-equilibrium probability densities the resulting value is always greater than Ω, i.e.:

$$\Omega[f] > \Omega, \quad \text{when } f \neq f^*. \tag{2.28}$$

This tells us that the grand potential functional (2.25) is minimised by the equilibrium probability density f^*. To develop the theory, we need to determine how this result relates to the density ρ of the system. The equilibrium density distribution $\rho^*(\mathbf{r})$ can be calculated from the ensemble average of the density operator $\hat{\rho}(\mathbf{r})$:

$$\rho^*(\mathbf{r}) = \langle \hat{\rho}(\mathbf{r}) \rangle, \tag{2.29}$$

where the density operator takes the form $\hat{\rho}(\mathbf{r}) = \sum_{i=1}^{N} \delta(\mathbf{r} - \mathbf{r}_i)$ and where $\delta(\mathbf{r} - \mathbf{r}_i)$ is the usual Dirac δ-function. Thus, for a given configuration of the atoms in the system, the density operator consists of a sum of δ-functions each located at the centres of each atom. The ensemble average density is calculated in the following way:

$$\langle \hat{\rho}(\mathbf{r}) \rangle = \mathrm{Tr}(f^* \hat{\rho}(\mathbf{r})). \tag{2.30}$$

It can be shown that the equilibrium probability density f^* is a functional of the density ρ^* and that for a given interaction potential Φ and a given external potential V_{ext}, the equilibrium density profile ρ^* is unique (see Ref. [3] for proof). This implies that for a given interaction potential, the following functional is unique and is applicable for any external potential V_{ext}:

$$\mathcal{F}[\rho] = \mathrm{Tr}\left[f^* \left(\sum_{i=1}^{N} \frac{\mathbf{p}_i^2}{2m} + \Phi(\mathbf{r}_1, \cdots, \mathbf{r}_N) + k_B T \ln(f^*) \right) \right]. \tag{2.31}$$

This functional is defined exactly here using microscopic quantities, but in reality this functional is usually unknown because the trace Tr cannot be evaluated and so approximations must be made.[2] We may also consider the following functional, which is equal to the grand potential Ω when the density is at equilibrium $\rho = \rho^*$:

$$\Omega[\rho] = \mathcal{F}[\rho] + \int d\mathbf{r} \rho(\mathbf{r}) V_{\mathrm{ext}}(\mathbf{r}) - \mu \int d\mathbf{r} \rho(\mathbf{r}). \tag{2.32}$$

This is an alternative notation for the functional given in Eq. (2.10). As discussed above in Sec. 2.1, the minimum of this functional corresponds to the equilibrium density profile and this leads to the minimisation principle Eq. (2.11). Using the minimisation principle we can calculate the equilibrium density ρ^* for a given Helmholtz free energy functional $\mathcal{F}$ and external potential V_{ext}.

[2] $\mathcal{F}[\rho]$ may be approximated by splitting it up an ideal gas and excess part $\mathcal{F}[\rho] = \mathcal{F}_{\mathrm{id}}[\rho] + \mathcal{F}_{\mathrm{ex}}[\rho]$, see Eq. (2.16) and discussion above in Sec. 2.1.

2.3 Dynamical Density Functional Theory

In the previous two sections we have considered equilibrium configurations and in particular we have shown how the equilibrium density profile ρ^* can be determined for a given external potential V_{ext} together with a suitable approximation for the Helmholtz free energy $\mathcal{F}$ using the minimisation principle Eq. (2.11). We now turn our attention to non-equilibrium systems and consider their dynamics. As with the equilibrium theory we seek to determine density profiles. Now however, as we are interested in the dynamics, we must calculate density profiles which vary temporally as well as spatially, i.e. $\rho(\mathbf{r}, t)$, where t is time. The following derivation of Dynamical Density Functional Theory (DDFT) closely follows the description presented in Ref. [4].

In order to discuss the dynamics of a system, we must first specify the equations of motion of the particles. We assume the fluid is composed of Brownian particles with stochastic equations of motion - i.e. we model a suspension of colloidal particles. For a system of N Brownian particles of mass m the equations of motion are given by the Langevin equation [4]:

$$m\frac{d^2\mathbf{r}_i(t)}{dt^2} + \Gamma^{-1}\frac{d\mathbf{r}_i(t)}{dt} = -\nabla_i U(\mathbf{r}^N, t) + \mathbf{X}_i(t), \tag{2.33}$$

where Γ^{-1} is the friction constant, $U(\mathbf{r}^N, t)$ is the potential energy of a system, determined by interparticle interactions $\Phi(\mathbf{r}, t)$ and any external field $V_{\text{ext}}(\mathbf{r}, t)$ acting on the liquid, $\mathbf{r}^N = \mathbf{r}_1, \mathbf{r}_2, \cdots, \mathbf{r}_N$ and $\mathbf{X}_i(t) = (\xi_i^x(t), \xi_i^y(t), \xi_i^z(t))$ is a white noise term where $\langle \xi_i^a(t) \rangle = 0$ and the correlations are $\langle \xi_i^a(t)\xi_j^b(t') \rangle = 2k_BT\delta_{ij}\delta^{ab}\delta(t - t')$. The noise term $\mathbf{X}_i(t)$ is used to model the random Brownian motion of the particles and the term $\Gamma^{-1}\frac{d\mathbf{r}_i(t)}{dt}$ is the viscous (Stokes) drag on the particles due to the solvent. In the limit when the friction constant Γ^{-1} becomes large, we may neglect the acceleration term $\frac{d^2\mathbf{r}_i(t)}{dt^2}$ and the equations of motion reduce to the following:

$$\frac{d\mathbf{r}_i(t)}{dt} = \Gamma(\mathbf{X}_i(t) - \nabla_i U(\mathbf{r}^N, t)). \tag{2.34}$$

The Fokker-Planck equation for the probability density distribution $f(\mathbf{r}^N, t)$ which corresponds to the equations of motion Eq. (2.34) is given by the Smoluchowski equation [4]:

$$\frac{\partial f(\mathbf{r}^N, t)}{\partial t} = \Gamma \sum_{i=1}^{N} \nabla_i \cdot [k_BT\nabla_i + \nabla_i U(\mathbf{r}^N, t)] f(\mathbf{r}^N, t), \tag{2.35}$$

which states that the time evolution of the probability density f is determined by a diffusion process (first term) and a drift (second term). We must consider how the probability density f relates to the density ρ to allow us to write dynamical equations in terms of the evolution

of density profiles. The one-body density is calculated by integrating over the probability distribution function:

$$\rho(\mathbf{r}_1, t) = N \int d\mathbf{r}_2 \cdots \int d\mathbf{r}_N \; f(\mathbf{r}^N, t), \tag{2.36}$$

and in a similar manner the two-body density is given by:

$$\rho^{(2)}(\mathbf{r}_1, \mathbf{r}_2, t) = N(N-1) \int d\mathbf{r}_3 \cdots \int d\mathbf{r}_N \; f(\mathbf{r}^N, t). \tag{2.37}$$

We assume that any external potential can be described as a one-body function acting on each individual particle $V_{\text{ext}}(\mathbf{r}_i, t)$ and that the particle interactions are a sum of pair interaction terms: $\nu(\mathbf{r}_i, \mathbf{r}_j)$:

$$U(\mathbf{r}^N, t) = \sum_{i=1}^{N} V_{\text{ext}}(\mathbf{r}_i, t) + \frac{1}{2} \sum_{j \neq i} \sum_{i=1}^{N} \nu(\mathbf{r}_i, \mathbf{r}_j), \tag{2.38}$$

where $\nu(\mathbf{r}_i, \mathbf{r}_j)$ is the pair potential and the factor of $\frac{1}{2}$ is included to prevent double counting. Using Eqs. (2.36), (2.37) and (2.38) we can integrate the Smoluchowski equation (2.35) to obtain a time evolution equation for the one-body density $\rho(\mathbf{r}_1, t)$. If we first consider the reduced case where $U(\mathbf{r}^N, t) = 0$ (i.e. an ideal gas of non-interacting Brownian particles) then we obtain:

$$N \frac{\partial}{\partial t} \left[\int d\mathbf{r}_2 \cdots \int d\mathbf{r}_N \; f(\mathbf{r}^N, t) \right] = \Gamma N k_B T \int d\mathbf{r}_2 \cdots \int d\mathbf{r}_N \sum_{i=1}^{N} \nabla_i^2 f(\mathbf{r}^N, t), \tag{2.39}$$

considering the $i = 1$ and the $i = 2 \cdots N$ cases on the right hand side separately we get:

$$\frac{\partial \rho(\mathbf{r}_1, t)}{\partial t} = \Gamma k_B T \left[\nabla_1^2 \rho(\mathbf{r}_1, t) + N \int d\mathbf{r}_2 \cdots \int d\mathbf{r}_N \sum_{i=2}^{N} \nabla_i^2 f(\mathbf{r}^N, t) \right]. \tag{2.40}$$

The second term on the right hand side of Eq. (2.40) contains the integrals $\int d\mathbf{r}_i \nabla_i^2 f(\mathbf{r}^N, t) = \nabla_i f(\mathbf{r}^N, t) \Big|_{-\infty}^{\infty}$. We assume that $f(\mathbf{r}^N, t) = 0$ far away from the system and so Eq. (2.40) becomes:

$$\frac{\partial \rho(\mathbf{r}_1, t)}{\partial t} = D \; \nabla_1^2 \rho(\mathbf{r}_1, t), \tag{2.41}$$

where $D = \Gamma k_B T$ is the diffusion coefficient. As we should expect, integrating over just the diffusive part of the Smoluchowski equation (2.35) we arrive at the diffusion equation (2.41). We now proceed by integrating over the drift term in the Smoluchowski equation (2.35). The potential energy in Eq. (2.38) contains two terms, and hence the drift term in the Smoluchowski

equation (2.35) can be split into two parts. For simplicity we integrate over these two parts separately. First we consider the term involving the external potential, which we denote $S_{\rm ext}$:

$$\begin{aligned} S_{\rm ext} &= \Gamma N \int d\mathbf{r}_2 \cdots \int d\mathbf{r}_N \sum_{i=1}^{N} \nabla_i \cdot \left[f(\mathbf{r}^N,t) \nabla_i \sum_{i=1}^{N} V_{\rm ext}(\mathbf{r}^N,t) \right] \\ &= \Gamma N \nabla_1 \cdot \left[\nabla_1 V_{\rm ext}(\mathbf{r}_1,t) \int d\mathbf{r}_2 \cdots \int d\mathbf{r}_N \, f(\mathbf{r}^N,t) \right] \\ &= \Gamma \nabla_1 \cdot \left[\rho(\mathbf{r}_1,t) \nabla_1 V_{\rm ext}(\mathbf{r}_1,t) \right]. \end{aligned} \tag{2.42}$$

In a manner similar to above, in order to go to the $2^{\rm nd}$ line we consider the $i = 1$ and the $i = 2 \cdots N$ cases separately, and in a similar way to above all the $i = 2 \cdots N$ terms are zero due to the assumption that if any of the components of $\mathbf{r}^N$ are $\pm\infty$ then $f(\mathbf{r}^N,t) = 0$. Finally we evaluate the term $S_{\rm in}$ containing the contribution due to the particle interactions i.e. involving the pair potentials $\nu(\mathbf{r}_i,\mathbf{r}_j)$:

$$S_{\rm in} = \Gamma N \int d\mathbf{r}_2 \cdots \int d\mathbf{r}_N \, \nabla_1 \cdot \left[f(\mathbf{r},t) \sum_{j=2}^{N} \nabla_1 \nu(\mathbf{r}_1,\mathbf{r}_j) \right], \tag{2.43}$$

when $j = 2$ we find that:

$$S_{\rm in}\Big|_{j=2} = \Gamma \nabla_1 \cdot \left[\int d\mathbf{r}_2 \nabla_1 \nu(\mathbf{r}_1,\mathbf{r}_2) \, N \int d\mathbf{r}_3 \cdots \int d\mathbf{r}_N f(\mathbf{r}^N,t) \right], \tag{2.44}$$

and for the other $N-2$ values of j similar expressions are obtained, so therefore the sum over all $N-1$ particles produces (c.f. Eq. (2.37)):

$$S_{\rm in} = \Gamma \nabla_1 \cdot \int d\mathbf{r}_2 \, \rho^{(2)}(\mathbf{r}_1,\mathbf{r}_2,t) \nabla_1 \nu(\mathbf{r}_1,\mathbf{r}_2). \tag{2.45}$$

Collecting the three results together (the diffusive term Eq. (2.41) and the external potential Eq. (2.42) and the particle interaction Eq. (2.45) parts of the drift term) we obtain the time evolution equation for the one-body density:

$$\begin{aligned} \Gamma^{-1} \frac{\partial \rho(\mathbf{r}_1,t)}{\partial t} &= k_B T \nabla_1^2 \rho(\mathbf{r}_1,t) + \nabla_1 \cdot \left[\rho(\mathbf{r}_1,t) \nabla_1 V_{\rm ext}(\mathbf{r}_1,t) \right] \\ &\quad + \nabla_1 \cdot \int d\mathbf{r}_2 \, \rho^{(2)}(\mathbf{r}_1,\mathbf{r}_2,t) \nabla_1 \nu(\mathbf{r}_1,\mathbf{r}_2). \end{aligned} \tag{2.46}$$

Now we have a dynamical equation for the time evolution of the one-body density $\rho(\mathbf{r}_1,t)$, but in its present form this equation is not very useful because the two-body density $\rho^{(2)}(\mathbf{r}_1,\mathbf{r}_2,t)$ is usually unknown. We make the assumption that the sum rule Eq. (2.19), which is exact when the system is in equilibrium, also holds when the system is out of equilibrium. This is equivalent to assuming the two-body correlations in the non-equilibrium fluid are the same as

in an equilibrium fluid with the same one-body density distribution. This allows us to rewrite Eq. (2.46) in the rather appealing and compact form:

$$\Gamma^{-1}\frac{\partial\rho(\mathbf{r}_1,t)}{\partial t} = \nabla_1\cdot\left[\rho(\mathbf{r}_1,t)\nabla_1\frac{\delta F[\rho(\mathbf{r}_1,t)]}{\delta\rho(\mathbf{r}_1,t)}\right], \tag{2.47}$$

where $F[\rho(\mathbf{r}_1,t)]$ is the equilibrium fluid Helmholtz free energy functional defined in Eq. (2.16). This is the key result of DDFT. Given an approximation for the Helmholtz free energy functional, one can determine the time evolution of the one-body density $\rho(\mathbf{r}_1,t)$. Here, for simplicity we have assumed that the particles only interact via pair potentials $\nu(\mathbf{r}_i,\mathbf{r}_j)$, however, the same result may be obtained when three-body and many-body potentials between the particles are taken into account [4]. For an alternative derivation of the DDFT equation see Refs. [7, 8].

The gradient of the functional derivative of the free energy $-\nabla\frac{\delta F[\rho(\mathbf{r}_1,t)]}{\delta\rho(\mathbf{r}_1,t)}$ in Eq. (2.47) may be thought of as the thermodynamic driving force, which determines the dynamics of the system. The potential:

$$\frac{\delta F[\rho(\mathbf{r}_1,t)]}{\delta\rho(\mathbf{r}_1,t)} \equiv \mu(\mathbf{r},t) = \mu_{\mathrm{id}}(\mathbf{r},t) + \mu_{\mathrm{ex}}(\mathbf{r},t) + \mu_{\mathrm{ext}}(\mathbf{r},t), \tag{2.48}$$

where $\mu(\mathbf{r},t)$ is a non-equilibrium chemical potential and the three terms that it is broken down into correspond to an ideal gas contribution $\mu_{\mathrm{id}}(\mathbf{r},t)$, a contribution $\mu_{\mathrm{ex}}(\mathbf{r},t)$ due to the interactions of the particles and $\mu_{\mathrm{ext}}(\mathbf{r},t)$ is the contribution from the external potential. We can therefore think of each term as contributing a driving force to the dynamics of the system. When the system relaxes towards an equilibrium state the driving force will continuously decrease, and so $\mu(\mathbf{r}) =$ constant when the system is in thermodynamic equilibrium.

In Chapter 4 we show how DDFT may be applied to derive a model for the evaporation of the solvent from a thin film of a colloidal suspension and in chapter 5 we show how the so called "phase field crystal" models for solidification may also be derived from DDFT.

Chapter 3

Evaporating thin films of colloidal suspensions

In this chapter we discuss the various patterns which are observed to form when a colloidal suspension evaporatively dewets from a surface. We start with a short introduction to the field, discussing pattern formation in dewetting systems. We then move on to discuss some experimental results and display some of the striking atomic force microscopic (AFM) images of the types of patterns which are formed. Finally, we discuss different mathematical models which have been employed to describe such systems and some of the important results and conclusions of these models.

3.1 Pattern formation in dewetting systems

Surface patterns resulting from structure formation occur naturally in many different systems and are extensively studied in various scientific fields. Classic examples are branched patterns, e.g. found in river networks [9] or formed by bacterial colonies [10], that sometimes form fractals. Other examples are the labyrinth patterns such as those formed via calcification and mineralisation processes [11]. Examples of naturally occurring branched and labyrinth patterns are shown in Fig. 3.1. Of particular interest here are the patterns which may arise from dewetting systems. Descriptions of patterns formed via dewetting processes may be found in the literature as far back as the late nineteenth century [12, 13]. A large variety of intricate structures can be formed even during the dewetting process of films of non-volatile fluids on solid substrates, e.g. networks, drops and labyrinth patterns. The dewetting process starts with the rupture of the initially homogeneous film of liquid caused either by a surface instability (spinodal dewetting [14]) or by the nucleation of holes which often occurs at surface defects [15–21]. When the dewetting process is initialised via a surface instability, one observes spontaneous dewetting everywhere. However, when dewetting is initialised via nucleation, one observes that the initial holes begin to grow [22]. As the holes become larger, they begin to compete for space and eventually the rims meet to form a global network, drop or labyrinth pattern [23–25].

Throughout the current and subsequent chapter we will be considering a colloidal suspension. A colloidal suspension is a mixture of one substance (the colloids) dispersed in a fluid medium. The colloidal particles are much larger than the particles of the fluid in which they

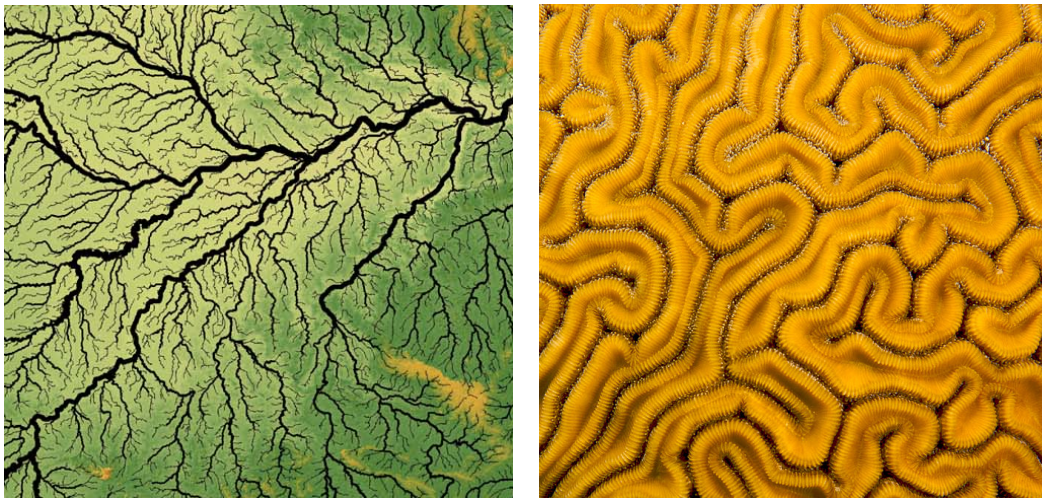

(a) Branched river network **(b)** Grooved brain coral

Figure 3.1: (a) Mapping of a section of the major river network in the Amazon Basin, data available from the U.S. Geological Survey [26]. This is a large scale example of a naturally occurring branched structure. (b) Close up of the "grooved brain coral", by Nick Hobgood [27]. This is an organic structure which naturally forms a labyrinth pattern.

are dispersed. Typically, the colloids range in size from a few nanometers up to a few microns. Here, we consider small colloidal particles (nanoparticles) which are sufficiently small, that they remain suspended in the fluid and do not sediment. The spontaneous self-assembly and self-organisation of atoms, molecules and nanoparticles at interfaces is a widely researched topic. A large range of interesting structures have been observed in various experimental set ups including the labyrinthine, network and branched structures which we focus on here, as well as stripes, rings and isolated islands [28]. Not only are the resulting structures interesting in their own right, but they may also be used in the manufacturing of nanostructures and functional surfaces, e.g. assembling colloids to form photonic bandgap crystals [29]. The properties of these structures need to be fine-tuned with a high level of precision as even small defects can drastically affect their functionality. Therefore, a large emphasis in the literature is placed on the understanding of the complex processes behind the formation of these various structures and how long range ordering may be obtained. The boundaries between different materials has a large effect on the structures which form, hence, understanding and developing ways in which to manipulate the physical processes at two-phase [30] and three-phase contact lines [31] is very important. Regular long range ordering is very difficult to achieve but recent advancements have led to solvent dewetting being a viable option for the formation of nanoparticle assemblies [28].

The inclusion of the nanoparticles complicates matters as the behaviour of the system is determined by the various transport processes of the solvent and the colloids. A large range of experiments have been conducted on such fluids, e.g. solutions of polymers [32–35], macromolecules like collagen and DNA [36–41] and nano particles [42–50]. The main objective of such experiments is usually to investigate the structures which are formed, which are often similar to those formed under the 'classical' dewetting of non-volatile liquids. Labyrinth structures are formed via spinodal decomposition when the fluid is unstable and polygonal networks are formed by the nucleation and growth of holes. The colloids are left behind after the solvent has evaporated from the surface leaving a 'dried in' structure, which becomes immobile without the 'Brownian kicks' of the solvent [38, 44]. The complex relationship between the colloids and the solvent also directly affects the thermodynamics of the fluid, meaning that the limit of linear stability (spinodal) and the coexistence (binodal) values differ from that of the pure solvent [51]. The complex fluid also has a different probability of nucleating holes compared to the pure solvent and the colloids may destabilise dewetting fronts. This unstable dewetting front gives rise to the formation of some intriguing structures, some examples of which are shown in Fig. 3.4.

If we consider volatile solvents then one finds that the contact lines recede even when the fluid is wetting. In this circumstance it has been observed that the moving contact line may deposit regular lines or rings of colloids [34, 52]. A single ring deposited in such a fashion is known as the well-studied "coffee-stain" effect [53]. A rich variety of structures may be observed for the dewetting of volatile solvents including multiple irregular rings, networks, regular droplet patterns, sawtooth patterns, Sierpinski carpets and liquid crystalline structures [32, 40, 54–58].

3.2 Experiments using gold nanoparticles in an organic solvent

The evaporative dewetting of polymer/macromolecule solutions [38, 59, 60] and colloidal (nanoparticle) suspensions [28, 42–44, 50] can produce a wide variety of patterns and has been intensely studied in various experimental settings over recent years. The particular experiments that directly motivate the theoretical work presented in the following chapter (Chapter 4) are those described in Refs. [28, 44, 47, 48, 50] that use a suspension of thiol-passivated gold nanoparticles dispersed in an organic solvent. Two different methods for depositing the suspension onto the substrate have been investigated (in Refs. [28, 44, 47, 48, 50]). One method

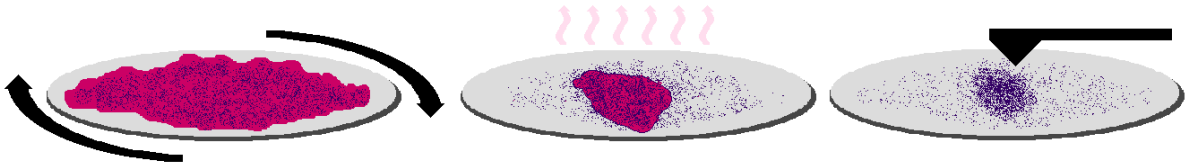

Figure 3.2: Illustration depicting a spin coating experiment for colloidal suspensions. First the solution is spin coated onto a substrate and then the remaining solvent is left to evaporate. Once the solvent has fully evaporated the position of the nanoparticles is measured using an atomic force microscope.

is to deposit a droplet onto a flat silicon substrate using a spin coating technique to form a thin film over the surface (as illustrated in Fig. 3.2). Depositing the fluid using this method results in a high evaporation rate, in fact the solvent can often fully evaporate during the spin-coating process. This leaves a 'dried in' nanoparticle structure on the surface of the substrate. In another experimental setup a drop of suspension is placed on the surface within a Teflon ring that is wetted by the solvent [61]. The evaporative dewetting is slower than in the case of spin-coating and the structuring may be observed using contrast enhanced microscopy [50]. What these experiments show is that branched structures are formed by transverse instabilities of the receding mesoscopic contact line. However, it has been observed that an ultrathin layer is left behind this mesoscopic contact line (as illustrated in Fig. 3.3 (b)). The height of this film is of the same order of magnitude as the diameter of the colloids. There is then a second dewetting stage where this ultrathin layer ruptures and dewets either from a surface instability (spinodal dewetting) or via the nucleation and growth of holes. It is this second dewetting stage of the ultrathin layer that interests us here, in particular, we wish to investigate the intriguing patterns which are formed by the nanoparticles in the ultrathin layer.

The formation of several different types of structures have been observed in this ultrathin layer: a labyrinth pattern formed during spinodal dewetting (as shown in Fig. 3.4 (a)), a dual-scaled network structure formed via the nucleation and growth of holes (as shown in Fig. 3.4 (b)) and a branched structure formed by a fingering instability that occurs at the dewetting front of nucleated holes (as shown in Fig. 3.4 (c)). The gold nanoparticles have a thin coating of alkyl-thiol molecules. In the experiments discussed here the length of the carbon chain of the thiol ranges from six to twelve carbon atoms ($C_6 - C_{12}$) [50]. The length of this chain directly influences the interaction energies between the particles and the diffusive mobility of the nanoparticles. It is also possible to change the wetting behaviour of the fluid by changing

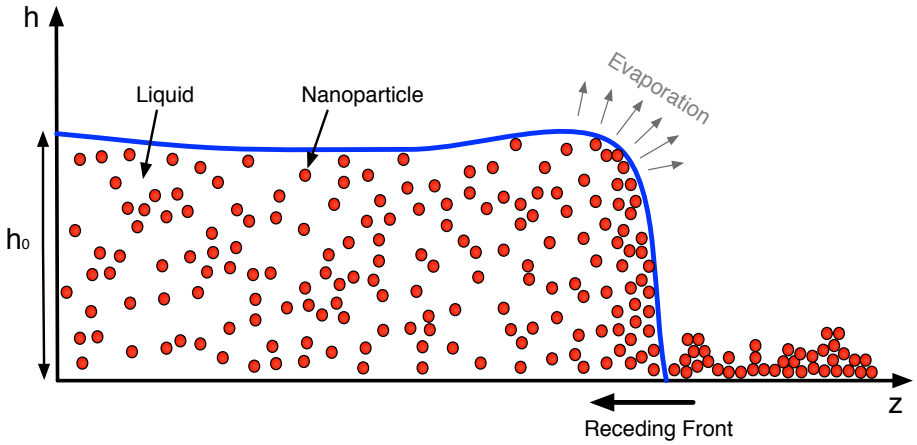

(a) Thin film

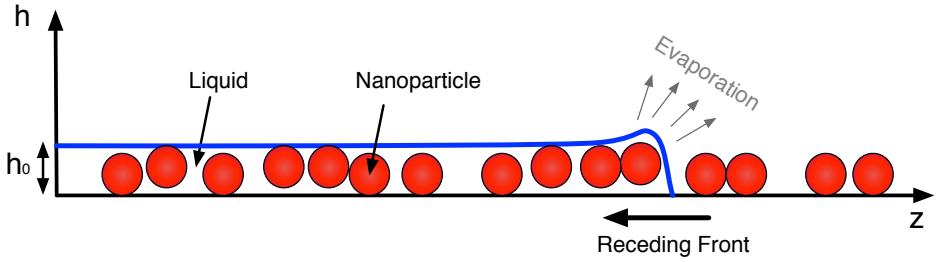

(b) Ultra thin film

Figure 3.3: Two dimensional illustrations depicting the evaporative dewetting of thin films of colloidal suspensions. In (a) we show the more general case where the film thickness h_0 is much larger than the particle diameter, whereas in (b) we show an ultra thin film where the height of the film h_0 is of the order of the diameter of the nanoparticles. It is this second case in (b) which the KMC (in Sec. 3.3) and the DDFT (in chapter 4) models describe.

the degree of oxidation of the silicon substrate. In the experiments they find that the fingering instability only occurs at relatively low nanoparticle mobilities.

We study this complex system in the hope of determining the different factors which influence the nano-structures that form. Two different mathematical models have been employed in the literature to try and describe this system. These are thin film hydrodynamical models, which are mesoscopic in character and so currently do not describe all of the observed effects. Another approach is based on a Kinetic Monte Carlo (KMC) model. In the following section we discuss the KMC method which was used in Refs. [45, 48, 50, 51]. The work in this thesis builds on this KMC model, and in chapter 4 we derive a DDFT model based on the theory discussed in chapter 2 and use the resulting free energy and dynamical equations to discuss the thermodynamics and the dynamics of the system.

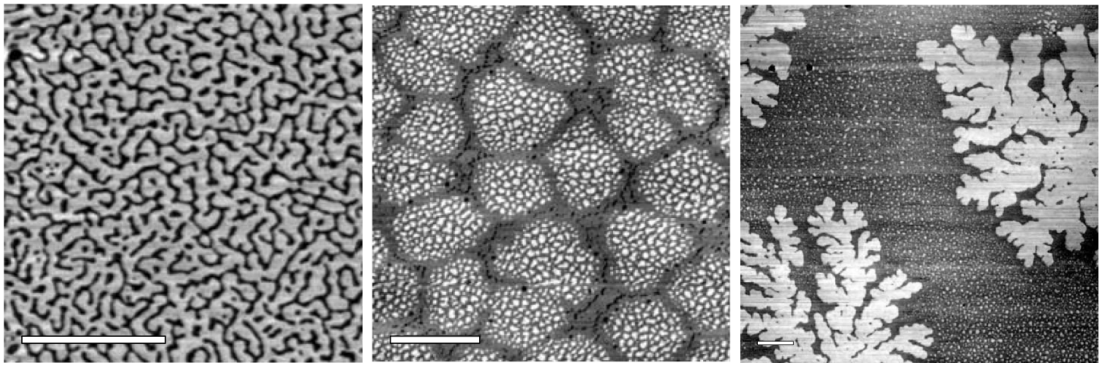

(a) Labyrinth Structure **(b)** Network Structure **(c)** Branched Pattern

Figure 3.4: Atomic Force Microscopic images of gold nanoparticle deposits which were dissolved in toluene and spin coated onto a silicon substrate for various concentrations and thiol chain lengths. The dark areas show where there are colloids and the light areas show empty substrate. In (a) we observe a labyrinth structure, where the scale bar shows $1\mu m$, in (b) we display a dual-scale network where the scale bar is $1\mu m$ and in (c) we show branched flower like patterns where the scale bar is $2\mu m$. Adapted with permission from I. Vancea et al. from Figs. 1 and 2 in Ref. [51].

3.3 Different modelling approaches

One approach that may be used for modelling such systems is based on thin-film hydrodynamical models, which are derived by making a long-wave approximation [62]. Recently, for example, line-pattern formation has been observed in a simple long-wave model for a thin film of colloidal suspension evaporatively dewetting from a surface [63]. Such thin film equation based models provide a good description of the system on mesoscopic length scales and are capable of reproducing many of the experimental results [31, 52, 64, 65]. However, they are unable to describe the dynamics of the system at the microscopic (single particle) level.

Alternatively, one may consider a Kinetic Monte Carlo (KMC) model, which is a microscopic theory for the liquid film. The set-up and the results of the KMC model discussed here follows the work of the authors of Ref. [51]. The KMC model for dewetting colloidal suspensions was developed using two major assumptions; i) all the important dynamics can be described using a 2D lattice gas model and ii) the dynamics are dominated by the diffusion of the nanoparticles and the evaporation of the solvent (i.e. the diffusion of the liquid over the surface has a negligible effect on the overall dynamics of the system). The model is based on the Ising model for the liquid-gas phase transition which is described in greater detail in the following chapter in Sec. 4.2 (see Fig. 4.1). In this coarse-grained model the surface is discretised into an array of

lattice sites, which can be empty ($l = 0$, $n = 0$), filled with solvent ($l = 1$, $n = 0$) or contain a nanoparticle ($l = 0$ and $n = 1$) where l and n are occupation numbers for each site. The total energy for a given configuration can then be calculated using the following Hamiltonian:

$$E = -\frac{\epsilon_{nn}}{2}\sum_{\langle ij\rangle} n_i n_j - \frac{\epsilon_{nl}}{2}\sum_{\langle ij\rangle} n_i l_j - \frac{\epsilon_{ll}}{2}\sum_{\langle ij\rangle} l_i l_j - \mu\sum_i l_i, \tag{3.1}$$

where ϵ_{nn}, ϵ_{nl} and ϵ_{ll} are the interaction energies for particle-particle, particle-liquid and liquid-liquid interactions respectively, $\sum_{\langle ij\rangle}$ is the sum over nearest neighbour pairs and μ is the effective chemical potential. $\epsilon_{ll} = 1$ is chosen as the unit of energy.

Two dynamical processes are simulated in the KMC model; i) the evaporation/condensation of the liquid and ii) the diffusion of the nanoparticles. During i) the evaporation cycle, the solvent may evaporate from a cell with liquid ($l = 1$, $n = 0$) or condense to a vacant site ($l = 0$, $n = 0$) if the process reduces the energy Eq. (3.1) of the system. If the proposed change would increase the overall energy of the system then the move is taken with the probability:

$$p_{\text{acc}} = e^{\frac{-\Delta E}{k_B T}}, \tag{3.2}$$

where ΔE is the change in energy associated with the potential move. Including this possibility for the system to make moves which increase the overall energy of the system prevents the system from jamming at a local energetic minimum and corresponds to the random thermal fluctuations in the real system. The ii) diffusive cycle of the KMC model allows nanoparticles to switch places with adjacent cells containing liquid if the potential move decreases the overall energy of the system or with probability p_{acc} (as defined in Eq. (3.2)) if $\Delta E > 0$. These moves lead to the nanoparticles diffusing over the surface through the liquid by only allowing nanoparticles to move to cells containing liquid. This is equivalent to imposing a zero mobility to particles not surrounded by any liquid, which allows the particles to form the 'dried in' patterns that were found in the experiments. An effective mobility M of the nanoparticles is defined as a ratio between the number of i) evaporative and ii) diffusive cycles. The value of this mobility M represents the physical ratio between the time scales of the two different dynamical processes.

Time simulations of the KMC model show that the nanoparticles form 'dried in' patterns on the substrate. Labyrinth and branched structures are observed which appear similar to the patterns that are formed in the corresponding experiments Fig. 3.4 (a) and (c). Network for-

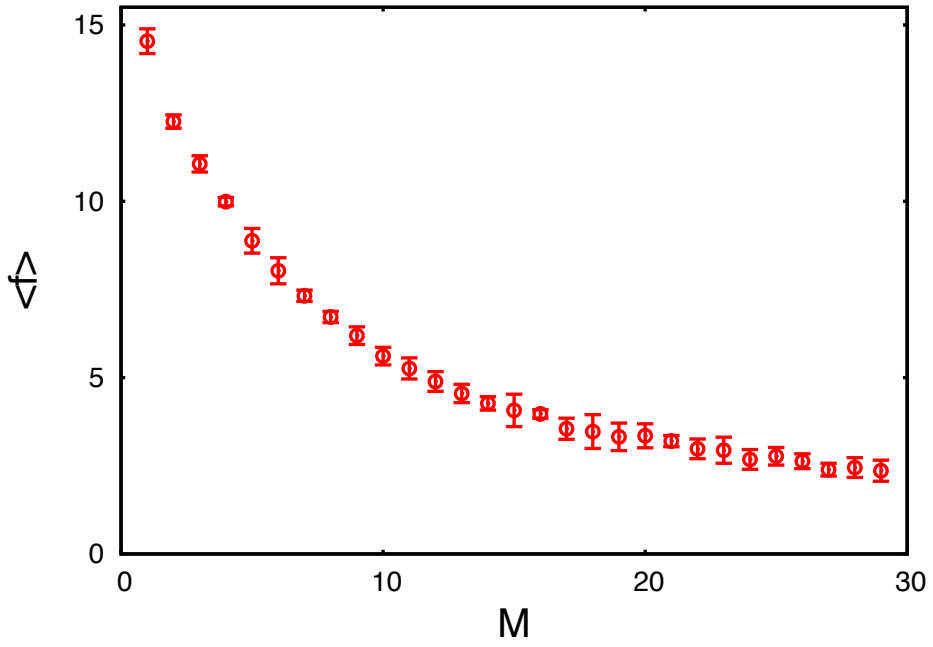

Figure 3.5: Mean finger number $\langle f \rangle$ in a system of size 1200×1200, plotted against the mobility M for the KMC model, reproduced from the data in Fig. 14 of Ref. [51]. The data is averaged over seven runs where the centre of each point corresponds to the mean value and the error bars show one standard deviation from the mean.

mation can also be found. However, these structures only have one typical length scale and do not resemble the dual-scaled network patterns found in some of the experiments, such as those displayed in Fig. 3.4 (b). A pseudo three-dimensional KMC model has also been considered [48, 49] which can reproduce these dual-scale network patterns. Of particular interest is the branched structures which form and how these structures depend on the various model parameters. Vancea et al. [51] made a detailed investigation of the characteristics of the branched structures. It was observed that as in the experiments a greater number of fingers are formed as the nanoparticle mobility is decreased, as shown in Fig. 3.5. This is an important result which tells us that the mobility of the nanoparticles is a key factor in the formation of the branched patterns. Note that in the experiments the nanoparticle mobility is determined by the length of the thiol length chains bonded to the particle surface.

An alternative approach to modelling such a system is the one developed in this thesis which is based on DDFT, using the theory described in chapter 2. This approach is discussed in detail in the following chapter.

Chapter 4

A DDFT Model for the evaporation of thin films of colloidal suspensions

Recent experiments have shown that various structures may be formed during the evaporative dewetting of thin films of colloidal suspensions. Nanoparticle deposits of strongly branched 'flower-like', labyrinthine and network structures are observed. They are caused by the different transport processes and the rich phase behaviour of the system. We develop a model for the system, based on a dynamical density functional theory, which reproduces these structures. The model is employed to determine the influences of the solvent evaporation and of the diffusion of the colloidal particles and of the liquid over the surface. Finally, we investigate the conditions needed for 'liquid-particle' phase separation to occur and discuss its effect on the self-organised nano-structures.

4.1 Introduction

In this chapter we develop a DDFT model based on the theory laid out in chapter 2 for the system described in chapter 3, i.e. we develop a DDFT model to describe an evaporatively dewetting thin film of a colloidal suspension. Although the model was developed specifically for the system described in chapter 3, we believe that our results also explain the generic features in other systems of evaporating colloidal solutions. The DDFT model goes beyond the 2D KMC model described in Sec. 3.3, by allowing us to investigate the influence of liquid diffusion over the surface.

This chapter takes the following structure: first, in Sec. 4.2, we present the coarse-grained model for the Hamiltonian and the resulting approximation for the free energy used in our model. This is followed in Sec. 4.3 by an alternative derivation of the dynamical equations of the DDFT, where we consider the flux which drives the dynamics, c.f. Eq. (2.48). In Sec. 4.4 we discuss the phase diagram and perform a linear stability analysis of homogeneous films of the pure solvent. We then go on to consider how the phase diagram and linear stability changes with the inclusion of the nanoparticles. In Sec. 4.5 we present fully nonlinear simulation results. In particular, we conduct a detailed investigation into the formation of the branched structures and discuss the

dependence of these patterns on the model parameters. In Sec. 4.6 we summarise our findings and draw some conclusions.

4.2 Free Energy for the System

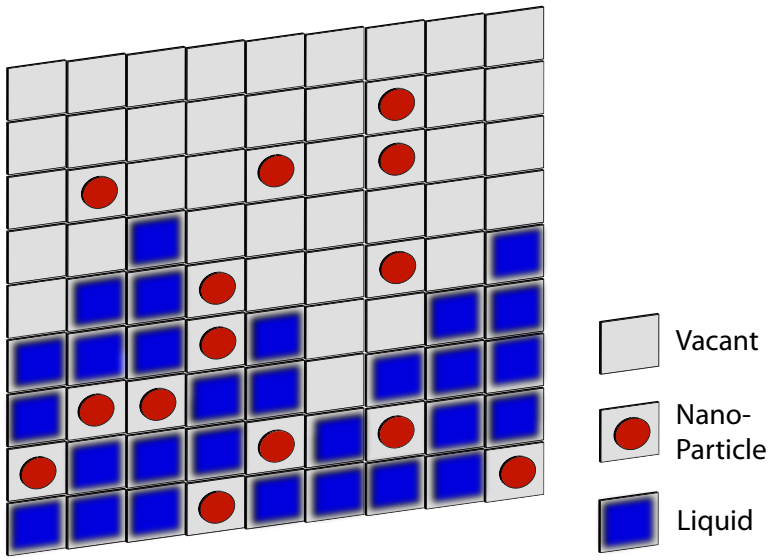

Figure 4.1: The sketch indicates how the substrate is divided into lattice sites and shows the three possible states of each lattice site.

Our starting point for obtaining an approximation for the free energy of the system to be used in the DDFT model is the simplified coarse-grained two-dimensional Hamiltonian model used in the Kinetic Monte Carlo model, discussed in Sec. 3.3. The surface of the substrate is divided into a square array of discrete lattice sites. We choose the cell size so that each cell may be occupied by at most one nanoparticle, i.e. the lattice spacing σ is roughly equal to the diameter of the nanoparticles. Note that previous studies of related models in the context of granular segregation have shown that having larger nanoparticles in the lattice model, i.e. having nanoparticles which have a diameter larger than σ, inevitably changes the thermodynamics of the system [66, 67]. However, in Ref. [51] it was discussed that setting the size of the nanoparticles to be 3σ in diameter has no qualitative effect on the structures that are formed.

Each lattice site must be in one of three possible states: (i) occupied by a nanoparticle, (ii) occupied by liquid or (iii) unoccupied (as displayed in Fig. 4.1). To characterise the state of

the system, we introduce two occupation numbers for each lattice site i: n_i for nanoparticles and l_i for liquid. These occupation numbers are binary values which describe the state of each site. The occupation numbers for (i) a lattice site containing a nanoparticle would be $n_i = 1$, $l_i = 0$, for (ii) a site occupied by a film of liquid we have $n_i = 0$, $l_i = 1$ and for (iii) a vacant site we have $n_i = 0$, $l_i = 0$. This type of lattice model has the following Hamiltonian [45]:

$$\begin{aligned} E &= -\epsilon_l \sum_{<ij>} l_i l_j - \epsilon_n \sum_{<ij>} n_i n_j - \epsilon_{nl} \sum_{<ij>} n_i l_j \\ &\quad -\mu \sum_i l_i + \sum_i \phi_i^l l_i + \sum_i \phi_i^n n_i \ , \end{aligned} \tag{4.1}$$

where $\sum_{<ij>}$ denotes a sum over pairs of nearest neighbours. ϕ_i^l and ϕ_i^n are external potentials acting on the liquid and nanoparticles respectively, at lattice site i. Three interaction terms are included which determine the strength of attraction between neighbouring cells. ϵ_l is the interaction energy between two adjacent cells containing films of liquid, ϵ_n is for adjacent cells which both contain nanoparticles and ϵ_{nl} is the energy between a cell containing a nanoparticle and a cell containing liquid. The amount of liquid on the surface is not a conserved quantity because it can evaporate to and condense from a reservoir of vapour above the surface. μ is the chemical potential of this reservoir. The Hamiltonian (4.1) has a symmetry between droplets (liquid layer) and holes (nearly dry substrate) ($l_i \to (1 - l_i)$) which is not present in the real fluid. While this has negligible effect on the qualitative behaviour of the model it is important to note that for any quantitative analysis the free energy derived below [Eq. (4.8)] should be replaced by a more reliable approximation.

From the Hamiltonian (4.1) we can derive an expression for the free energy of the system. The probability that a lattice site i is covered by a liquid film in an equilibrium configuration is given by the following integral over time t:

$$\rho_i^l = \lim_{\tau \to \infty} \frac{1}{\tau} \int_0^\tau l_i(t) dt. \tag{4.2}$$

Similarly, the probability that a lattice site i contains a nanoparticle is given by the following expression:

$$\rho_i^n = \lim_{\tau \to \infty} \frac{1}{\tau} \int_0^\tau n_i(t) dt. \tag{4.3}$$

By choosing the grid spacing σ to be our unit of length, equal to one, these probabilities are also equal to the local number densities for the liquid and nanoparticles. Following the

approach described in Refs. [68, 69], we make a Bragg-Williams mean field approximation for the (semi-grand) free energy of the system:

$$\begin{aligned} F &= k_B T \sum_i [\rho_i^l \ln \rho_i^l + (1-\rho_i^l)\ln(1-\rho_i^l) + \rho_i^n \ln \rho_i^n \\ &\quad + (1-\rho_i^n)\ln(1-\rho_i^n)] - \epsilon_l \sum_{<ij>} \rho_i^l \rho_j^l - \epsilon_n \sum_{<ij>} \rho_i^n \rho_j^n \\ &\quad - \epsilon_{nl} \sum_{<ij>} \rho_i^n \rho_j^l - \mu \sum_i \rho_i^l + \sum_i \phi_i^l \rho_i^l + \sum_i \phi_i^n \rho_i^n \ , \end{aligned} \tag{4.4}$$

where k_B is Boltzmann's constant and T is the temperature. This is a semi-grand free energy because the liquid is treated in the grand canonical ensemble (the reservoir of vapour fixes the chemical potential μ), whereas the number of nanoparticles in the system is a conserved quantity (so these are treated canonically). Eq. (4.4) is derived using a 'zeroth-order' mean-field approximation and thus higher order terms are omitted (e.g. the terms involving $\ln(1-\rho_i^n-\rho_i^l)$ which describe the excluded area correlations between the nanoparticles and the liquid). This approximation allows the sum of the two density values ρ^n and ρ^l at site i to be greater than one. However, in the work presented here we consider cases where initially ρ_n is small and so the effect of omitting such excluded area correlations and the other higher order terms should not qualitatively affect the behaviour of the model. If we assume that the density values only vary on length scales $\gg \sigma$, then we can define a gradient operator for this discrete system:

$$\begin{aligned} \nabla \rho_{x,y}^l &\equiv \left(\rho_{x+1,y}^l - \rho_{x,y}^l, \rho_{x,y+1}^l - \rho_{x,y}^l\right), \\ \nabla \rho_{x,y}^n &\equiv \left(\rho_{x+1,y}^n - \rho_{x,y}^n, \rho_{x,y+1}^n - \rho_{x,y}^n\right), \end{aligned} \tag{4.5}$$

where each lattice site i is now represented by the coordinates (x, y). Using the operators (4.5) we can express the summation over pairs of nearest neighbours as

$$\begin{aligned} \sum_{<ij>} \rho_i^\alpha \rho_j^\beta &= \sum_{x,y} \rho_{x,y}^\alpha (\rho_{x+1,y}^\beta + \rho_{x-1,y}^\beta + \rho_{x,y+1}^\beta + \rho_{x,y-1}^\beta) \\ &= 4\sum_{x,y} \rho_{x,y}^\alpha \rho_{x,y}^\beta + \sum_{x,y} \rho_{x,y}^\alpha (\rho_{x+1,y}^\beta + \rho_{x-1,y}^\beta + \rho_{x,y+1}^\beta + \rho_{x,y-1}^\beta - 4\rho_{x,y}^\beta) \\ &= 4\sum_{x,y} \rho_{x,y}^\alpha \rho_{x,y}^\beta - \sum_{x,y} \Big[(\rho_{x+1,y}^\alpha - \rho_{x,y}^\alpha)(\rho_{x+1,y}^\beta - \rho_{x,y}^\beta) \\ &\quad + (\rho_{x,y+1}^\alpha - \rho_{x,y}^\alpha)(\rho_{x,y+1}^\beta - \rho_{x,y}^\beta) \Big] \\ &= 4\sum_i \rho_i^\alpha \rho_i^\beta - \sum_i (\nabla \rho_i^\alpha) \cdot (\nabla \rho_i^\beta), \end{aligned} \tag{4.6}$$

where $\alpha, \beta = n, l$. Substituting (4.6) into our lattice free energy (4.4) we obtain

$$
\begin{aligned}
F &= k_B T \sum_i [\rho_i^l \ln \rho_i^l + (1-\rho_i^l)\ln(1-\rho_i^l) + \rho_i^n \ln \rho_i^n \\
&\quad + (1-\rho_i^n)\ln(1-\rho_i^n)] - \sum_i \left[\frac{4}{2}\epsilon_l(\rho_i^l)^2 + \frac{4}{2}\epsilon_n(\rho_i^n)^2 + 4\epsilon_{nl}\rho_i^n\rho_i^l\right] \\
&\quad + \sum_i \left[\frac{\epsilon_l}{2}(\nabla\rho_i^l)^2 + \frac{\epsilon_n}{2}(\nabla\rho_i^n)^2 + \epsilon_{nl}(\nabla\rho_i^n)\cdot(\nabla\rho_i^l)\right] \\
&\quad - \mu\sum_i \rho_i^l + \sum_i \phi_i^l\rho_i^l + \sum_i \phi_i^n\rho_i^n \ , \qquad (4.7)
\end{aligned}
$$

where the factor of $\frac{1}{2}$ is included to avoid double counting. Taking the continuum limit, so that $\sum_i \to \int d\mathbf{r}$, $\rho_i^n \to \rho_n(\mathbf{r})$, $\rho_i^l \to \rho_l(\mathbf{r})$, $\phi_i^n \to \phi_n(\mathbf{r})$ and $\phi_i^l \to \phi_l(\mathbf{r})$ where the vector $\mathbf{r} = (x, y)$ is a continuous variable, we obtain for the free energy of the system:

$$
\begin{aligned}
F[\rho_l, \rho_n] &= \int d\mathbf{r}\Big[f(\rho_l(\mathbf{r}), \rho_n(\mathbf{r})) + \frac{\epsilon_l}{2}(\nabla\rho_l(\mathbf{r}))^2 \\
&\quad + \frac{\epsilon_n}{2}(\nabla\rho_n(\mathbf{r}))^2 + \epsilon_{nl}(\nabla\rho_n(\mathbf{r}))\cdot(\nabla\rho_l(\mathbf{r}))\Big] \\
&\quad + \int d\mathbf{r}\rho_l(\mathbf{r})(\phi_l(\mathbf{r}) - \mu) + \int d\mathbf{r}\rho_n(\mathbf{r})\phi_n(\mathbf{r}), \qquad (4.8)
\end{aligned}
$$

where

$$
\begin{aligned}
f(\rho_l, \rho_n) &= k_B T[\rho_l \ln \rho_l + (1-\rho_l)\ln(1-\rho_l) + \rho_n \ln \rho_n \\
&\quad + (1-\rho_n)\ln(1-\rho_n)] - 2\epsilon_l\rho_l^2 - 2\epsilon_n\rho_n^2 - 4\epsilon_{nl}\rho_n\rho_l. \qquad (4.9)
\end{aligned}
$$

This free energy functional may be employed to determine the phase diagram of the system – i.e. the state of the system in the thermodynamic limit (see Section 4.4). However, the observed patterns are often non-equilibrium structures that are 'dried in', i.e., that evolve towards the equilibrium state on a time scale that is much longer than the typical observation times. To model the non-equilibrium processes that result in the observed self-organised structures, one needs kinetic equations for the time evolution of the densities. They are developed in the following section.

4.3 Modelling the Dynamics of the System

The chemical potential of the nanoparticles may be calculated using the following functional derivative (c.f. Eq. (2.48)):

$$
\mu_n = \frac{\delta F[\rho_n, \rho_l]}{\delta\rho_n} = \ln\left(\frac{\rho_n}{1-\rho_n}\right) - \epsilon_n(4\rho_n + \nabla^2\rho_n) - \epsilon_{nl}(4\rho_l + \nabla^2\rho_l). \qquad (4.10)
$$

In equilibrium systems the chemical potentials take a uniform value throughout the system. However, this is not the case for non-equilibrium configurations that the system takes during its time evolution. There, the chemical potential varies temporally and spatially over the surface. In particular, non-equilibrium density profiles $\rho_l(\mathbf{r},t)$ and $\rho_n(\mathbf{r},t)$ give, via Eq. (4.10), a non-equilibrium chemical potential for the nanoparticles $\mu_n(\mathbf{r},t)$. Thus, the time-dependent densities are coarse-grained 'average' quantities. Assuming that locally, the system is in equilibrium, we may define these non-equilibrium density fields in a similar way as the equilibrium densities (see Eqs. (4.2) and (4.3)):

$$\rho_i^l = \frac{1}{\tau_M}\int_0^{\tau_M} l_i(t)dt, \tag{4.11}$$

$$\rho_i^n = \frac{1}{\tau_M}\int_0^{\tau_M} n_i(t)dt, \tag{4.12}$$

where τ_M is now a finite time that is large compared to the solvent molecular collision time, but is small compared to the time scale for a nanoparticle to move from one lattice site to a neighbouring lattice site. In Sec. 2.3 we discussed how the driving force for the dynamics is given by the gradient of the chemical potential. Thus the driving force which causes a flux of the nanoparticles over the surface of the substrate is given by the gradient of the chemical potential of the nanoparticles μ_n, hence the nanoparticle current is given by

$$\mathbf{j}_n = -M_n(\mathbf{r},t)\nabla\frac{\delta F[\rho_n,\rho_l]}{\delta\rho_n(\mathbf{r},t)}, \tag{4.13}$$

where $M_n(\mathbf{r},t)$ is a mobility coefficient which we assume to depend on the local densities $\rho_n(\mathbf{r},t)$ and $\rho_l(\mathbf{r},t)$. Since the number of nanoparticles in the system is conserved we can combine Eq. (4.13) with the continuity equation to get

$$\frac{\partial\rho_n(\mathbf{r},t)}{\partial t} = \nabla\cdot\left[M_n(\rho_n,\rho_l)\nabla\frac{\delta F[\rho_n,\rho_l]}{\delta\rho_n(\mathbf{r},t)}\right]. \tag{4.14}$$

We expect that when the liquid density is uniform throughout the system ($\rho_l(\mathbf{r})=\rho$) and the density of the nanoparticles is small everywhere ($\rho_n(\mathbf{r})\ll 1$) then the nanoparticle dynamics given by Eq. (4.14) must reduce to the diffusion equation (i.e. Eq. (4.13) becomes Fick's law). When we apply this to Eq. (4.10), for small ρ_n, we get the leading order term:

$$\mu_n(\mathbf{r}) \approx k_BT\ln\rho_n(\mathbf{r}) + C + O(\rho_n), \tag{4.15}$$

where $C = C(\rho_l)$ represents constant terms. Substituting Eq. (4.15) into Eq. (4.14) we see that in order for Eq. (4.14) to reduce to the diffusion equation the mobility M_n has to be proportional to $\rho_n(\mathbf{r},t)$. Therefore, we write the nanoparticle mobility as:

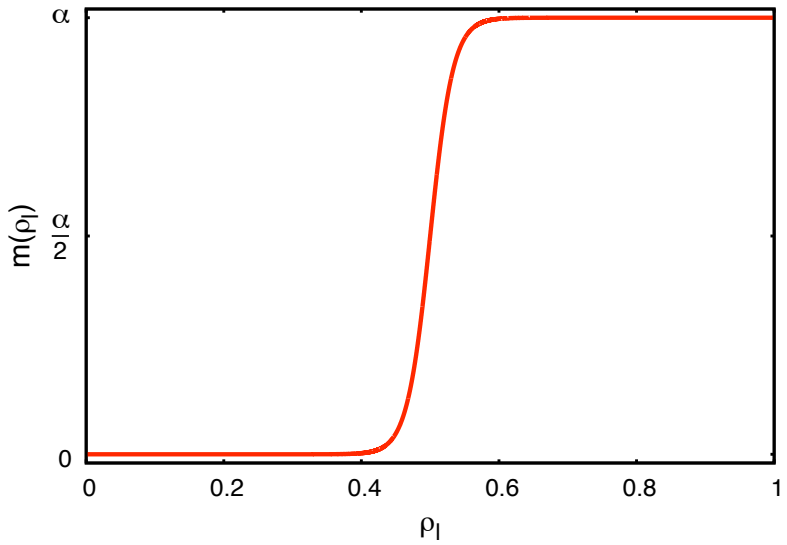

Figure 4.2: Plot showing how nanoparticle mobility function Eq. (4.17) depends on the liquid density ρ_l. The mobility at low values of ρ_l is practically zero and at high values of ρ_l the mobility is approximately equal to α.

$$M_n = \rho_n(\mathbf{r}, t) m(\rho_l(\mathbf{r}, t)), \tag{4.16}$$

where $m(\rho_l(\mathbf{r}, t))$ is a function of the local liquid density. We assume that the diffusion of the nanoparticles over the surface is caused by the Brownian 'kicks' from the molecules in the liquid. Therefore when the liquid density is low (on the dry substrate) the nanoparticles are almost immobile. However, when the density of the liquid on the surface is high (where the substrate is covered by the liquid film), the nanoparticles are much more mobile. We model this behaviour by a function $m(\rho_l(\mathbf{r}, t))$ which switches between a very small value, when ρ_l is small and α, which is the mobility coefficient for the nanoparticles in a liquid film, when $\rho_l > 0.5$. The precise form of $m(\rho_l)$ has a negligible effect on the qualitative behaviour of the system. Here we use:

$$m(\rho_l) = \frac{\alpha}{2}\{1 + \tanh[30(\rho_l - \frac{1}{2})]\}. \tag{4.17}$$

A plot showing how the mobility $m(\rho_l)$ varies with the liquid density ρ_l is shown in Fig. 4.2. Note that dynamical equations of the form in Eq. (4.14), taken together with various expressions for the free energy, have been developed. A notable early example is the Cahn Hilliard equation [70]. In various recent studies, equations of this form with alternative mobility functions are used. These are chosen in order to model various physical effects. For example, the

mobility function may take the form $m(\rho) = (1 - \frac{\rho}{\rho_c})^{\phi}$ [63, 71], where ρ_c is a critical density value [1]. As the local density approaches this critical value the mobility goes to zero, making ρ_c an upper bound of the density field. The effect of using such a mobility function in the model presented here is briefly examined in Sec. 4.5.5. A mobility function of this type is used to model glassy transitions, in systems where jamming of the nanoparticles occurs as the density is increased. Another example is Ref. [73], in which a density dependent mobility was used in order to model the effect of hydrodynamic interactions between colloidal particles.

Next we consider the time evolution of the liquid density $\rho_l(\mathbf{r}, t)$. The dominant process governing the dynamics of the liquid is the evaporation and condensation of the liquid between the surface and the vapour reservoir above the substrate. We define two different chemical potentials: μ is the chemical potential of the liquid in the reservoir (cf. Eq. (4.4)) and $\mu_S(\mathbf{r}, t) = \frac{\delta F}{\delta \rho_l} + \mu$ denotes the local chemical potential of the liquid on the substrate, where $\frac{\delta F}{\delta \rho_l} = \ln\left(\frac{\rho_l}{1-\rho_l}\right) - \epsilon_l(4\rho_l + \nabla^2\rho_l) - \epsilon_{nl}(4\rho_n + \nabla^2\rho_n) - \mu$. We assume that the evaporative contribution to the time evolution of the liquid density is proportional to the difference between $\mu_S(\mathbf{r}, t)$ and μ. This gives us the following expression:

$$\frac{\partial \rho_l(\mathbf{r}, t)}{\partial t} = -M_l^{nc} \frac{\delta F[\rho_n, \rho_l]}{\delta \rho_l(\mathbf{r}, t)}, \tag{4.18}$$

where the dynamical coefficient M_l^{nc} is assumed to be a constant. The value of M_l^{nc} determines the rate of the non-conserved (evaporation) dynamics of the liquid. We should also allow for (conserved) diffusive motion of the liquid over the surface. We assume from DDFT that the diffusion of the liquid takes a similar form as the diffusion of the nanoparticles given in Eq. (4.14). We therefore model the full liquid dynamics by combining the diffusive and the evaporative terms

$$\frac{\partial \rho_l(\mathbf{r}, t)}{\partial t} = \nabla \cdot \left[M_l^c \rho_l \nabla \frac{\delta F[\rho_n, \rho_l]}{\delta \rho_l(\mathbf{r}, t)} \right] - M_l^{nc} \frac{\delta F[\rho_n, \rho_l]}{\delta \rho_l(\mathbf{r}, t)}. \tag{4.19}$$

The mobility coefficient M_l^c for the conserved part of the dynamics is assumed to be constant. The ratio between the conserved and non-conserved mobility coefficients determines the influence that the diffusive/evaporative terms have on the overall dynamics of the liquid (i.e. $M_l^{nc}/M_l^c \gg 1$ corresponds to the case when the liquid dynamics are strongly dominated by evaporation and $M_l^{nc}/M_l^c \ll 1$ corresponds to the case when liquid diffusion plays an important

[1] Note that to write the thin film model in Ref. [63] in the gradient dynamics form used here, the procedure presented in Ref. [72] must be followed.

role in the dynamics). Thus, equations (4.8), (4.9), (4.14) and (4.19), taken together, define our model equations, which govern the dynamics of the system.

Note that when the liquid density $\rho_l(\mathbf{r}, t)$ is a constant, the theory reduces to the DDFT described in Sec. 2.3, that may be obtained by approximating the Fokker-Planck equation for a system of Brownian particles with overdamped stochastic equations of motion (see Sec. 2.3 for details) [4, 7, 8, 68, 74]. Equations similar to (4.19) can also be derived in the context of hydrodynamics. The resulting mesoscopic hydrodynamic thin film equations contain different mobilities and local energies [75, 76]. The combination of the diffusive and the evaporative terms can also be seen as a combination of a conserved Cahn-Hillard-type dynamics with a non-conserved Allen-Cahn-type dynamics [77–79].

4.4 Phase Behaviour

4.4.1 One component fluid

It is important to understand the equilibrium behaviour of the fluid in our system as this gives us some insight into how the system behaves when it is out of equilibrium. Of particular importance is to determine what phases we may observe and the stability of these phases. Since we are modelling the evaporative dewetting of the liquid we initially seek parameter values which lead to a high density liquid phase (liquid film) coexisting with a low density phase ('dry' substrate). Employing a linear stability analysis, we calculate the spinodal curve, i.e., the limit of linear stability for an infinitely extended system. The spinodal curve is defined as the locus of points where the curvature of the free energy is zero, $\frac{d^2F}{d\rho^2} = 0$, which is equivalent to the isothermal compressibility being zero [1]. Note that in this subsection we set $\rho_l = \rho$, for simplicity. We also calculate the binodal curve, i.e., the coexisting density values for a system in equilibrium, by equating the chemical potentials, temperature and pressure in each of the coexisting phases. The area outside the binodal curve is a stable region where we see no phase separation. Inside the binodal curve we have phase separation in the thermodynamic limit. However, the linear stability of the fluid depends on whether the curvature of free energy is positive or negative. When we have positive curvature (outside the spinodal curve), the system at this state point rests within a local minimum of the free energy, i.e., it is linearly but not absolutely stable. There is a free energy barrier that must be traversed to cross into the (absolutely stable) equilibrium phase. This is known as the metastable region, where local

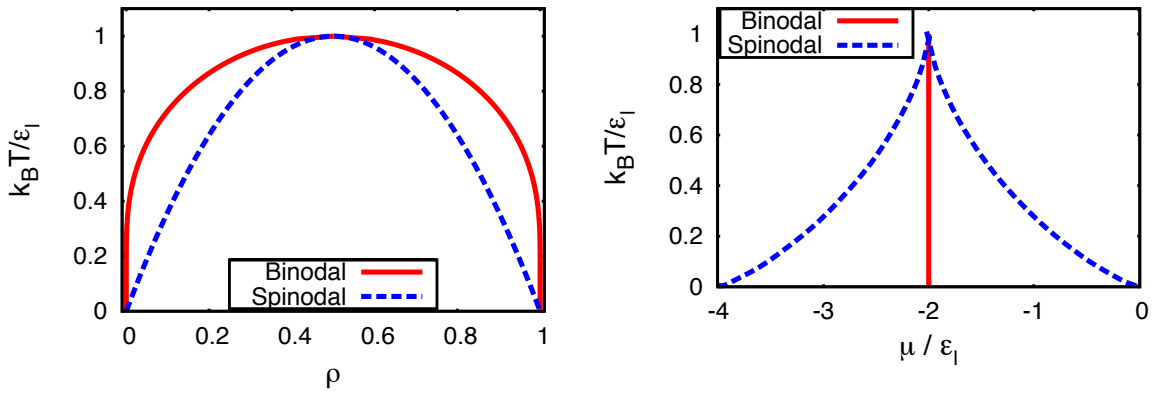

(a) Temperature versus density

(b) Temperature versus chemical potential

Figure 4.3: Phase diagrams showing the binodal (solid line) and spinodal (dotted line) for the one component pure fluid. In (a) we plot the phase diagram in the temperature T versus density ρ plane and in (b) we display the same phase diagram in the temperature versus chemical potential μ plane.

fluctuations in the density (if sufficient in size) create nucleation points for the phase transition to occur. When the curvature of the free energy is negative (inside the spinodal curve) there is no free energy barrier. This is the unstable region where we have spontaneous phase separation, i.e. where fluctuations in the densities spontaneously grow. One may also say that the homogenous fluid layer is linearly unstable to harmonic perturbations with certain wavenumbers.

We first consider the phase behaviour of the reduced case where we have a single component fluid with no nanoparticles (i.e. $\rho_n = 0$), as shown in Fig. 4.3. We set the external potential $\phi_l(\mathbf{r}) = 0$ which results in a uniform fluid density $\rho_l(\mathbf{r}) = \rho = \frac{N}{A}$, where N is the number of 'particles' of liquid (i.e. filled lattice sites) and A is the area of the system. From Eq. (4.9) we find that the Helmholtz free energy per unit area of the uniform system is

$$f = \frac{F}{A} = k_B T \left[\rho \ln \rho + (1-\rho)\ln(1-\rho)\right] - 2\epsilon_l \rho^2. \tag{4.20}$$

We define the Helmholtz free energy per 'particle' as

$$a \equiv \frac{F}{N} = k_B T \left[\ln \rho + \frac{(1-\rho)}{\rho}\ln(1-\rho)\right] - 2\epsilon_l \rho. \tag{4.21}$$

From this, we may calculate other thermodynamic quantities: the pressure P and chemical potential μ, which are given by the following relations [1]:

$$P = \rho^2 \left(\frac{\partial a}{\partial \rho}\right), \tag{4.22}$$

$$\mu = a + \rho \left(\frac{\partial a}{\partial \rho}\right). \tag{4.23}$$

We can calculate the spinodal for the one component fluid from the free energy Eq. (4.20) and the definition of the spinodal $\frac{d^2 f}{d\rho^2} = 0$, giving us the following equation:

$$\frac{k_B T}{\epsilon_l} = 4\rho(1-\rho). \tag{4.24}$$

Equations (4.21) and (4.22) give the following expression for the pressure in the system:

$$P = -k_B T \ln(1-\rho) - 2\epsilon_l \rho^2. \tag{4.25}$$

In order to simplify the task of determining the phase diagram, we may use the symmetry between filled and empty lattice sites, which is present in the Hamiltonian (4.1). This means that for the one component fluid, the phase diagram is symmetric around the line $\rho = \frac{1}{2}$, i.e. for a phase on the binodal with a density of $\rho = \rho_1$ the coexisting phase has a density of $\rho_2 = (1 - \rho_1)$. Using Eq. (4.25) and this symmetry of the Hamiltonian, we obtain the following expression for the density along the binodal, by equating the pressure in the two phases ($P_1 = P_2$):

$$\frac{k_B T}{\epsilon_l} = \frac{2(2\rho - 1)}{\ln[\rho/(1-\rho)]} \tag{4.26}$$

The maximum on this curve is at $\rho = \frac{1}{2}$ and corresponds to the critical temperature $k_B T/\epsilon_l = 1$. Below the critical temperature there are two solutions; these are the coexisting densities. The binodal and spinodal curves for the pure liquid are plotted in Fig. 4.3 (a). Fig. 4.3 (b) shows the value of the chemical potential along these curves.

The spinodal region can also be calculated from the dynamical equations (4.14) and (4.19) employing a linear stability analysis. This allows us to determine the typical length scales of the density fluctuations in the liquid film which might exist during the evaporation process. To perform the linear stability analysis we consider a liquid density which varies in space and time $\rho_l = \rho(\mathbf{r}, t)$. The free energy for the single component fluid ($\rho_n = 0$) is given by:

$$F = \int d\mathbf{r} \left[f(\rho) + \frac{\epsilon}{2}(\nabla\rho)^2 - \mu\rho \right], \tag{4.27}$$

where the subscript on the liquid interaction variable ϵ_l is dropped for simplicity. The steady state solutions of the liquid dynamical equation Eq. (4.19) represent the equilibrium density configurations. There are several steady states for this system, (e.g. a density profile containing a free interface between two co-existing densities with $\mu = \mu_{\text{coex}}$) but here we consider the simplest steady state: a flat homogeneous film with a density $\rho = \rho_0$ which is defined by:

$$\left.\frac{\delta F}{\delta \rho}\right|_{\rho_0} = 0. \tag{4.28}$$

We consider small amplitude perturbations $\delta\rho$ from ρ_0 of the form $\rho = \rho_0 + \delta\rho = \rho_0 + \phi e^{i\mathbf{k}\cdot\mathbf{r}} e^{\beta t}$, where the amplitude $\phi \ll 1$ is a small positive constant, $k = |\mathbf{k}|$ is the wavenumber and β is the rate of growth/decay with time (for positive/negative values) of the perturbation. We substitute this expression for ρ into the dynamical equation (4.19) and expand in powers of $\delta\rho$. Then taking just the leading order terms allows us to derive a simple expression for β which can be solved analytically.

A Taylor series expansion of the functional derivative of the free energy (4.27) yields:

$$\begin{aligned} \frac{\delta F}{\delta \rho} &= \frac{\partial f}{\partial \rho} - \epsilon \nabla^2 \rho - \mu \\ &= \left.\frac{\partial f}{\partial \rho}\right|_{\rho_0} + \left.\frac{\partial^2 f}{\partial \rho^2}\right|_{\rho_0} \delta\rho + \epsilon k^2 \delta\rho - \mu + O(\delta\rho^2). \end{aligned} \tag{4.29}$$

Substituting this approximation for the functional derivative (4.29) into the dynamical equation (4.19) we obtain

$$\begin{aligned} \beta\delta\rho &= M_c \nabla \cdot \left[\rho_0 (ik \left.\frac{\partial^2 f}{\partial \rho^2}\right|_{\rho_0} \delta\rho + i\epsilon k^3 \delta\rho)\right] - \\ &\quad M_{nc}\left(\left.\frac{\partial f}{\partial \rho}\right|_{\rho_0} + \left.\frac{\partial^2 f}{\partial \rho^2}\right|_{\rho_0} \delta\rho + \epsilon k^2 \delta\rho - \mu\right) + O(\delta\rho^2). \end{aligned} \tag{4.30}$$

Using the definition of ρ_0 [Eq. (4.28)] gives $\left.\frac{\partial f}{\partial \rho}\right|_{\rho_0} - \mu = 0$ and neglecting second order terms $O(\delta\rho^2)$ we arrive at the expression for the growth rate

$$\beta = -\left(M_c \rho_0 k^2 + M_{nc}\right)\left(\left.\frac{\partial^2 f}{\partial \rho^2}\right|_{\rho_0} + \epsilon k^2\right). \tag{4.31}$$

When β is positive, small perturbations from the steady state ρ_0 with the wavenumber k grow in amplitude over time. Conversely, if β is negative then small perturbations decay. Since M_c, ρ_0, k^2, M_{nc} and ϵ are all positive quantities, β is always negative (i.e. the fluid is stable for all wavenumbers k) when the second derivative $\left.\frac{\partial^2 f}{\partial \rho^2}\right|_{\rho_0}$ is positive. However, when $\left.\frac{\partial^2 f}{\partial \rho^2}\right|_{\rho_0}$ is

negative, we find that β is positive for small values of k and negative when k is large - i.e. the fluid is unstable against long wavelength (small wave number) fluctuations in density. This corresponds to the thermodynamic definition of the spinodal as previously discussed. We may define a critical wavenumber k_c, as the wavenumber at which $\beta(k_c) = 0$. When $\frac{\partial^2 f}{\partial \rho^2}\big|_{\rho_0} < 0$ the relevant critical wavenumber k_c is given by:

$$k_c = \pm\sqrt{-\frac{1}{\epsilon}\frac{\partial^2 f}{\partial \rho^2}\bigg|_{\rho_0}}. \tag{4.32}$$

The real system we are modelling is very large ($L \gg 2\pi/k_c$), which means fluctuations can occur on the full spectrum of wavenumbers. The mode with wavenumber $k = k_m$, which has the largest positive value for β grows the fastest. The wavenumber k_m corresponds to a typical length scale $2\pi/k_m$ which is visible during the early stages of spinodal decomposition. However, at later stages (beyond the linear stage) the length scale of the modulations is likely to deviate from this value as the pattern coarsens. For the purely evaporative case when $M_c = 0$, the maximum value of $\beta(k)$ occurs at $k = k_m = 0$, which means there is no typical length scale in the early stages of the evaporation process. However, in the purely diffusive case $M_{nc} = 0$ (and $\frac{\partial^2 f}{\partial \rho^2}\big|_{\rho_0} < 0$), $\beta(k = 0) = 0$ due to mass conservation, and the maximum value of $\beta(k)$ occurs at a non-zero value of k_m, so the typical length scale $2\pi/k_m$ is visible during the spinodal decomposition–evaporation. In all other cases the following expression is both a necessary and sufficient condition for the existence of the typical length scale (i.e. $k_m \neq 0$):

$$\frac{M_{nc}}{M_c} < -\frac{\rho_0}{\epsilon}\frac{\partial^2 f}{\partial \rho^2}\bigg|_{\rho_0}. \tag{4.33}$$

If a typical length scale does exist, then the corresponding wavenumber k_m is given by:

$$k_m = \sqrt{-\frac{1}{2}\left(\frac{1}{\epsilon}\frac{\partial^2 f}{\partial \rho^2}\bigg|_{\rho_0} + \frac{M_{nc}}{\rho_0 M_c}\right)}. \tag{4.34}$$

Figure 4.4 displays (a) typical $\beta(k)$ curves for a one component fluid and (b) the values of $1/\epsilon$ and ρ_0 where each type of curve is found (for the case when $M_{nc}/M_c = 1$ and $k_B T = 1$). Three distinct cases are displayed: Case (i) the red solid line in (a) and the red striped area in (b) display the case when one observes the growth of density fluctuations with a typical length scale. Case (ii), the blue dashed line in (a) and the blue hashed area in (b) correspond to the situation when the fluid is unstable for density fluctuations corresponding to small wavenumbers k but no typical length scale is observed, because the fastest growing mode is the $k = 0$ fluctuation. Case (iii), the green dotted line in (a), corresponding to the green solid area in (b), displays the

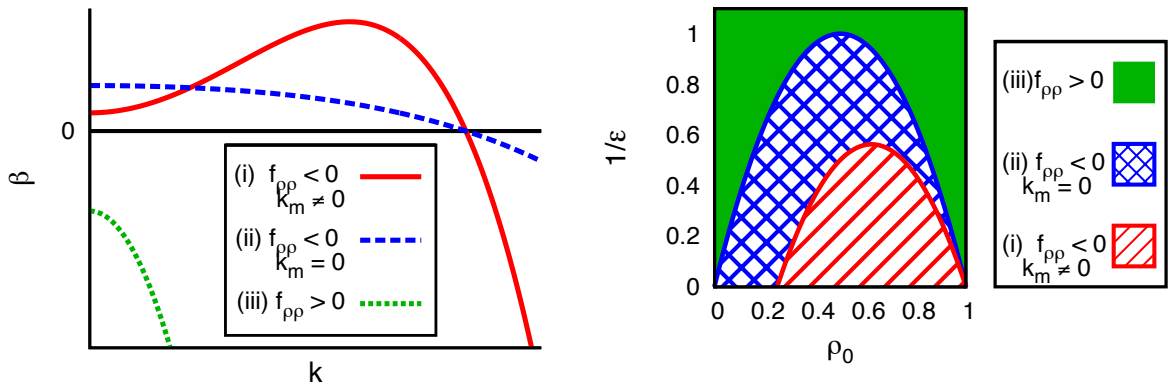

(a) Typical dispersion relations

(b) Classification by parameter space

Figure 4.4: There are three possible forms for $\beta(k)$: (a) shows an example of each form and (b) shows the regions in parameter space where these different types of $\beta(k)$ curves occur, for the case when $M_{nc}/M_c = 1$ and $k_BT = 1$.

situation when the liquid is linearly stable against density fluctuations with all wavenumbers k.

4.4.2 Binary mixture

To determine the binodal and spinodal curves for the binary mixture is more challenging than for the one component system. There are many more parameters defining the model. In particular, the behaviour of the system strongly depends on the ratios between the different interaction strengths ϵ_l, ϵ_n and ϵ_{nl}. Ref. [80] gives a good overview of the equilibrium bulk fluid phase behaviour for binary fluid mixtures and the different classes of phase diagrams that may be observed. Here, we only describe the influence of the chemical potential of the nanoparticles μ_n on the densities in the coexisting phases and on the critical point.

For two phases of a binary mixture to coexist in thermodynamic equilibrium, there are four conditions that must be satisfied. We denote these two phases as (i) the low density phase (LDP) or 'dry' substrate and (ii) the high density phase (HDP) or substrate covered by a colloidal film:

$$T^{LDP} = T^{HDP}, \tag{4.35}$$

$$\mu_l^{LDP} = \mu_l^{HDP}, \tag{4.36}$$

$$\mu_n^{LDP} = \mu_n^{HDP}, \tag{4.37}$$

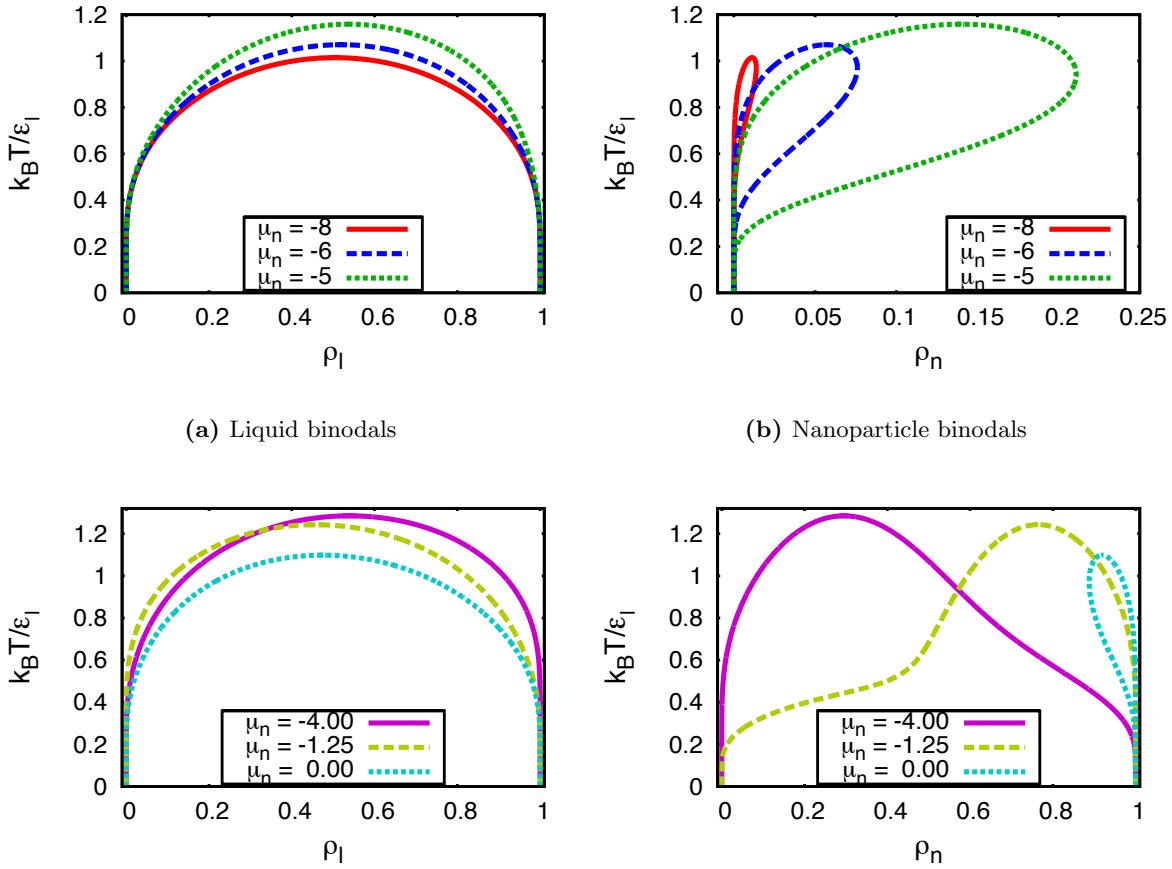

(a) Liquid binodals

(b) Nanoparticle binodals

(c) Liquid binodals

(d) Nanoparticle binodals

Figure 4.5: Binodal curves for the binary mixture for varying fixed values of the chemical potential of the nanoparticles μ_n, for the case when $\epsilon_n/\epsilon_l = 0.43$ and $\epsilon_{nl}/\epsilon_l = 0.57$.

$$P^{LDP} = P^{HDP}, \tag{4.38}$$

where T is the temperature, μ_l and μ_n are the chemical potentials of the liquid and nanoparticles respectively, P is the pressure and the superscript denotes the phase. The first of these equations is trivial to satisfy in our model. We may then fix the chemical potential of the nanoparticles, to some value η, and then solve equations (4.36), (4.38), $\mu_n^{LDP} = \eta$ and $\mu_n^{HDP} = \eta$ for the four density values: ρ_l^{LDP}, ρ_n^{LDP}, ρ_l^{HDP} and ρ_n^{HDP}. The curves of the coexisting density values (binodals) for the parameters $\epsilon_{nl}/\epsilon_l = 0.57$ and $\epsilon_n = 0.43$ are displayed in Fig. 4.5. The density values calculated for the two phases meet at a critical temperature to form binodal curves similar to the one found for the one component system, displayed in Fig. 4.3 (a). However, we find that the reflection symmetry w.r.t. the liquid density $\rho_l = 1/2$ seen for the one component fluid is broken. In particular, the critical point of the liquid is no longer at $\rho_l = 1/2$. The liquid

binodal reduces to the one for the pure liquid as $\mu_n \to \pm\infty$. The curves for $\mu_n \to -\infty$ and $\mu_n \to \infty$ are identical within our model due to the symmetry of the Hamiltonian (4.1). We observe that the density of the nanoparticles ρ_n becomes very small as the chemical potential decreases $\mu_n \to -\infty$. Conversely, the density becomes very large $\rho_n \to 1$ as the chemical potential increases $\mu_n \to \infty$. The critical point on the nanoparticle binodal curve shifts in a similar manner to that of the liquid binodal.

We now consider the linear stability of the fluid for the two component case. There are many different possible steady states for the binary system including some with interfaces between coexisting phases. However, here we limit ourselves to investigating the linear stability of the simplest steady state: where both components have a uniform constant density over the surface. The uniform density of the nanoparticle film is denoted by $\rho_n = \rho_n^0$ and the density of the liquid is given by $\rho_l = \rho_l^0$ where ρ_l^0 is determined from the condition:

$$\left.\frac{\delta F}{\delta \rho_l}\right|_{\rho_l^0} = 0. \tag{4.39}$$

We consider small amplitude perturbations in the density of both components from this steady state. We assume these perturbations to take the form:

$$\rho_l = \rho_l^0 + \delta\rho = \rho_l^0 + \phi e^{i\mathbf{k}\cdot\mathbf{r}} e^{\beta t}, \tag{4.40}$$

$$\rho_n = \rho_n^0 + \chi\delta\rho = \rho_n^0 + \chi\phi e^{i\mathbf{k}\cdot\mathbf{r}} e^{\beta t}, \tag{4.41}$$

where the amplitude $|\phi| \ll 1$ and the parameter χ is the ratio between the perturbation in the densities of the two components. The sign of χ determines whether any instabilities are in-phase (positive) or anti-phase (negative) between the two coupled density fields. From the magnitude of χ we can determine whether an instability is driven by the liquid component ($|\chi| \ll 1$), the nanoparticles ($|\chi| \gg 1$) or stems from the interaction between the two components ($|\chi| = O(1)$). Making a Taylor series expansion of the functional derivative of the free energy with respect to the liquid density and using the result from Eq. (4.39), we get

$$\frac{\delta F}{\delta \rho_l} = \left.\frac{\partial^2 f}{\partial \rho_l^2}\right|_{\rho_l^0\rho_n^0} \delta\rho + \chi \left.\frac{\partial^2 f}{\partial \rho_l \partial \rho_n}\right|_{\rho_l^0\rho_n^0} \delta\rho + k^2\epsilon_l\delta\rho + k^2\chi\epsilon_{nl}\delta\rho + O(\delta\rho^2). \tag{4.42}$$

Keeping only terms linear in $\delta\rho$ and substituting this expression into the liquid dynamical equation (4.19) we obtain

$$\begin{aligned}\beta\delta\rho &= M_c^l\nabla\cdot\left[(\rho_l^0+\delta\rho)\left(ik\frac{\partial^2 f}{\partial\rho_l^2}\bigg|_{\rho_l^0,\rho_n^0}\delta\rho+ik\chi\frac{\partial^2 f}{\partial\rho_l\partial\rho_n}\bigg|_{\rho_l^0\rho_n^0}\delta\rho+ik^3\epsilon_l\delta\rho+ik^3\chi\epsilon_{nl}\delta\rho\right)\right]\\ &\quad -M_{nc}^l\left(\frac{\partial^2 f}{\partial\rho_l^2}\bigg|_{\rho_l^0,\rho_n^0}\delta\rho+\chi\frac{\partial^2 f}{\partial\rho_l\partial\rho_n}\bigg|_{\rho_l^0\rho_n^0}\delta\rho+k^2\epsilon_l\delta\rho+k^2\chi\epsilon_{nl}\delta\rho\right),\end{aligned}$$

for which we obtain

$$\beta=-(M_c^l\rho_l^0k^2+M_{nc}^l)\left(\frac{\partial^2 f}{\partial\rho_l^2}\bigg|_{\rho_l^0,\rho_n^0}+\chi\frac{\partial^2 f}{\partial\rho_l\partial\rho_n}\bigg|_{\rho_l^0,\rho_n^0}+k^2\epsilon_l+k^2\chi\epsilon_{nl}\right). \tag{4.43}$$

Turning our attention now to the nanoparticles: in order to linearise Eq. (4.14), we must first examine the nanoparticle mobility function $M^n(\rho_l,\rho_n)=\rho_n m(\rho_l)$, given by Eqs. (4.16) and (4.17) in our model. Making a Taylor series expansion of the function $m(\rho_l)$ we obtain

$$\frac{m}{\alpha}=\gamma_0+\gamma_1\delta\rho+O(\delta\rho^2), \tag{4.44}$$

where $\gamma_0\approx 0$ for small values of ρ_l ($\rho_l<0.45$) and $\gamma_0\approx 1$ for large values of ρ_l ($\rho_l>0.55$). Making a Taylor series expansion of the functional derivative with respect to the density of the nanoparticles we find

$$\frac{\delta F}{\delta\rho_n}=\frac{\partial f}{\partial\rho_n}\bigg|_{\rho_l^0\rho_n^0}+\chi\frac{\partial^2 f}{\partial\rho_n^2}\bigg|_{\rho_l^0\rho_n^0}\delta\rho+\frac{\partial^2 f}{\partial\rho_l\partial\rho_n}\bigg|_{\rho_l^0\rho_n^0}\delta\rho+k^2\chi\epsilon_n\delta\rho+k^2\epsilon_{nl}\delta\rho+O(\delta\rho^2). \tag{4.45}$$

Substituting this expression (4.45) together with Eq. (4.44), into the time evolution equation for the nanoparticles Eq. (4.14) we obtain

$$\begin{aligned}\chi\beta\delta\rho &= \alpha\nabla\cdot\left[(\rho_n^0+\chi\delta\rho)(\gamma_0+\gamma_1\delta\rho)\left(ik\chi\frac{\partial^2 f}{\partial\rho_n^2}\bigg|_{\rho_l^0\rho_n^0}\delta\rho\right.\right.\\ &\quad \left.\left.+ik\frac{\partial^2 f}{\partial\rho_l\partial\rho_n}\bigg|_{\rho_l^0\rho_n^0}\delta\rho+ik^3\chi\epsilon_n\delta\rho+ik^3\epsilon_{nl}\delta\rho\right)\right],\end{aligned}$$

which leads to

$$\chi\beta=-\alpha\rho_n^0\gamma_0k^2\left(\chi\frac{\partial^2 f}{\partial\rho_n^2}\bigg|_{\rho_l^0,\rho_n^0}+\frac{\partial^2 f}{\partial\rho_n\partial\rho_l}\bigg|_{\rho_l^0,\rho_n^0}+k^2\chi\epsilon_n+k^2\epsilon_l\right). \tag{4.46}$$

When ρ_l is small, $\gamma_0\approx 0$. In consequence, $\chi=0$ and the Eqs. (4.43) and (4.46) reduce to the one of the one component fluid (with a local free energy that depends also on ρ_n^0). We now address the case when $\rho_l>0.55$, and we therefore assume $\gamma_0=1$. The expressions for the time dependency of the amplitudes of the two density fields (Eq. (4.43) and Eq. (4.46)) can be solved simultaneously to determine β and χ as a function of the wavenumber k. This allows us to determine the stability of the fluid for different values of the system parameters. A fact

that simplifies the analysis is that these two equations may be written in matrix form (similar to the case of two coupled mesoscopic hydrodynamic equations for dewetting two-layer films [81]):

$$\beta \begin{pmatrix} 1 \\ \chi \end{pmatrix} = \mathbf{M} \cdot \mathbf{G} \begin{pmatrix} 1 \\ \chi \end{pmatrix}, \tag{4.47}$$

where,

$$\begin{aligned} \mathbf{M} &= \begin{pmatrix} -\alpha \rho_n^0 k^2 & 0 \\ 0 & -(M_c^l \rho_l^0 k^2 + M_{nc}^l) \end{pmatrix}, \\ \mathbf{G} &= \begin{pmatrix} k^2 \epsilon_n + f_{nn} & k^2 \epsilon_{nl} + f_{nl} \\ k^2 \epsilon_{nl} + f_{nl} & k^2 \epsilon_l + f_{ll} \end{pmatrix}, \end{aligned}$$

and we have used the shorthand notation $f_{ij} \equiv \frac{\partial^2 f}{\partial \rho_i \partial \rho_j}\big|_{\rho_l^0 \rho_n^0}$, where $i, j = n, l$ and where n denotes the nanoparticles and l denotes the liquid. We can determine $\beta(k)$ using the following expression for the eigenvalues of a 2×2 matrix:

$$\beta(k) = \frac{\mathrm{Tr}(\mathbf{M} \cdot \mathbf{G})}{2} \pm \sqrt{\frac{\mathrm{Tr}(\mathbf{M} \cdot \mathbf{G})^2}{4} - |\mathbf{M} \cdot \mathbf{G}|}. \tag{4.48}$$

We define critical wavenumbers $k = k_c$ for the density fluctuations in the two component fluid as the wave numbers at which one of the two solutions of Eq. (4.48) is equal to zero. Below [Eqs. (4.51) and (4.52)] we derive explicit expressions for k_c which can be used to determine the conditions for the linear stability of the two component fluid (i.e. the fluid is stable when there is no solution for k_c and the function $\beta(k) < 0$ for all wavenumbers k). Since the matrix $\mathbf{M}$ is diagonal and all diagonal elements are non-zero the inverse $\mathbf{M^{-1}}$ exists, allowing us to rewrite Eq. (4.47) as a generalised eigenvalue problem

$$(\mathbf{G} - \mathbf{M^{-1}} \beta) \begin{pmatrix} 1 \\ \chi \end{pmatrix} = 0. \tag{4.49}$$

Setting $\beta = 0$ in this equation in order to find the critical wavenumbers k_c, we find that the determinant $|\mathbf{G}| = 0$, implying that

$$k_c^4(\epsilon_n \epsilon_l - \epsilon_{nl}^2) + k_c^2(\epsilon_n f_{ll} + \epsilon_l f_{nn} - 2\epsilon_{nl} f_{nl}) + f_{nn} f_{ll} - f_{nl}^2 = 0. \tag{4.50}$$

In the special case when $\epsilon_n \epsilon_l = \epsilon_{nl}^2$, the critical wavenumber is given by:

$$k_c = \sqrt{\frac{f_{nl}^2 - f_{nn} f_{ll}}{\epsilon_n f_{ll} + \epsilon_l f_{nn} - 2\epsilon_{nl} f_{nl}}}. \tag{4.51}$$

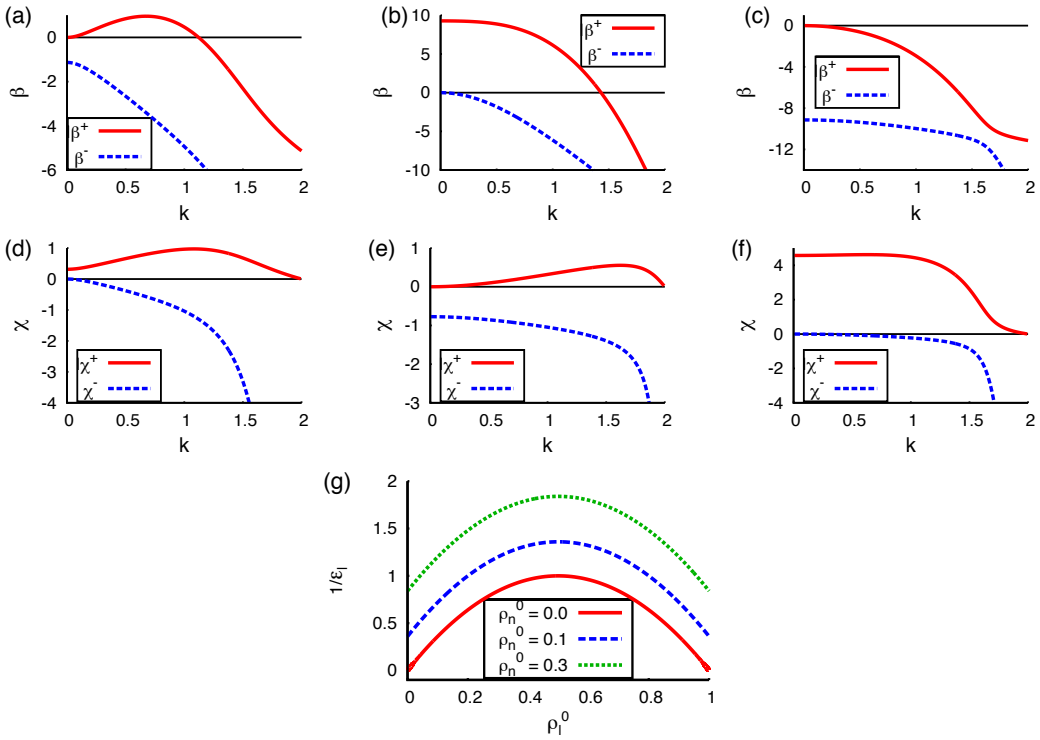

Figure 4.6: (a) - (f) Dispersion relations for the reduced case when $\epsilon_n\epsilon_l = \epsilon_{nl}^2$, and $k_BT = 1$. The graphs in the top row show $\beta(k)$ and the graphs in the middle row show $\chi(k)$. In (a) and (d) the parameters are: $\rho_l^0 = 0.735, \rho_n^0 = 0.3, \epsilon_l = 1, \epsilon_n = 0.81, \epsilon_{nl} = 0.9, \mu = -3, M^n = 1, M_c^l = 0$ and $M_{nc}^l = 1$. In (b) and (e) the parameters are: $\rho_l^0 = 0.715, \rho_n^0 = 0.3, \epsilon_l = 2, \epsilon_n = 0.5, \epsilon_{nl} = 1, \mu = -6, M^n = 1, M_c^l = 0$ and $M_{nc}^l = 3$. In (c) and (f) the parameters are: $\rho_l^0 = 0.9, \rho_n^0 = 0.3, \epsilon_l = \epsilon_n = \epsilon_{nl} = 0.5, \mu = -0.2, M^n = 1, M_c^l = 0$ and $M_{nc}^l = 1$. (g) shows how the spinodal line shifts for increasing ρ_n^0, where $\epsilon_n = \epsilon_l = \epsilon_{nl}$ and $k_BT = 1$.

However, more generally, when $\epsilon_n\epsilon_l \neq \epsilon_{nl}^2$, we have

$$k_c = \sqrt{\frac{-b \pm \sqrt{b^2 - 4ac}}{2a}}, \tag{4.52}$$

where

$$\begin{aligned} a &= \epsilon_n\epsilon_l - \epsilon_{nl}^2, \\ b &= \epsilon_n f_{ll} + \epsilon_l f_{nn} - 2\epsilon_{nl} f_{nl}, \\ c &= f_{nn}f_{ll} - f_{nl}^2. \end{aligned} \tag{4.53}$$

Note that the locus $c = 0$ is the spinodal curve [82, 83]. We categorise the linear behaviour of the system by the signs of a and b in Eq. (4.53) as they have a profound impact on the shape of the dispersion curves. In Figs. 4.6 to 4.10 we display all the different possible $\beta(k)$ curves, together with the corresponding $\chi(k)$. From Eq. (4.48) we see that there are two branches for

$\beta(k)$, which we denote $\beta^+(k)$ and $\beta^-(k)$. The corresponding $\chi(k)$ curves are denoted χ^+ and χ^-, respectively. The β^+ branch (red solid lines) corresponds to the second term in Eq. (4.48) being positive and the β^- branch (blue dashed lines) corresponds to the second term being negative. Due to mass conservation of the nanoparticles, there is always one $\beta(k)$ branch that is zero at $k = 0$, and $\chi = 0$ at $k = 0$ for the curve that corresponds to the $\beta(k)$ that is not zero at $k = 0$. If $f_{ll} \geq 0$ then $\beta^+(k = 0) = 0$ and $\chi^-(k = 0) = 0$. Alternatively, if $f_{ll} \leq 0$ then $\beta^-(k = 0) = 0$ and $\chi^+(k = 0) = 0$.

We begin by discussing the simplified case when $a = 0$ (shown in Fig. 4.6). For this case b is always positive. We find that there are three possible forms for $\beta(k)$, similar to the one component fluid case (c.f. Fig. 4.4). In Fig. 4.6 (a) there is a maximum in β^+ at $k \neq 0$. This indicates that the fluid is unstable and that one will observe the growth of density fluctuations with a typical length scale $\frac{2\pi}{k_m^+}$ during the early stages of the spinodal process. Here k_m^+ refers to the wavenumber at the maximum of β^+. In the second case (Fig. 4.6 (b)) the fluid is linearly unstable for density fluctuations with small wavenumbers k as in Fig. 4.6 (a), but the maximum in $\beta^+(k)$ occurs at $k_m^+ = 0$, i.e. there is no typical length scale visible in the density profiles. In the last case, shown in Fig. 4.6 (c), the fluid is stable for all wavenumbers k. We can use Eq. (4.52) for the critical wavenumber k_c to determine the stability of the system. Since b is positive when $a = 0$, the fluid is only stable when $c > 0$ (i.e. inside the spinodal). Fig. 4.6 (g) shows how the spinodal line shifts as the density of the nanoparticles in the film ρ_n^0 increases. We observe that the spinodal shifts upwards as ρ_n^0 is increased; this, of course, corresponds to the shifting upwards of the binodal line in Fig. 4.5

We now discuss the case when $a > 0$. In this circumstance at least one of the two species are more attracted to their own kind rather than the other component. When a is positive, b can be either positive or negative. Fig. 4.7 shows the case when $a > 0$ and $b > 0$. The behaviour in this case is very similar to that of the previous case, where $a = 0$. We observe the same three types of dispersion relations: the case in (a) where we observe spinodal decomposition leading to the growth of density modulations having a typical length scale, the case in (b) where the fluid is unstable, but with no typical length scale visible and the case in (c) where the fluid is stable. We can use Eq. (4.52) for the critical wavenumber k_c to determine the stability of the system. Since $a > 0$ and $b > 0$ we observe that there is at most one positive root of $\beta(k)$, which only exists if $c < 0$ (i.e. inside the spinodal). The spinodal curve when $a > 0$ and $b > 0$

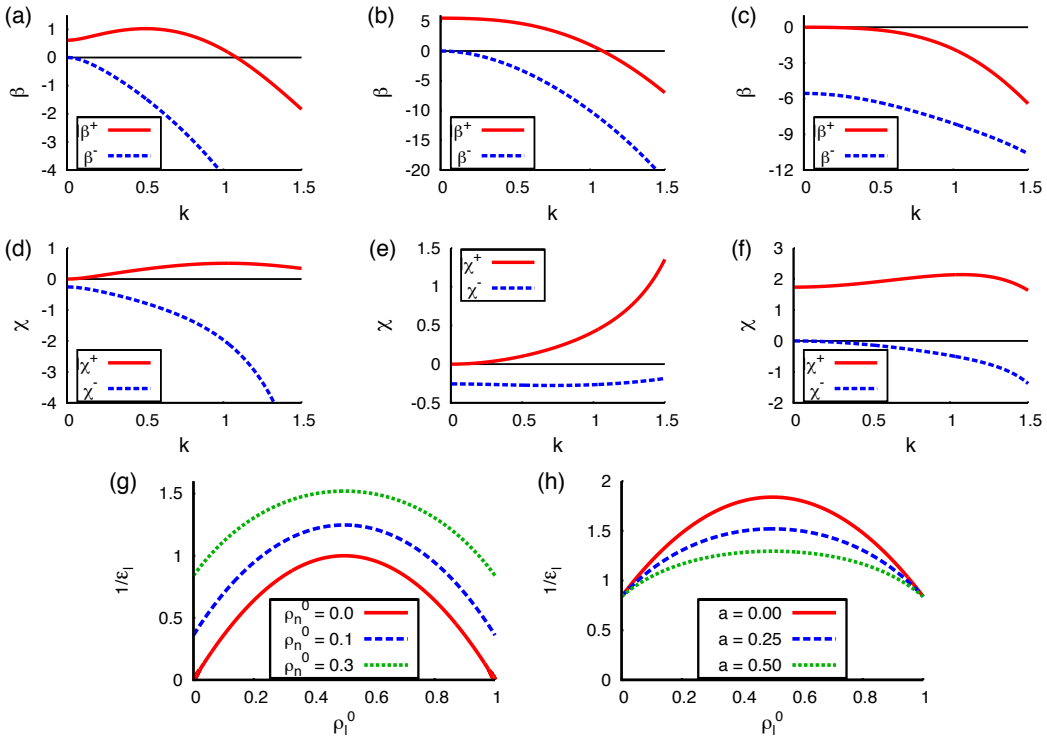

Figure 4.7: (a) - (f) Dispersion relations for the case when $\epsilon_n\epsilon_l > \epsilon_{nl}^2, \quad \epsilon_n f_{ll} + \epsilon_l f_{nn} - 2\epsilon_{nl} f_{nl} > 0$ (i.e. in Eq. (4.53) $a > 0, b > 0$) and $k_B T = 1$. The graphs in the top row show $\beta(k)$ and the graphs in the middle row show $\chi(k)$. In (a) and (d) the parameters are: $\rho_l^0 = 0.648, \rho_n^0 = 0.3, \epsilon_l = 1.25, \epsilon_n = 0.5, \epsilon_{nl} = 0.6, \mu = -3.35, M^n = 1, M_c^l = 0$ and $M_{nc}^l = 1$. In (b) and (e) the parameters are: $\rho_l^0 = 0.648, \rho_n^0 = 0.3, \epsilon_l = 1.25, \epsilon_n = 0.5, \epsilon_{nl} = 0.6, \mu = -3.35, M^n = 1, M_c^l = 0$ and $M_{nc}^l = 9$. In (c) and (f) the parameters are: $\rho_l^0 = 0.901, \rho_n^0 = 0.3, \epsilon_l = 1.4, \epsilon_n = 0.6, \epsilon_{nl} = 0.8, \mu = -3.8, M^n = 1, M_c^l = 0$ and $M_{nc}^l = 1$. (g) shows how the spinodal line shifts for increasing ρ_n^0, where $\epsilon_n\epsilon_l - \epsilon_{nl}^2 = 0.25$, $\epsilon_n = \epsilon_l$ and $k_B T = 1$. (h) shows how the spinodal line shifts as the value of $a = \epsilon_n\epsilon_l - \epsilon_{nl}^2$ increases, when $\rho_n^0 = 0.3$, $\epsilon_n = \epsilon_l$ and $k_B T = 1$.

is plotted in Figs. 4.7 (g) and (h). In (g) we show how the spinodal line moves upwards in $1/\epsilon_l$ as the nanoparticle density ρ_n^0 is increased. In (h) we show how the shape of the spinodal changes as the value of the parameter a is increased. We find that larger values of a make the spinodal curve flatter.

When $a > 0$ and $b < 0$ we observe that the fluid is unstable for all values of the parameters. There is a striking variety of possible dispersion relations. From the expression for the critical wavenumbers Eq. (4.52), we see that it is possible to have either one or two positive non-zero roots. In Fig. 4.8 we display dispersion relations where β has two roots and in Fig. 4.9 we show the possible cases where β has only one root. If there are two positive roots (when $a > 0$ and $b < 0$) then one will occur in each branch. Furthermore, we find that $\beta^-(k = 0) = 0$

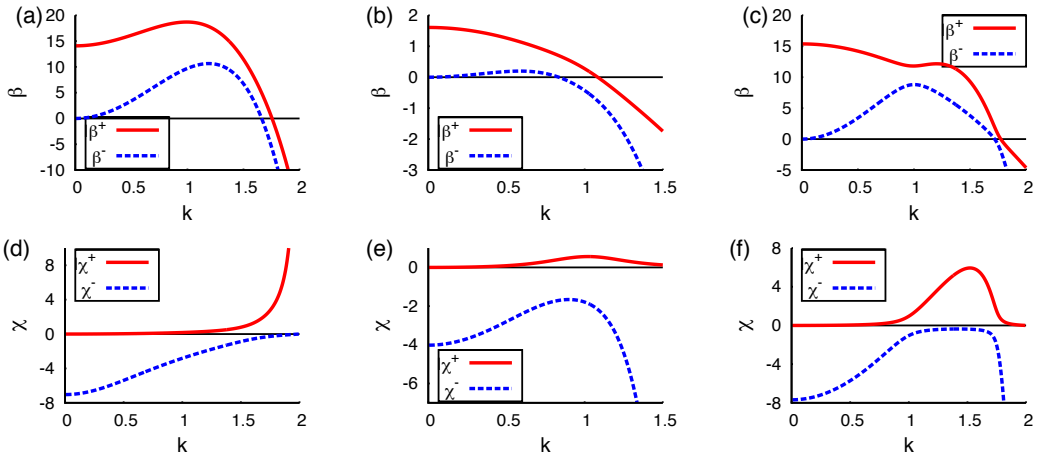

Figure 4.8: (a) - (f) Dispersion relations for the case when $\epsilon_n\epsilon_l > \epsilon_{nl}^2, \quad \epsilon_n f_{ll} + \epsilon_l f_{nn} - 2\epsilon_{nl} f_{nl} < 0$ (i.e. in Eq. (4.53) $a > 0, b < 0$), $k_BT = 1$ and $\beta(k)$ has two positive roots. The graphs in the top row show $\beta(k)$ and the graphs in the second row show $\chi(k)$. In (a) and (d) the parameters are: $\rho_l^0 = 0.785, \rho_n^0 = 0.3, \epsilon_l = 5, \epsilon_n = 5, \epsilon_{nl} = 0.5, \mu = -15, M^n = 1, M_c^l = 1$ and $M_{nc}^l = 1$. In (b) and (e) the parameters are: $\rho_l^0 = 0.649, \rho_n^0 = 0.3, \epsilon_l = 1.5, \epsilon_n = 1.5, \epsilon_{nl} = 0.1, \mu = -3.4, M^n = 1, M_c^l = 0$ and $M_{nc}^l = 1$. In (c) and (f) the parameters are: $\rho_l^0 = 0.683, \rho_n^0 = 0.3, \epsilon_l = 5, \epsilon_n = 5, \epsilon_{nl} = 0.5, \mu = -13.5, M^n = 1, M_c^l = 0$ and $M_{nc}^l = 1$..

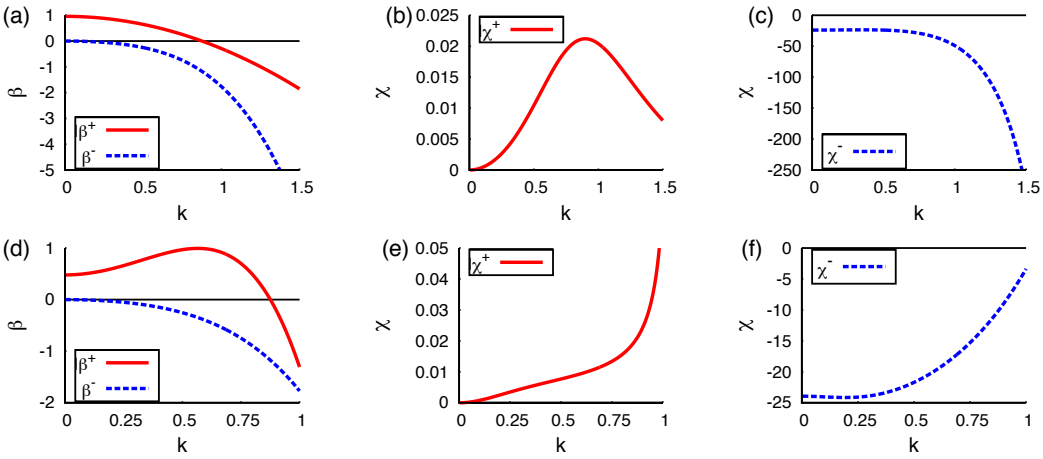

Figure 4.9: (a) - (f) Dispersion relations for the case when $\epsilon_n\epsilon_l > \epsilon_{nl}^2, \quad \epsilon_n f_{ll} + \epsilon_l f_{nn} - 2\epsilon_{nl} f_{nl} < 0$ (i.e. in Eq. (4.53) $a > 0, b < 0$), $k_BT = 1$ and $\beta(k)$ has one positive root. The graphs on the left show $\beta(k)$ and the graphs in the centre and right column show $\chi(k)$. In (a), (b) and (c) the parameters are: $\rho_l^0 = 0.551 \rho_n^0 = 0.3, \epsilon_l = 1.25, \epsilon_n = 1, \epsilon_{nl} = 0.01, \mu = -2.56, M^n = 1, M_c^l = 0$ and $M_{nc}^l = 1$. In (d), (e) and (f) the parameters are: $\rho_l^0 = 0.551, \rho_n^0 = 0.3, \epsilon_l = 1.25, \epsilon_n = 1, \epsilon_{nl} = 0.01, \mu = -2.56, M^n = 1, M_c^l = 4$ and $M_{nc}^l = 0.5$.

so the curve β^- always has a maximum at $k \neq 0$. However, this does not necessarily indicate that one will see the growth of density fluctuations with a typical modulation length, since $\beta^+(k) > \beta^-(k), \forall k$, which means that density fluctuations with the wavenumber which corresponds to the maximum in β^+ will grow faster than those with the wavenumber at the

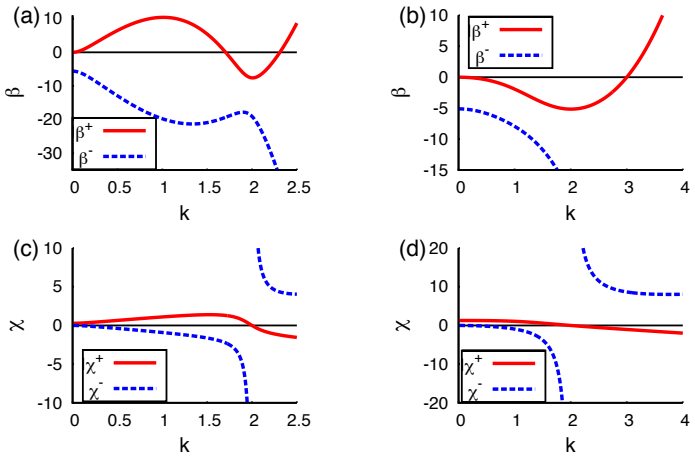

Figure 4.10: Dispersion relations for the case when $\epsilon_n\epsilon_l < \epsilon_{nl}^2$ and $k_BT = 1$. The graphs in the top row display $\beta(k)$ and the graphs in second row show $\chi(k)$. In (a) and (c) the parameters are: $\rho_l^0 = 0.884, \rho_n^0 = 0.3, \epsilon_l = 0.5, \epsilon_n = 0.5, \epsilon_{nl} = 5, \mu = -6, M^n = 1, M_c^l = 0$ and $M_{nc}^l = 1$. In (b) and (d) the parameters are: $\rho_l^0 = 0.737, \rho_n^0 = 0.3, \epsilon_l = 0.01, \epsilon_n = 0.01, \epsilon_{nl} = 1, \mu = -0.2, M^n = 1, M_c^l = 0$ and $M_{nc}^l = 1$.

maximum in β^-. In Fig. 4.8 (a) we show a typical example where there is a maximum in β^+ at $k \neq 0$, so one should expect to observe spinodal decomposition with the growth of density modulations having a typical length scale $\frac{2\pi}{k_m^+}$. Fig. 4.8 (b) shows the case where the maximum in β^+ occurs at $k = 0$. In Fig. 4.8 (c) we also display a rather interesting dispersion relation where the global maximum is at $k = 0$ but on increasing k we see a local minimum and a local maximum at $k \approx 1.3$. When there is a single root of $\beta(k)$ it always occurs in the β^+ branch. We observe that $\beta^+(k)$ may have a maximum at $k = 0$ (shown in Fig. 4.9 (a)) or at $k \neq 0$ (shown in Fig. 4.9 (d)). In both of these cases we find that the corresponding $\chi^+(k)$ curves (shown in Figs. 4.9 (b) and (e)) are very small in magnitude which suggests that the instability in the mixture is heavily influenced by the behaviour of the liquid component.

Finally, we address the case when $a < 0$, where at least one of the components in the mixture is more attracted to the other component rather than itself. For this case we find that b is always positive. We observe two types of dispersion relations; one where $\beta^+(k)$ has two roots (shown in Fig. 4.10 (a)) and another where $\beta^+(k)$ has only one root (plotted in Fig. 4.10 (b)). We can determine when $\beta^+(k)$ has one root from the expression for the critical wavenumber Eq. (4.52). If $c > 0$ then $\beta^+(k)$ has one root, otherwise $\beta^+(k)$ has two roots. In this regime, we observe that as $k \to \infty$, $\beta^+(k) \to \infty$ and $\beta^-(k) \to -\infty$. This indicates that the density fluctuations with an infinitesimally small typical length scale will grow fastest. This behaviour corresponds to a mixture that exhibits micro-phase separation. This behaviour is common in

block copolymer systems, where chemical bonding prevents macroscopic demixing and instead demixing on the nano-scale is witnessed [84, 85]. Micro-phase separation is also observed in certain colloidal suspensions [86–90]. If we impose a 'cut off' which prevents modulations from forming with large wavenumbers (e.g. by discretising the system and imposing a minimum length scale of Δx we would be essentially ignoring wavenumbers $k > \frac{2\pi}{\Delta x}$) then one would not observe micro-phase separation and the spinodal would be given by the locus $c = 0$. See appendix A for further discussion on this issue.

An important consideration which must be made with the binary system is whether 'liquid-particle' phase separation can occur as well as the 'liquid-gas' (low density - high density) phase separation that we have already discussed. The former corresponds to the coexistence of two phases, both having a high density. In terms of our system this would mean that we have coexisting phases with a high liquid density (i.e. $\rho_l \gtrsim 0.6$) in each phase. The coexisting values depend upon the temperature T, chemical potential μ and the interaction energies ϵ_l, ϵ_n and ϵ_{nl}. It is known that the following condition must be satisfied for 'liquid-particle' demixing to occur [80]:

$$\epsilon_{nl} < \frac{\epsilon_n + \epsilon_l}{2}. \tag{4.54}$$

The existence of liquid-particle phase separation in addition to the gas-liquid phase separation implies that for certain parameter values we may have three co-existing phases. This situation has the potential to lead to dramatic consequences for the pattern formation in our dynamical system. We return to this issue in Sec. 4.5.4 below.

4.5 Nonlinear Dynamics

We now go beyond the linear analysis presented above and discuss numerical results for the fully non-linear time evolution.

4.5.1 Numerical setup

Recall that the dynamics of our model is governed by the coupled partial differential equations (4.14) and (4.19), together with the free energy functional Eq. (4.8). We numerically solve these non-linear partial differential equations using a finite difference scheme on a square lattice with grid spacing $\Delta x = 1$. The time step size Δt varies between simulations, as the stability of

our numerical scheme depends strongly on the values of the parameters in the model. Central difference approximations are made for the partial derivatives with respect to space and forward difference approximations are made for the partial derivatives with respect to time. The Laplacian terms (∇^2) are approximated using the eight-neighbour discretisation [91]:

$$\nabla^2\rho = \frac{1}{2(\Delta x)^2}\left(\sum \rho^{NN} + \frac{1}{2}\sum \rho^{NNN} - 6\rho\right), \tag{4.55}$$

where, $\sum \rho^{NN}$ denotes a sum over the nearest neighbour lattice sites and $\sum \rho^{NNN}$ denotes a sum over the next nearest neighbour lattice sites. Alternative approximations may be used [92]. However, the choice of Laplacian approximation has little effect on the qualitative behaviour of the system. For further details on discretisation of the Laplacian term see appendix B.

Our numerical results show that as the various parameters in the model are varied, several different patterns are formed. We begin in Sec. 4.5.2 by considering the effect of changing the chemical potential μ of the vapour reservoir. We then focus on the fingering instability. In Sec. 4.5.3 we discuss the effect of varying the parameter α in the nanoparticle mobility and also the role which the conserved part of the liquid dynamics plays in the overall dynamics of the system, by varying the mobility coefficient M_l^c. Finally, in Sec. 4.5.4 we discuss the influence of 'liquid-particle' demixing at the receding front and how this affects the fingering mechanism. For the simulation results shown in Sec. 4.5.2 and Sec. 4.5.3 we set the interaction energies to $\epsilon_l = 1.4$, $\epsilon_n = 0.6$ and $\epsilon_{nl} = 0.8$. Using the linear stability analysis we have shown that it is possible to obtain stable phases with these parameter values (Fig. 4.7 (c), $a > 0$ and $b > 0$ in Eq. (4.53)]). In appendix A we present additional results for a different set of parameters where $a < 0$ in Eq. (4.53). This should lead to micro-phase separation, but by imposing an artificial cut-off for the wavenumber, we prevent the system from exhibiting micro-phase separation and observe regions in parameter space where the fluid is linearly stable, metastable and unstable. The resulting structures are qualitatively very similar to those obtained below (where $a > 0$ and $b > 0$ in Eq. (4.53)).

4.5.2 Influence of the vapour chemical potential μ

In section 4.4.1 we have discussed how changing the value of μ, the chemical potential of the vapour reservoir above the surface, affects the structures displayed by the system as the pure liquid evaporatively dewets from the surface. Recall that as μ is decreased below its coexistence value μ_{coex}, the dewetting mechanism is at first via the nucleation of holes and then when μ

is further decreased, via spinodal dewetting. This sequence as μ is decreased is also observed when there are nanoparticles dispersed in the liquid, although as previously discussed, the phase boundaries are shifted and there is the possibility of other (liquid-particle) phase transitions. Choosing a binary mixture with the parameter values $k_BT = 1.0$, $\epsilon_n = 0.6$, $\epsilon_l = 1.4$ and $\epsilon_{nl} = 0.8$ gives a phase with a high liquid density coexisting with a low density of the liquid. We also set $M_l^c = 0$ and $M_l^{nc} = 1$ to allow us to initially focus on just the evaporative non-conserved dynamics of the liquid. We set the initial density profiles corresponding to a (high density) uniform film of liquid with density $\rho_l(x, t = 0) = 1 - 10^{-6}$ mixed with nanoparticles having an average density of $\rho_n^{av} = 0.3$. In order to allow for the growth of density fluctuations when the system is (linearly) unstable, we add a small amplitude random noise to the density profile of the nanoparticles. Thus the initial nanoparticle density profile is $\rho_n(x, t = 0) = \rho_n^{av} + 2\lambda(Y - 0.5)$, where Y is a random real number uniformly distributed between 0 and 1 and λ is the magnitude of the noise. Without these random density fluctuations the density profiles would remain uniform under the evolution of the DDFT with a film of liquid remaining. Our boundary conditions are periodic in all directions.

The $c = 0$ spinodal curve (as calculated in the previous section, Fig. 4.7) defines the limit of stability, i.e. inside this line the fluid becomes linearly unstable. Thus, the fluid is unstable when $\beta\mu < -3.869$, where $\beta = 1/k_BT$. The speed of the process increases with decreasing values of $\beta\mu$. For very low values of $\beta\mu$ the evaporation process is so fast that we do not see any pattern formation in the nanoparticles - the liquid evaporates too quickly for the nanoparticles to diffuse. For the parameters $\epsilon_l = 1.4$, $\epsilon_n = 0.6$, $\epsilon_{nl} = 0.8$, $\alpha = 0.5$, $M_l^c = 0$ and $M_l^{nc} = 1$ this occurs when $\beta\mu \lesssim -4.2$. Fig. 4.11 shows the particular case when $\beta\mu = -4.08$. We see that the liquid behaves in a similar manner to that of a single component fluid by spontaneously dewetting everywhere. Now the evaporation is slow enough for the nanoparticles to move into areas with a high density of liquid during this evaporative process which creates a fine network structure (as shown in Fig. 4.11 (e) and (f)). However, this diffusion of the nanoparticles is limited as it is still a much slower process than the evaporation of the liquid. We observe that towards the end of the process small heaps of nanoparticles are formed, where the density is significantly larger. This effect is enhanced by the attraction between the nanoparticles ($\epsilon_n > 0$). Increasing the value of μ, we move from the linearly unstable (spinodal) region into the metastable region of the phase diagram (c.f. Fig. 4.3). Note however, that the actual values of $\beta\mu$ on the binodal and spinodal now differ from those in Fig. 4.3 because of the inclusion of

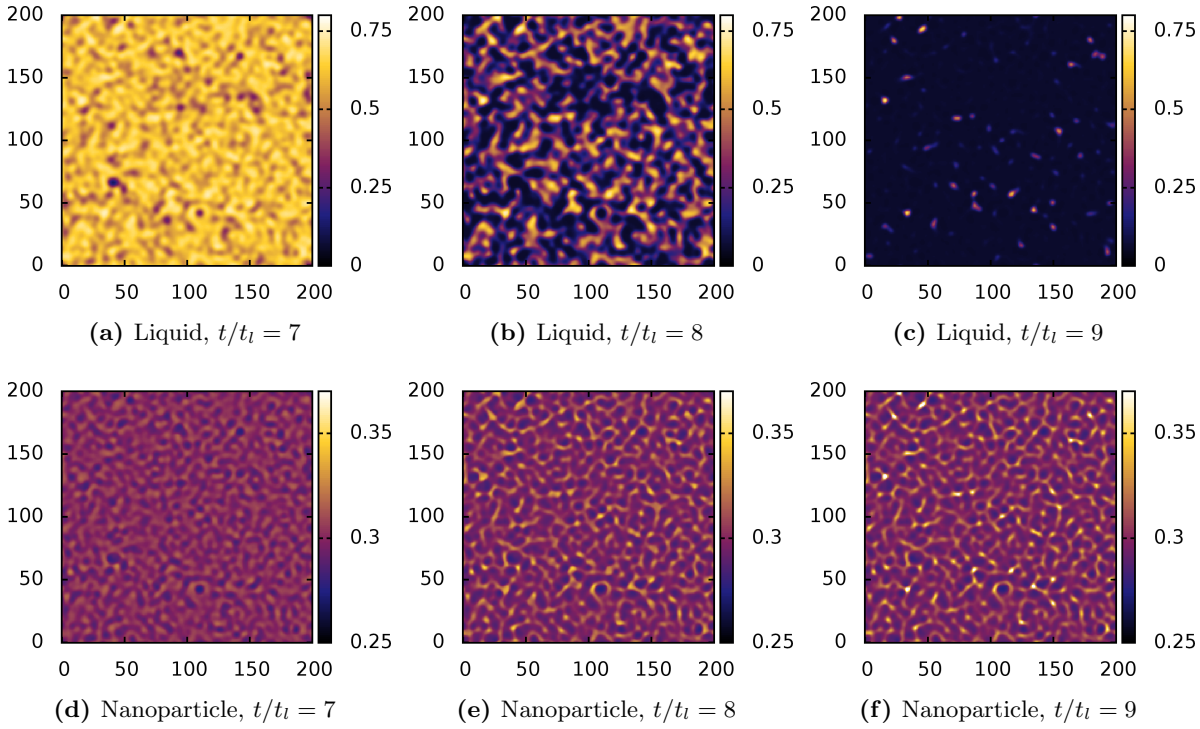

(a) Liquid, $t/t_l = 7$ **(b)** Liquid, $t/t_l = 8$ **(c)** Liquid, $t/t_l = 9$

(d) Nanoparticle, $t/t_l = 7$ **(e)** Nanoparticle, $t/t_l = 8$ **(f)** Nanoparticle, $t/t_l = 9$

Figure 4.11: Density profiles displaying evaporation via spinodal decomposition. The top row shows the liquid density profiles and the bottom row shows the nanoparticle profiles at times $t/t_l = 7$ (left), $t/t_l = 8$ (centre) and $t/t_l = 9$ (right), where $t_l \equiv \frac{\beta}{M_l^{nc}}$. The system parameter values are: $k_BT = 1$, $\epsilon_l = 1.4$, $\epsilon_n = 0.6$, $\epsilon_{nl} = 0.8$, $M_l^c = 0$, $M_l^{nc} = 1$, $\alpha = 0.5$, $\beta\mu = -4.08$ and $\lambda = 0.005$.

nanoparticles, c.f. Fig. 4.5.

On increasing the chemical potential into the range $-3.869 < \beta\mu \lesssim -3.8$, the liquid film becomes metastable but may still evaporate through the nucleation and growth of holes. Fig. 4.12 shows the case when $\beta\mu = -3.86$. The nucleation is caused by the random fluctuations in the density distributions (the initial density profiles are defined in a similar manner to the previous case: $\rho_l(x, t = 0) = 1 - 10^{-6}$, $\rho_n(x, t = 0) = \rho_n^{av} + 0.4(Y - 0.5)$). The amount of noise used and the free energy 'barrier' for forming a hole determine the probability of a nucleation event occurring. There is a critical hole radius R^c which can be determined from the free-energy of the system. If a hole is smaller than this critical radius then it will shrink and the liquid density will return to its bulk high density value in this region. However, if the size of the hole is larger than this critical value then this hole will begin to grow. We can apply classical nucleation theory to calculate an estimate for the critical hole radius R^c by determining the change in free energy ΔF when a low density (thin film) circular 'hole' with a radius of R is

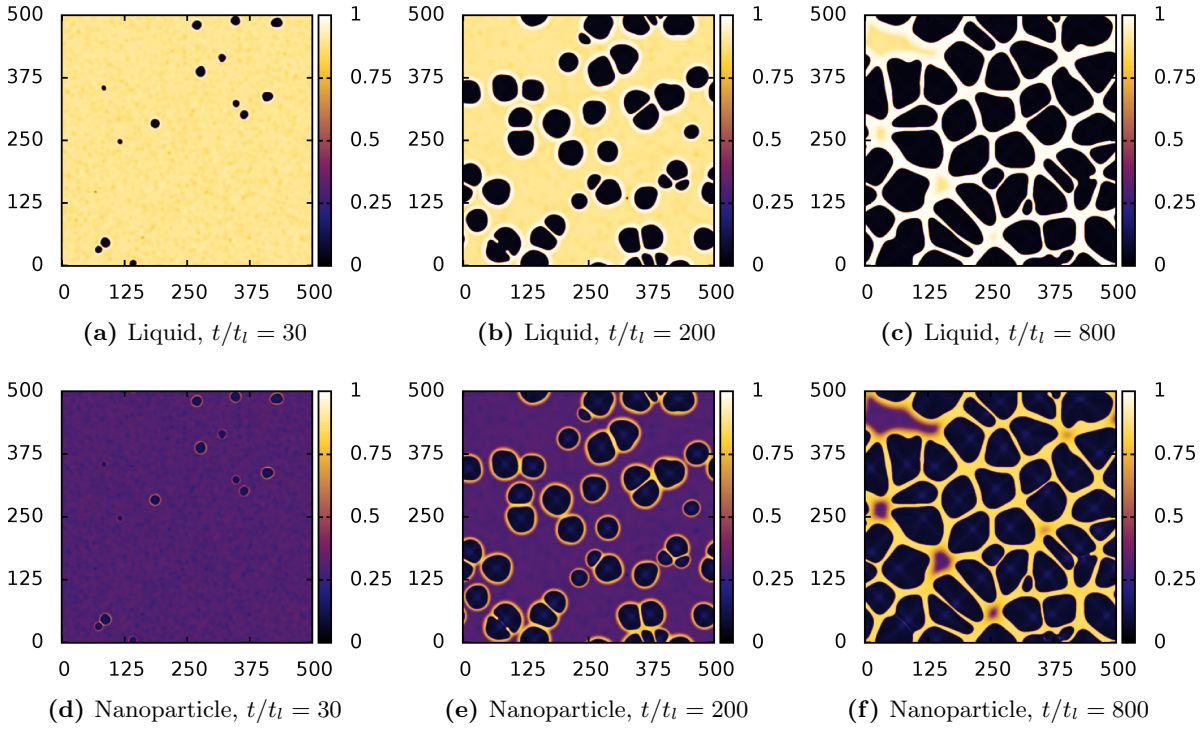

(a) Liquid, $t/t_l = 30$ **(b)** Liquid, $t/t_l = 200$ **(c)** Liquid, $t/t_l = 800$

(d) Nanoparticle, $t/t_l = 30$ **(e)** Nanoparticle, $t/t_l = 200$ **(f)** Nanoparticle, $t/t_l = 800$

Figure 4.12: Density profiles displaying nucleation and growth of holes which leads to the development of a network pattern. The top row shows the liquid density profiles and the bottom row shows the nanoparticle profiles at times $t/t_l = 30$ (left), $t/t_l = 200$ (centre) and $t/t_l = 800$ (right). The system parameter values are: $k_BT = 1$, $\epsilon_l = 1.4$, $\epsilon_n = 0.6$, $\epsilon_{nl} = 0.8$, $M_l^c = 0$, $M_l^{nc} = 1$, $\alpha = 0.5$, $\beta\mu = -3.86$ and $\lambda = 0.2$.

inserted into the metastable liquid film. The radius R which corresponds to the maximum in ΔF is the critical hole radius R^c. We approximate the change in free energy using the formula:

$$\Delta F = \pi R^2 \Delta P + 2\pi R\gamma, \tag{4.56}$$

where ΔP is the pressure difference between the two phases (the hole and the fluid film). γ is the interfacial tension (excess free energy) for creating a straight interface between the two phases at coexistence $\mu = \mu_{\text{coex}}$. It is important to note that the density values at coexistence are different to the density values out of coexistence. The density of the thin film of fluid inside the hole is such that its chemical potential is equal to that of the bulk film of fluid surrounding the hole. The critical hole radius R^c is given by the maximum of Eq. (4.56) - i.e. when $\frac{\partial \Delta F}{\partial R} = 0$. Thus, the critical hole radius is $R^c = -\frac{\gamma}{\Delta P}$. Fig. 4.13 shows how R^c depends on the chemical potential μ for different nanoparticle densities $\rho_n = 0$, 0.1 and 0.3. This analysis only applies to the metastable region of the phase diagram (c.f. Fig. 4.3) and therefore the critical hole radius R^c curves are bounded on the left by the spinodal curve and

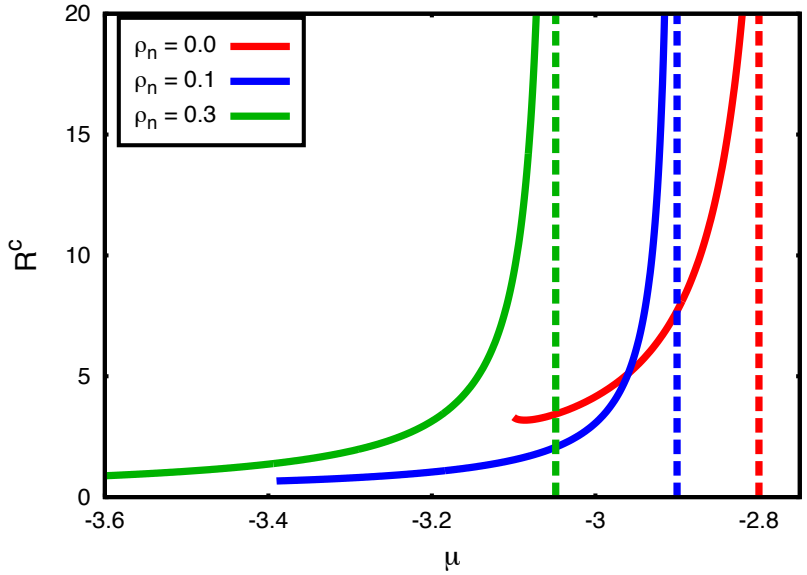

Figure 4.13: The solid lines display the critical hole radius R^c in units of the lattice grid spacing σ versus the chemical potential μ for different nanoparticle densities ρ_n. The lines start at the lowest value of μ for which the system is linearly stable. The dotted lines show the value of the chemical potential at coexistence μ_{coex}, which the curves approach asymptotically. Here $k_BT = 1$, $\epsilon_l = 1.4$, $\epsilon_n = 0.6$ and $\epsilon_{nl} = 0.8$.

on the right by the binodal curve. Note that classical nucleation theory incorrectly predicts a finite value for R^c at the spinodal, due to the fact that the theory assumes a sharp interface as one approaches the spinodal. For further discussion on this see e.g. Ref. [93]. The probability for a hole to be nucleated by random thermal fluctuations is proportional to $e^{-\beta\Delta F}$. The curves in Fig. 4.13 show that as we approach μ_{coex} the size of the critical hole increases. Hence, the probability of nucleation is greater nearer the limit of stability (spinodal curve) and decreases greatly as we approach coexistence (binodal curve). We observe that increasing the density of the nanoparticles ρ_n shifts the metastable region to lower chemical potential values and increases the range of the metastable region. This is due to the increase in the critical temperature associated with the increase in the nanoparticle density ρ_n, as previously discussed.

In the case shown in Fig. 4.12, we are near the limit of stability where the critical radius of a hole is very small. This results in many nucleation points where holes are formed and begin to grow. The nanoparticles are picked up by these growing holes which creates a rim around each hole with a high density of nanoparticles in the rim. The holes in the liquid film continue to grow until their rims meet, creating a random polygonal network pattern of nanoparticles. The liquid wets the surface of the nanoparticles, which means the liquid remains on the surface

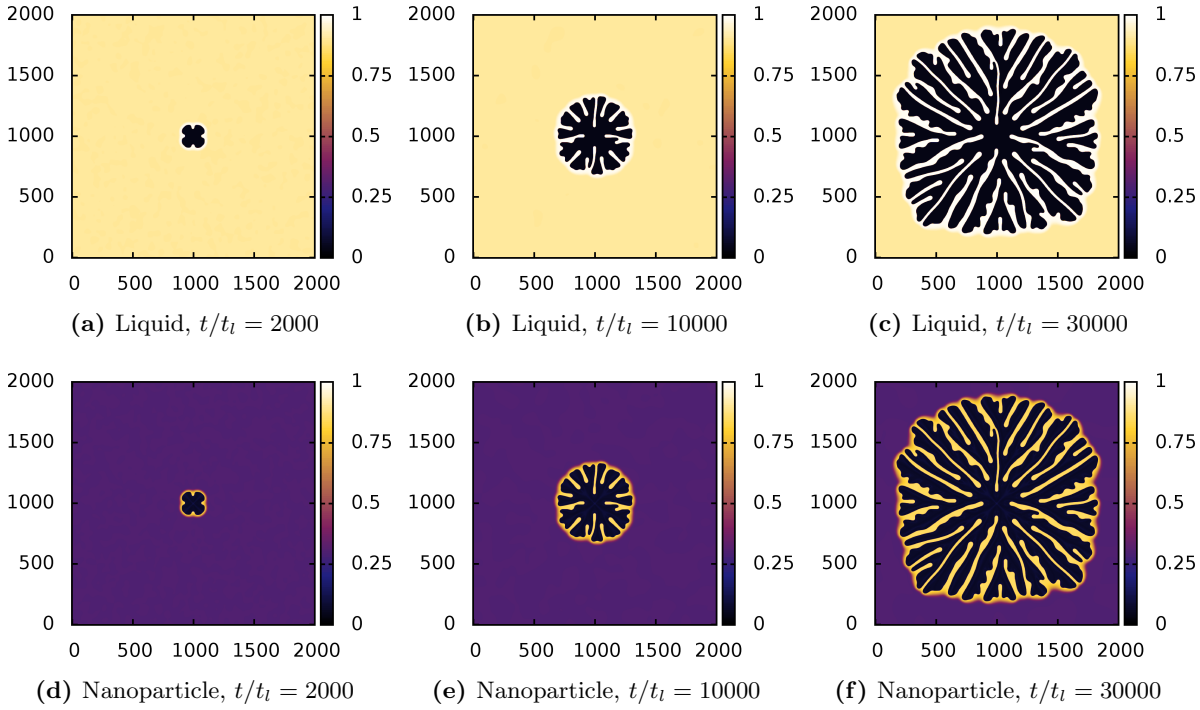

(a) Liquid, $t/t_l = 2000$ **(b)** Liquid, $t/t_l = 10000$ **(c)** Liquid, $t/t_l = 30000$

(d) Nanoparticle, $t/t_l = 2000$ **(e)** Nanoparticle, $t/t_l = 10000$ **(f)** Nanoparticle, $t/t_l = 30000$

Figure 4.14: Density profiles displaying the growth of an artificially nucleated hole which develops branched structures. The top row shows the liquid density profiles and the bottom row shows the nanoparticle profiles at times $t/t_l = 2000$ (left), $t/t_l = 10000$ (centre) and $t/t_l = 30000$ (right). The system parameter values are: $k_BT = 1$, $\epsilon_l = 1.4$, $\epsilon_n = 0.6$, $\epsilon_{nl} = 0.8$, $M_l^c = 0$, $M_l^{nc} = 1$, $\alpha = 0.5$, $\beta\mu = -3.8$ and $\lambda = 0.1$. Note that instead of using Eq. (4.55), here the Laplacian term is approximated using: $\nabla^2\rho = \frac{1}{6(\Delta x)^2}\left(\sum 4\rho^{NN} + \sum \rho^{NNN} - 20\rho\right)$ (c.f. appendix B).

in areas with a high density of nanoparticles. This is due to the positive interaction energy between the liquid and the nanoparticles ($\epsilon_{nl} > 0$).

If we increase the chemical potential further into the metastable range $-3.8 \lesssim \beta\mu < \mu_{\text{coex}}$, then the probability of a hole being nucleated becomes much smaller. In an experiment, in this parameter range, all holes that are formed are normally nucleated at defects or impurities of the surface (heterogeneous nucleation). Any interfaces between a high density liquid phase and a low liquid density phase will recede as the liquid evaporates. The velocity of the receding front depends on the value of $\beta\mu$. For small values of $\beta\mu$ we have a fast front, but the speed of the front reduces as μ approaches μ_{coex}. If we choose $\mu = \mu_{\text{coex}}$ then any straight front remains stationary. On a completely structureless substrate, one would usually expect such an interface to recede homogeneously; this is certainly the case for the pure liquid, when $\rho_n = 0$. However, in our system when $\rho_n > 0$ we see the formation of fingers as the front recedes, due to the pres-

ence of the nanoparticles. Fig. 4.14 shows a case when $\beta\mu = -3.8$. The initial density profiles in this situation differ slightly from the previous cases. Here we create an artificial nucleation point by setting the density of the liquid and the nanoparticles to $\rho_l = \rho_n = 10^{-6}$ in a central $2\sigma \times 2\sigma$ region. Without this seed nucleus the initial noise on the density profiles slowly decays and the densities of the two species return to their (metastable) equilibrium values. The liquid surrounding this nucleation point slowly recedes via evaporation, creating a circular dewetting front. As the front recedes, it begins to collect the nanoparticles, as was also observed for the case in Fig. 4.12. However, here the growing hole does not meet any other holes and there is time for an instability to develop at the front which causes the liquid to evaporate faster in some regions and slower in others creating a 'wavy' front, as seen in Fig. 4.14 (a) and Fig. 4.14 (d). The 'bumps' at the front then appear to stop moving while the rest of the front continues to recede. As the front recedes and the hole circumference increases, more fingers develop, leaving a branched 'fingered' nanoparticle structure behind - Figs. 4.14 (e) and (f). The time scale for this dewetting process is rather long and so we also observe some long-time coarsening effects on the finger structures.

Recall that one of the goals of our work is to develop an understanding of how the different self-organised structures of nanoparticles observed in the experiments [44, 47, 48, 50] are formed. Distinct observed structures are a) network structures and b) branched structures. Results from our model have shown how two different types of network structures can develop: i) a fine network structure created by a spinodal evaporation process (Fig. 4.11) in which the nanoparticle density varies over a fairly small range $0.27 \lesssim \rho_n \lesssim 0.45$, ii) a large well defined network structure created by the nucleation and growth of holes in the liquid (Fig. 4.12), in which the nanoparticle density varies over a large range $0.05 \lesssim \rho_n \lesssim 0.9$. Our model also shows how instabilities at the evaporative dewetting front can create branched structures for certain parameter values (Fig. 4.14). Note that there is also evidence of early stages of the fingering instability in the nucleation case shown in Fig. 4.12. There one can observe that small bumps begin to develop in the edges of some of the larger holes. We now consider the formation of the branched structures in more detail. In particular, we investigate the dependence of these 'fingered' structures on the parameters of the model.

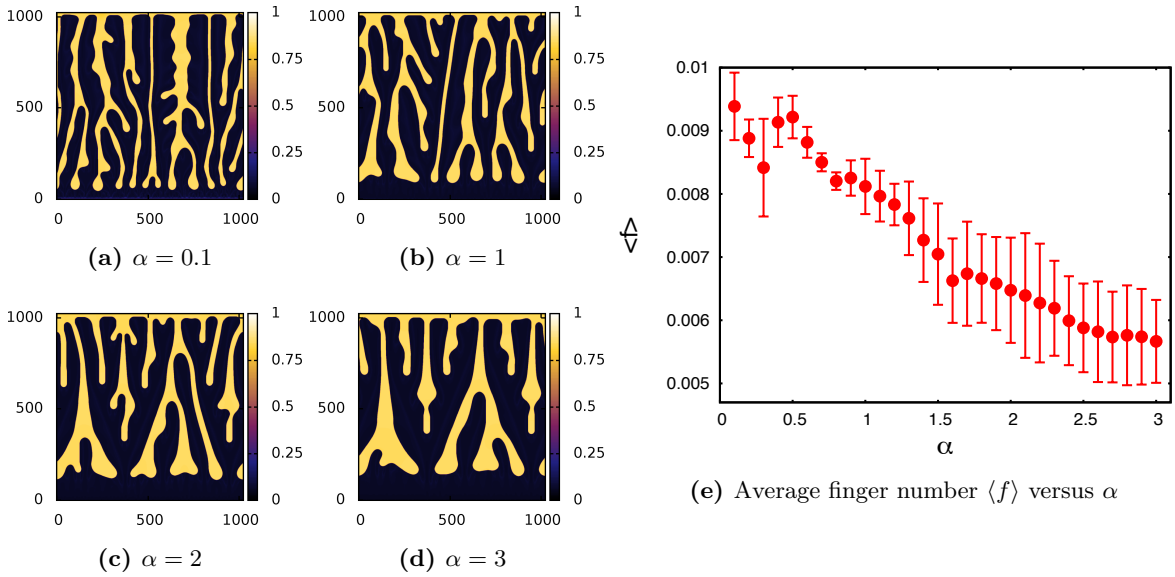

(a) $\alpha = 0.1$ **(b)** $\alpha = 1$ **(c)** $\alpha = 2$ **(d)** $\alpha = 3$ **(e)** Average finger number $\langle f \rangle$ versus α

Figure 4.15: Nanoparticle density profiles for calculations with (a) $\alpha = 0.1$, (b) $\alpha = 1$, (c) $\alpha = 2$ and (d) $\alpha = 3$. In (e) we display a plot showing the dependence of the number of fingers on the parameter value α. The parameter values are: $k_B T = 1$, $\epsilon_l = 1.4$, $\epsilon_n = 0.6$, $\epsilon_{nl} = 0.8$, $M_l^c = 0$, $M_l^{nc} = 1$, $\beta\mu = -3.8$, $\Delta x = 1$ and $\lambda = 0.1$.

4.5.3 Influence of mobilities on the fingering

To make a detailed investigation of the branched finger structures it is important to maximise the distance a front can recede. This allows us to obtain better statistics which is important due to the fact that solving the DDFT in the fingering regime on a large grid can be time consuming. To achieve this objective we create a straight dewetting front along the bottom edge of the system (i.e. we set the two density values to $\rho_l = \rho_n = 10^{-6}$ for the first five horizontal lines). We also set no-flux boundary conditions at the top and the bottom, to prevent a dewetting front forming at the top. The periodic boundary conditions on the left and the right side of the system domain remain. This set-up also allows for easier analysis of the branched structures since we begin with an initially straight front. We define a measure for the average number of fingers $\langle f \rangle$ to be the average number of branched structures per unit length in the final density profile, after the dewetting front has reached the top of the system. To calculate this quantity we implemented an algorithm which counts the number of transitions between a high density of nanoparticles and a low density of nanoparticles on each horizontal line of the system. We then determine the number of fingers on a given horizontal line by dividing this value by two. We set a minimum and maximum line for a given set of final density profiles and calculate the average number of fingers between these two lines. This value is then divided

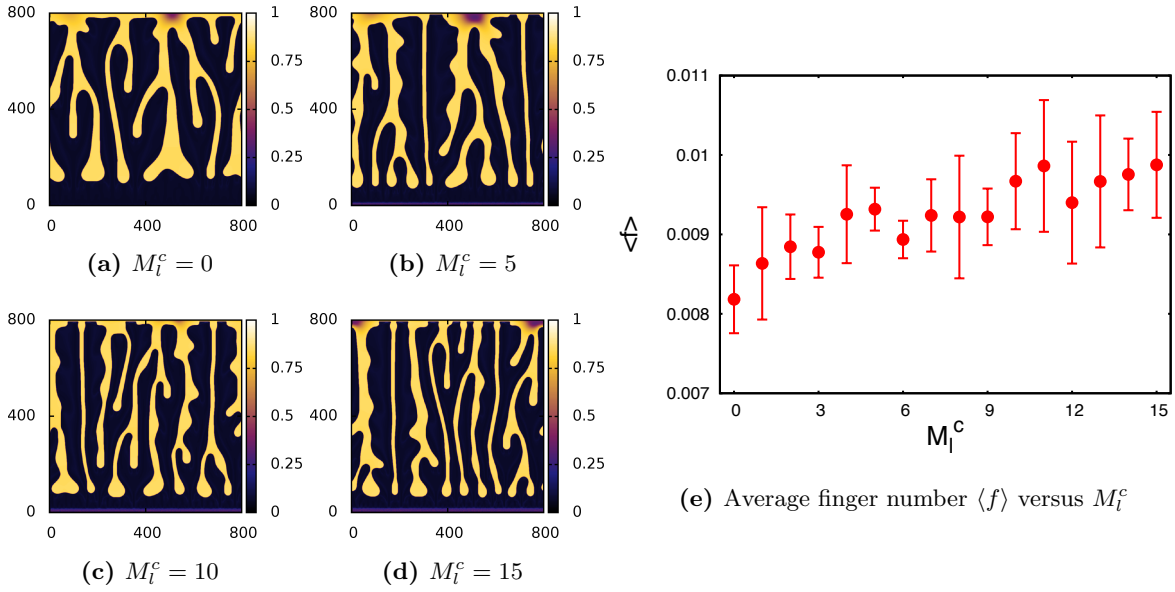

(a) $M_l^c = 0$ **(b)** $M_l^c = 5$ **(c)** $M_l^c = 10$ **(d)** $M_l^c = 15$

(e) Average finger number $\langle f \rangle$ versus M_l^c

Figure 4.16: Nanoparticle density profiles for (a) $M_l^c = 0$, (b) $M_l^c = 5$, (c) $M_l^c = 10$ and (d) $M_l^c = 15$. In (e) we display a plot showing how the number of fingers $\langle f \rangle$ depends on the value of M_l^c. The parameter values are: $k_B T = 1$, $\epsilon_l = 1.4$, $\epsilon_n = 0.6$, $\epsilon_{nl} = 0.8$, $M_l^{nc} = 1$, $\alpha = 1$, $\beta\mu = -3.8$ and $\lambda = 0.1$.

by the size of the system to give a value that is independent of the system size. We have investigated how this measure is affected by the different parameters of the system.

We begin by discussing the effect that varying the parameter α has on $\langle f \rangle$ (recall that α determines the mobility of the nanoparticles in the liquid film). We use the same parameter values as above, with $\beta\mu = -3.8$ and α varying between 0.1 and 3. Fig. 4.15 shows final nanoparticle density profiles for several values of α and also a plot of $\langle f \rangle$ versus α, which is calculated from the average of five runs. We see that the value of α has a significant influence on the average finger number. Increasing the mobility of the nanoparticles results in fewer fingers being developed, which is in (qualitative) agreement with the experiments [50] and the KMC model results shown in Fig. 3.5 [51]. The mobility of the nanoparticles directly influences the speed of the receding front, so evaporation is much slower when α is small. When α is very small ($\alpha \lesssim 0.002$) we find that the two density fields become practically decoupled, with the liquid evaporating at high speed leaving the nanoparticles behind as a homogeneous film of the initial density ρ_n^{av}.

The effect of liquid diffusion over the surface has also been investigated by varying the liquid conserved mobility M_l^c. Using the same parameter values as above, and setting $\alpha = 1$, we

display in Fig. 4.16 final nanoparticle density profiles for varying M_l^c from 0 to 15 and also the average finger number $\langle f \rangle$ versus M_l^c averaged over five runs. We see that the diffusive mobility of the liquid M_l^c does affect the average number of fingers but to a much smaller extent than the mobility of the nanoparticles. The average finger number generally increases as M_l^c is increased.

4.5.4 Influence of liquid-particle demixing on the fingering

We now discuss the effect of possible liquid-particle phase separation on the front instability. Such a phase separation may occur near the front even for nanoparticle concentrations inside the liquid film that are far smaller than the binodal value for liquid-particle phase separation. This occurs because as a dewetting front recedes it collects nanoparticles (as previously discussed) and therefore increases the value of ρ_n near the front. For certain parameter values we find that if ρ_n increases above a certain threshold value, then liquid-particle phase separation occurs in the front region. The liquid separates into two liquid phases, a mobile one poor in colloids and a less mobile one rich in colloids. To investigate the resulting effects we set the interaction energies to $\epsilon_l = 1.7$, $\epsilon_{nl} = 1$ and vary ϵ_n from 0 to 1.2. Eq. (4.54) indicates that we should observe liquid-particle phase separation for $\epsilon_n > 0.3$. We set the average nanoparticle density to be low, $\rho_n^{av} = 0.1$, so that there is no liquid-particle phase separation in the bulk of the fluid film. For the value of the chemical potential that we use $\mu = -4$, the fluid is linearly stable for all values of ϵ_n and leads to a relatively fast dewetting front.

In Fig. 4.17 (a)–(d) we display typical final nanoparticle density profiles for various ϵ_n and the average finger number $\langle f \rangle$ versus ϵ_n, averaged over five runs. As ϵ_n is increased from $\epsilon_n = 0$, we initially see a linear increase in the average number of fingers $\langle f \rangle$. This reaches a peak at $\epsilon_n \approx 0.6$, after which we begin to see the development of droplets. When $0.6 \lesssim \epsilon_n \lesssim 0.9$ we observe separation between regions of high density of nanoparticles and low density of nanoparticles occurring locally at the dewetting front. The areas with a lower density of nanoparticles form very thin fingers which quickly rupture into a series of droplets, whereas the areas with a higher density form thicker fingers which are much more stable as shown in Fig. 4.17 (c). The sections of the front with a lower density of nanoparticles recede faster than the rest of the front. This results in a 'doublon' pattern (as shown in Fig. 4.18) which has been observed in many different systems, e.g. in the thin film directional solidification of a non-faceted cubic crystal [94]. As we increase ϵ_n further, for $\epsilon_n > 1$ we observe that the

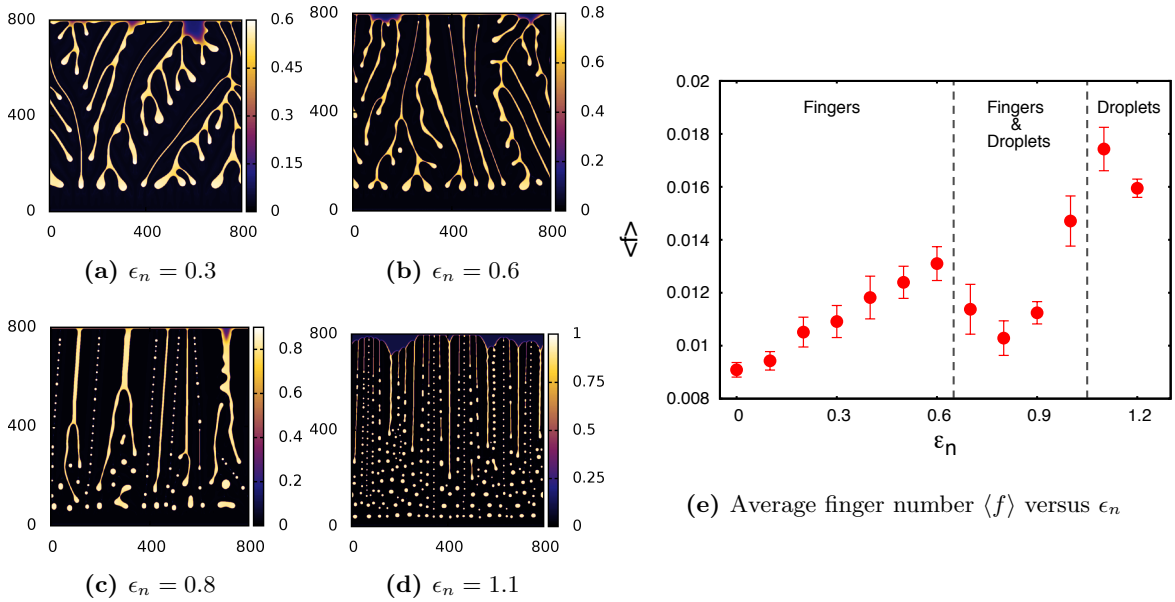

(a) $\epsilon_n = 0.3$ **(b)** $\epsilon_n = 0.6$ **(c)** $\epsilon_n = 0.8$ **(d)** $\epsilon_n = 1.1$ **(e)** Average finger number $\langle f \rangle$ versus ϵ_n

Figure 4.17: Nanoparticle density profiles for (a) $\epsilon_n = 0.3$, (b) $\epsilon_n = 0.6$, (c) $\epsilon_n = 0.8$ and (d) $\epsilon_n = 1.1$. In (e) we display a plot showing how the mean number of fingers $\langle f \rangle$ depends on the parameter ϵ_n. When $\epsilon_n > 0.6$ we begin to observe droplets being deposited along with the branched structures (as shown in (c)). The parameter values for these calculations are: $k_BT = 1$, $\epsilon_l = 1.7$, $\epsilon_{nl} = 1.0$, $M_l^c = 0$, $M_l^{nc} = 1$, $\alpha = 0.5$, $\beta\mu = -4$, $\rho_n^{av} = 0.1$ and $\lambda = 0.025$.

dynamics at the front remains similar, however, now all the finger structures are very thin and therefore quickly break up into droplets. One also notices that the tendency to form side branches decreases with increasing ϵ_n whereas the orientation of the branches becomes increasingly perpendicular to the receding front. We also observe an increase in the density of the nanoparticles within the fingers/droplets as ϵ_n is increased. This is due to the increased attraction between the nanoparticles. These results agree qualitatively with the KMC model [51]. The KMC results also show an initial increase in the number of fingers followed by a transition from fingers to droplets as the interaction energy between the nanoparticles ϵ_n is increased. Fig. 17 of Ref. [51] displays a plot of $\langle f \rangle$ versus ϵ_n which shows a similar trend as the DDFT results displayed in Fig. 4.17 (e). However, as it is a discrete stochastic model, the details of the transition in the way the branching occurs are less discernible than in the present DDFT model.

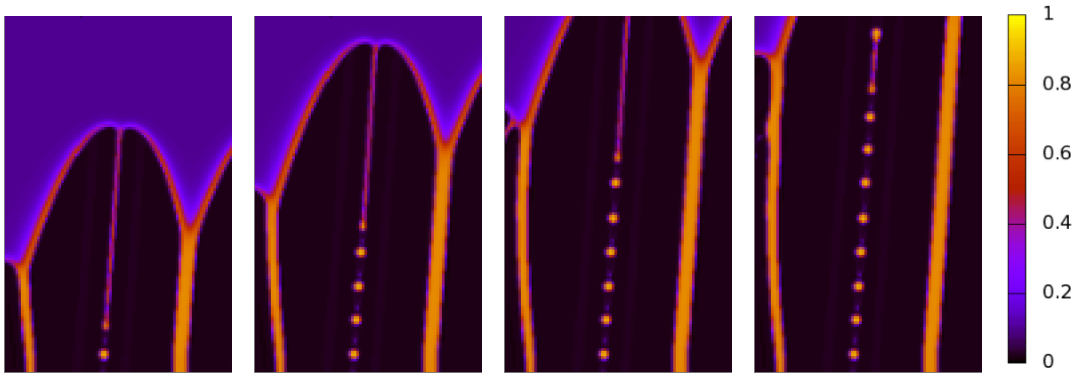

Figure 4.18: The time evolution of nanoparticle density profiles displaying the formation of fingers and droplets at a receding front. This is a magnification of a region of size 190×300, taken from the simulation with the final nanoparticle density profile shown in Fig. 4.17 (c) and shows how the doublon structures are dynamically formed. The parameter values are: $k_BT = 1$, $\epsilon_l = 1.7$, $\epsilon_n = 0.8$, $\epsilon_{nl} = 1$, $M_l^c = 0$, $M_l^{nc} = 1$, $\alpha = 0.5$ and $\mu = -4$.

4.5.5 Mobility function which is dependent on the nanoparticle density

For all results presented above we assumed that the nanoparticle mobility function takes the form given by Eq. (4.16). As Fig. 4.2 shows, this means that the mobility of the nanoparticles is approximately equal to $\alpha\rho_n(\mathbf{r}, t)$ when surrounded by a high density of liquid (i.e. a thick film of liquid) and the mobility is approximately zero when $\rho_l \lesssim 0.45$. This models the fact that the nanoparticles only move by Brownian motion due to the thermal 'kicks' they receive when immersed in the liquid and are immobile when there is no liquid surrounding them. One may also consider the effect of the local nanoparticle density on the mobility of the nanoparticles using the following mobility function:

$$M_n^* = \rho_n(\mathbf{r}, t)m(\rho_l(\mathbf{r}, t))g(\rho_n(\mathbf{r}, t)), \tag{4.57}$$

where the function $g(\rho_n)$ should be chosen to model the fact that as the density of the nanoparticles increases, their mobility decreases due to the fact that they become jammed and impede one another. In a system where as the nanoparticle density $\rho_n \to \rho_c$, there is a 'jamming' (i.e. glass or gel formation), an appropriate choice for $g(\rho_n)$ is:

$$g(\rho_n(\mathbf{r}, t)) = \begin{cases} \left(1 - \frac{\rho_n(\mathbf{r},t)}{\rho_c}\right)^R & \text{if } \rho_n(\mathbf{r}, t) < \rho_c \\ 0 & \text{otherwise,} \end{cases}$$

where, ρ_c is a critical density above which the nanoparticles become immobile, R is a positive parameter which determines the shape of the g curve and $m(\rho_l(\mathbf{r}, t))$ is defined as above in

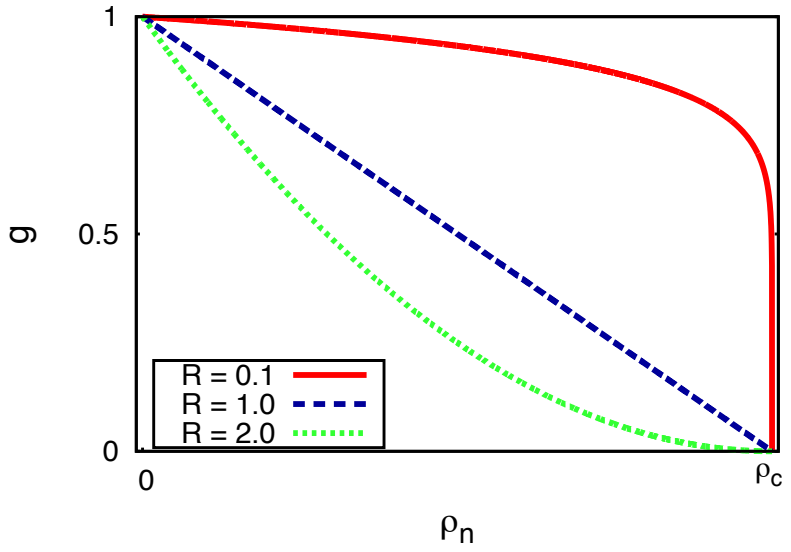

Figure 4.19: Plot showing how the function $g(\rho_n)$ depends on the local nanoparticle density ρ_n. The different lines display the $g(\rho_n)$ curve for different values of R.

Eq. (4.17). Fig. 4.19 shows how $g(\rho_n)$ changes as R is varied; when $R > 1$ the curve takes a concave form and when $R < 1$ the curve takes a convex form.

The value of the exponent R has a significant effect on the branched structures that are formed. In Fig. 4.20 we display the final nanoparticle density profiles for (a) $R = 0.1$, (b) $R = 0.7$, (c) $R = 1.3$ and (d) $R = 2.0$ in the case when $k_BT = 1$, $\epsilon_l = 1.4$, $\epsilon_n = 0.6$, $\epsilon_{nl} = 0.8$, $M_l^c = 0$, $M_l^{nc} = 1$, $\alpha = 1$, $\beta\mu = -3.8$ and $\rho_c = 0.7$. In (e) we display a plot showing the average finger number $\langle f \rangle$ plotted as a function of the exponent R. The most notable effect of this new mobility function is the massive increase in the number of fingers. We previously found that reducing the value of the nanoparticle mobility coefficient α increases the average number of fingers - see Fig. 4.15. The new form for the mobility function in Eq. (4.57) reduces the mobility of the nanoparticles, especially in areas with a high density of nanoparticles (i.e. at a receding front). This results in the significant increase in the number of fingers. We observe that increasing the value of R (i.e. increasing the gradient of $g(\rho_n)$ near $\rho_n = \rho_c$) reduces the number of fingers in the resulting pattern.

For values of R near $R = 2$ we observe that the branched structures begin to form at an angle $\theta \approx \pm 30^\circ$ to the dewetting front. Fig. 4.20 (d) displays an example of the triangle shaped branched structures which develop in this parameter range. As the structures develop at angles $\theta \approx \pm 30^\circ$ to the (horizontal) dewetting front, the structures depend greatly on the

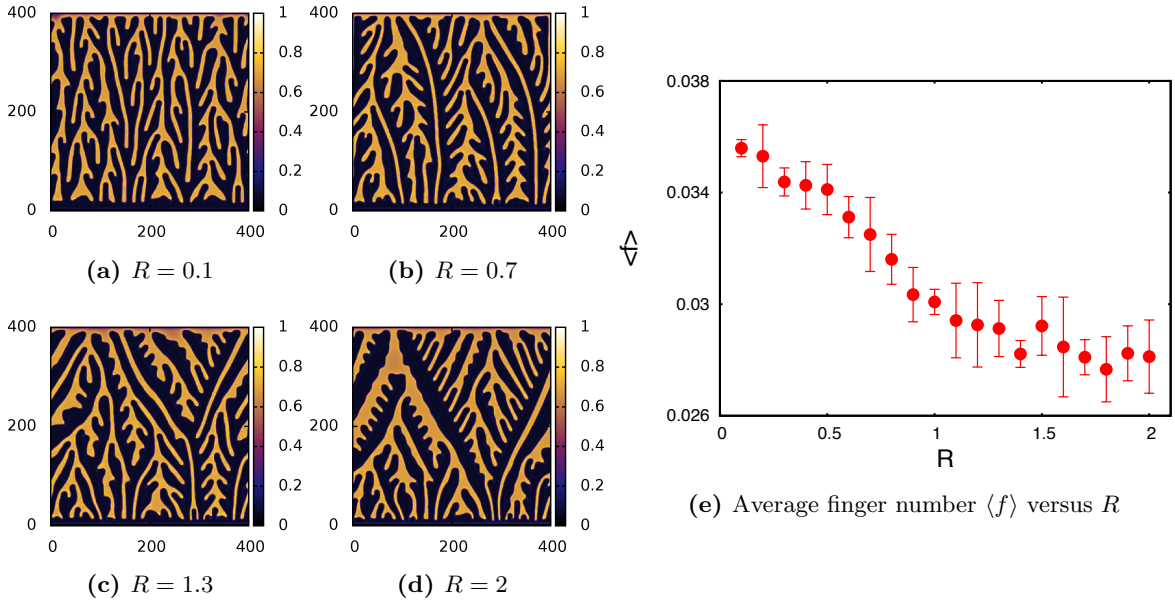

(a) $R = 0.1$ **(b)** $R = 0.7$

(c) $R = 1.3$ **(d)** $R = 2$

(e) Average finger number $\langle f \rangle$ versus R

Figure 4.20: Nanoparticle density profiles for (a) $R = 0.1$, (b) $R = 0.7$, (c) $R = 1.3$ and (d) $R = 2$. In (e) we display a plot showing how the mean number of fingers $\langle f \rangle$ depends on the parameter R. The parameter values for these calculations are: $k_B T = 1$, $\epsilon_l = 1.4$, $\epsilon_n = 0.6$, $\epsilon_{nl} = 0.8$, $M_l^c = 0$, $M_l^{nc} = 1$, $\alpha = 1$, $\beta\mu = -3.8$ and $\rho_c = 0.7$.

next neighbour contributions of the Laplacian approximation. Hence, these structures vary greatly when a different Laplacian approximation is used - see appendix B for details. This angled growth of branched structures is visible in other systems, e.g. in thin-film directional solidification in non-faceted cubic crystal [94].

4.6 Concluding remarks

We have presented a DDFT based model for the evaporative dewetting of an ultrathin film of a colloidal suspension. We have derived an expression for the free energy of the system using a mean-field approximation for a coarse-grained Hamiltonian model (4.1) for the system. We have also derived dynamical equations which describe the diffusive dynamics of the solvent and of the colloids as well as the evaporation of the solvent. We have considered the equilibrium phase behaviour of the pure solvent and of the two component fluid and identified parameter ranges where unstable, metastable and stable phases exist. We then solved the coupled dynamical equations numerically to investigate the different dynamical pathways of the phase transition and the resulting self-organised patterns of the nanoparticles.

The model successfully describes the various self-organised structures found in experiments [50]

and is in qualitative agreement with the discrete stochastic KMC model [51]. Our numerical results show how nanoparticle network structures can form either from a spinodal processes (Fig. 4.11) or through the nucleation and growth of holes (Fig. 4.12). We have also observed how branched structures develop from a fingering instability of the receding dewetting front (Fig. 4.14).

The transverse front instability results from a build-up of the nanoparticles close to the front as the solvent evaporates, when diffusion is too slow to disperse them. This slows down the front and renders it unstable. As a result, density fluctuations along the front grow into an evolving fingering pattern. This transverse front instability can be considered to be a self-optimisation process which maintains the mean front velocity constant [51] (see also the discussion of this in the context of a similar front instability occurring in the dewetting of non-volatile polymer films [95]). One may also say that the constant average front velocity is maintained by depositing some of the nanoparticles onto the dry substrate creating the branched structures. Experimental observations show that the branched structures found in the ultra-thin film behind the mesoscopic dewetting front are initiated from random nucleation sites. The holes which are nucleated then grow, initially creating circular dewetting fronts. We subsequently observe that the fingering instabilities and the development of branched structures form on the circular interfaces. Fig. 4.14 shows how these circular branched patterns develop from a single nucleation point; our numerical results bare a striking resemblance to the experimental AFM images of this phenomenon [50].

We have studied the branched structures in greater detail using a planar geometry, i.e., by creating initially straight dewetting fronts. We have considered how the different mobilities affect the fingering. The nanoparticle mobility in liquid films has a significant effect on the average number of fingers in the branched structure (Fig. 4.15). The finger number decreases rapidly with increasing mobility in agreement with earlier KMC results [51]. This behaviour can be attributed to the lower-mobility of the nanoparticles that hinders re-distribution by diffusion and also reduces the speed of the dewetting front. For the system to attain a higher front speed it must deposit nanoparticles onto the surface at a greater rate. Therefore, if the mobility of the nanoparticles is low this leads to the creation of more fingers because in this case the average distance a nanoparticle has to travel to reach a finger is smaller. Increasing the mobility for the conserved diffusive dynamics of the liquid has the opposite effect on the

average number of fingers (Fig. 4.16). The complex relationship between the diffusion of the liquid and the average finger number is not yet fully understood. Our hypothesis is that increasing the mobility of the liquid results in an effective increase in the speed of the dewetting dynamics of the liquid for fixed nanoparticle mobility. Thus, the mobility of the nanoparticles becomes lower in comparison. The increased finger number then results from the increased mobility contrast, in agreement with the general instability mechanism laid out above.

The basic front instability as described above is a purely dynamic effect and does not depend on particle-liquid and particle-particle attractive interactions that favour demixing of the liquid and the nanoparticles. However, beside this regime (that we call the 'transport regime') we have investigated how interactions that favour demixing influence the instability (Fig. 4.17). In general, when increasing the interaction energy between the nanoparticles one increases the tendency towards liquid-particle demixing. However, this has no practical effect as long as the nanoparticle concentration is low, so that it is outside of the two-phase region. This is normally the case for our initial densities. However, in the course of the evaporative dewetting the density increases close to the receding front. Increasing the interaction energy between the nanoparticles causes demixing to occur close to the front (but not in the bulk film). The demixing makes the fingering instability stronger (we call this the 'demixing regime'). At first, one finds a linear increase in the average finger number with increasing interaction energy. At higher values of ϵ_n, when the localised phase separation sets in, the fingers become straight with less side branches, before finally lines of drops are emitted directly at the front. In this regime, the mean number of fingers is determined by the dynamics and the energetics of the system.

The results we have obtained with our DDFT model confirm that jamming of discrete particles (as discussed in Ref. [96]) is not a necessary factor for the fingering instability to occur. Our model is a continuum model with a diffusion constant that is independent of the nanoparticle concentration. The present two-dimensional DDFT model has several advantages over the two-dimensional KMC model [45, 51]: In particular, the early instability stages are more easy to discern without the background noise of the KMC. Furthermore, the underlying free energy may be employed to analyse the equilibrium phase behaviour in detail, in a similar manner to Ref. [80]. Many standard tools for the analysis of partial differential equations can be applied to the coupled evolution equations, such as, e.g., the linear stability analysis of the homogeneous

films. In the future, one may perform a linear stability analysis for the receding straight front and also investigate steady state solutions as has been done for evaporating films of pure liquids [76]. There are many details that would merit further investigations such as, for example, the doublon structure mentioned in Sec. 4.5.4 (an example is shown in Fig. 4.18) and its relation to such structures formed in directional solidification [97].

The present DDFT model does not include the effect of surface forces, i.e., wettability effects (substrate-film interactions). Therefore, a non-volatile liquid film would not dewet the substrate. This implies that an important avenue for future improvement is to incorporate wettability effects into the model. This could be done by making a mean-field approximation to derive an expression for the free energy for a fully three-dimensional KMC model [98, 99] (after incorporating substrate-particle and substrate-liquid interactions). The resulting three-dimensional DDFT could then either be used directly or be averaged perpendicularly to the substrate employing e.g., a long-wave approximation. Another possible option consists of combining a mesoscopic hydrodynamic approach, e.g., a thin film evolution equation (see [62, 76, 100]) with elements of DDFT. For a brief discussion of such an approach see Ref. [72].

As a final remark, we recall that in the present work we have only considered dewetting from homogeneous substrates. However, it is straightforward to include surface heterogeneities in our model via the external potentials $\phi_i(\mathbf{r})$ in Eq. (4.8). As future work, it would be interesting to study the influence of surface patterning on the finger formation displayed by the present system.

Chapter 5

The phase field crystal model

In this chapter we examine the phase field crystal (PFC) model. We begin by considering how the governing equations of the PFC model may be formulated from DDFT by performing a gradient expansion of the excess free energy F_{ex} and expanding the free energy in powers of the order parameter/density ϕ. This is followed by a brief overview of the extensive PFC literature, where the various forms, derivations and applications are summarised. We then go on to describe the basic thermodynamics and the stability of the model and present some key results.

We now move on to consider a new type of model; the PFC model. The PFC model consists of a particular type of free energy equation, which may be minimised by an order parameter profile $\phi(\mathbf{x}, t)$ containing periodic structures, and having a conserved diffusive dynamics. The PFC model is a theory for studying freezing and crystal formation. Unlike regular phase field models, where ϕ takes a different uniform value in each phase, in the PFC the order parameter has 'bumps' which can be interpreted as atoms/molecules. This allows the model to describe the microstructure of crystalline materials. It is possible to obtain the free energy from DFT for freezing and to derive the dynamics from DDFT, i.e. the model equations describe the microscopic properties of materials. We discuss this in more detail below in Sec. 5.1.

5.1 Derivation of the PFC model from DDFT

In chapter 2 we discussed DFT which is a microscopic theory which describes the free energy of a system using functionals of the one body density distribution $\rho(\mathbf{x})$. We then went on to discuss how time evolution equations for the one body density can be derived from the stochastic equations of motion of Brownian colloidal particles. In this section we start from DDFT to derive the PFC model in its commonly used form. In our derivation we closely follow the arguments laid out in Ref. [101]. The starting point is the results obtained in chapter 2, specifically the free energy functional in Eq. (2.16) and the DDFT equation for the dynamics of the one body density $\rho(\mathbf{x})$, Eq. (2.47). Recall, that the free energy $F[\rho(\mathbf{x})]$ of a system can be split into three parts (see Eq. (2.16)): the ideal gas contribution $F_{\text{id}}[\rho(\mathbf{x})]$, the excess free energy part $F_{\text{ex}}[\rho(\mathbf{x})]$ which deals with the interactions between the particles and the contribution due

to any external potentials, $F_{\rm ext}[\rho(\mathbf{x})] = \int d\mathbf{r} V_{\rm ext}(\mathbf{x})\rho(\mathbf{x})$. The excess free energy $F_{\rm ex}$ is usually an unknown quantity. Here, we make an approximation for the excess part of the free energy by making a Taylor series expansion in powers of $\Delta\rho(\mathbf{x}) = \rho(\mathbf{x}) - \rho_0$, where ρ_0 is a reference density, giving [5]:

$$\begin{aligned} F_{\rm ex}[\rho(\mathbf{x})] &= F_{\rm ex}[\rho_0] + \int d\mathbf{x}\, \Delta\rho(\mathbf{x}) \frac{\delta F_{\rm ex}[\rho(\mathbf{x})]}{\delta\rho(\mathbf{x})}\bigg|_{\rho_0} \\ &\quad + \frac{1}{2}\iint d\mathbf{x} d\mathbf{x}'\, \Delta\rho(\mathbf{x})\Delta\rho(\mathbf{x}') \frac{\delta^2 F_{\rm ex}[\rho(\mathbf{x})]}{\delta\rho(\mathbf{x})\delta\rho(\mathbf{x}')}\bigg|_{\rho_0} + O(\Delta\rho^3). \end{aligned} \tag{5.1}$$

The functional derivatives of the excess free energy which enter into Eq. (5.1) are related to the n-body direct correlation functions in the following way [5]:

$$\frac{\delta^n F_{\rm ex}[\rho(\mathbf{x})]}{\delta\rho(\mathbf{x}_1)\delta\rho(\mathbf{x}_2)\cdots\delta\rho(\mathbf{x}_n)}\bigg|_{\rho_0} = -k_B T c^{(n)}(\mathbf{x}_1, \mathbf{x}_2, \cdots, \mathbf{x}_n). \tag{5.2}$$

In particular, the first member of this series is the one-body direct correlation function, as shown earlier in Eq. (2.18). Note that the one body direct correlation function evaluated in the bulk is equal to the excess chemical potential $-k_B T c^{(1)}(\mathbf{x})\Big|_{\rho_0} = \mu_{\rm ex}$ (c.f. Eq. (2.48)). The second member of the series in Eq. (5.2) is the pair direct correlation function:

$$\frac{\delta^2 F_{\rm ex}}{\delta\rho(\mathbf{x})\delta\rho(\mathbf{x}')} = -k_B T c^{(2)}(\mathbf{x}, \mathbf{x}'). \tag{5.3}$$

Substituting in these expressions for the functional derivatives Eqs. (2.18) and (5.3) and neglecting third and higher order terms, Eq. (5.1) becomes:

$$F_{\rm ex}[\rho(\mathbf{x})] \approx F_{\rm ex}[\rho_0] + \mu_{\rm ex}\int d\mathbf{x}\, \Delta\rho(\mathbf{x}) - \frac{k_B T}{2}\iint d\mathbf{x} d\mathbf{x}'\, \Delta\rho(\mathbf{x})\Delta\rho(\mathbf{x}') c^{(2)}(\mathbf{x}, \mathbf{x}') \tag{5.4}$$

The second term in this equation corresponds simply to a shift in the chemical potential and so this approximation is commonly used without the second term explicitly written down [101–103] and was originally proposed by Ramakrishnan and Yussouff [104]. To derive the PFC free energy, we make a gradient expansion of the two body direct correlation function and truncate at the forth order term, giving [101, 105]:

$$c^{(2)}(\mathbf{x}, \mathbf{x}') \approx -\beta(\hat{C}_0(\rho(\mathbf{x})) + \hat{C}_2\nabla^2 + \hat{C}_4\nabla^4)\Delta\rho(\mathbf{x})\delta(\mathbf{x} - \mathbf{x}'), \tag{5.5}$$

where in principle all the coefficients $\hat{C}_i$ are functions of $\rho(\mathbf{x})$, but we will assume that the coefficients $\hat{C}_2$ and $\hat{C}_4$ are constants. Inserting this approximation for the two body direct correlation function Eq. (5.5) into the approximate excess free energy Eq. (5.4), produces:

$$F_{\text{ex}}[\rho(\mathbf{x})] \approx F_{\text{ex}}[\rho_0] + \mu_{\text{ex}} \int d\mathbf{x}\, \Delta\rho(\mathbf{x}) + \frac{1}{2} \int d\mathbf{x}\, \Delta\rho(\mathbf{x})(\hat{C}_0 + \hat{C}_2\nabla^2 + \hat{C}_4\nabla^4)\Delta\rho(\mathbf{x}), \tag{5.6}$$

which makes $F_{\text{ex}}[\rho(\mathbf{x})]$ a local functional. Using this expression for the excess free energy term we can now write the Helmholtz free energy for the system as:

$$F[\rho(\mathbf{x})] = \int d\mathbf{x} \left[f_0(\rho(\mathbf{x})) + \frac{1}{2}\Delta\rho(\hat{C}_2\nabla^2 + \hat{C}_4\nabla^4)\Delta\rho \right], \tag{5.7}$$

where

$$f_0(\rho) = k_B T\rho(\ln(\rho) - 1) + f_{\text{ex}}[\rho_0] + \mu_{\text{ex}}\Delta\rho + \frac{1}{2}\Delta\rho\hat{C}_0(\rho), \tag{5.8}$$

where the first term in $f_0(\rho(\mathbf{x}))$ comes from the ideal gas contribution, see Eq. (2.16). We also make a further approximation by making a Taylor expansion of the function $f_0(\rho)$ around the reference density ρ_0, giving:

$$f_0(\rho) \approx f_0(\rho_0) + f_0'(\rho_0)\Delta\rho + \frac{f_0''(\rho_0)}{2}\Delta\rho^2 + \frac{f_0^{(3)}(\rho_0)}{3!}\Delta\rho^3 + \frac{f_0^{(4)}(\rho_0)}{4!}\Delta\rho^4. \tag{5.9}$$

We choose the reference density ρ_0 such that the third derivative of the function $f_0(\rho)$ disappears at $\rho = \rho_0$ - i.e. $f_0^{(3)}(\rho_0) = 0$, this gives the following:

$$f_0(\rho) \approx f_0(\rho_0) + f_0'(\rho_0)\Delta\rho + \frac{f_0''(\rho_0)}{2}\Delta\rho^2 + \frac{f_0^{(4)}(\rho_0)}{4!}\Delta\rho^4. \tag{5.10}$$

We now introduce a change of variables. We use the non-dimensional variable $\phi = \frac{\Delta\rho}{\rho_1}$, where ρ_1 is a constant density. So Eqs. (5.7) and (5.10) become:

$$F[\phi(\mathbf{x})] = \int d\mathbf{x} \left[f_0(\phi(\mathbf{x})) + \frac{1}{2}\phi(C_2\nabla^2 + C_4\nabla^4)\phi \right], \tag{5.11}$$

where $C_2 = \hat{C}_2/\rho_1^2$, $C_4 = \hat{C}_4/\rho_1^2$ and

$$f_0(\phi) \approx a + b\phi + \frac{c\phi^2}{2} + \frac{d\phi^4}{4}, \tag{5.12}$$

where a, b, c and d are constant. We now consider the dynamics of the model. We start with the DDFT equation (2.47), with a mobility coefficient M:

$$\frac{\partial\rho(\mathbf{x},t)}{\partial t} = \nabla \cdot \left[M\rho(\mathbf{x},t)\nabla \frac{\delta F[\rho(\mathbf{x},t)]}{\delta\rho(\mathbf{x},t)} \right], \tag{5.13}$$

In the limit when $\rho_1\phi$ is small, the density preceding the gradient of the functional derivative becomes constant, i.e. $M\rho = M(\rho_0 + \rho_1\phi) \approx M\rho_0$ and Eq. (5.13) reduces to the following equation:

$$\frac{\partial\rho(\mathbf{x},t)}{\partial t} = M\rho_0\nabla^2\frac{\delta F[\rho(\mathbf{x},t)]}{\delta\rho(\mathbf{x},t)}. \tag{5.14}$$

This is often referred to as "model B" dynamics in the classification of Hohenberg and Halperin [106]. With the change of variables $\phi = \frac{\Delta\rho}{\rho_1}$, we get the following equation for the time evolution of the order parameter $\phi(\mathbf{x},t)$:

$$\frac{\partial\phi(\mathbf{x},t)}{\partial t} = \alpha\nabla^2\frac{\delta F[\phi(\mathbf{x},t)]}{\delta\phi(\mathbf{x},t)}, \tag{5.15}$$

where $\alpha = \frac{M\rho_0}{\rho_1^2}$ is the mobility coefficient. Since the constant and linear terms in Eq. (5.12) are irrelevant for the dynamics, we may drop the terms $a+b\phi$ from the function $f_0(\phi)$ in Eq. (5.12). The functional derivative of the free energy is then given by the following expression:

$$\begin{aligned}
\frac{\delta F}{\delta\phi} &= c\phi + d\phi^3 + \frac{C_2}{2}\nabla^2\phi + \frac{C_4}{2}\nabla^4\phi + \nabla^2(\frac{C_2}{2}\phi) + \nabla^4(\frac{C_4}{2}\phi) \\
&= c\phi + d\phi^3 + C_2\nabla^2\phi + C_4\nabla^4\phi \\
&= d(\frac{c}{d}\phi + \phi^3 + \frac{C_2}{d}\nabla^2\phi + \frac{C_4}{d}\nabla^4\phi).
\end{aligned} \tag{5.16}$$

We may absorb the parameter d into the mobility coefficient α. We may choose ρ_1 so that $\frac{C_4}{d} = 1$ and writing the parameter values $\frac{C_2}{d} = 2q^2$ and $\frac{c}{d} = r + q^4$ we arrive exactly to the commonly used PFC free energy:

$$F[\phi(\mathbf{x})] = \int d\mathbf{x}\, f(\phi(\mathbf{x})), \tag{5.17}$$

where

$$\begin{aligned}
f(\phi) &= \frac{r+q^4}{2}\phi^2 + \frac{\phi^4}{4} + \frac{1}{2}\phi(2q^2\nabla^2 + \nabla^4)\phi, \\
&= \frac{\phi}{2}\big[r + (q^2+\nabla^2)^2\big]\phi + \frac{\phi^4}{4}.
\end{aligned} \tag{5.18}$$

Inserting these parameter values into the functional derivative of the free energy (Eq. (5.16)), we obtain $\frac{\delta F}{\delta\phi} = (r+q^4)\phi + \phi^3 + 2q^2\nabla^2\phi + \nabla^4\phi$. The PFC model is then given by the conserved dynamics in Eq. (5.15), where the free energy is given by Eqs. (5.17) and (5.18).

5.2 Background to the PFC model

There is an extensive and rapidly growing literature on the PFC model. In a large proportion of this literature, the free energy used in the model is of the form given by Eqs. (5.17) and (5.18) [107–114], as such, this model will hereby be referred to as the regular PFC model. In Sec. 5.3 we briefly discuss the equilibrium behaviour and display some of the key results for the regular PFC model. Inevitably, variations of the regular PFC model exist and it is common practice to modify the free energy or append extra terms to fashion a model which exhibits the desired physical effects. It is clear from the DDFT based derivation of the regular PFC model above in Sec. 5.1, that by truncating the gradient expansions for the free energy at different points, choosing alternative reference densities ρ_0 and ρ_1 and picking the resulting variables differently we could arrive at a whole host of different free energy equations with varying powers of ϕ and different gradient terms with different coefficients. Another common form used for the free energy of PFC models is where a ϕ^3 term is included in the free energy Eq. (5.18) [101, 115, 116]. In terms of the derivation presented here, if the reference density ρ_0 is not chosen in such a way that the ρ^3 term disappears in Eq. (5.9) then the resulting free energy would contain a ϕ^3 term. However, it has been discussed that the inclusion of a ϕ^3 term in the free energy has no qualitative effect in the model [115, 116]. In refs. [115, 116] the authors derive a PFC free energy with a ϕ^3 term, but they then set the coefficient of the term to zero, noting that excluding the third order term has no effect on the grand potential, Euler-Lagrange equation or the equation of motion. In ref. [117], Wu et al. present a modified PFC model where they include extra gradient terms which changes the thermodynamics of the system, which results in the formation of structures which are not usually observed for the regular PFC model. The additional terms resulted in structures with square ordering (rather than the usual hexagonal ordering) in two dimensions. A recent modification to the free energy equation of the regular PFC model is the inclusion of a vacancy term [118, 119]. The vacancy term is a piecewise function which is zero for positive values of ϕ, but takes the value $-H\phi^3$ for negative ϕ, where H is a large positive constant. The addition of this vacancy term penalises negative values of ϕ, which breaks the $\phi \to -\phi$ symmetry of the free energy equation and drastically changes the behaviour of the model. In chapter 6 we investigate the behaviour of this modified PFC model in detail.

The dynamics we use for the regular PFC model in Sec. 5.3 and the modified PFC model in

chapter 6 is given by Eq. (5.15) and can be derived from DDFT (c.f. Sec. 5.1). This simple equation is commonly used to model the time evolution of the order parameter ϕ [101, 111–114, 120]. It is also possible to include a second time derivative which allows the model to capture processes on both the fast time scale, e.g. elastic interactions, and on the slower diffusive time scale [110, 118]. Often, an extra white noise term is included in the dynamical equation to account for thermal fluctuations [107–109, 115, 116, 118]. Considering the DDFT derivation described above in Sec. 5.1: the order parameter $\phi(\mathbf{x}, t)$ is derived from the one-body ensemble averaged density $\rho(\mathbf{x}, t)$ (c.f. Sec. 2.2). This definition of the density already accounts for thermal fluctuations and so appending a noise term actually leads to an overcounting of the fluctuations [74, 101]. However, if we consider the order parameter $\phi(\mathbf{x}, t)$ to be a time averaged 'coarse grained' quantity instead, then it can be argued that the white noise term can be legitimately included [74]. Note that the derivation presented in Sec. 5.1 assumes that $\rho(\mathbf{x}, t)$ is an ensemble averaged quantity. We return to this issue in Sec. 6.4 of chapter 6.

In this thesis, the regular PFC model equations are obtained using DFT and DDFT, which naturally follows from the theory presented in chapter 2. This is a fairly modern justification of the PFC model, which has appeared in recent publications [101, 105, 109, 115, 116, 121]. However, the origins of the PFC literature predates this derivation by several years, with the model being introduced in 2002 by Elder et al. [107] while the first paper linking the PFC model to classical DFT appeared in 2007 [105]. Initially, the equations of the model were presented phenomenologically, with the PFC model equations being chosen for their simplicity and the periodic structures which they form [107]. Later, in 2004, Elder et al. described how a free energy may be constructed which exhibits the periodic structuring desired [108]. The starting point for this description is based on phase field models, where the value of the order parameter ϕ is linked to the local time averaged density field $\rho(\mathbf{x}, t)$ [108]. The form of the free energy can then be constructed by considering a system exhibiting liquid-solid phase coexistence, where the liquid is represented by a homogeneous order parameter profile, while in the solid phase the order parameter is a periodic array of 'bumps', in much the same way that the distribution of the density in a liquid is approximately uniform, while in crystalline structures the distribution is given by a series of peaks with long range order. The second and forth order gradient terms are needed in order for the free energy to be minimised by a spatially periodic structure. Taking these aspects into account Elder et al. [108] arrive at a simple free energy of the form shown in Eqs. (5.17) and (5.18). This formulation of the free energy is not unique to

the regular PFC model and was originally introduced by Swift and Hohenberg in 1977 [122], where they considered non-conserved dynamics. Similar models to the PFC, where the free energy takes the form of the Swift-Hohenberg equation and the dynamics are conserved, arise in different contexts as well [123, 124].

The free energy of the regular PFC model (Eqs. (5.17) and (5.18)) is minimised by either periodic structures or by a homogeneous flat profile, depending on the values of q, r and

$$\bar{\phi} = \frac{1}{L^d} \int d\mathbf{x}\, \phi(\mathbf{x}, t), \tag{5.19}$$

where L^d is the size of the system. In two dimensions ($d = 2$), one observes a homogeneous phase, two hexagonal phases (hexagonally ordered bumps/holes) and a stripe phase (the 2D phase diagram is plotted in Fig. 5.4) [107–109, 112]. The literature largely focuses on the region of the 2D phase diagram which contains the hexagonally arranged bumps and their transition to the homogeneous state [101, 105, 107–109, 111, 112, 117]. The uniform profile $\phi(\mathbf{x}, t) = \bar{\phi}$ represents the order parameter in a uniform liquid and the hexagonal phase is treated as a crystal, which is consistent with both the DFT and DDFT descriptions. As such, the applications of PFC models are generally associated with crystalline structures or the transition between liquid and solid states. Specifically, PFC models have been successfully applied to problems including melting and freezing [101, 105], grain boundary effects [107, 108, 112], glass formation [119], the propagation of crystallisation fronts [109, 114–116] and the orientation of the symmetry in crystalline structures [117]. In chapter 6 we consider the application of a modified PFC model to modelling colloidal fluids and how the concentration in a binary mixture can change the crystalline ordering.

The PFC model may be extended to consider binary systems [105, 119–121, 125]. In order to model binary mixtures we can either consider two coupled order parameter fields which correspond to the density of each species [119] or the total density of the system and the concentration of one of the species in the mixture [105, 120, 125]. In chapter 6 we show how the modified PFC model can be extended to a simple two component model. PFC models are also studied in three dimensions [113, 115, 116, 125]. The extra dimension has a profound affect on the phase behaviour, with the introduction of rods and body-centred cubic, face-centred cubic and hexagonally close packed ordered arrays of bumps [113]. Obviously, the extension into another dimension makes simulations of the model over long time scales much more com-

putationally demanding.

The PFC model is a fairly simple model for studying solids and liquids which can be derived from the microscopic properties of materials with an extensive list of assumptions. As such, PFC models can qualitatively describe many different systems which involve crystalline materials or the transition between the solid and liquid states. This versatility is reflected in the many different variations and applications of PFC models that can be found in the extensive PFC literature. In this thesis we present some of the key results of the regular PFC model (below in Sec. 5.3), we discuss a modified PFC model in one and two dimensions (Sec. 6.2 in chapter 6) and a two component modified PFC model (Sec. 6.3 in chapter 6).

5.3 Thermodynamics and the phase behaviour of the regular PFC model

In this section, we examine the regular PFC model and determine the phase diagram in one and two dimensions and display some of the order parameter profiles obtained from time simulations.

5.3.1 Linear stability of a homogenous steady state

We begin by using a linear stability analysis to determine the limit of linear stability of a homogeneous flat state in the system. In the context of colloidal suspensions exhibiting micro-phase separation and fluids of charged particles, this limit of linear stability is referred to as a "λ-line" [126–129].

We assume that the form of the order parameter ϕ is given by a uniform distribution with an additional small amplitude harmonic modulation:

$$\phi = \bar{\phi} + \delta\phi = \bar{\phi} + \xi e^{i\mathbf{k}\cdot\mathbf{x}} e^{\beta t}, \tag{5.20}$$

where $\bar{\phi}$ is the average order parameter value, as defined in Eq. (5.19) and $\xi \ll 1$ is a small amplitude. Substituting this order parameter profile Eq. (5.20) into the functional derivative of the free energy Eqs. (5.17) and (5.18) we obtain:

$$\frac{\delta F}{\delta \phi} = (r + q^4)\bar{\phi} + \bar{\phi}^3 + \left[(k^2 - q^2)^2 + \Delta_R\right]\delta\phi + O(\delta\phi^2), \tag{5.21}$$

where

$$\Delta_R = r + 3\bar{\phi}^2, \tag{5.22}$$

where the subscript R signifies that Δ is defined here for the regular PFC model (note that later we define a Δ_V for the vacancy PFC model in Eq. (6.4)). Inserting this expression for the functional derivative Eq. (5.21) into the dynamical equation (5.15) and linearising we obtain:

$$\beta = -k^2\alpha[(k^2 - q^2)^2 + \Delta_R]. \tag{5.23}$$

We may use this dispersion relation Eq. (5.23) to determine the linear stability of the system in a similar manner as before in Sec. 4.4 of chapter 4. From the assumed order parameter profile we can see that the sign of $\beta(k)$ determines whether or not an initial modulation will grow or decay. Hence, when $\beta(k) < 0, \forall k$, the amplitude of the modulation will decrease over time, but when $\beta(k) > 0$ for any wavenumber k, any modulation with wavenumber $k = |\mathbf{k}|$ will increase in amplitude. There is a local maximum in β (which becomes the global maximum when the uniform state is unstable) at the wavenumber:

$$k_m = \frac{1}{3}\sqrt{6q^2 + 3\sqrt{q^4 - 3\Delta_R}}. \tag{5.24}$$

Thus, if one considers an initially almost flat profile $\phi(\mathbf{x}, t = 0) = \bar{\phi} + \mathcal{X}(\mathbf{x})$, where $\mathcal{X}(\mathbf{x})$ is composed of a sum of a large number of harmonic modulations [c.f. Eq. (5.20)], having a range of wavenumbers k (in practice $\mathcal{X}(\mathbf{x})$ is generated by adding a small random number to the discretised initial profile), then as the system evolves in time, typical length scale modulations will form in $\phi(\mathbf{x}, t)$. The typical length scale for the modulations is $\frac{2\pi}{k_m}$, since this corresponds to the maximum of $\beta(k)$. The length scale has an inverse dependency on the value of q, i.e. increasing the value of q will reduce the size of the structures which are formed.

The limit of linear stability is defined as the locus of points in parameter space where the maximum in the dispersion relation (5.23) is at zero, i.e. $\beta(k_m) = 0$. Solving $\beta = \frac{\partial\beta}{\partial k} = 0$, when $\alpha \neq 0$ and $k \neq 0$ we find that $k_m = \pm q$ and $\Delta_R = 0$ at the limit of linear stability. Hence, Δ_R in Eq. (5.22) can be considered as a measure of stability: when $\Delta_R < 0$ the system is linearly unstable and when $\Delta_R > 0$ the system is linearly stable. The magnitude of Δ_R shows how 'far' we are from the limit of stability. Fig. 5.1 shows the dispersion relations for various values of Δ_R. In accordance with Eq. (5.24) we note that when $\Delta_R > \frac{q^4}{3}$ the maximum at $k_m \approx q$

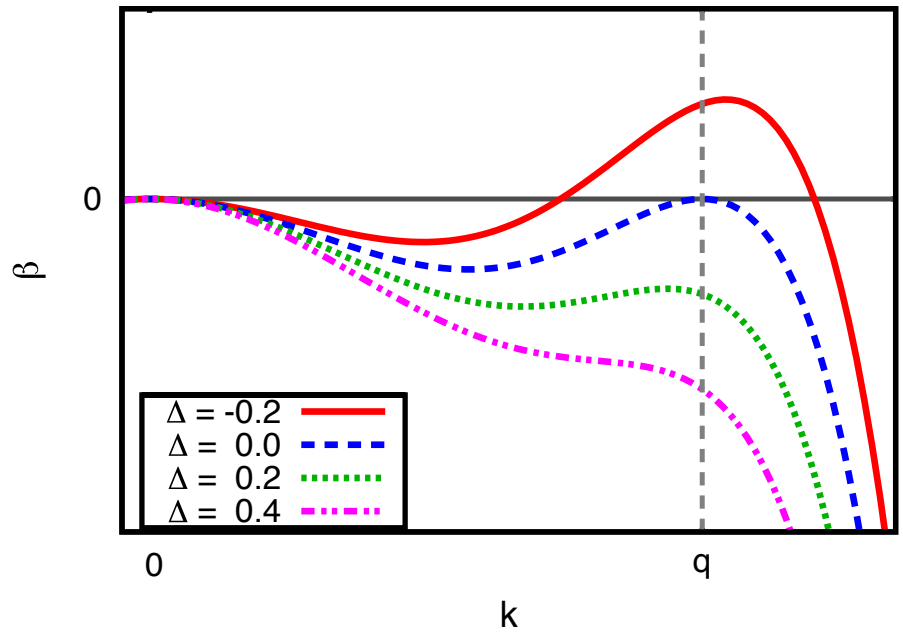

Figure 5.1: Dispersion relation curves for the PFC model (Eqs. (5.17) and (5.18)), when $q = 1$. Four cases are shown; i) when the maximum of $\beta > 0$, (red solid line), ii) when the maximum of $\beta = 0$ (blue dashed line), iii) when the maximum of $\beta < 0$ and k_m exists (green dotted line) and iv) when the maximum of $\beta < 0$ and k_m does not exist (magenta dash-dotted line).

disappears and therefore there is only one remaining maximum at $k = 0$. It is important to note that these dispersion relations are identical to those of the vacancy PFC model studied in the following chapter for positive values of the order parameter $\bar{\phi} > 0$.

5.3.2 Phase diagram in one dimension

We now have an expression for the limit of linear stability of homogeneous films, but in order to complete the phase diagrams of the regular PFC model we need to consider what phases are observed and calculate the coexistence curves between these different phases. Due to the symmetry of the free energy Eq. (5.18) the phase diagrams are symmetrical about $\bar{\phi} = 0$. First of all, we construct the 1D phase diagram. The regular PFC model in one dimension exhibits two distinct phases [108]: a non-uniform state in which the order parameter profile resembles a sinusoid and a uniform state in which the order parameter is a constant. There exist two tricritical points in the phase diagram - see Fig. 5.3. Above the tricritical points the transition between the periodic and homogeneous phases is of second order and occurs at the limit of linear stability $\Delta_R = 0$. Below the tricritical points, we observe a first order transition between the two states, meaning that a periodic phase with $\bar{\phi} = \bar{\phi}_p$ coexists with a uniform phase with

$\bar{\phi} = \bar{\phi}_{\rm h}$ - i.e. the temperature, chemical potential and pressure are equal at these two different state points. To calculate the location of the tricritical points, one must obtain an expression for the free energy in both the periodic and the homogeneous phases. Since the wavenumber near $\Delta_R = 0$ is $k_m \approx q$ we assume that the order parameter profile in the periodic phase takes the form:

$$\phi = \bar{\phi}_p + A\cos qx + B\cos 2qx + \cdots . \tag{5.25}$$

This two-mode approximation is reliable around the limit of linear stability $\Delta_R = 0$. Moreover, the two-mode approximation appears to be exact at the tricritical point, since the location of the tricitical point is unaffected by the inclusion of $\cos 3qx$ and higher order modes. In contrast, the mode $B\cos 2qx$ must be retained in order to obtain the correct value of the amplitude A in the vicinity of the tricritical point. Substituting the two mode approximation into the free energy Eq. (5.18) and integrating over the period 0 to $2\pi/q$ we obtain the following expression for the free energy per unit length $f_p = F/L$ of the periodically modulated phase:

$$\begin{aligned} f_p &= \frac{1}{2}(r+q^4)\bar{\phi}_p^2 + \frac{1}{4}\bar{\phi}_p^4 + \frac{1}{4}rA^2 + \frac{1}{4}(r+9q^4)B^2 \\ &\quad + \frac{3}{4}\bar{\phi}_p^2(A^2+B^2) + \frac{3}{4}\bar{\phi}_p A^2 B + \frac{3}{32}(A^4 + 4A^2B^2 + B^4). \end{aligned} \tag{5.26}$$

Now, we minimise the free energy of the periodic phase f_p with respect to the two amplitudes A and B giving the following two conditions:

$$\Delta_p + 3\bar{\phi}_p B + \frac{3}{4}A^2 + \frac{3}{2}B^2 = 0, \tag{5.27}$$

$$\Delta_p B + 9q^4 B + \frac{3}{2}\bar{\phi}_p A^2 + \frac{3}{2}A^2 B + \frac{3}{4}B^3 = 0, \tag{5.28}$$

where

$$\Delta_p = r + 3\bar{\phi}_p^2. \tag{5.29}$$

Solving the first of these expressions Eq. (5.27) for A, we obtain the following:

$$A = \frac{1}{3}\sqrt{-12\Delta_p - 36\bar{\phi}_p B - 18B^2}. \tag{5.30}$$

Inserting this amplitude of A Eq. (5.30) into Eq. (5.28) and linearising in terms of B, we find:

$$\begin{aligned} \Delta_p B + 9q^4 B + \frac{3}{2}\bar{\phi}_p\big[-\frac{12}{9}\Delta_p - 4\bar{\phi}_p B\big] + \frac{3}{2}\big[-\frac{12}{9}\Delta_p\big]B + O(B^2) &= 0, \\ -2\Delta_p\bar{\phi}_p + \big(9q^4 - 6\bar{\phi}_p^2 - \Delta_p\big)B + O(B^2) &= 0, \end{aligned} \tag{5.31}$$

hence, we obtain the amplitude

$$B \equiv \frac{2\Delta_p \bar{\phi}_p}{9q^4 - 6\bar{\phi}_p^2 - \Delta_p}. \tag{5.32}$$

Note that in the limit that $\bar{\phi}_p \to 0$ the amplitude A reduces to that obtained when performing a one mode approximation $A = (2/3)\sqrt{-3\Delta_p}$ [108]. Therefore, the one mode approximation is only accurate at small values of $\bar{\phi}_p$ and Δ_p, i.e. near the point $r = 0$, $\bar{\phi} = 0$. Substituting these amplitudes (Eqs. (5.30) and (5.32)) into the expression for the free energy of the periodic phase (5.26) gives a good approximation of the free energy near the $\Delta_R = 0$ curve. This can then be used in conjunction with an expression for the free energy of the homogeneous state to calculate the coexistence curves below the tricritical point. The free energy for a homogeneous flat film with $\bar{\phi} = \bar{\phi}_h$ is simply given by ignoring the gradient terms in Eq. (5.18) (or equivalently setting $A = B = 0$ in Eq. (5.26)), which gives the expression

$$f_h = \frac{r + q^4}{2}\bar{\phi}_h^2 + \frac{\bar{\phi}_h^4}{4}. \tag{5.33}$$

Using the expressions we have obtained for the free energy of the periodic phase (Eq. (5.26) together with Eqs. (5.30) and (5.32)), and the homogeneous phase Eq. (5.33) we may calculate the coexistence region between the two phases. For two phases to coexist they must have the same temperature, pressure and chemical potential, (c.f. Sec. 4.4). Geometrically, this corresponds to making a common tangent construction on the free energy. When the two phases coexist, one will be able to draw a straight line which lies tangent to both curves, the value of $\bar{\phi}_p$ and $\bar{\phi}_h$ where these tangents occur are the coexisting values. This is equivalent to solving the following for $\bar{\phi}_p$ and $\bar{\phi}_h$:

$$\frac{\partial f_p}{\partial \bar{\phi}_p} = \frac{\partial f_h}{\partial \bar{\phi}_h} = \frac{f_h - f_p}{\bar{\phi}_h - \bar{\phi}_p}. \tag{5.34}$$

Note that the first derivative of the free energy with respect to the order parameter is the chemical potential $\mu_p = \frac{\partial f_p}{\partial \phi_p}$ and $\mu_h = \frac{\partial f_h}{\partial \phi_h}$. In Fig. 5.2 we plot the chemical potential of the two different phases versus the average order parameter $\bar{\phi}$ for three different values of r. We observe that when there are two coexisting phases (as in Fig. 5.2 (c)), there is a maximum in μ_p that occurs before the limit of linear stability $\Delta_R = 0$ (the point where the two chemical potentials intersect). The coexisting values will be an order parameter value $\bar{\phi}_p$ between the maximum and the intersection and the corresponding value $\bar{\phi}_h$ where $\mu_p = \mu_h$ (The exact order parameter values can be found using Eq. (5.34)). When the transition between the two phases is second order, there is no maximum of μ_p - i.e. there is no range of values of μ for which

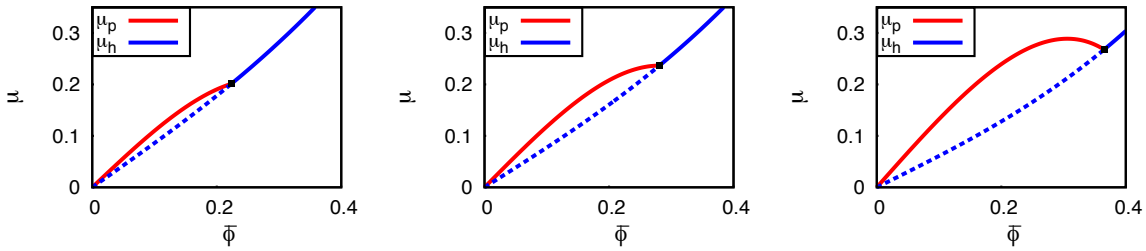

(a) $r = -0.15$ **(b)** $r = -0.237$ **(c)** $r = -0.4$

Figure 5.2: Plots of the chemical potentials μ_p and μ_h for varying values of r, where $q = 1$. On the left we show a case where we observe second order phase transition and on the right we observe a first order transition. The plot in the middle displays the two chemical potentials for the value of r at which the tricritical point occurs. The dashed blue line shows the continuation of the (unstable) homogeneous phase beyond the limit of linear stability. The black square shows where the limit of linear stability of the homogeneous phase occurs.

there are two different $\bar{\phi}$ values with the same μ. Hence, there is no coexistence between the two phases for this r value (an example is shown in Fig. 5.2 (a)). It therefore follows that the tricritical point at which the phase transition switches from second to first order must occur when the maximum in μ_p coincides with the limit of linear stability. This is equivalent to solving the following pair of equations:

$$\begin{aligned} \frac{\partial^2 f_p}{\partial \bar{\phi}^2} &= 0, \\ \Delta_R &= 0. \end{aligned} \tag{5.35}$$

Solving these equations (5.35) we obtain the solution for the tricritical point $r = -(9/38)q^4$ and $\bar{\phi} = \sqrt{3/38}q^2$. These values may also be obtained in a some what different manner - see appendix D.

In Fig. 5.3 we display the phase diagram for the 1D regular PFC model. Due to the symmetry of the free energy Eq. (5.18) ($\bar{\phi} \to -\bar{\phi}$) the phase diagram is symmetrical around $\bar{\phi} = 0$. The blue dashed line shows the limit of linear stability and the red dots show the tricritical points. The red curves show the coexistence curves calculated using the two mode approximation. Above the tricritical points we observe a second order phase transition which occurs at the limit of linear stability. However, below the tricritical points there is a region of coexistence, as depicted by the striped area in Fig. 5.3. The coexistence curves are calculated below the tricritical points using a common tangent construction on the free energy equations for the periodic (5.26) and the homogeneous (5.33) phases.

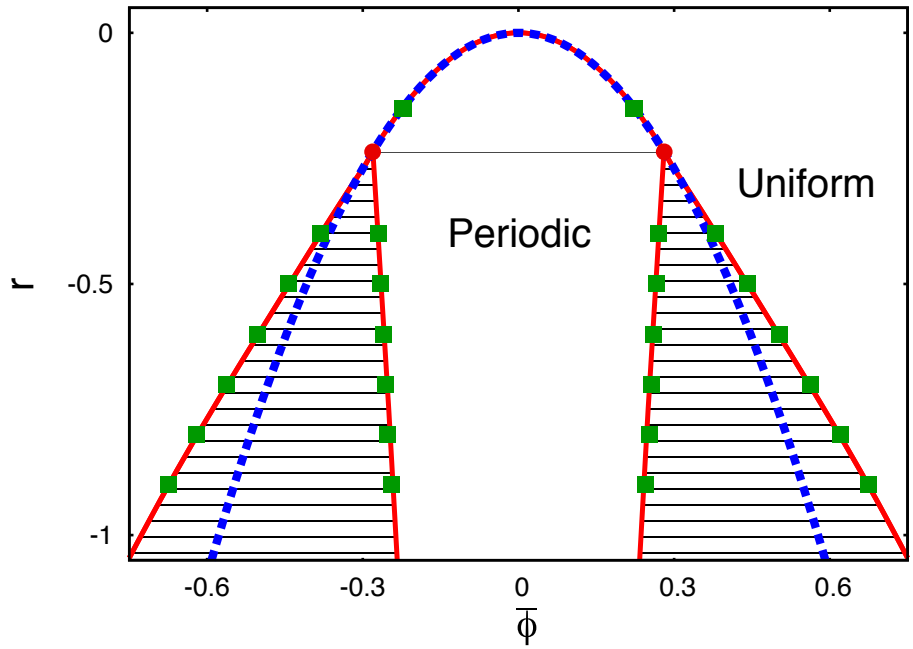

Figure 5.3: The phase diagram for the 1D regular PFC model for the case when $q = 1$. The red solid lines are the coexistence curves between the periodic and uniform phases calculated using the two mode approximation. The green squares show the coexistence values calculated from simulations. The red circles are the tricritical points. The blue dashed line is the locus $\Delta_R = 0$, which is the limit of linear stability for uniform profiles.

The coexistence curves may also be obtained from time simulation solutions for the system. We pick a value of r and use a finite difference scheme to minimise the free energy at discrete values of $\bar{\phi}$, i.e. we run the simulation until the system reaches a state of equilibrium. For each value of $\bar{\phi}$ we minimise the free energy with respect to the system size using periodic boundary conditions, so that we are effectively calculating the free energy of an infinite system. We start with a value of $\bar{\phi}_i$ in the middle of the periodic phase with an initial order parameter profile with a small amplitude noise ($\phi_i(\mathbf{x}, t = 0) = \bar{\phi}_i + 10^{-6}(Y - 0.5)$, where Y is a random real number uniformly distributed between 0 and 1) and find the order parameter profile ϕ_i^* which minimises the free energy. We then increment the value of $\bar{\phi}$ and use the previously calculated profile for the initial profile of the next step $\phi_{i+1}(\mathbf{x}, t = 0) = \phi_i^* + \Delta\phi + 10^{-6}(Y - 0.5)$, where $\Delta\phi = \bar{\phi}_{i+1} - \bar{\phi}_i$. This process is repeated until the equilibrium order parameter profile ϕ^* is no longer periodic. The same process is repeated starting from $\bar{\phi}_i$ and decreasing $\bar{\phi}$, so that we obtain the free energy of the periodic phase for $\bar{\phi}$ values across the full range of the periodic phase. A polynomial is fitted to the free energy values corresponding to these curves using a least squares method, which gives an expression for the free energy of the periodic phase. A

common tangent construction is made using the fitted polynomial and the analytic expression for the free energy of the homogenous phase Eq. (5.33) to obtain the coexistence values for the chosen value of r. The coexistence values obtained using this method are displayed as green boxes in Fig. 5.3. We observe an outstanding agreement between the two mode approximation and the simulation results.

5.3.3 Phase diagram in two dimensions

The PFC model is most commonly studied in two dimensions, where stripes (see Fig. 5.4 (d)) and hexagonally ordered bumps (see Fig. 5.4 (b)) and holes (see Fig. 5.4 (e)) are observed. Hence, the 2D phase diagram of the regular PFC model receives a lot of interest in the literature [105, 107–110, 112, 116]. The phase diagram is commonly constructed using a one mode approximation [107–109, 116], but as previously discussed in Sec. 5.3.2, this approximation is only accurate in the vicinity of the critical point at $r = 0$, $\bar{\phi} = 0$. Here, we determine the coexistence curves using the numerical time simulation based method discussed above. The phase diagram is plotted in Fig. 5.4 (a), the blue dashed line is the limit of linear stability of homogenous films $\Delta_R = 0$, the red solid lines are the coexistence curves for the different phases and the grey striped areas are coexistence regions. The free energy curves for the striped and the hexagonal (bumps and holes) phases are determined from simulation and the free energy for the uniform phase is given by Eq. (5.33). Coexistence $\bar{\phi}$ values are calculated for a particular value of r by performing a common tangent construction between the corresponding free energy curves (c.f. Eq. (5.34)). After the coexistence values have been determined for a sufficient number of r values we fit a smooth curve to the data to obtain the coexistence curves.

The symmetry observed in the one dimensional phase diagram (c.f. Fig. 5.3) remains, with stripes appearing for small magnitudes of $\bar{\phi}$, hexagonal structures appearing at intermediate values of $|\bar{\phi}|$ and flat films are observed when $r > 0$ or when $|\bar{\phi}|$ is large. In the coexistence regions, the equilibrium order parameter profiles resemble a hybrid of the two coexisting structures (e.g. the profile in Fig. 5.4 (c) shows a coexistence between bumps and stripes). In the hexagonal phase for positive values of $\bar{\phi}$, one observes hexagonally arranged holes in a background region with a high value for the order parameter. Hence, from the symmetry, one observes bumps in a background region having a low value of ϕ in the negative hexagonal phase. In Figs. 5.4 (b)–(e) we show the order parameter profiles obtained from time simulations where $r = -0.9$ and $q = 1$ for different values of $\bar{\phi}$. Similarly to the 1D simulations, we use a finite

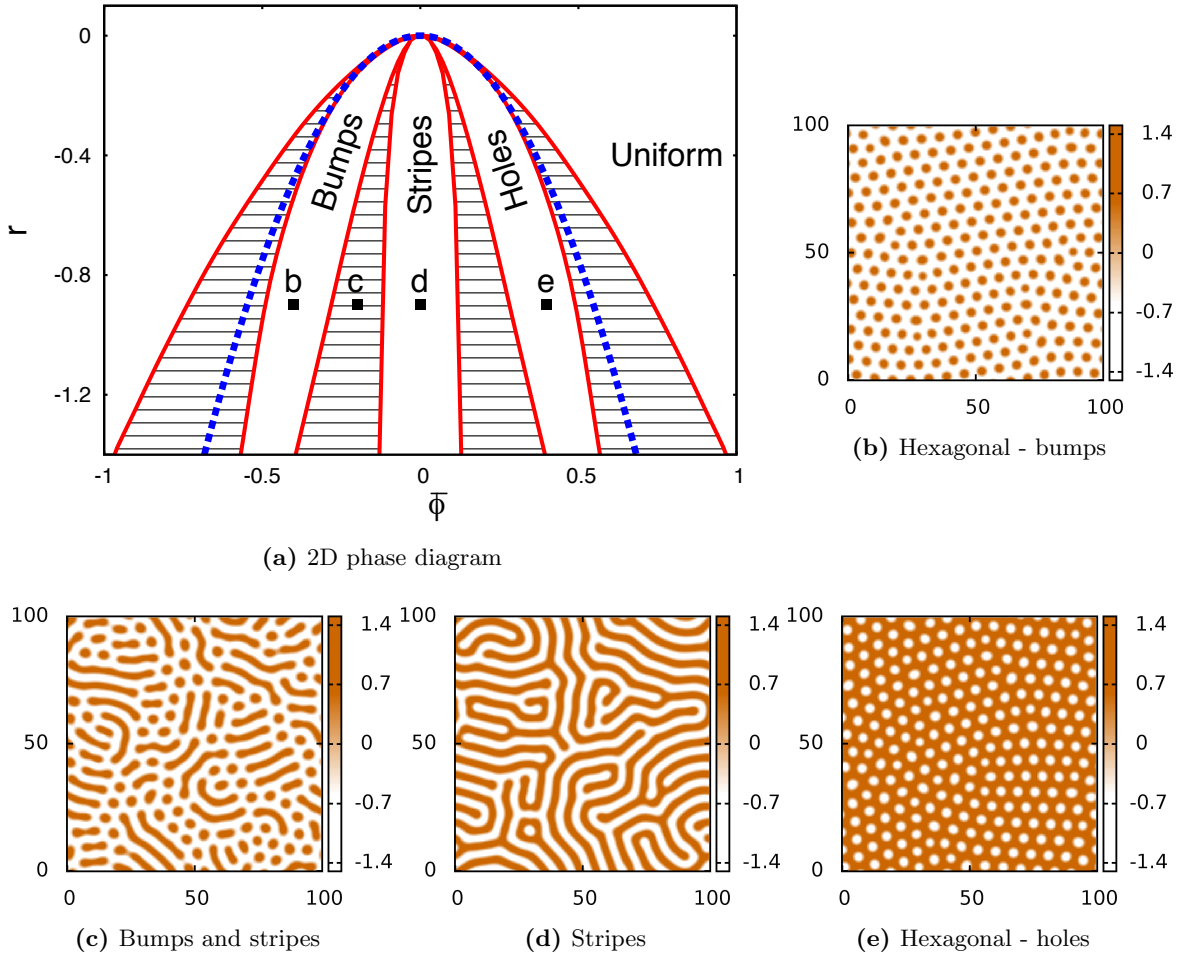

(a) 2D phase diagram

(b) Hexagonal - bumps

(c) Bumps and stripes

(d) Stripes

(e) Hexagonal - holes

Figure 5.4: (a) Phase diagram for the 2D regular PFC model (Eqs. (5.15), (5.17) and (5.18)) when $q = 1$. The red solid lines show the various coexistence curves, the blue dotted line shows the limit of linear stability and the grey striped areas show the miscible regions. We display simulation results of (d) the striped phase, (b) and (e) the hexagonal phases and (c) the coexistence of striped and hexagonal phases. Parameters for simulations are: $q = 1$, $r = -0.9$, $\alpha = 1$, (b) $\bar{\phi} = -0.4$, (c) $\bar{\phi} = -0.2$, (d) $\bar{\phi}$ and (e) $\bar{\phi} = 0.4$.

difference scheme, the boundary conditions are periodic and the initial order parameter profile is a uniform film with small amplitude noise added. In the three distinct phases (b) bumps, (d) stripes and (e) holes we observe various defects and grain boundaries which are dependent on the initial noise profiles and in (c) we find that we do not obtain full phase separation between bumps and stripes. This is because the simulations become 'stuck' at a local minimum in the free energy and even though they have not yet reached equilibrium, the cost in energy to remove all the defects is too high. We return to this issue in Sec. 6.2. Note, that the simulations used to calculate the phase diagram are much smaller than those shown here, as they must be defect free in order to avoid large errors induced by the increase in energy associated with any defects.

In the next chapter, we describe the so called vacancy PFC model in which one appends an extra term to the free energy of the regular PFC. This extra term breaks the symmetry of the phase diagrams and has a substantial effect on the general phase behaviour of the model.

Chapter 6

Modelling fluids and crystals using a two component modified phase field crystal model

A modified phase field crystal model in which the free energy may be minimised by an order parameter profile having isolated bumps is investigated. The phase diagram is calculated in one and two dimensions and we locate the regions where modulated and uniform phases are formed and also regions where localised states are formed. We investigate the effectiveness of the phase field crystal model for describing fluids and crystals with defects. We further consider a two component model and elucidate how the structure transforms from hexagonal crystalline ordering to square ordering as the concentration changes. Our conclusion contains a discussion of possible interpretations of the order parameter field.

6.1 Introduction

Modelling materials at the atomic scale is a task which, for example, may be performed using Molecular Dynamics simulations. This involves solving coupled equations of motion to calculate the position of each particle at every time step. The resulting calculations can be very computationally expensive, especially when one seeks to consider phenomena which involve a large number of particles. Only short atomic time scales can be feasibly accessed with this or other such approaches. However, there are some instances where it is important to consider materials on the atomic length scale for much longer diffusive time scales, e.g., when investigating freezing or glass transitions. One approach to such problems that may be adopted is to develop a phase field model capable of describing the structure of materials on the scale of the individual particles. In contrast to traditional phase field models, the recently developed phase field crystal (PFC) models are capable of just such a description and are now widely used in the literature to model crystalline structures [107–114]. See chapter 5 above, for a general review of the PFC models. The regular PFC model is governed by Eqs. (5.15), (5.17) and (5.18). For certain parameter values, the regular PFC free energy functional is minimised by an order parameter profile consisting of a periodic array of bumps which somewhat resembles the density distribution of particles in a crystalline material. This interpretation is bolstered by the fact that it has been shown that the PFC model (Eqs. (5.15), (5.17) and (5.18)) may

be derived from the density functional theory of freezing [105] and the dynamical density functional theory for colloidal particles [101, 121] with certain approximations (this derivation is outlined above in Sec. 5.1).

In the regular PFC model (Eqs. (5.15), (5.17) and (5.18)) the hexagonally arranged bumps are considered to be particles/colloids in a crystalline structure. The interpretation of the striped and hexagonally ordered hole structures is unclear and as such these phases are commonly ignored. The conjecture that the ordered bumps represent crystalline particle structures can be extended by including a 'vacancy term' in the free energy [118, 119] which strongly breaks the hole-bump ($\phi \to -\phi$) symmetry of Eq. (5.17):

$$F[\phi] = \int d\mathbf{x} \ \left[f(\phi) + f_{vac}(\phi) \right], \tag{6.1}$$

where $f(\phi)$ is defined as before in Eq. (5.18). Using this free energy (6.1), it is possible to obtain structures which contain a mixture of bumps and vacant areas (areas where the order parameter is approximately uniform around the value $\phi \approx 0$), which in the interpretation of Ref. [118] resemble snapshots of fluid configurations or crystalline structures with defects. We will return to the issue of the precise interpretation of the nature of the order parameter field in the conclusion. In this chapter we investigate the thermodynamics and the structures formed in this augmented conserved Swift-Hohenberg model, or 'vacancy phase field crystal' (VPFC) model, and also in a two component generalisation of this model. The vacancy term takes the following form [118, 119]:

$$f_{vac}(\phi) = H\phi^2(|\phi| - \phi), \tag{6.2}$$

where H is a constant. We use the value $H = 1500$, as in Refs. [118, 119]. This acts as a piecewise function which is zero for positive values of ϕ and takes an increasingly large value when $\phi < 0$. Hence, this term penalises negative values of ϕ. This leads to the VPFC model forming periodic structures which are somewhat different from those of the regular PFC. In addition, the VPFC model has a large region of parameter space at small $\bar{\phi}$, where spatially localised structures form. The time evolution of the order parameter ϕ is governed by the conserved dynamics used in the regular PFC model (5.15).

We begin in Sec. 6.2 by considering the phase behaviour of the model, investigating the transition between periodic and localised states. We focus on understanding the bifurcation diagrams

connecting the various uniform, periodic and localised states exhibited by the model. We then go on to consider how individual localised states or particles interact with one another. In Sec. 6.3 we extend the model to consider a two component system, and we determine how the particles in the binary mixture interact with one another. We find a transition between hexagonal and square ordering of the particles as the concentration changes. Our conclusions follow in Sec. 6.4, and include a discussion of the proper interpretation of the order parameter field ϕ.

6.2 One Component System

6.2.1 Linear stability of a homogeneous profile

We begin by considering the phase behaviour of the VPFC model (Eqs. (5.15) and (6.1)). We calculate the limit of linear stability for a homogeneous flat state using a linear stability analysis. Since f_{vac} is non-differentiable at $\phi = 0$ we treat it in a piecewise manner, by treating the two cases $\bar{\phi} > 0$ and $\bar{\phi} < 0$ separately. If $\phi(\mathbf{x})$ takes the form of Eq. (5.20) and $\bar{\phi} > |\xi|$, then $f_{vac} = 0$ everywhere and the thermodynamics of the VPFC model reduces to that of the regular PFC model (described in Sec. 5.3.1). To perform the linear stability analysis, we assume that the order parameter takes the form given in Eq. (5.20) and we follow the same steps used in Sec. 5.3.1, but now we include the extra term $f_{vac}(\phi)$. This produces the following dispersion relation:

$$\beta(k) = -k^2\alpha[(k^2 - q^2)^2 + \Delta_V], \tag{6.3}$$

where

$$\Delta_V = r + 6H(|\bar{\phi}| - \bar{\phi}) + 3\bar{\phi}^2 = \Delta_R + 6H(|\bar{\phi}| - \bar{\phi}). \tag{6.4}$$

When the growth rate $\beta(k) > 0$, any small amplitude modulation with wavenumber $k = |\mathbf{k}|$ will grow over time. Continuing to follow the arguments laid out in Sec. 5.3.1, we find the maximum in β occurs at the wavenumber:

$$k_m = \frac{1}{3}\sqrt{6q^2 + 3\sqrt{q^4 - 3\Delta_V}}. \tag{6.5}$$

As previously discussed, the wavenumber k_m corresponds to a typical length scale of $\frac{2\pi}{k_m}$, which will be visible as the system relaxes from the initial perturbations. This length scale therefore influences the size of the structures which are formed. The VPFC dispersion relation Eq. (6.3)

is identical to that obtained for the regular PFC model in Eq. (5.23) with Δ_V in place of Δ_R. Therefore, the dispersion relation curves are identical to the regular PFC relations curves shown in Fig. 5.1. Hence, the limit of linear stability occurs on the curve $\Delta_V = 0$ (obtained by solving $\beta = \frac{\partial \beta}{\partial k} = 0$ with the condition that $k_m \neq 0$). When $\bar{\phi} > 0$, Δ_V reduces to Δ_R and so the limit of linear stability is identical. However, When $\bar{\phi} < 0$ one observes similar dispersion relations but now the limit of linear stability occurs at very small negative values of $\bar{\phi}$.

6.2.2 One-dimensional model

In order to develop a better understanding of the effect of the 'vacancy term' (6.2) we initially consider the phase diagram for the system in one spatial dimension. As shown above in Fig. 5.3, the 1D regular PFC model (Eqs. (5.15), (5.17) and (5.18)) exhibits two distinct phases: a modulated state and a uniform state. The phase diagram of the regular PFC model is symmetric around $\bar{\phi} = 0$ owing to the symmetry of the free energy (5.17) with respect to $\phi \to -\phi$. This is no longer the case when the vacancy term (6.2) is added.

The phase diagram for the 1D VPFC model is shown in Fig. 6.1 (a) and is very different from that of the regular PFC (see Fig. 5.3). As with the regular PFC model, modulated profiles are present below the limit of linear stability $\Delta = 0$ (blue dashed line) provided $\bar{\phi} < \sqrt{3/2}q^2$. However, with the added vacancy term (6.2) the lower limit for the presence of the modulated phase is at $\bar{\phi} \gtrsim 0$ ($H \gg 1$). The tricritical point with $\bar{\phi} > 0$ (red dot) familiar from the PFC model remains. Above this point the phase transition between the periodic and homogeneous phases is of second order. Below this point a periodic phase with $\bar{\phi} = \bar{\phi}_p$ coexists with a homogeneous phase with $\bar{\phi} = \bar{\phi}_h$ and the phase transition between these phases is of first order. Figure 6.1 (a) shows the coexisting phases using fixed temperature (horizontal) tie-lines connecting $\bar{\phi}_p$ and $\bar{\phi}_h$ (solid red lines). The amplitude of the modulations become small as we approach the tricritical point and so the contribution to the free energy from the vacancy term disappears. Therefore, the location of the tricritical point in the VPFC model is exactly the same as in the regular PFC model; at $r = -9/38q^4$, $\bar{\phi} = \sqrt{3/38}q^2$. The tricritical point can be calculated using a two mode approximation - c.f. Sec. 5.3.2 and appendix D.

Since the transition between the periodic and the uniform phases is of first order below the tricritical point, at coexistence the amplitude of the modulated structures does not go to zero. As r decreases, the coexistence region of the phase diagram is increasingly affected by the

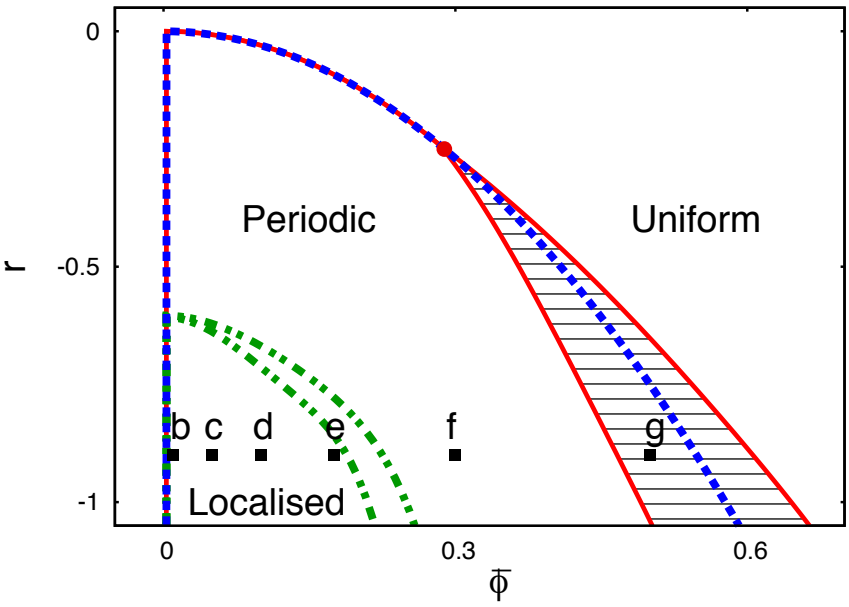

(a) 1D phase diagram

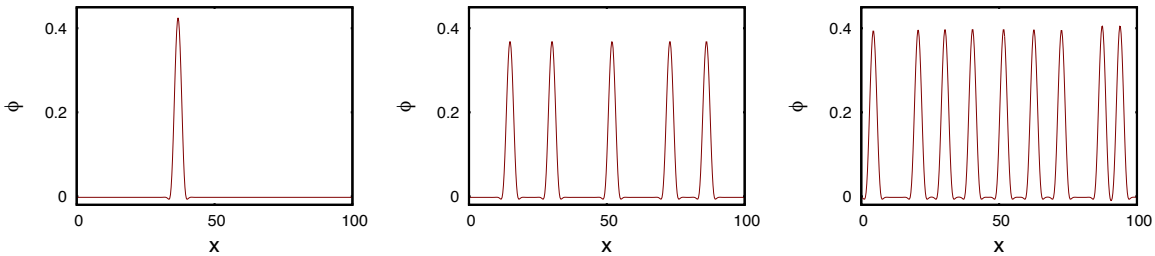

(b) $\bar{\phi} = 0.01$ **(c)** $\bar{\phi} = 0.05$ **(d)** $\bar{\phi} = 0.1$

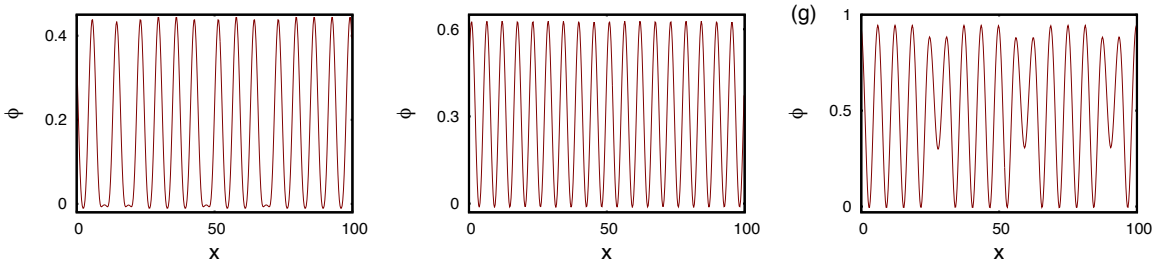

(e) $\bar{\phi} = 0.175$ **(f)** $\bar{\phi} = 0.3$ **(g)** $\bar{\phi} = 0.5$

Figure 6.1: The phase diagram for the 1D VPFC model (Eqs. (5.15) and (6.1)) is displayed in (a) for the case $q = 1$. The red solid lines are the coexistence curves between the periodic and uniform phases; the red circle is the tricritical point. The blue dashed line is the locus $\Delta_V = 0$, which is the limit of linear stability for uniform profiles. The green dot-dashed lines are a guide showing the parameter space where local and periodic structures are formed. (b) - (g) show examples of order parameter profiles from numerical simulations corresponding to (local) minima of the free energy, for the values of $\bar{\phi}$ and r indicated in (a). The parameter values are: $q = 1$, $r = -0.9$ and $\alpha = 1$.

vacancy term (6.2), as the amplitude of the structures becomes large enough to reach negative ϕ values. We observe that including the vacancy term (6.2) decreases the distance between the coexistence curves. This is because the vacancy term increases the free energy of the profiles in the periodic phase, which decreases the difference between the free energy of the periodic structures and the homogeneous state and hence a common tangent construction between the two yields values which are closer to the linear stability line $\Delta_V = 0$. Recall that the two mode approximation for the free energy of the periodic phase in the regular PFC model works very well, agreeing with the results obtained from simulations, see Fig. 5.3. However, in the VPFC model, the two mode approximation becomes inaccurate when $r < -0.3$. This is due to the large contribution of the vacancy term to the overall free energy of the periodic phase at values of r below the tricritical point. Therefore, we calculate the coexistence values below the tricritical point by numerically solving for the order parameter profiles. The numerical method to obtain the free energy of the periodic phase is identical to that discussed in the previous chapter for the regular PFC model Sec. 5.3.2.

The periodic structures which are formed by the VPFC model (Fig. 6.1 (f)) are qualitatively very similar to the structures which can be found in the regular PFC model. However, the amplitude of the modulations is restricted by the large penalty in the free energy accumulated when $\phi < 0$. Inside the coexistence region between the periodic and uniform states, we observe interesting structures where the amplitude of the peaks does not remain constant and a second length scale is visible in the structures (Fig. 6.1 (g)). This is also an effect which is present in the regular PFC model and should be focused on in future work. What is most intriguing, and is perhaps the most appealing aspect of the VPFC model, is the appearance of localised states for small positive values of $\bar{\phi}$ when the magnitude of r is sufficiently large ($r \lesssim -0.6$). We obtain order parameter profiles by numerically integrating forward in time Eqs. (5.15) and (6.1) until a stationary solution is reached, starting from the initial profile $\phi(\mathbf{x}, t = 0) = \bar{\phi} + \mathcal{X}(\mathbf{x})$, where $\mathcal{X}$ is a small amplitude random noise profile with zero mean. A rich variety of different patterns are observed, including periodic structures mixed with almost flat regions (Fig. 6.1 (d)) and individual isolated peaks (Figs. 6.1 (b) and (c)). In Fig. 6.1 (a) the green dot-dashed curves indicate the boundary of the region where one observes regular periodic structures and where the localised structures are formed. Note that these are guidelines only and are not thermodynamic coexistence curves. The lower-left dot-dash curve roughly denotes the linear stability limit of the regular periodic structures, such as that in Fig. 6.1 (f). This is determined

numerically. We begin with a periodic profile and reduce the value of $\bar{\phi}$ gradually, minimising the free energy at each step, while keeping r constant. The limit point is then defined as the value of $\bar{\phi}$ where the periodic profile becomes linearly unstable and a vacancy is introduced. In a similar way, we determine the upper-right dot-dash line, which is the limit of linear stability of the structures with defects. This is found by starting with a profile containing a single vacancy and increasing $\bar{\phi}$ until the vacancy disappears. These two points are calculated for different values of r and then a best fit to this data is shown in Fig. 6.1 (a). There is some hysteresis in the region between these two curves, with the type of profile produced depending heavily upon the initial conditions.

Within the localised state region of the phase diagram it is possible to obtain order parameter profiles with a varying number of peaks for a given system of length L. Keeping $r \lesssim -0.6$ constant and varying $\bar{\phi}$ allows us to control the number (density) of bumps as shown in Figs. 6.1 (b)–(e). Beginning with $\bar{\phi} = 0$ we find isolated peaks in large vacant areas (where ϕ is approximately uniform with $\phi \lesssim 0$). As $\bar{\phi}$ is increased the number of peaks increases until we return to the familiar regular periodic structures. The assumption of Ref. [118] is that unlike in the regular PFC, where the uniform phase is associated with the liquid and the modulated phase with the crystal, in the VPFC model one may associate each bump in $\phi(\mathbf{x})$ as corresponding to a particle and so the model can describe fluids (Figs. 6.1 (c) and (d)), crystals with vacancies and defects (Fig. 6.1 (e)) and regular crystals (Fig. 6.1 (f)).

The findings presented in Fig. 6.1 indicate the existence of a hysteretic transition between periodic and localised states, and are a consequence of homoclinic snaking [130–133] in the present system [1]. In the standard homoclinic scenario such localised states are present within a part of the coexistence region called the pinning region. The localised states in the lower left part of the parameter plane $(\bar{\phi}, r)$ in Fig. 6.1 (a) correspond to the global energy minimum or to other deep but local energy minima. Families of such steady state solutions can be obtained by employing the path continuation techniques bundled in the package AUTO07p [134]. As an example, in Figs. 6.2 and 6.3 we show the characteristics of localised solutions along cuts through the plane $(\bar{\phi}, r)$. In particular, in Fig. 6.2 we give results for changing r at constant $\bar{\phi} = 0.1$ and in Fig. 6.3 we display results for changing $\bar{\phi}$ at constant $r = -0.9$. All solu-

[1] The bifurcation analysis and the resulting figures (Figs. 6.2 - 6.4) were produced by Uwe Thiele as part of a collaborative publication.

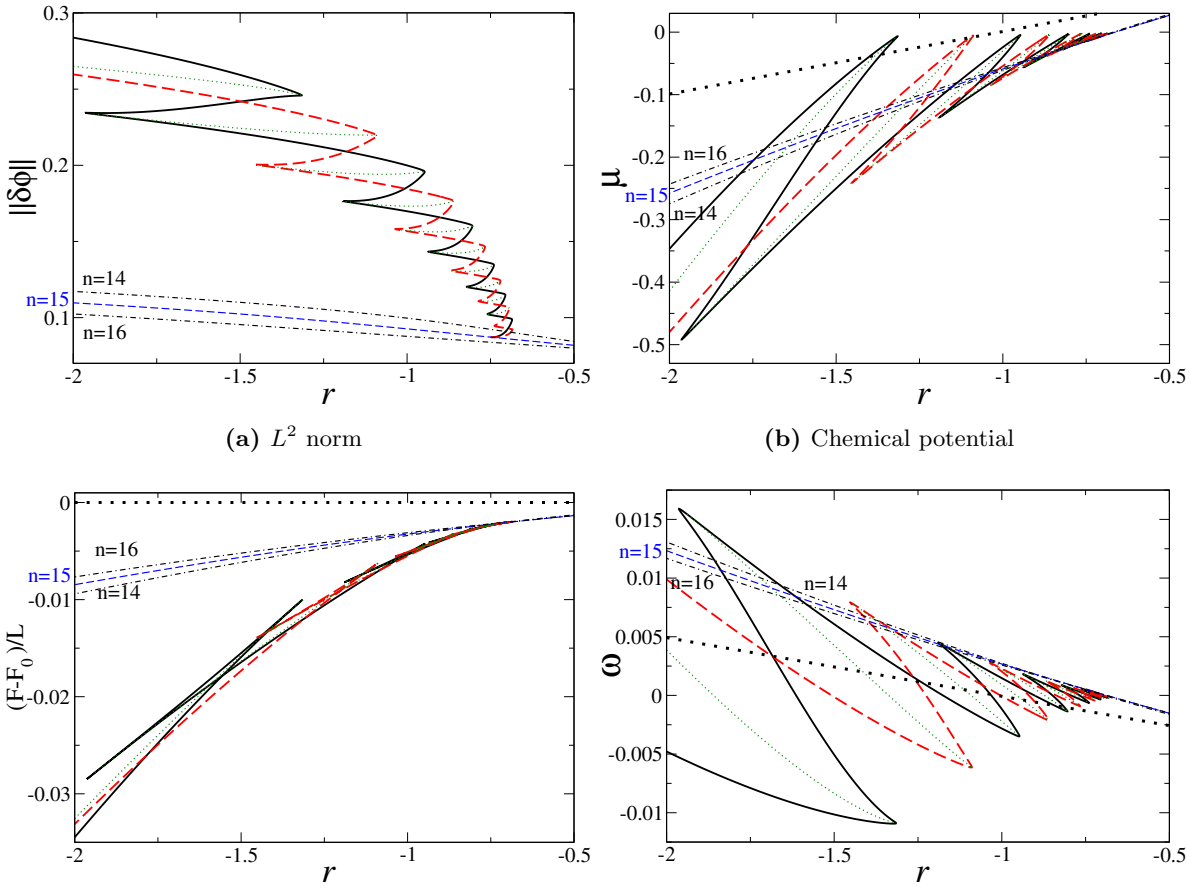

(a) L^2 norm

(b) Chemical potential

(c) Mean free energy density

(d) Mean grand potential density

Figure 6.2: Bifurcation diagram showing localised solutions of the VPFC model with $H = 1500$, as a function of the parameter r, for the mean order parameter $\bar{\phi} = 0.1$ and a fixed domain size of $L = 100$. We display the (a) L^2 norm, (b) chemical potential μ, (c) mean free energy density $(F - F_0)/L$, and (d) mean grand potential density $\omega \equiv F/L - \bar{\phi}\mu$. The heavy black dash-dotted line corresponds to the homogeneous solution $\phi(x) = \bar{\phi}$. Periodic solutions with $n = 15$ bumps are shown as a thin blue dashed line, whereas the nearby thin black dotted lines represent the $n = 14$ and $n = 16$ solutions as indicated in the plot. The heavy solid black and dashed red lines that bifurcate from the $n = 15$ periodic solution represent symmetric localised states with a maximum (odd states) and a minimum (even states) at the centre, respectively. The green dotted lines that connect the two branches of symmetric localised states correspond to asymmetric localised states. Together the branches of localised states form a slanted snakes-and-ladders structure.

tions are characterised by their L^2 norm $||\delta\phi|| \equiv \sqrt{(1/L)\int_0^L (\phi(x) - \bar{\phi})^2 dx}$, chemical potential $\mu = \delta F/\delta\phi$, mean free energy density difference $(F[\phi(x)] - F_0)/L$, where $F_0 = F[\bar{\phi}]$ and mean grand potential density $\omega \equiv F[\phi(x)]/L - \bar{\phi}\mu$, and satisfy periodic boundary conditions on the domain $0 \leq x \leq L$.

There exists three types of localised steady states: (i) the heavy solid black line consists of

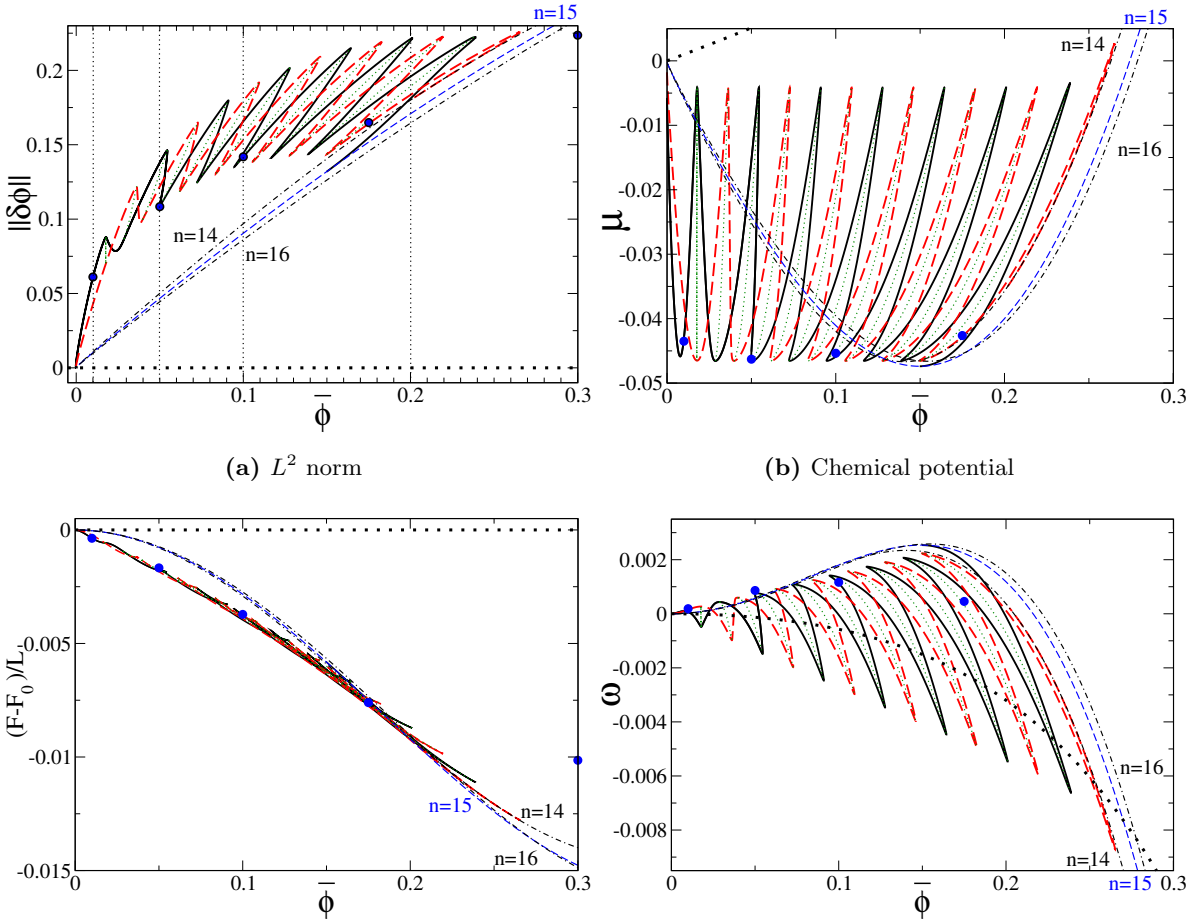

(a) L^2 norm

(b) Chemical potential

(c) Mean free energy density

(d) Mean grand potential density

Figure 6.3: Bifurcation diagram showing localised solutions of the VPFC as a function of the mean order parameter $\bar{\phi}$, for $r = -0.9$ and a fixed domain size of $L = 100$. We display the (a) L^2 norm, (b) chemical potential μ, (c) mean free energy density $(F - F_0)/L$, and (d) mean grand potential density $\omega \equiv F/L - \bar{\phi}\mu$. The line styles are as in Fig. 6.2. Here, however, the heavy solid black and dashed red lines bifurcate at large $\bar{\phi}$ from the $n = 15$ and $n = 14$ periodic solutions, respectively. Typical profiles for all the branches of localised states are given in Fig. 6.4. The vertical dotted lines in (a) correspond to values of $\bar{\phi}$ for results in Fig. 6.4. The blue dots correspond to the five time simulation profiles shown in Fig. 6.1 (b)–(f).

$x \to -x$ symmetric localised states that have a maximum at the centre, i.e., the overall number of bumps within the structure is odd. (ii) The dashed red line also represents $x \to -x$ symmetric localised states but this time with a hole (minimum) at the centre. (iii) The localised solutions of the third type are not symmetric under $x \to -x$ and are called "asymmetric states". These reside on branches that connect (via pitchfork bifurcations) the two branches of symmetric localised states. These branches are included in the bifurcation diagrams as dotted green lines.

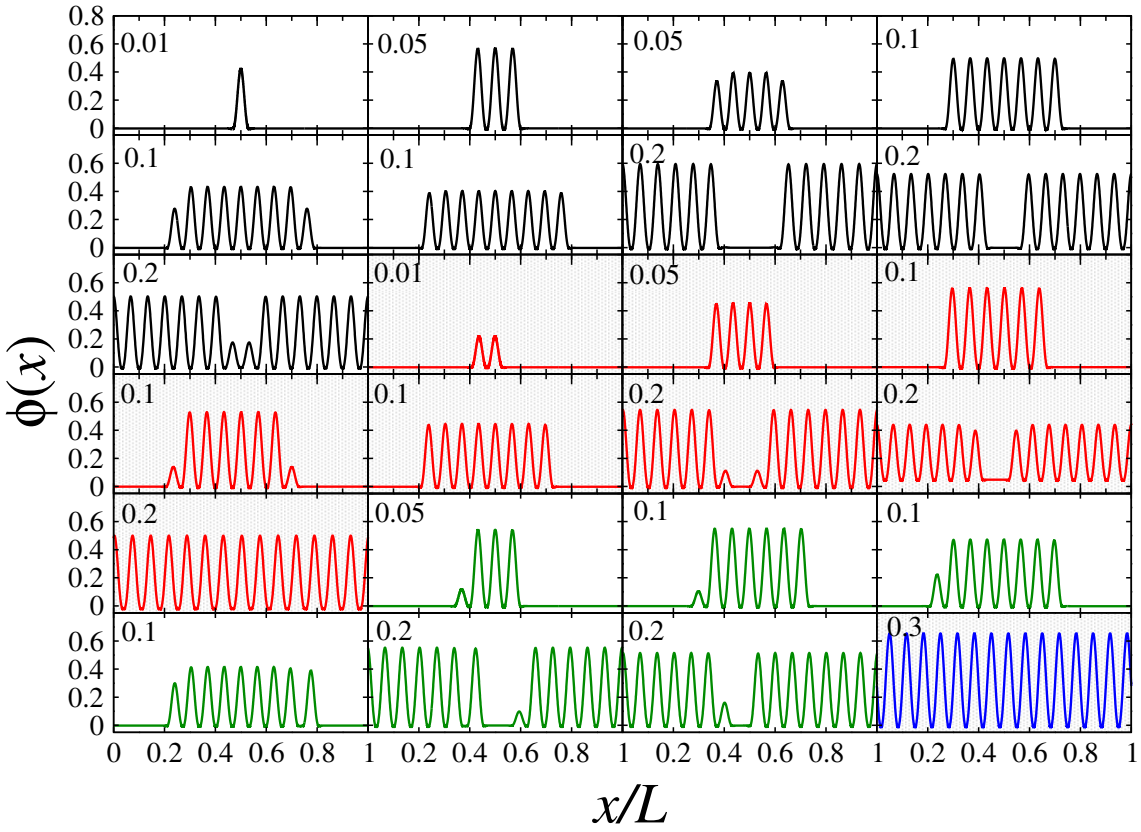

Figure 6.4: A selection of steady state profiles $\phi(x)$ for $r = -0.9$ at $\bar{\phi} = 0.01$, 0.05, 0.1, and 0.2. From top left to bottom right we show first nine type (i) solutions, i.e., symmetric localised states with an odd number of maxima (in black), then eight type (ii) solutions, i.e., symmetric localised states with an even number of maxima (in red), followed by six type (iii) solutions, i.e., asymmetric localised states (in green). The final image is the $n = 15$ periodic solution at $\bar{\phi} = 0.3$ (in blue). The number in each panel indicates the corresponding value of $\bar{\phi}$. The solutions from the symmetric branches are shown in the sequence that follows the respective branch in Fig. 6.3 (a), starting from the left. The asymmetric states for identical $\bar{\phi}$ are shown in the order of decreasing norm.

Examples of order parameter profiles of types (i)–(iii) are presented in Fig. 6.4, corresponding to the various solution branches displayed in Fig. 6.3. This sequence of profiles expands upon the few examples shown in Figs. 6.1 (b)–(g). Recall, however, that the results in Figs. 6.1 (b)–(g) are obtained starting from an order parameter profile with a small amplitude random noise and so they do not always exactly agree with the steady states at the same $\bar{\phi}$ resulting from the path continuation. The L^2 norm, chemical potential μ, mean free energy density $(F - F_0)/L$ and the mean grand potential $F/L - \bar{\phi}\mu$ have been calculated for the profiles obtained from time simulations (Figs. 6.1 (b)–(f)) and are plotted as blue dots in Fig. 6.3. A close inspection reveals that the energy of the time simulation results is often slightly higher than that from the continuation results, indicating that in these cases the time simulation converges

to a local and not the global energy minimum. This is to be expected as the solutions shown in the bifurcation diagrams are only the 'tip of the iceberg'. For instance, there exist a whole family of solutions, with various non-equidistant positions of bumps. This is related to the fact that individual bumps have oscillatory tails and the 'locking of these tails' allows for different equilibrium distances [135]. The solutions presented in Figs. 6.2 and 6.3 represent the solution having the lowest energy in the respective class. However, the energy differences between these and the 'less symmetric' solutions are often tiny. Thus, it is not surprising that time simulations starting from random initial profiles often converge to solutions with greater disorder and energies than those shown in Fig. 6.3. For instance, the solution in Fig. 6.1 (c) at $\bar{\phi} = 0.1$ is a nine-bump solution similar to the odd symmetric localised states shown in the first two panels of the second row of Fig. 6.4. The amplitudes agree well and although the arrangements of the nine bumps are different, the free energy and norm still agree to $< 1\%$. However, at large average order parameter values $\bar{\phi}$ the time simulation results can converge to metastable states with energies quite different from the minimum energy states for domains of this size $L = 100$. For example, the periodic solution obtained from the time simulation (shown in Fig. 6.1 (f)) when $\bar{\phi} = 0.3$ has eighteen bumps. However, from Fig. 6.3 (c) we observe that the energetic minimum is obtained by a periodic profile with fifteen bumps, as shown by the steady state solution in Fig. 6.4. The convergence to a different number of bumps in the time simulation may be caused by discretisation effects or by the initial noise profile used. As one would expect, the free energy associated with the eighteen bump periodic structure is significantly larger than the fifteen bumped profile.

In Fig. 6.2 ($\bar{\phi} = 0.1$) the localised states bifurcate subcritically from the periodic solution branch (that itself emerges from the trivial homogeneous solution that is displayed as the heavy black dotted line). Therefore, one expects hysteretic behaviour as encountered in the time simulations. A magnification (not shown) allows us to determine the threshold values for the hysteretic transition. When decreasing r in the region where periodic solutions are always found, one first passes $r_{\mathrm{sn}} = -0.685$ where the last 2 branches of localised solutions annihilate in a saddle-node bifurcation (Fig. 6.2 (a)). Slightly below r_{sn}, both the periodic solution and the localised state with a single bump are local energetic minima. Although the periodic solution represents the global minimum, particular time simulations sometimes converge to the localised state. The differences in energy between the two is $< 1\%$ in the case of Fig. 6.2. When r is further decreased below $r_{\mathrm{en}} = -0.7$ the energy of the even symmetric states becomes smaller

than the one of the $n = 16$ periodic solution, that is however still linearly stable. The situation changes at $r_c = -0.749$ where both symmetric localised branches bifurcate from the $n = 16$ branch, i.e., below r_c the latter is linearly unstable. Furthermore, below r_c the energy of all localised states rapidly becomes much smaller than the energy of all periodic states (Fig. 6.2 (c)). The hysteresis range displayed in Fig. 6.1 provides a good approximation for the region between r_c and r_{sn}. This region becomes larger as $\bar{\phi}$ is increased.

The situation is very similar when $\bar{\phi}$ is changed for fixed r (Fig. 6.3). The resulting hysteresis range is between $\bar{\phi} = 0.150$ and 0.239 for symmetric localised states with an odd number of maxima and between $\bar{\phi} = 0.202$ and 0.265 for symmetric states with an even number of maxima. Overall, one should therefore expect a wide hysteresis region roughly between $\bar{\phi} = 0.15$ and $\bar{\phi} = 0.25$. The hysteresis range obtained from the time simulations (indicated in Fig. 6.1 (a)) is roughly $0.19 < \bar{\phi} < 0.22$. This is narrower than the range deduced from the path continuation analysis of the localised steady states, but lies right in the middle of it.

Before we move on to discuss the two-dimensional case, we should comment on how our results fit into the wider context of research on localised states. Much research on localised states focuses on the non-conserved Swift-Hohenberg equation [130–132]. There, such states can only exist if the primary bifurcation of periodic states from the homogeneous base state is subcritical. The localised states exist in a sub-range of the existence range of the periodic states bounded on either side by the saddle-node bifurcations of the branches of symmetric localised states. In the non-conserved Swift-Hohenberg equation these accumulate exponentially rapidly towards the parameter values corresponding to the first and last tangencies between the unstable manifold of the homogeneous state in space and the stable manifold of the periodic state. These tangencies define the pinning region containing the different localised structures. In contrast, in the presence of a conserved quantity, localised states may exist outside the existence region of periodic states, may occur even in the supercritical case and the saddle-node bifurcations of the localised states are no longer aligned, i.e., one finds slanted snaking [136]. This is typically a finite size effect [137].

For the regular PFC (conserved Swift-Hohenberg equation) (Eq. (5.15) with Eqs. (5.17) and (5.18)), localised states are briefly mentioned in Ref. [124]. However, no systematic results along the lines of those presented in Refs. [130] for non-conserved or [136] for conserved order

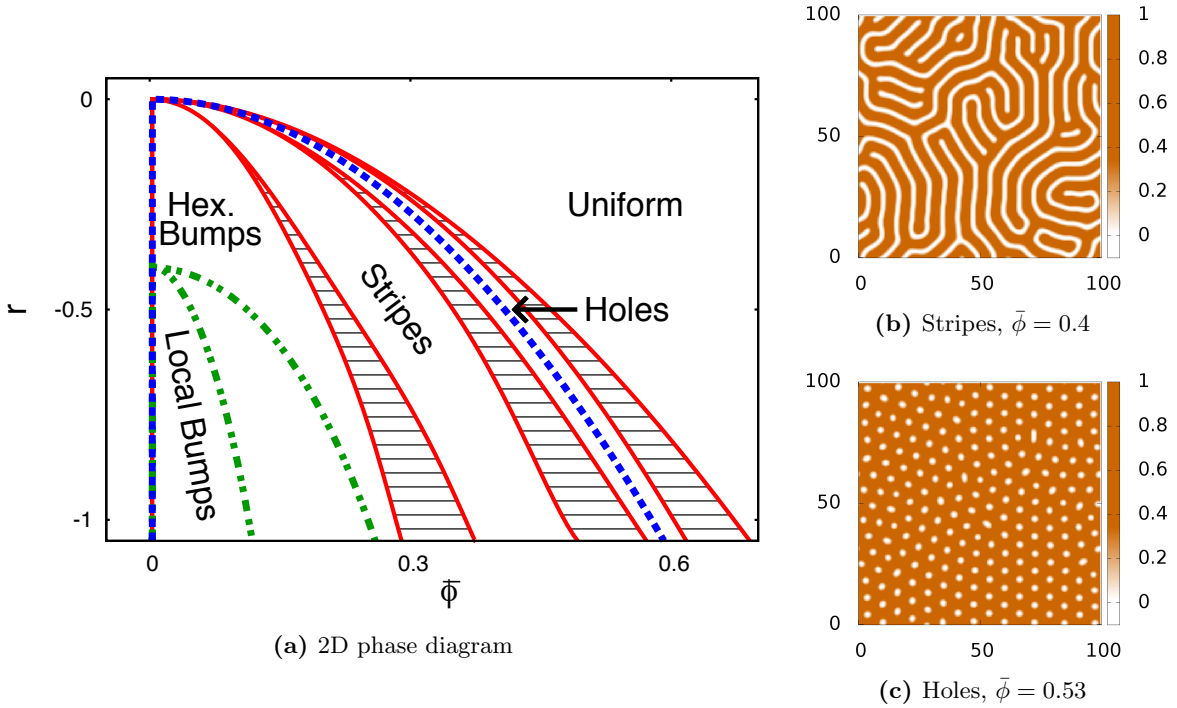

(a) 2D phase diagram

(b) Stripes, $\bar{\phi} = 0.4$

(c) Holes, $\bar{\phi} = 0.53$

Figure 6.5: The phase diagram for the 2D VPFC model (Eqs. (5.15) and (6.1)) is displayed in (a) for the case $q = 1$. The red solid lines are the coexistence curves between the various phases. The blue dashed line is the limit of linear stability for uniform profiles $\Delta_V = 0$. The green dash-dotted lines indicate the region where localised and hexagonally ordered bump structures coexist. Simulations of (b) stripes and (c) hexagonally ordered holes are also shown. The parameter values for these simulations are: $q = 1$, $r = -0.9$, $\alpha = 1$ and (b) $\bar{\phi} = 0.4$ and (c) $\bar{\phi} = 0.53$.

parameter fields are available. The model used here is a special case because it includes the non-analytic vacancy term (6.2). However, a similar bifurcation structure is found for the classical conserved Swift-Hohenberg equation, this should be addressed in future work.

6.2.3 Two dimensional model

We now move on to consider how the VPFC model behaves in two dimensions. As with the regular PFC model (the phase diagram is shown in Fig. 5.4), when we expand into two dimensions we observe stripes (see Fig. 6.5 (b)) and hexagonally ordered bumps or holes (see Fig. 6.5 (c)). In Fig. 6.5 (a) we display the phase diagram of the VPFC model in two dimensions and typical time simulation results from the striped 6.5 (b) and hole 6.5 (c) phases, calculated on a regular grid with grid spacing $dx = 0.5$. Square ordering of bumps or holes does not appear in the phase diagram because these structures always have a higher free energy. However, this can be changed through appropriate alterations to the free energy [117]. Square ordering can also occur when extending to a two component mixture (cf. Sec. 6.3.3 below). Using the

same method as outlined above, we calculate the regions of the phase diagram where there is coexistence between hexagonally ordered holes and the uniform distribution, between holes and stripes and between stripes and hexagonally ordered bumps. The vacancy term (6.2) shifts the modulated phases into the positive $\bar{\phi} > 0$ plane. The section of the phase diagram where holes are observed is much smaller when compared to the regular PFC model (Fig. 5.4) and now extends beyond the limit of linear stability of the flat state (at $\Delta_V = 0$). This means that for certain values of $\bar{\phi}$ (where $0 < \Delta_V \ll 1$), hexagonally arranged holes are energetically favourable but are only observed in time simulations for certain initial conditions - i.e., when starting with an order parameter profile $\phi(\mathbf{x}, t = 0)$ which already has modulations which are sufficiently large in amplitude. As r is decreased (i.e., for larger $|r|$) it becomes increasingly difficult to obtain structures with holes up to and inside of the coexistence region between the hole and the uniform phases. This is a direct consequence of the limit of linear stability occurring in the middle of the hole phase. Therefore, the accuracy of results for the coexistence region between the hole and uniform phases decreases as $|r|$ becomes larger. The stripe phase occurs in between the two hexagonal phases. In the simulation order parameter profiles displayed in Fig. 6.5 (b) and (c) we observe various defects and in (c) 'grain' boundaries between regions with different orientations, which depend on the initial conditions (our initial profile was a flat state with additional small amplitude white noise). The true minimum profile for case (b) is a series of parallel stripes which are identical to the periodic profiles in the 1D system (shown in Fig. 6.1 (f)).

The most important portion of the phase diagram from the materials modelling point of view, is the bump phase because the basic assumption is that each bump represents a particle. When $r \gtrsim -0.4$ or when $\bar{\phi}$ has a value close to that in the coexistence region between bumps and stripes, we observe hexagonally arranged bumps, similar to those in the regular PFC model. However, in a similar manner to the 1D system, we observe localised structures at small values of $\bar{\phi}$ when $r \lesssim -0.4$. In the phase diagram 6.5 (a) the green dot-dashed lines are numerically obtained estimates for the location in the phase diagram of the limits of linear stability of the uniform periodic states (lower curve) and the localised (vacancy) states (upper curve). They are determined in the same manner as discussed above for the one dimensional system for a square system of side length $L = 25$. It is important to note that the parameter range where localised bumps coexist with regular periodically ordered bumps is much broader for the 2D system, implying a large amount of hysteresis.

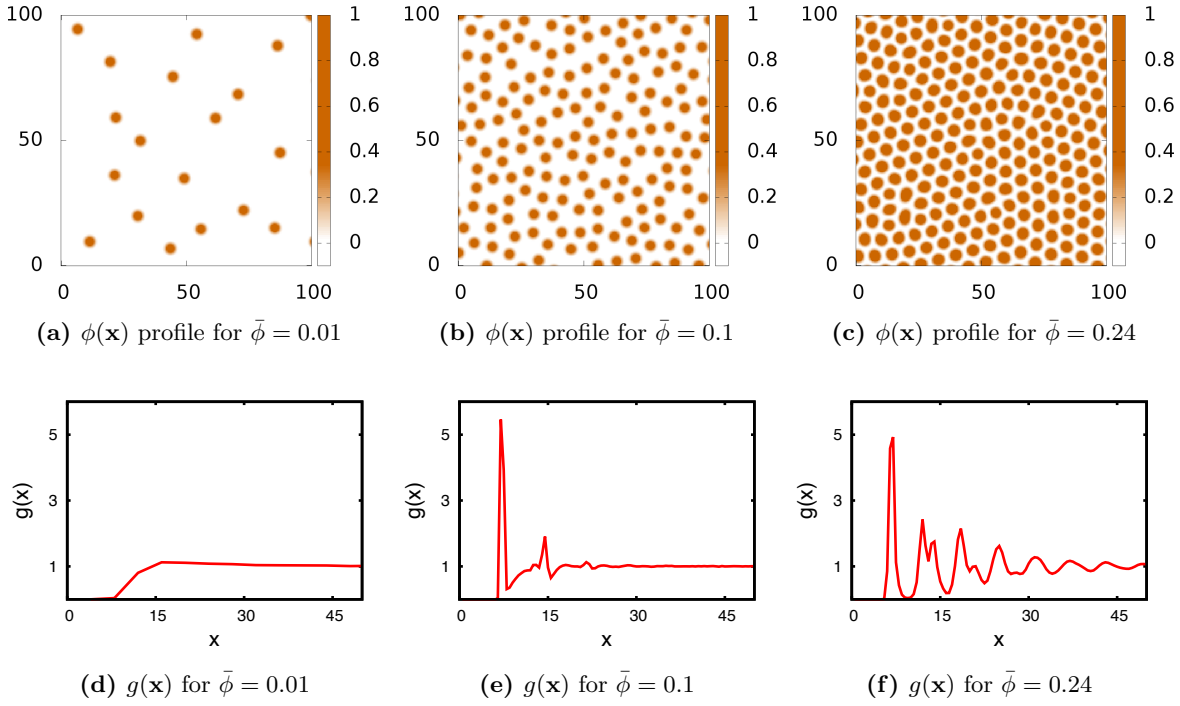

(a) $\phi(\mathbf{x})$ profile for $\bar{\phi} = 0.01$ **(b)** $\phi(\mathbf{x})$ profile for $\bar{\phi} = 0.1$ **(c)** $\phi(\mathbf{x})$ profile for $\bar{\phi} = 0.24$

(d) $g(\mathbf{x})$ for $\bar{\phi} = 0.01$ **(e)** $g(\mathbf{x})$ for $\bar{\phi} = 0.1$ **(f)** $g(\mathbf{x})$ for $\bar{\phi} = 0.24$

Figure 6.6: (a)–(c) Typical steady state order parameter profiles obtained in time simulations for increasing $\bar{\phi}$. (d)–(f) show the corresponding radial distribution function $g(x)$ calculated from multiple simulations. The parameter values are: $\alpha = 1$, $q = 1$, $r = -0.9$ and in (a), (d) $\bar{\phi} = 0.01$, in (b), (e) $\bar{\phi} = 0.1$ and in (c), (f) $\bar{\phi} = 0.24$.

We now focus our discussion on the portion of the phase diagram where isolated bumps form. As can be seen in Fig. 6.6, these profiles resemble particle configurations in gases, liquids and crystalline solids and so the VPFC may be a valuable model for describing materials on the microscale [118]. This region of the phase diagram is full of complexity and many varied structures may be observed. However, here we forego a full systematic study of this large region in parameter space and limit ourselves to showing representative results obtained for a single value of the undercooling parameter $r = -0.9$ for which there is a fairly large range in $\bar{\phi}$ with isolated bumps. We set the initial order parameter profile to be a uniform state with a small amplitude noise $\phi(\mathbf{x}, t = 0) = \bar{\phi} + \lambda(Y - 0.5)$, where Y is a random real number uniformly distributed between 0 and 1 and $\lambda = 10^{-6}$ is the amplitude of the noise. We consider three cases; i) $\bar{\phi} = 0.01$ and ii) $\bar{\phi} = 0.1$ where a disordered arrangement of localised bumps forms and iii) $\bar{\phi} = 0.24$ which is in the region where bumps are hexagonally ordered. We average over many simulations to calculate the two point correlation function for each of these cases. This is done by locating all the maxima in the equilibrium profile $\phi(\mathbf{x})$, for a given initial realisation of the

noise; i.e., we locate the position of all the bumps. From these sets of coordinates we calculate the radial distribution function $g(x)$ in the usual way [138]. We display a simulation result for case i) in Fig. 6.6 (a) and the corresponding radial distribution function $g(x)$ in Fig. 6.6 (d). We find that there is almost no correlation between the bumps in this circumstance except for the core repulsion and a very small peak at $x \approx 16$, indicating that there is a weak attraction between the bumps. Therefore, simulations with these parameter values appear to qualitatively describe gas-like formations of particles/colloids. In Fig. 6.6 (b) and (e) we plot a typical order parameter profile and the corresponding $g(x)$ for case ii). We observe a large increase in the number of bumps as compared to the previous case. The radial distribution function shows that we have strong short range ordering, but without any long range order. This is very reminiscent of the ordering in liquids. There is a very sharp peak in $g(x)$ at around $x = 7.5$ (which is approximately the diameter of the bumps) and a smaller peak around $x = 15$. A similar example is also given in Ref. [118]. If we further increase the value of $\bar{\phi}$ we eventually find the more familiar hexagonally structured array of bumps which is reminiscent of the ordering in simple crystalline solids. In Fig. 6.6 (c) we display an example of the order parameter profile for case iii) and in Fig. 6.6 (f) we show the corresponding $g(x)$. For this case we observe that $g(x)$ is highly structured indicating the system has very strong short range correlations with a significant degree of long range ordering. We observe the split second and third peaks, which is a classic sign of crystalline order. These results indicate that the VPFC model may be used to model crystalline structures, much like the regular PFC model. The major difference between the two models is the existence of the fluid-like configuration of bumps observable in the VPFC model. In contrast, the fluid phase in the PFC model corresponds to the homogeneous state.

The variation in the size and shape of the bumps that are formed is fairly small. In Fig. 6.7 (a) we display a selection of results for the order parameter profile through the centre of the bumps for the case when $r = -0.9$ and $\bar{\phi} = 0.01$. We determine the shape of the bumps by plotting the value of the order parameter ϕ against the distance from the peak of each bump (as shown by the data points). We can then fit functions which take the following form:

$$\theta(x) = \beta_0 e^{-\beta_1 x^2 - \beta_2 x^4 - \beta_3 x^6} \cos(\beta_4 x) + \beta_5. \tag{6.6}$$

We fit this form to the data using a least squares method. The exponential part of $\theta(x)$ describes the decay of the modulation as the distance from the peak increases and the cosine function captures the oscillatory tail of the modulations which is an important factor in their

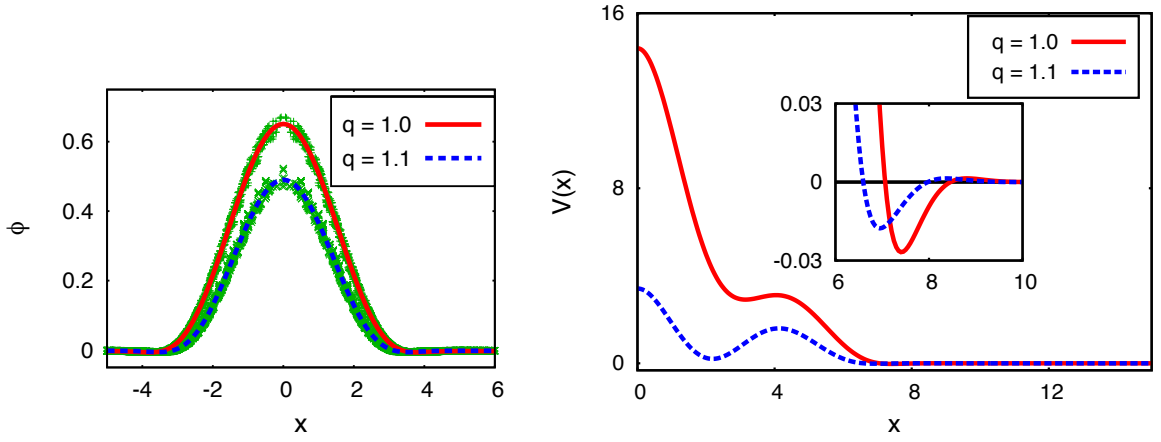

(a) Bump profile **(b)** Effective pair potential

Figure 6.7: (a) Several sets of numerical results for the order parameter profile through the centre of a bump (+) for $q = 1$ and (×) for $q = 1.1$, together with fits to the data (solid red and blue dashed lines). These fits are then used to calculate the effective pair potential between two bumps. These pair potentials are displayed in (b). The inset displays a magnification of the tails of $V(x)$. The parameters values are: $r = -0.9$ and $\bar{\phi} = 0.01$.

interaction with other bumps [115, 116]. Figure 6.7 (a) displays two cases; the (+) points and red solid line show the case $q = 1$ and the (×) points and blue dashed line show the case where $q = 1.1$. The size of the bump is reduced as we increase the value of q. This is because increasing the value of q increases the typical wavenumber which results in a smaller typical length scale (cf. Fig. 5.1 and Eq. (6.5)).

The curves obtained from fitting the bump profile can be used to obtain an approximation for the effective pair potential $V(x)$ between two isolated bumps, where x is the distance between the centres of the bumps. We take a uniform system with the value of ϕ equal to that in the uniform areas between bumps found in simulations for $\bar{\phi} = 0.01$, corresponding to the results in Fig. 6.6 (a). We then impose upon this the profiles for two bumps using the fitted curves shown in Fig. 6.7 (a). We vary the distance between the superposed bumps and calculate the free energy of the system. We assume thereby that the two bumps retain their shape when they are close, despite the fact that in reality the bump shapes become distorted as bumps are pushed close together.

In Fig. 6.7 (b) we display the results for $q = 1$ (red solid line) and $q = 1.1$ (blue dashed line). We observe that there is a shallow minimum in the potential at the distance $x \approx 7.5$ when $q = 1$

and at $x \approx 7$ when $q = 1.1$ (see inset of Fig. 6.7 (b)). The minimum is at a smaller distance when q is larger because of the decreased diameter of the bumps - recall that q determines the size of the bumps. The resulting weak attraction between the bumps may also be inferred from the radial distribution function $g(x)$ calculated for the low density case $\bar{\phi} = 0.01$ when $q = 1$ displayed in Fig. 6.6 (d). We observe a second minimum in the potentials at $x \approx 3.15$ when $q = 1$ and at $x \approx 2.3$ when $q = 1.1$, where the former rather appears like a 'shoulder'. The order parameter profiles at the second minima resemble the elongated almost elliptical shapes which are observed in and around the coexistence region between bumps and stripes. See also Fig. 6.5 (c) where we observe elliptical holes along some of the grain boundaries.

6.3 Two Component System

We now extend the model to consider a binary mixture in perhaps the most simple way possible, by adding together free energies like Eq. (6.1) for two order parameter fields $\phi_a(\mathbf{x}, t)$ and $\phi_b(\mathbf{x}, t)$. We introduce a simple coupling term which allows the two components to interact with each other. This gives us the following expression for the free energy:

$$F = \int d\mathbf{x} \left[f(\phi_a(\mathbf{x}, t)) + f_{vac}(\phi_a(\mathbf{x}, t)) + f(\phi_b(\mathbf{x}, t)) + f_{vac}(\phi_b(\mathbf{x}, t)) + \eta\phi_a\phi_b \right], \tag{6.7}$$

where η is the coupling coefficient and the functions f and f_{vac} are defined as before in Eqs. (5.18) and (6.2). The value of r is set equal for both components. However, we allow the value of q to be different for each species, so we now refer to these values as q_a and q_b, where the subscript denotes the corresponding component. Setting different values for q in the two components (i.e., $q_a \neq q_b$) results in an asymmetrical system in which the size of the bumps/modulations in ϕ_a differs from that in ϕ_b, as discussed further below in Secs. 6.3.2 and 6.3.3. Note that a different coupling term is used in Ref. [119]; a somewhat different two component PFC model is presented in Ref. [120].

Here, just as for the one component model, we assume the dynamics of the system is governed by the following pair of equations (cf. Eq. (5.15)):

$$\begin{aligned} \frac{\partial \phi_a}{\partial t} &= \alpha_a \nabla^2 \frac{\delta F}{\delta \phi_a}, \\ \frac{\partial \phi_b}{\partial t} &= \alpha_b \nabla^2 \frac{\delta F}{\delta \phi_b}. \end{aligned} \tag{6.8}$$

We also assume that the two mobility coefficients are equal: $\alpha_a = \alpha_b = \alpha$. The two components are coupled purely by the term $\eta\phi_a\phi_b$ in the free energy. When $\eta > 0$, this coupling term leads to a repulsion between the two species and so penalises structures which overlap or form on top of each other. The value of the parameter η determines the 'strength' of the coupling, and so the two component model reduces to two disconnected one component models in the limit $\eta \to 0$.

6.3.1 Phase behaviour

When the coupling coefficient is fairly large $\eta \geq 0.1$, the coupling term has a significant impact on the phase behaviour of the model. In particular, the limit of linear stability and the phase coexistence curves extend to much larger values of $\bar{\phi} = \bar{\phi_a} + \bar{\phi_b}$ than for the one component model. We now determine the linear stability of a flat state in the model. We assume that the order parameter profiles of both components take the form:

$$\begin{aligned} \phi_a &= \bar{\phi_a} + \delta\phi = \bar{\phi_a} + \xi e^{ik\mathbf{x}} e^{\beta t}, \\ \phi_b &= \bar{\phi_b} + \chi\delta\phi = \bar{\phi_b} + \chi\xi e^{ik\mathbf{x}} e^{\beta t}, \end{aligned} \tag{6.9}$$

where the amplitude $|\xi| \ll 1$ and the parameter χ is the ratio between the amplitude of the modulations in the two components. The sign of χ indicates whether instabilities are in-phase ($\chi > 0$) or anti-phase ($\chi < 0$) between the two coupled order parameter fields. From the magnitude of χ we can deduce whether the instability is initiated from species a ($|\chi| \ll 1$), species b ($|\chi| \gg 1$), or a combination of both ($|\chi| = O(1)$). We make a Taylor series expansion of the functional derivatives of the free energy with respect to the two order parameters ϕ_a and ϕ_b, to obtain:

$$\begin{aligned} \frac{\delta F}{\delta \phi_a} &= (r + q_a^4)\bar{\phi_a} + 3H\bar{\phi_a}(|\bar{\phi_a}| - \bar{\phi_a}) + \bar{\phi_a}^3 + \eta\bar{\phi_b} \\ &\quad + \big[(k^2 - q_a^2)^2 + \Delta_a + \chi\eta\big]\delta\phi + O(\delta\phi^2), \\ \frac{\delta F}{\delta \phi_b} &= (r + q_b^4)\bar{\phi_b} + 3H\bar{\phi_b}(|\bar{\phi_b}| - \bar{\phi_b}) + \bar{\phi_b}^3 + \eta\bar{\phi_a} \\ &\quad + \big[\chi(k^2 - q_b^2)^2 + \chi\Delta_b + \eta\big]\delta\phi + O(\delta\phi^2). \end{aligned} \tag{6.10}$$

where $\Delta_i = r + 6H(|\bar{\phi_i}| - \bar{\phi_i}) + 3\bar{\phi_i}^2$ and where $i = a, b$ (c.f. Eq. (6.4)). We substitute these expressions into the dynamical equations (6.8), which gives us the following coupled relations:

$$\begin{aligned} \beta &= -k^2\alpha((k^2 - q_a^2)^2 + \Delta_a + \chi\eta) \\ \chi\beta &= -k^2\alpha(\chi(k^2 - q_b^2)^2 + \chi\Delta_b + \eta). \end{aligned} \tag{6.11}$$

This set of equations can be represented in matrix form, allowing for easier analysis [81] (in a similar manner as before for the thin film system, in Sec. 4.4.2):

$$\beta \begin{pmatrix} 1 \\ \chi \end{pmatrix} = \mathbf{M} \begin{pmatrix} 1 \\ \chi \end{pmatrix}, \tag{6.12}$$

where

$$\mathbf{M} = -k^2\alpha \begin{pmatrix} (q_a^2 - k^2)^2 + \Delta_a & \eta \\ \eta & (q_b^2 - k^2)^2 + \Delta_b \end{pmatrix}.$$

We can now determine the dispersion relation $\beta(k)$ by calculating the eigenvalues of $\mathbf{M}$:

$$\beta(k) = \frac{\mathrm{Tr}(\mathbf{M})}{2} \pm \sqrt{\frac{\mathrm{Tr}(\mathbf{M})^2}{4} - |\mathbf{M}|}. \tag{6.13}$$

The resulting dispersion relation $\beta(k)$ is a double-valued function. However, since the growth rate along the + branch is always larger than that along the − branch, the limit of linear stability can be determined from the + branch alone. If we assume that $q_a = q_b = q$, the dispersion relation simplifies significantly, yielding:

$$\beta(k) = -\frac{\alpha k^2}{2}\left[2(k^2 - q^2)^2 + \Delta_a + \Delta_b - \sqrt{(\Delta_a - \Delta_b)^2 + 4\eta^2}\right]. \tag{6.14}$$

There is a local maximum of this expression which occurs at the positive wavenumber:

$$k_m = \frac{1}{6}\left[24q^2 + 6\left(4q^4 - 6(\Delta_a + \Delta_b) + 6\sqrt{(\Delta_a - \Delta_b)^2 + 4\eta^2}\right)^{\frac{1}{2}}\right]^{\frac{1}{2}}. \tag{6.15}$$

Substituting this wavenumber back into the dispersion relation (6.14), allows us to calculate the parameter values such that $\beta(k_m) = 0$ (i.e., the limit of linear stability of a flat state). We arrive at the following relation:

$$\Delta_a \Delta_b = \eta^2. \tag{6.16}$$

When the system is linearly unstable it is possible for $\beta(k = 0)$ to be a minimum or maximum (this transition occurs at $\Delta_V = -q^2$ in the one component model). This is equivalent to the coefficient of k^2 changing from a positive value (minimum) to a negative value (maximum). The sign of the coefficient of k^2 is determined by the sign of the following quantity:

$$\begin{aligned} C_2 &= \frac{\partial^2 g}{\partial \phi_a^2}\frac{\partial^2 g}{\partial \phi_b^2} - \left(\frac{\partial g}{\partial \phi_b \partial \phi_a}\right)^2, \\ &= (q_a^4 + \Delta_a)(q_b^4 + \Delta_b) - \eta^2, \end{aligned} \tag{6.17}$$

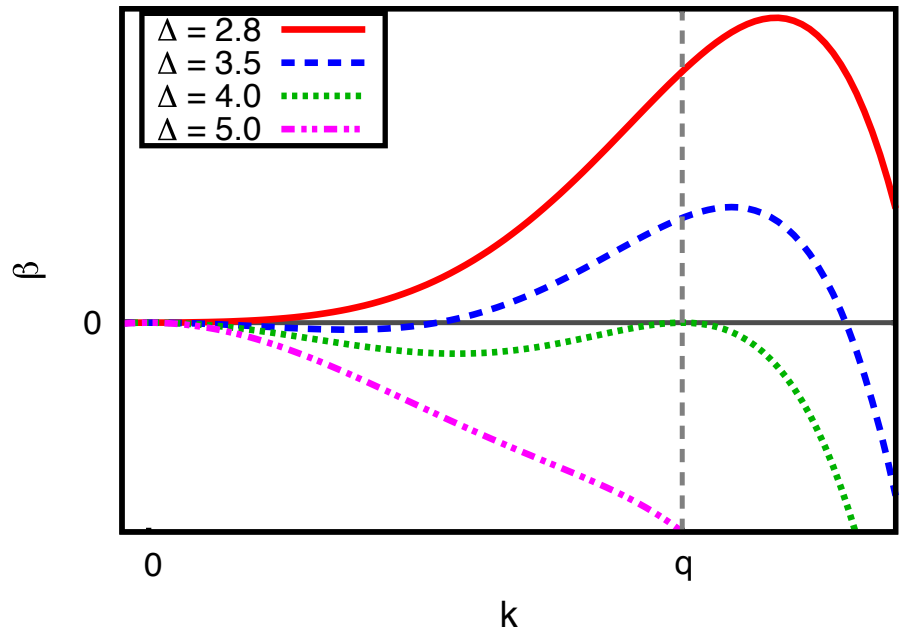

Figure 6.8: Dispersion relation curves for the two component VPFC model (Eqs. (6.7) and (6.8)), when $q_a = q_b = 1$, $\Delta_a = \Delta_b = \Delta$ and $\eta = 4$. Four cases are shown: (i) $\beta(k_m) > 0$ with $\beta(k = 0)$ a minimum (red solid line), (ii) $\beta(k_m) > 0$ and $\beta(k = 0)$ a maximum (blue dashed line), (iii) $\beta(k_m) = 0$ and (iv) $\beta(k_m) < 0$ (magenta dash-dotted line).

where $g(\phi_a, \phi_b) = f(\phi_a) + f_{vac}(\phi_a) + f(\phi_b) + f_{vac}(\phi_b) + \eta\phi_a\phi_b$. When C_2 is negative/positive $\beta(k = 0)$ is a minimum/maximum, this relation also holds for asymmetric systems where $q_a \neq q_b$. In figure 6.8 we display typical dispersion relations when $q_a = q_b = 1$, $\Delta_a = \Delta_b = \Delta$ and $\eta = 4$. We show the case when i) the system is linearly unstable and C_2 (Eq. (6.17)) is negative (red solid line), ii) the system is linearly unstable and Eq. (6.17) is positive (blue dashed line), iii) the system is at the limit of linear stability (i.e., Eq. (6.16) holds) (green dotted line) and iv) the system is linearly stable (magenta dash-dotted line). We observe that when $q_a = q_b$, the typical wavenumber $k_m \to q_a$ as we approach the limit of linear stability $\Delta_a\Delta_b - \eta^2 \to 0$. In the more general case with $q_a \neq q_b$ the dispersion relation may have two maxima at positive values of k neither of which occurs at q_a and q_b. In this case the stability boundary is defined by the vanishing of growth rate $\beta(k_m) = 0$ of the larger of the two possible maxima of β.

From Eq. (6.16) it is clear that depending on the value of the coupling coefficient η, the region of parameter space where the system is linearly unstable can be greatly larger than that for the one component system. For example, picking the value $\eta = 4$ when $r = -0.9$ and setting the average value of both order parameters to be equal $\bar{\phi_a} = \bar{\phi_b} = \bar{\phi}$, we find that the limit of

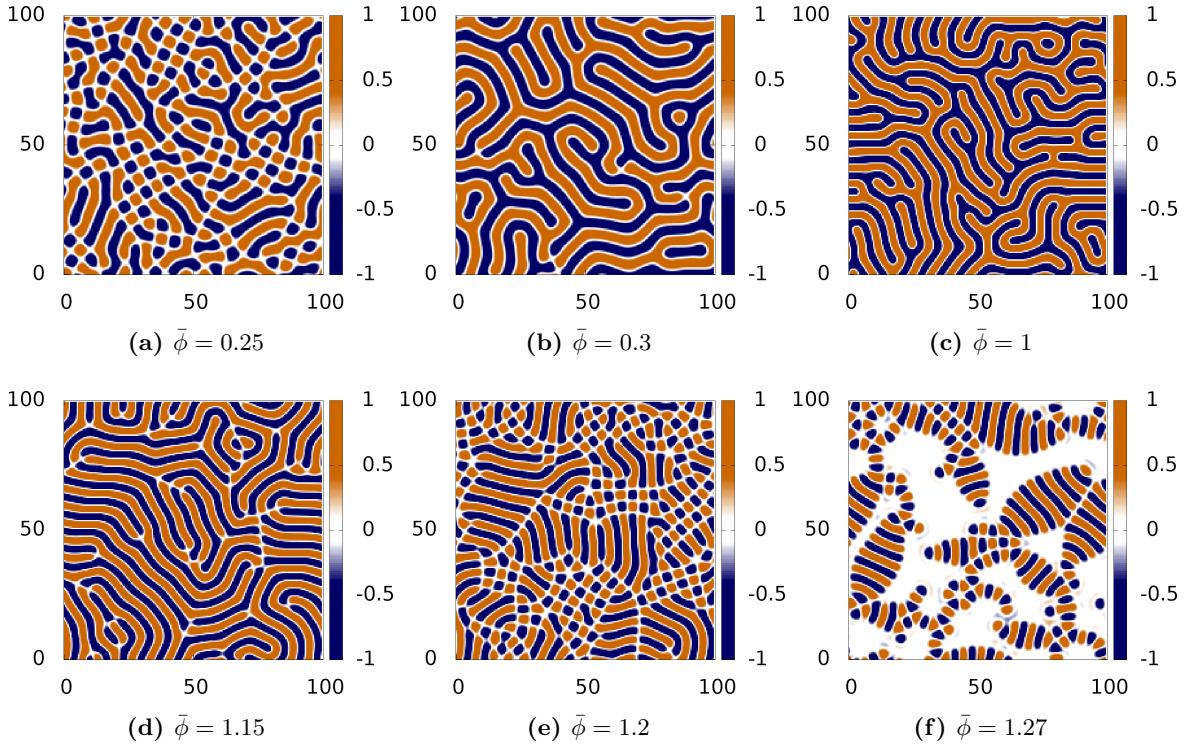

(a) $\bar{\phi} = 0.25$ **(b)** $\bar{\phi} = 0.3$ **(c)** $\bar{\phi} = 1$

(d) $\bar{\phi} = 1.15$ **(e)** $\bar{\phi} = 1.2$ **(f)** $\bar{\phi} = 1.27$

Figure 6.9: The scaled order parameter $\Delta\hat{\phi}$ for the two component model, corresponding to minima of the free energy. The peaks in species a are shown in orange, peaks in species b are shown as blue and white areas show regions where $\phi_a \approx \phi_b$. The parameter values are: $\eta = 4$, $r = -0.9$, $q_a = q_b = 1$, $\bar{\phi_a} = \bar{\phi_b} = \bar{\phi}$, where (a) $\bar{\phi} = 0.25$, (b) $\bar{\phi} = 0.3$, (c) $\bar{\phi} = 1$, (d) $\bar{\phi} = 1.15$, (e) $\bar{\phi} = 1.2$ and (f) $\bar{\phi} = 1.27$.

linear stability increases from $\bar{\phi} = 0.548$ (for the one component case) to $\bar{\phi} = 1.278$. As one would expect, this also increases the region of the phase diagram where modulated structures are formed. Our focus here is on the regions of parameter space where bumps are formed as this is the regime relevant to modelling crystalline solids. However, before proceeding to this, we make a brief survey of some of the structures which may be observed for larger values of ϕ_a and ϕ_b which lie outside of the bump phase. For the parameter values $r = -0.9$, $\eta = 4$, $q_a = q_b = 1$ and $\bar{\phi_a} = \bar{\phi_b} = \bar{\phi}$ we show in Fig. 6.9 a sequence of order parameter profiles with increasing $\bar{\phi}$, for values of $\bar{\phi}$ that lie above the region where bumps are observed (see later sections for a detailed analysis of the bump structures found in the two component model). In Fig. 6.9 we display scaled plots of order parameter profiles which are stationary states obtained from time simulations. We plot an order parameter defined as the normalised difference between the $\phi_i(\mathbf{x})$ values of the two components:

$$\Delta\hat{\phi}(\mathbf{x}) \equiv \phi_a(\mathbf{x})/\hat{\phi}_a - \phi_b(\mathbf{x})/\hat{\phi}_b \tag{6.18}$$

where

$$\hat{\phi}_i = \frac{\phi_a^{\max}\phi_b^{\max} - \phi_a^{\min}\phi_b^{\min}}{\phi_i^{\max} + \phi_i^{\min}} \tag{6.19}$$

and where $\phi_i^{\max}$ and $\phi_i^{\min}$ are, respectively, the maximum and minimum values of $\phi_i(\mathbf{x})$. $\Delta\hat{\phi}$ is defined so as to take a value in the range $[-1, 1]$. When $\Delta\hat{\phi} \approx 1$, the local value of ϕ_a is high whilst the value of ϕ_b is low. Conversely, when $\Delta\hat{\phi} \approx -1$, the local ϕ_a is low and ϕ_b is high. The average order parameter values in Fig. 6.9 are: (a) $\bar{\phi} = 0.25$, (b) $\bar{\phi} = 0.3$, (c) $\bar{\phi} = 1$, (d) $\bar{\phi} = 1.15$, (e) $\bar{\phi} = 1.2$, (f) $\bar{\phi} = 1.27$. The most palpable change from the one component model is that the phase diagram is largely dominated by the striped profiles, with stripes appearing in the range $0.22 \lesssim \bar{\phi} \lesssim 1.28$. Just outside the range of $\bar{\phi}$ where bump structures are formed, we observe order parameter profiles which contain a mixture of bumps and stripes, see Fig. 6.9 (a), this value of $\bar{\phi}$ must lie inside the coexistence region between the bump and stripe phases. As we increase the value of $\bar{\phi}$ we enter the large region of parameter space where stripe structures are formed (Fig. 6.9 (b) and (c)), the only significant change as we increase $\bar{\phi}$ from 0.3 to 1 is the decrease in the width of the stripes; this is due to the fact that the typical length scale in the system is $2\pi/k_m$, where the wavenumber k_m given by Eq. (6.15), is inversely proportional to the average order parameter values $\bar{\phi_a}$ and $\bar{\phi_b}$. Increasing the value of $\bar{\phi}$ further, we continue to observe striped profiles, but now there are points where the stripes of one species 'connect' to stripes of the other species – see Fig. 6.9 (d) (these 'connections' appear as white lines in Fig. 6.9 (d)). Increasing $\bar{\phi}$ further, we observe a mixture of holes and stripes (Fig. 6.9 (e)). Close to the instability curve Eq. (6.16) we find interesting profiles where we observe a mixture of stripes, holes and regions where the profile is approximately uniform $\phi_a \approx \phi_b \approx \bar{\phi}$ (Fig. 6.9 (e)). Various modulated structures are observed over a large range of parameter values. It would be possible to consider the structures formed for different values of the coupling coefficient η and different values of the average order parameters, where $\bar{\phi_a} \neq \bar{\phi_b}$. However, here we do not make a systematic study of the entire parameter space and instead focus on the various bump formations. These structures closely resemble the configurations of particles/colloids in condensed matter systems and we believe that in this regime the model may be useful to understanding the fluid and solid phases of such systems.

6.3.2 Intermolecular interactions

For the remainder of this chapter, we pursue the idea that the bumps in this two component model represent two different types of molecules or colloidal particles suspended in a fluid medium. We perform time simulations of the two component model choosing parameter values

which result in the formation of bump structures. We run these simulations until the order parameter profiles reach an (almost) stationary state, which corresponds to being at (near) an energetic minimum. We then determine the coordinates of the particles by locating the position of the maximum of each of the peaks. The radial distribution functions are calculated by analysing these coordinates. We also calculate the effective pair potentials between the bumps. Later in Sec. 6.3.3 we consider the nearest neighbour bond angles and the ordering in crystalline configurations.

The bump phase in the two component model appears to behave in a similar manner to that of the one component model (c.f. Fig. 6.5). We observe bump structures when the average value of the order parameters $\bar{\phi_a}$ and $\bar{\phi_b}$ are small. In particular, when $\bar{\phi_a} = \bar{\phi_b} = \bar{\phi}$ and $r = -0.9$ we observe bumps within the range $0 \lesssim \bar{\phi} \lesssim 0.15$. We study and compare two different systems: the symmetric case where $q_a = q_b = 1$ and the asymmetric case where $q_a = 1$ and $q_b = 1.1$. In the symmetric case, interactions between bumps of the same type (aa and bb) are identical in both components, but the nature of the interaction between a bump in ϕ_a and a bump in ϕ_b (ab) is determined by the coupling term in the free energy. In the asymmetrical case, the different values of q mean that the size of the bumps are different in ϕ_a and ϕ_b, hence, all possible interactions aa, bb and ab are different.

We begin by considering how the two order parameter profiles change as we alter their average values $\bar{\phi_a} = \bar{\phi_b} = \bar{\phi}$. Thus we keep the concentration of the mixture fixed at $c = 0.5$, where

$$c = \frac{\bar{\phi_a}}{\bar{\phi_a} + \bar{\phi_b}}. \tag{6.20}$$

We set the other parameter values to $\alpha = 1$, $r = -0.9$ and $\eta = 4$. In Fig. 6.10 we display typical results. We plot the normalised difference between the two order parameters $\Delta\hat{\phi}$ (as defined in Eq. (6.19)). In (a), (b), (g) and (h) we show profiles from the symmetric case and in (c), (d), (i) and (j) we display the profiles from the asymmetric system. In (e), (f), (k) and (l) we present the radial distribution functions, which are obtained by averaging over at least fifty runs, each with different realisations of the initial noise. The solid lines show the radial distribution functions for the symmetric case and the dashed lines show the asymmetric case. It is very apparent that this region of the parameter space shares many similarities with the one component model in both one and two dimensions. If we select a small value of $\bar{\phi}$ we find localised peaks surrounded by vacant areas, as shown in Fig. 6.10 (a) and (c). We observe a

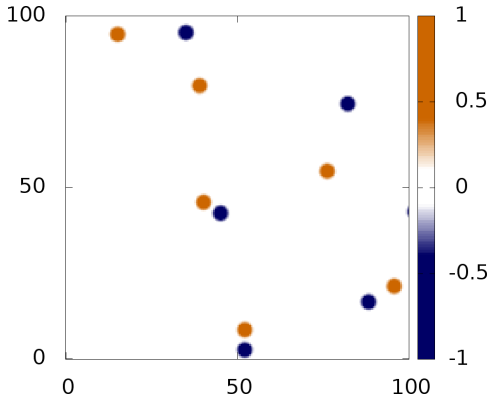

(a) $\bar{\phi} = 0$, $q_b = 1$

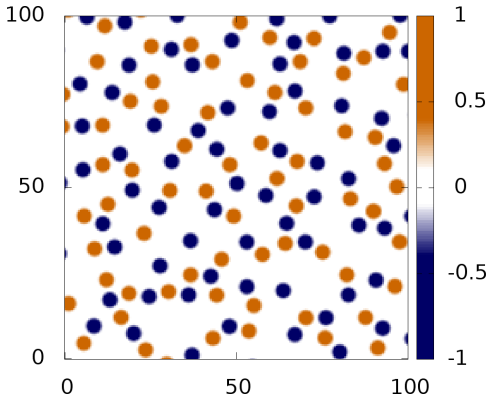

(b) $\bar{\phi} = 0.04$, $q_b = 1$

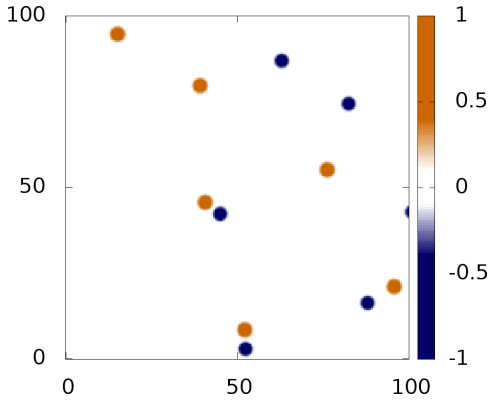

(c) $\bar{\phi} = 0$, $q_b = 1.1$

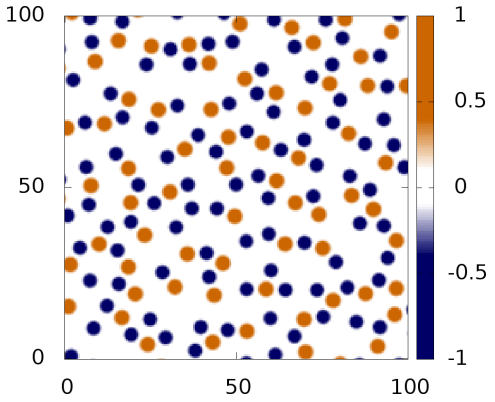

(d) $\bar{\phi} = 0.04$, $q_b = 1.1$

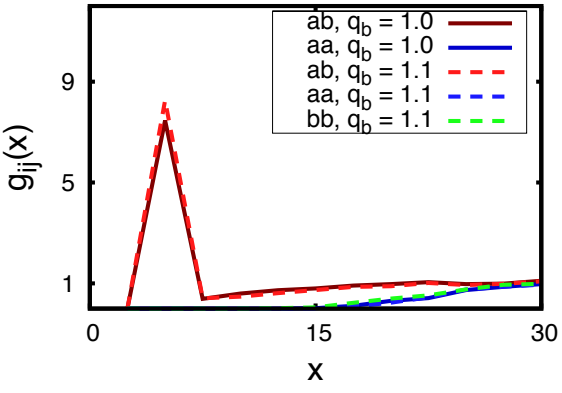

(e) $\bar{\phi} = 0$

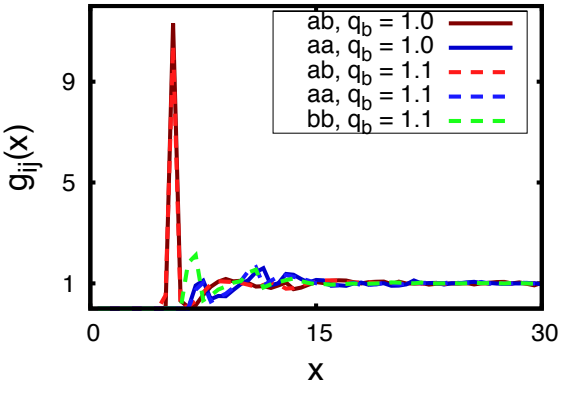

(f) $\bar{\phi} = 0.04$

Figure 6.10: Continues on the next page

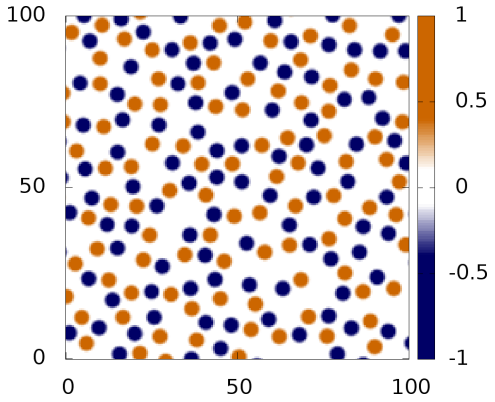

(g) $\bar{\phi} = 0.06$, $q_b = 1$

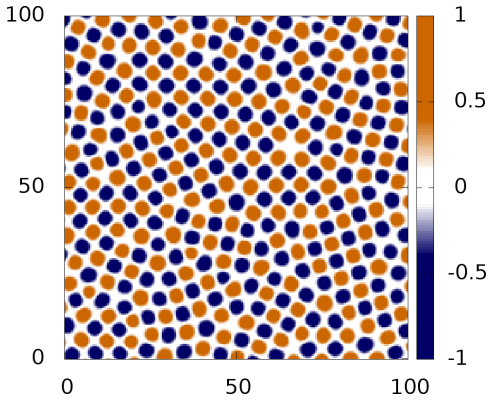

(h) $\bar{\phi} = 0.15$, $q_b = 1.1$

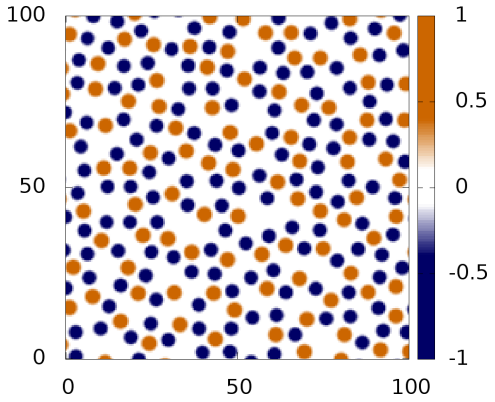

(i) $\bar{\phi} = 0.06$, $q_b = 1$

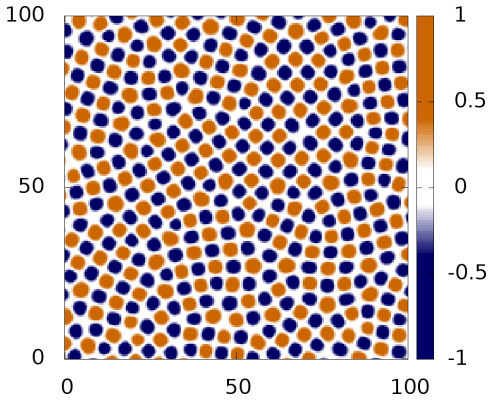

(j) $\bar{\phi} = 0.15$, $q_b = 1.1$

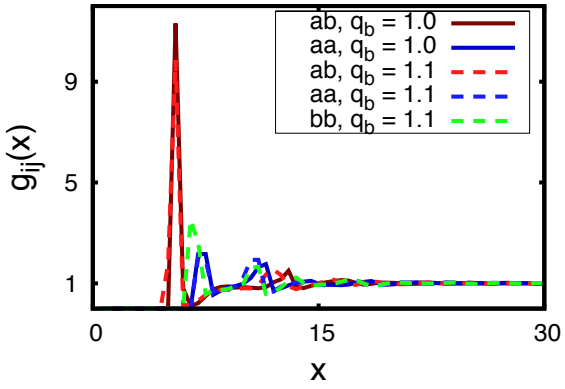

(k) $\bar{\phi} = 0.06$

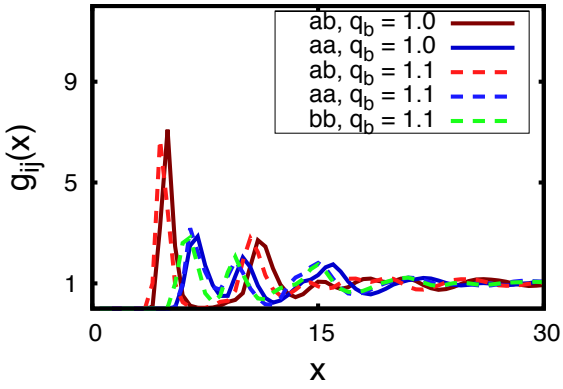

(l) $\bar{\phi} = 0.15$

Figure 6.10: Continued from the previous page: In (a), (b), (g) and (h) we display typical simulation results for $\Delta\hat{\phi}$ for the symmetrical case where $q_a = q_b = 1$. In (c), (d), (i) and (j) we display results from the asymmetrical case where $q_a = 1$ and $q_b = 1.1$. The orange regions show where there is a ϕ_a bump, while the blue show the ϕ_b bumps which are slightly smaller in the asymmetric mixture. In the (e), (f), (k) and (l) the radial distribution functions $g_{ij}(x)$ are shown for the symmetrical case (solid lines) and the asymmetrical case (dashed lines). The parameter values are: $\alpha = 1$, $\eta = 4$, $r = -0.9$ and $\bar{\phi_a} = \bar{\phi_b} = \bar{\phi}$.

tendency for bumps in ϕ_a and in ϕ_b to sit pairwise next to each other resembling configurations occurring in mixtures of oppositely charged colloidal particles [139–141]. When $\bar{\phi_a} \approx \bar{\phi_b}$, the arrangement of the bumps also resembles snapshots of monovalent salts. It is very difficult to differentiate between the structures formed by the symmetric and asymmetric models for small values of $\bar{\phi}$. This is because structurally, there is very little difference between the two cases. If we examine the radial distribution functions g_{ij} (where $i, j = a, b$) for the symmetric and asymmetric systems (Fig. 6.10 (e)) we observe that the average distance between the different bumps seems to be independent of the q values (any differences between the curves is of the same order of magnitude as the statistical error). This is due to the large vacant areas, which means that there are not many bumps which are close to one another, especially between bumps in the same species (aa and bb).

As we increase the values of $\bar{\phi}$ we find that the number of bumps of both species increases. In Fig. 6.10 (b), (d) and (f) we show the case where $\bar{\phi} = 0.04$ and in Fig. 6.10 (g), (i) and (k) we show the case where $\bar{\phi} = 0.06$. There is now a clear difference between the symmetric (b), (g) and the asymmetric (d), (i) cases. We observe a larger number of bumps in ϕ_b when $q_b = 1.1$. This is because the larger value of q reduces the length scale of the modulations, meaning that more bumps can be created before the value of ϕ_b becomes small (and negative) in vacant areas. There is an optimum value of ϕ_a and ϕ_b in the vacant (uniform) areas which depends on the parameter values. This explains why increasing the value of $\bar{\phi}$ increases the number of bumps (i.e., more modulations are needed in order to reach the optimum value of ϕ in the vacant regions). These intermediate values of $\bar{\phi}$ produce profiles with bump configurations that resemble real fluid structures. However, in stark contrast to the one component system (shown in Fig. 6.6 (b)), we now find the formation of chains of alternating bumps reminiscent of structures observed in charged fluids. The radial distribution functions in Fig. 6.10 (f) and (k) show that the asymmetry induced by the different values of q begins to take effect at these intermediate values of $\bar{\phi}$. We observe that statistically the bumps sit closer together in the asymmetrical case, especially when two bumps in ϕ_b are next to each other (bb, shown by green dashed line). This is due to the decreased size of the bumps in ϕ_b, allowing them to sit slightly closer to their neighbours.

Increasing the average order parameter values $\bar{\phi}$ further we begin to observe the formation of crystalline structures as shown by Fig. 6.10 (h), (j) and (l). The interesting thing is that now

we observe square ordering of the particles instead of the hexagonal ordering which is present in the regular PFC model and the one component VPFC model. This implies that as we increase the concentration of one of the species from $c = 0$ (almost a pure one component system) to $c = 0.5$ there must be a transition from hexagonal to square ordering of bumps, this is something we return to below in Sec. 6.3.3. Just as for the one component system, we find that there are more modulations in ϕ_b when $q_b = 1.1$. The profiles obtained with these parameter values resemble a compound crystal structure with vacancies and grain boundaries. The radial distribution functions in Fig. 6.10 (l) show that the smaller size difference of the ϕ_b bumps in the asymmetric mixture has a large impact on the average position of the bumps in the structure compared to the symmetric mixture. This is because the higher concentration of particles forces them all closer together resulting in all pairs of bumps aa, bb and ab being closer together.

In Fig. 6.11 (a)–(b) we show the shape of the individual bumps in ϕ_a and ϕ_b obtained in the low density limit $\bar{\phi} \to 0$. To determine these radially symmetric profiles we fit functions of the form $\theta(x)$ as defined above in Eq. (6.6). The bumps in ϕ_a are virtually identical for both the symmetrical and asymmetrical systems. The ϕ_a bump in the symmetric system and the ϕ_b bump in the asymmetric system decay to different values due to the different values of ϕ_a and ϕ_b in the vacant areas of the asymmetrical system. We observe that in this two component model, a bump in one order parameter profile coincides with a small depression in the other order parameter profile. This is caused by the coupling term, which means that the combination of a bump in one order parameter and a hole in the other order parameter reduces the free energy of the system. In Fig. 6.11 (c)–(d) we show the shape of the 'holes' which form in one profile under the bumps in the other order parameter field. These are determined the same way as the bump profiles: by fitting a function of the form shown in Eq. (6.6) to data points obtained from simulations. The depth of the holes is much smaller in size than the height of the bumps. This is because the vacancy term prevents the hole from reaching large negative values of ϕ_a or ϕ_b.

Using the fitted functions shown in Fig. 6.11 (a)–(d) we calculate effective pair potentials $V_{ij}(x)$ between the different particles in the system ($i, j = a, b$). We do this by determining the free energy for a system containing two bumps and their corresponding holes at various distances apart. In Fig. 6.11 (e) we display the effective pair potentials for both the symmetric (solid lines) and the asymmetric (dashed lines) systems. The results show that there is an

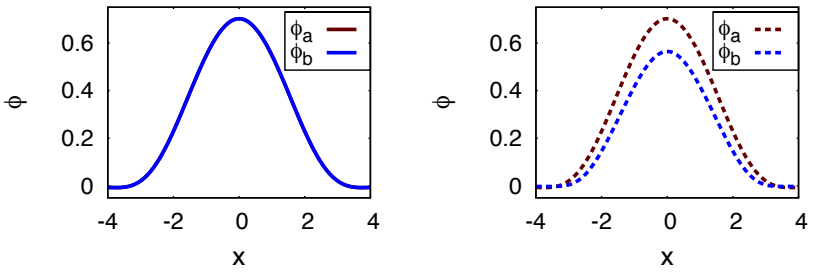

(a) Bump profiles, $q_b = 1$ **(b)** Bump profiles, $q_b = 1.1$

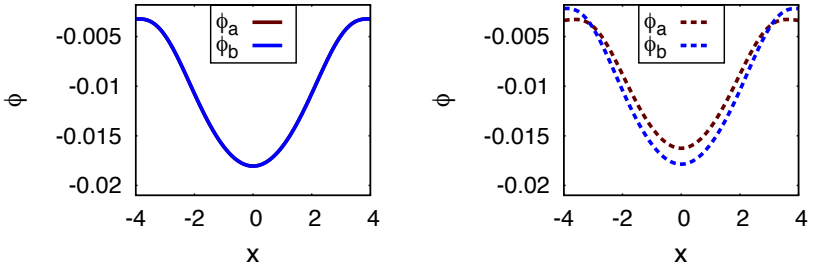

(c) Dip profiles, $q_b = 1$ **(d)** Dip profiles, $q_b = 1.1$

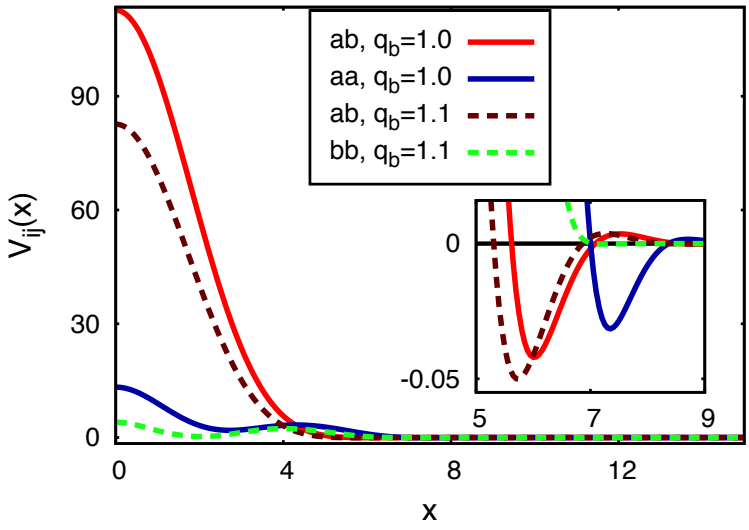

(e) Effective pair potentials

Figure 6.11: Fits to the shape of individual bumps (cf. Fig. 6.7) in the (a) symmetric, when $q_b = 1$, and (b) asymmetric, when $q_b = 1.1$, systems and the corresponding dips in the other order parameter profile which occur under the bumps in (c) the symmetric and (d) the asymmetric systems. In the symmetric profiles (a) and (c) the ϕ_a and ϕ_b curves are equal everywhere. The bump profile in ϕ_a is virtually identical in the cases where $q_b = 1$ and $q_b = 1.1$. These fits are then used to calculate the effective pair potential between bumps, which are displayed in (e). The inset displays a magnification of the tails of $V_{ij}(x)$. The resulting pair potential $V(x)$ between two bumps in ϕ_a when $q_b = 1.1$ lies on top of the $aa, q_b = 1$ curve. The parameter values are: $\alpha = 1$, $r = -0.9$, $\eta = 4$, and $\bar{\phi_a} = \bar{\phi_b} = 0$.

attraction between all of the bumps, just as we found for the one component system (Fig. 6.7 (b)). In both the symmetric and asymmetric cases we find that the attraction between two bumps from different species (ab) is stronger and occurs at a smaller value of x than that of two bumps of the same species (aa and bb). This explains the tendency for the bumps to form chains at intermediate values of ϕ_a and ϕ_b (Figs. 6.10 (b), (d), (g) and (i)) and square ordered crystalline structures at larger values of ϕ_a and ϕ_b (Fig. 6.10 (h) and (j)). This is also consistent with the appearance of the large peak in $g_{ab}(x)$ which occurs at a smaller x value than the main peaks in $g_{aa}(x)$ and $g_{bb}(x)$ - see Figs. 6.10 (f), (k) and (l). The effective pair potential $V_{aa}(x)$ is almost identical in the symmetric and the asymmetric systems. This suggests that the small hole which appears in ϕ_b has little effect on the interaction between the bumps. The major difference between the symmetrical and asymmetrical systems is that in the asymmetric mixture the minimum of the pair potentials $V_{ab}(x)$ and $V_{bb}(x)$ are at smaller values of x than in the symmetric mixture. This is due to the reduced size of the ϕ_b bumps in the latter. The minimum in $V_{bb}(x)$ is at a slightly larger value of x than the minimum in $V_{aa}(x)$ and the attraction is also much weaker (in fact it is so much weaker that the minimum is barely visible in this plot). This to some extent explains why the effect of the asymmetry is not visible for smaller values of ϕ_a and ϕ_b, but becomes apparent for larger values of ϕ_a and ϕ_b, where the vacant areas become smaller and we observe a close packing of the particles.

6.3.3 Bond angles and the transition between hexagonal and square ordering

In the two dimensional one component model (Eqs. (5.15) and (6.1)) we observe hexagonally ordered structures for certain parameter values (Fig. 6.5 (a) and Fig. 6.6 (c)). However, in the two component model when $\bar{\phi}_a = \bar{\phi}_b$, we instead observe a square ordered crystalline structure which alternates between species a and species b (Figs. 6.10 (h) and (j)). Thus, as the composition of the mixture is varied we should see a transition/crossover from hexagonal to square ordering. The number of bumps observed in each field ϕ_i depends on the respective average value $\bar{\phi}_i$. When the concentration $c \approx 0$ or $c \approx 1$, where c is defined in Eq. (6.20), (i.e., when either $\bar{\phi}_b \gg \bar{\phi}_a$ or $\bar{\phi}_a \gg \bar{\phi}_b$) then the resulting order parameter profile $\Delta\hat{\phi}(x)$ has many more bumps of one type than of the other, and in these two limits we again observe hexagonal ordering. Note that c in Eq. (6.20) is not a bump concentration, but instead is a ratio between the two average order parameter values. As the ϕ_i may take a negative value, for $c = 0$ there are still a few bumps of a and similarly there are still some species b bumps when $c = 1$. When $c = 0.5$ the number of bumps is roughly the same in both species for the symmetrical case (q_a

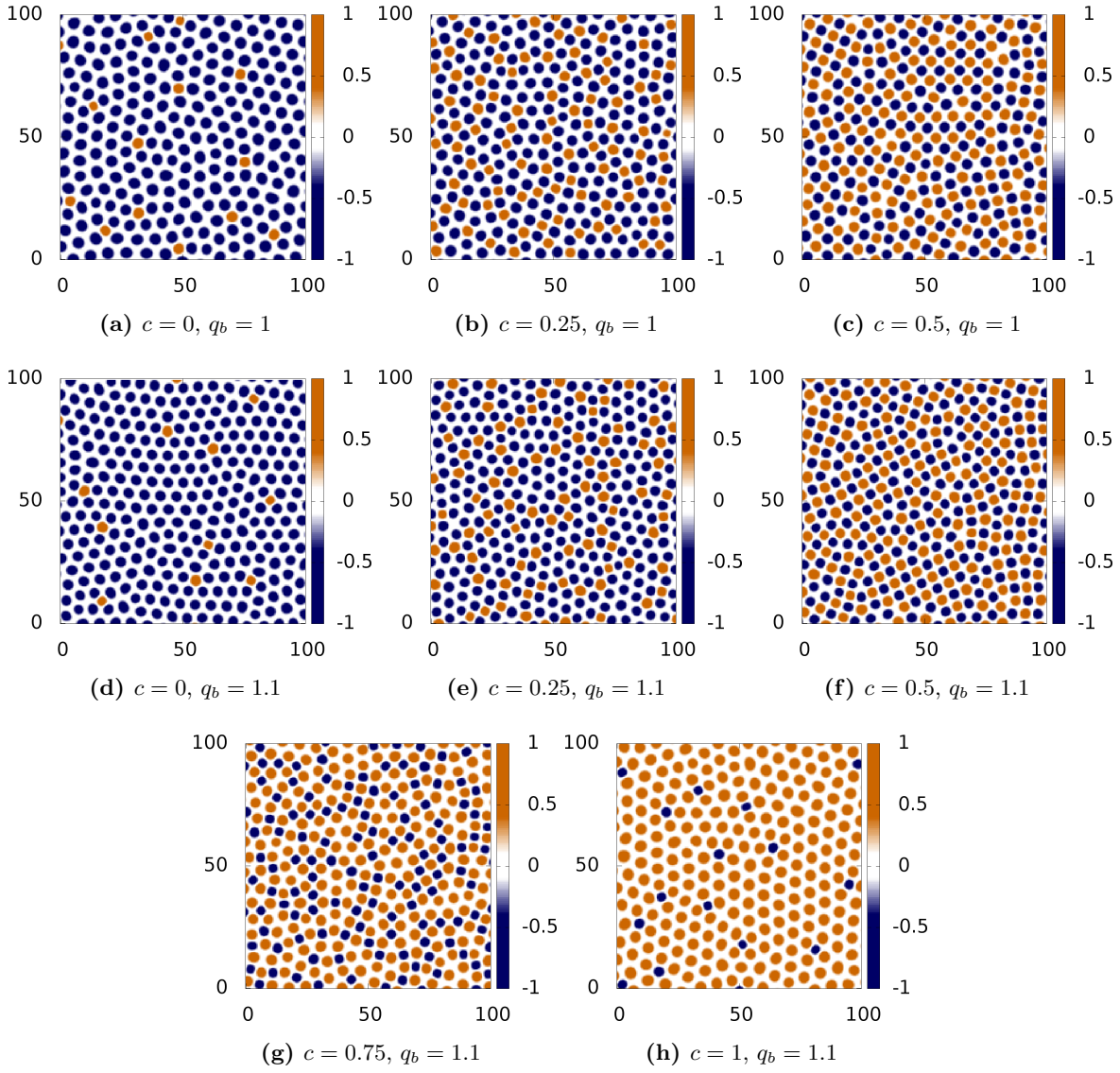

(a) $c = 0$, $q_b = 1$ **(b)** $c = 0.25$, $q_b = 1$ **(c)** $c = 0.5$, $q_b = 1$

(d) $c = 0$, $q_b = 1.1$ **(e)** $c = 0.25$, $q_b = 1.1$ **(f)** $c = 0.5$, $q_b = 1.1$

(g) $c = 0.75$, $q_b = 1.1$ **(h)** $c = 1$, $q_b = 1.1$

Figure 6.12: Plots of the order parameter $\Delta\hat{\phi}$, in which bumps in species a appear in orange and bumps in species b appear in blue, for a constant total order parameter value $\bar{\phi_a} + \bar{\phi_b} = 0.24$. In (a) - (c) we show results from the symmetric mixture ($q_a = q_b = 1$) where the concentration of species a is (a) $c = 0$, (b) $c = 0.25$ and (c) $c = 0.5$. In (d) - (h) we show the results from the asymmetric mixture ($q_a = 1$ and $q_b = 1.1$) where (d) $c = 0$, (e) $c = 0.25$, (f) $c = 0.5$, (g) $c = 0.75$ and (h) $c = 1$. The parameter values are: $\eta = 4$ and $r = -0.9$.

$= q_b$), but this is not necessarily true for the asymmetrical system ($q_a \neq q_b$). When $\bar{\phi_a} = \bar{\phi_b}$ and $q_a < q_b$ there are more b bumps than a bumps.

In Figs. 6.12 (a)–(c) we show the order parameter $\Delta\hat{\phi}$ for varying values of c for the symmetric mixture ($q_a = q_b$). We fix the total 'density' $\bar{\phi_a} + \bar{\phi_b} = 0.24$ and investigate how the crystalline structures change as the concentration c is varied. In Fig. 6.12 (a), when $c = 0$ we observe a profile which is dominated by species b bumps. The crystal is hexagonally ordered with some

defects (these tend to occur in the vicinity of the ϕ_a bumps). There are only a few ϕ_a bumps, which means the bumps in b are usually sitting next to each other, resulting in them ordering themselves in a similar manner to that observed in the one component model Fig. 6.6 (c). Increasing the value of c from 0 to 0.25, we observe a loss of crystalline structure, as shown in Fig. 6.12 (b). The loss of long range order is clearly visible in the associated radial distribution functions (not shown). The profile in Fig. 6.12 (b) shows a somewhat amorphous structure which appears to include both square and hexagonal ordering in equal measure. Increasing the concentration further to $c = 0.5$, we observe a similar square ordering of bumps as in Figs. 6.10 (h) and (j) (in Fig. 6.10 (h): $q_b = 1$, whereas in Fig. 6.10 (j): $q_b = 1.1$, all other parameter values are the same). The crystalline structure in Fig. 6.12 (c) at $\bar{\phi_a} = \bar{\phi_b} = 0.12$ contains more vacancies and defects than the one in Fig. 6.10 (h) at $\bar{\phi_a} = \bar{\phi_b} = 0.15$, as both average order parameter values are smaller. Owing to the symmetry induced by choosing $q_a = q_b$ (i.e., $\phi_a \to \phi_b$ as $c \to 1 - c$), a case with concentration c is equivalent to the case with concentration $1 - c$. Thus Fig. 6.12 (b) also shows the case $c = 0.75$ if one interchanges the orange and blue bumps. For this reason values $c > 0.5$ are not shown.

For the asymmetric system the $c \to 1 - c$ symmetry does not exist and we therefore show five cases for c varying from 0 to 1 in Figs. 6.12 (d) $c = 0$, (e) $c = 0.25$, (f) $c = 0.5$, (g) $c = 0.75$ and (h) $c = 1$. We again observe a transition from hexagonal ordering in Fig. 6.12 (d) to square ordering in Fig. 6.12 (f) and back to hexagonal ordering in Fig. 6.12 (h) as the value of c is increased from 0 to 1. In between the highly structured states we observe the mixed ordered states (Figs. 6.12 (e) and (g)) that were also present in the symmetrical system. By eye, it is very difficult to pick out the differences between the symmetrical and the asymmetrical cases. As previously discussed, the different value of q_b in the asymmetrical system changes the shape, size and quantity of b bumps. In appendix E we display the $\Delta\hat{\phi}$ profiles for different values of c where $\bar{\phi_a} + \bar{\phi_b} = 0.24$ and also repeat the analysis for the case where $\bar{\phi_a} + \bar{\phi_b} = 0.15$. In order to characterise and better understand the organisation of the crystalline structures that are formed, we require a measure which may be used to quantify the structures and distinguish between hexagonal and square ordering in both the symmetric and the asymmetric systems. To do this, we use Delaunay triangulation [142, 143] to calculate the distribution of the bond angles $p(\Theta)$ between nearest neighbours. We could have used other measures from stochastic geometry [144], which were used to characterise the hexagon-square transition in Bénard convection [145].

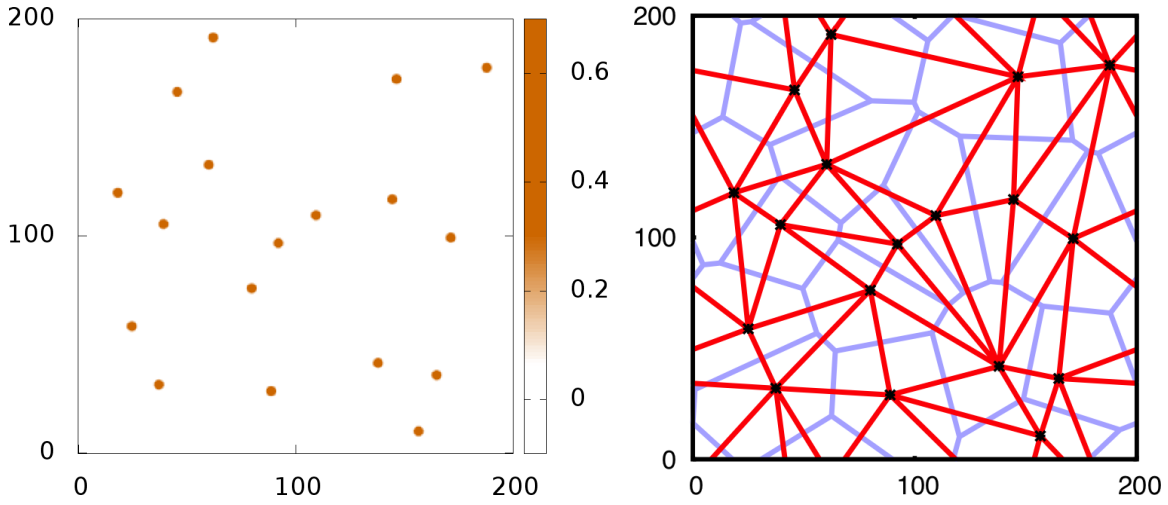

(a) One component ϕ profile

(b) Voronoi diagram and Delaunay triangulation

Figure 6.13: An example Delaunay triangulation is shown for a simple one component case. In (a) we display a typical order parameter profile for the one component model where we observe isolated peaks. The coordinates of the maxima are calculated, these are shown as black points in (b). In (b) we show the Voronoi diagram (light blue polygon network) and the Delaunay triangulation (red triangles) for this particular set of coordinates.

The Delaunay triangulation is a triangulation of points (in our case the coordinates of the peaks of the bumps in both order parameter fields) which maximises the minimum angles of every triangle (i.e., avoids 'skinny' triangles). This triangulation can be calculated from the Voronoi diagram [142, 143] of any set of points on a 2D plane. The Voronoi diagram is a set of polygons, where each polygon represents an area in 2D space which is closer to a particular point than to any of the other points (i.e., the locus of points contained in each polygon is closer to the bump inside the polygon than any other bump). In Fig. 6.13 we show an example of how we calculate the Delaunay triangulation for a given order parameter profile. The example shows the triangulation for a one component profile (as the pairing between bumps in the two component model makes the triangulation harder to see) but the process is applied in the same manner to the two component model. We take the coordinates of all the bumps to be our points on a 2D plane. We then calculate the Voronoi diagram (shown as the light blue lines in Fig. 6.13 (b)) which can be used to calculate the Delaunay triangulation (shown as the red lines in Fig. 6.13 (b)). This can be done using any of the algorithms outlined in Refs. [142, 143]. For an efficient method of calculating Voronoi diagrams and Delaunay triangulations see Ref. [146]. (Note that Delaunay triangulation becomes degenerate when points appear in certain lines of symmetry. However, the initial noise added to the order parameter fields prevents bumps from forming in perfect symmetry). We use the statistics of the triangles in the Delaunay triangulation to

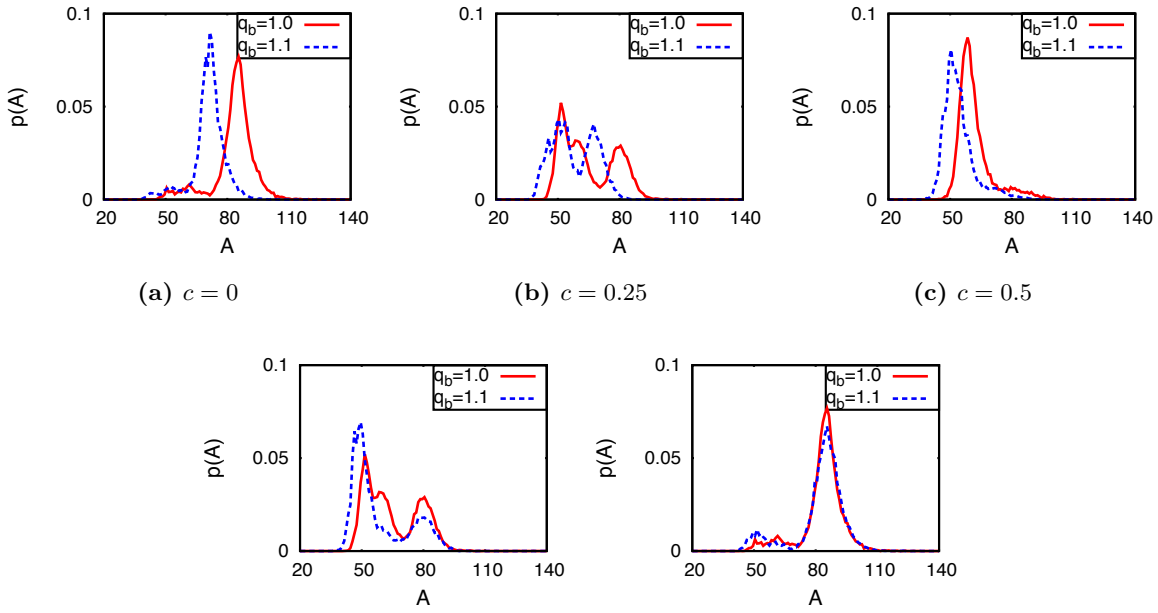

(a) $c = 0$ **(b)** $c = 0.25$ **(c)** $c = 0.5$

(d) $c = 0.75$ **(e)** $c = 1$

Figure 6.14: The area distribution $p(A)$ for a constant total order parameter value $\bar{\phi}_a + \bar{\phi}_b = 0.24$. The concentration of species a is (a) $c = 0$, (b) $c = 0.25$, (c) $c = 0.5$, (d) $c = 0.75$, and (e) $c = 1$ (corresponding to the simulation snapshots shown in Fig. 6.12). Results for the symmetric system are shown as the red solid lines and the asymmetric system results are shown as blue dashed lines. The parameter values are: $q_a = 1$, $\eta = 4$ and $r = -0.9$.

characterise the structures produced by the bumps.

We extract three quantities from the triangulation: the area of the triangles, the length of the sides and the angles in each of the triangles. This information is gathered for five different realisations of the initial noise profile for systems of size 200×200 and the information is sorted into bins. From these bins we obtain the probability distribution function for each quantity. Comparing the different distributions for various values of c allows us to observe how the triangles in the triangulation change as we go from hexagonal to square ordering. When bumps exhibit hexagonal ordering the triangulation should be dominated by roughly equilateral triangles and conversely when there is square ordering, one observes roughly right angled triangles. Therefore, hexagonal ordering should lead to larger areas, length distributions with a single peak and angle distributions with a single peak around 60°. When there is square ordering, one would expect to observe smaller areas, length distributions with two peaks and angle distributions with one peak at 90° and another peak at 45°.

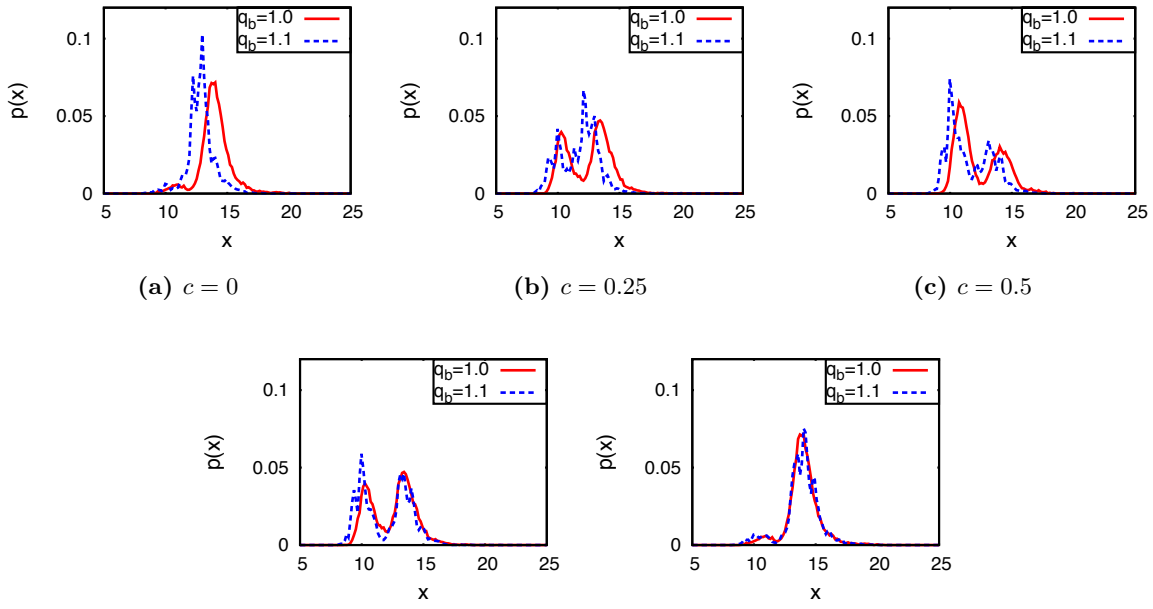

(a) $c = 0$ **(b)** $c = 0.25$ **(c)** $c = 0.5$

(d) $c = 0.75$ **(e)** $c = 1$

Figure 6.15: The length distribution $p(x)$ for a constant total order parameter value $\bar{\phi_a} + \bar{\phi_b} = 0.24$. The concentration of species a is (a) $c = 0$, (b) $c = 0.25$, (c) $c = 0.5$, (d) $c = 0.75$, and (e) $c = 1$ (corresponding to the simulation snapshots shown in Fig. 6.12). Results for the symmetric system are shown as the red solid lines and the asymmetric system results are shown as blue dashed lines. The parameter values are: $q_a = 1$, $\eta = 4$ and $r = -0.9$.

In Fig. 6.14 we display the probability distribution $p(A)$ for the area of the triangles in the Delaunay triangulation as the concentration is varied from 0 to 1. We show results for the symmetric (solid red line) and the asymmetric (dashed blue line) systems. The distribution of the areas of the triangles clearly shows the transition between hexagonal and square ordering. We consistently observe two peaks; one peak is associated with the area of the equilateral triangles formed when the bumps are organised hexagonally and the other is the area of the right-angled triangles formed in square ordering. As c is varied from 0 to 1 we see a continuous shift of mass from the higher peak (hexagonal order) in Fig. 6.14 (a) to the lower peak (square order) in Fig. 6.14 (c) and back again (shown in Fig. 6.14 (e)) in both the symmetric and the asymmetric systems. However, the value where the peak occurs changes as the value of c is varied due to the increase in the number of modulations. Additionally, the peaks occur at different values for the asymmetrical case because of the different shapes and number of bumps which occur in the asymmetrical system. The difference between the area distributions between the symmetric and asymmetric systems decreases as $c \to 1$, due to the decreased number of ϕ_b modulations.

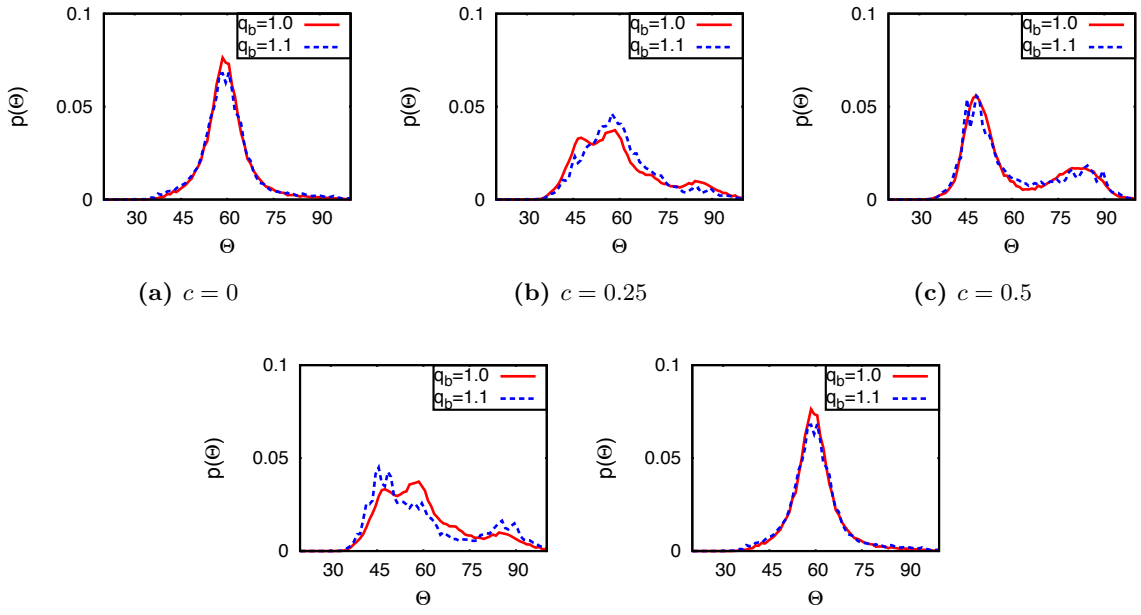

(a) $c = 0$ **(b)** $c = 0.25$ **(c)** $c = 0.5$

(d) $c = 0.75$ **(e)** $c = 1$

Figure 6.16: The angle distribution $p(\Theta)$ for a constant total order parameter value $\bar{\phi}_a + \bar{\phi}_b = 0.24$. The concentration of species a is (a) $c = 0$, (b) $c = 0.25$, (c) $c = 0.5$, (d) $c = 0.75$, and (e) $c = 1$ (corresponding to the simulation snapshots shown in Fig. 6.12). Results for the symmetric system are shown as the red solid lines and the asymmetric system results are shown as blue dashed lines. The parameter values are: $q_a = 1$, $\eta = 4$ and $r = -0.9$.

The probability distribution of the length of the sides of the triangles $p(x)$ shown in Fig. 6.15 also shows a smooth transition between hexagonal and square ordering of bumps. We observe a shift from a single peak (hexagonal order) to two peaks (square order) where the peak at the lower length is twice as high as the peak at the higher length. Once again we observe that the lengths where these peaks appear is different for different values of c and between the symmetric and the asymmetric systems.

In Fig. 6.16 we display the probability distribution $p(\Theta)$ for the triangle corner angles, as the concentration c is varied from 0 to 1. The transition between hexagonal and square ordering is again evident in the distribution at different values of c. When $c = 0$ the hexagonal ordering leads to angle distributions which have a single peak at 60°, as shown in Fig. 6.16 (a). As the value of c increases and we observe square ordering, the structural change is reflected in the angle distributions by the formation of a peak slightly above the value 45° and another peak (half the size) slightly below 90°, as shown in Fig. 6.16 (c). Increasing the concentration further to $c = 1$ restores the hexagonal ordering, hence the angle distribution returns to the single

peak at 60° (Fig. 6.16 (e)). In between the purely hexagonal and the purely square ordered structures we observe states where the distribution of bond angles is more evenly spread, with small peaks occurring just above 45°, at around 60° and just below 90° (Figs. 6.16 (b) and 6.16 (d)). These represent the somewhat amorphous structures which lack the long range ordering which is present in the hexagonally and square ordered structures. The position of these peaks in the bond angle distributions $p(\Theta)$ does not depend on the quantity or size of the bumps and so the peaks occur in (almost) the same position for the symmetric and the asymmetric systems for all values of c (this is not the case for the area or length distributions). This makes the bond angle distributions ideal for comparing the structure of bump formations in different systems. On comparing the symmetrical and the asymmetrical cases we observe that $p(\Theta)$ appears smoother in the symmetrical case, which is also evident in the area and length distributions. The distribution function $p(\Theta)$ has a more jagged appearance for the asymmetrical mixture, which we believe is due to the fact that there are different sized bumps in this mixture, making it more difficult for the bumps to organise themselves into regular structures. In Figs. 6.16 (a) and 6.16 (e) the distributions appear very similar for the symmetric and the asymmetrical cases, however, in the other distributions (in particular, Figs. 6.16 (b) and 6.16 (d)) we observe a distinct difference in the height of the three peaks. This suggests that the transition between the different ordered states occurs differently in the symmetric and the asymmetric systems. In Fig. E.3 of appendix E we display the bond angle distributions for intermediate values of c.

To examine more closely the transition from the hexagonal to the square ordered states we introduce an order parameter Φ which is calculated from the distribution of the angles from the Delaunay triangulation. We integrate the angle distributions over three regions which cover the three different peaks (these regions are determined arbitrarily from close examination of the angle distributions in Fig. 6.16) and define the quantities:

$$\begin{aligned} R_0 &= \int_{25}^{53} p(\Theta)\, d\Theta, \\ R_1 &= \int_{53}^{72} p(\Theta)\, d\Theta, \\ R_2 &= \int_{72}^{115} p(\Theta)\, d\Theta. \end{aligned} \tag{6.21}$$

We then define the order parameter Φ in the following way:

$$\Phi = \frac{R_0 + R_2}{R_1}. \tag{6.22}$$

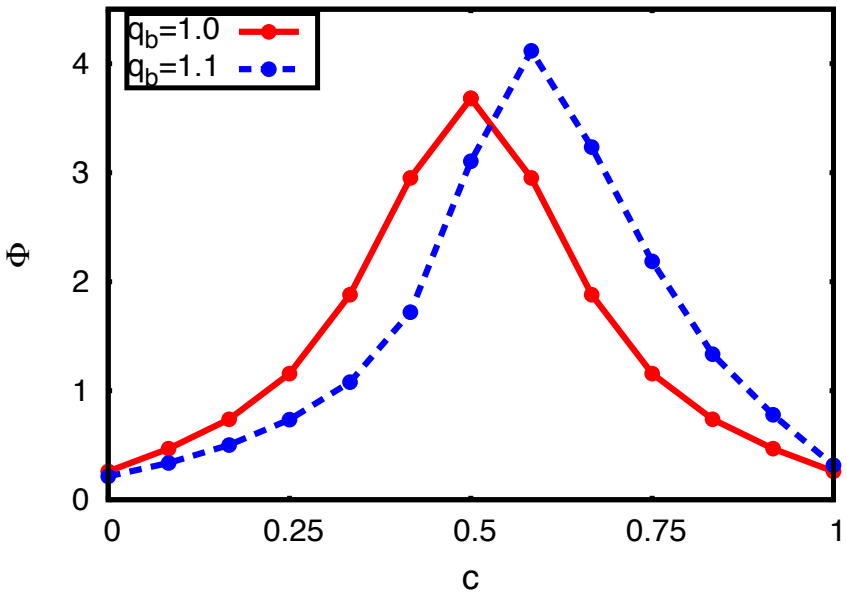

Figure 6.17: Plot showing the order parameter Φ (defined in Eq. (6.22)) as a function of the concentration c of species a, where $\bar{\phi_a} + \bar{\phi_b} = 0.24$. The red solid line and points show the symmetric case and the blue dashed line and points show the asymmetrical case. The parameter values are: $q_a = 1$, $\eta = 4$ and $r = -0.9$.

When a structure consists of mainly hexagonal configurations of bumps the value of Φ is small (since $\Phi \to 0$ as $R_0 \to 0$ and $R_2 \to 0$) and when a profile is dominated by square ordering the value of Φ is large (since $\Phi \to \infty$ as $R_1 \to 0$). Calculating this quantity for the angle distributions for different values of c gives a measure for the hexagonal versus square ordering of the bumps.

In Fig. 6.17 we show how the order parameter Φ changes with the concentration c for the symmetric (solid red line) and the asymmetric (dashed blue line) mixtures. Both curves show a smooth continuous transition from hexagonal ordering to square ordering and back again. The different sized bumps in the asymmetric system break the symmetry around $c = 0.5$ and we observe that the maximum (which corresponds to the strongest square ordering) occurs at around $c \approx 0.6$, and is actually higher than the peak in the symmetric case. This is clearly visible in the angle distributions; comparing the distributions when $c = 0.5$ in Fig. 6.16 (c) with the distributions when $c = 0.58$ in Fig. E.3 (e). The transition to and from square ordering appears to be slightly sharper in the asymmetrical case. Even though there is a difference in the transition between the different ordered states in the symmetric and the asymmetric mixtures, they appear to be qualitatively similar. It may be the case that for a larger difference in the values of q_a and q_b a different type of transition from hexagonal to square ordering might occur,

e.g., a discontinuous transition. However, the effect of varying the ratio q_a/q_b is not studied in detail here.

6.4 Conclusions

In this chapter we have investigated the VPFC model and its application to materials modelling. We first considered the one component model proposed by Chan et al. in Ref. [118]. We determined the linear stability of the homogeneous state and discussed the dispersion relation. We examined the phase behaviour in one dimension and calculated the phase diagram, computing exactly the location of the tricritical point between the homogeneous and periodic states, and identified the region of phase space where localised structures occur. Focusing on the latter region of the phase diagram, we investigated the localised steady state profiles and discussed the slanted homoclinic snaking which occurs in the bifurcation diagrams. The one component model was also studied in two dimensions and we determined the phase diagram, radial distribution functions and effective pair potentials from our simulation data. Some of the behaviour we have identified - the presence of transitions resembling transitions from a solid phase to a liquid phase and then to a gas-like phase - replicates behaviour observed in non-conserved systems [147]. In section 6.3 of this chapter, we extended the model to include two coupled order parameter fields. We have considered how the coupling affects the linear stability of flat films and then briefly touched on the phase behaviour of this two component model. We have focused on the bump structures which form, considering both a symmetrical mixture where the bumps are of equal size and an asymmetrical system where one of the bump species is slightly smaller than the other species. The radial distribution functions and effective pair potentials for these systems are somewhat similar to those in binary mixtures of oppositely charged colloidal particles. We have investigated how varying the concentration c of the mixture produces a crossover from hexagonal to square ordered crystalline structures and how the transition differs between the symmetrical and the asymmetrical systems.

A key issue on which we should comment concerns the question of what precisely does the order parameter profile $\phi(\mathbf{x}, t)$ in the VPFC model represent? In the regular PFC model, the phase with the uniform flat profile is taken to represent the liquid phase, whilst the bump phase corresponds to the crystalline solid. This interpretation is underpinned by the fact that the regular PFC can be derived from density functional theory (DFT) [108] and dynamical density functional theory (DDFT) [101], which is a theory for the dynamics of a system of interacting

Brownian (colloidal) particles [4, 7, 8, 74] (see chapter 2 for more details). As discussed in chapter 2, DFT [1, 3, 5] is a statistical mechanics theory for the one-body number density $\rho(\mathbf{x})$ of a system of particles, where $\rho(\mathbf{x}) = \langle\hat{\rho}(\mathbf{x})\rangle$ and where $\hat{\rho}(\mathbf{x}) = \sum_i \delta(\mathbf{x} - \mathbf{x}_i)$ is the density operator and $\langle\cdot\rangle$ denotes a statistical ensemble average [3]. The central quantity in DFT is the Helmholtz free energy functional $F[\rho]$ and the equilibrium fluid density profile $\rho^*(\mathbf{x})$ is that which minimises the grand free energy $\Omega[\rho] = F[\rho] - \mu\int \mathrm{d}\mathbf{x}\rho(\mathbf{x})$. The DDFT for Brownian particles [4, 7, 8, 74] takes as input this functional and so yields the correct equilibrium fluid density profile. Making a truncated gradient expansion approximation for $F[\rho]$, expanding the free energy around that of a reference liquid state with uniform density ρ_0, one can argue that the free energy is approximately given by Eqs. (5.17) and (5.18), where the order parameter $\phi(\mathbf{x}) \propto \rho(\mathbf{x}) - \rho_0$ (see Sec. 5.1 for further details). Thus it is clear that in a bulk liquid, where $\rho(\mathbf{x})$ is a constant, so too is $\phi(\mathbf{x})$ a constant and in the solid phase, where $\rho(\mathbf{x})$ consists of a periodic array of density peaks, then $\phi(\mathbf{x})$ also contains periodic modulations. However, there are some problems extending this interpretation to the VPFC. Consider for example Fig. 6.6 (a) where we see a few isolated localised peaks surrounded by a uniform background where $\phi(\mathbf{x}) \approx 0$. Maintaining the above PFC interpretation, this would correspond to a few individual 'frozen' particles, surrounded by a fluid of mobile particles. One might be tempted to think of this as some sort of glass transition [1, 148, 149], but the glass transition is a collective phenomenon: in a glass one does see 'dynamical heterogeneity' i.e., regions where the particles are totally jammed and other regions which are more mobile, but to our knowledge one never sees a single particle that is jammed on its own surrounded by more mobile particles. Thus, it may be possible to assume this interpretation may be maintained for the VPFC, i.e., by considering the localised peaks surrounded by a uniform background to be a dynamically heterogeneous glassy system, but there are problems with this point of view.

An alternative interpretation for the order parameter profile in the VPFC model is that $\phi(x)$ is related to a coarse-grained density profile (rather than an ensemble average density profile) for the system $\tilde{\rho}(\mathbf{x}, t)$, i.e., $\phi(\mathbf{x}, t) \propto \tilde{\rho}(\mathbf{x}, t)$. Following Ref. [74], we may define the temporally coarse-grained density profile for a system of Brownian colloidal particles as $\tilde{\rho}(\mathbf{x}, t) = \int K(t - t')\hat{\rho}(\mathbf{x}, t)\mathrm{d}t'$, where $K(t)$ is a normalised function of finite support which defines a time window over which the density is coarse-grained. One can then argue [74] that the time evolution equations for $\tilde{\rho}(\mathbf{x}, t)$ must be very similar or even the same as the DDFT equations for the time evolution of the ensemble average density $\rho(\mathbf{x}, t)$, as long as the width

in time τ of $K(t)$ is large enough. By choosing the time τ so that it is large compared to the time between the colloidal particles receiving Brownian 'kicks' from the solvent, but is short compared to the diffusive time scale, corresponding to the typical time for a particle to diffuse a distance equal to its own diameter, then the coarse-grained density $\tilde{\rho}(\mathbf{x}, t)$ and the order parameter $\phi(\mathbf{x}, t)$ will be quantities which contain peaks, each of which correspond to an individual particle in the system. Thus, in a low density colloidal suspension one should see isolated peaks in the coarse-grained density, surrounded by regions where $\phi(\mathbf{x}, t) \approx 0$, corresponding to no particles being present in that region of the system. This is the justification for the interpretation made by Chan *et al.* in Ref. [118], that the peaks in the order parameter correspond to particles and the uniform background corresponds to a portion of solvent free of particles. In order to observe the long time Brownian motion of the particles in this description, one should add a stochastic noise term to the dynamical equations for the system (6.8), that continuously drives the system (as opposed to the small amount of noise that is present in our initial order parameter profiles). However, in numerical simulations there can be problems with such an approach, because the particles can become pinned in place by the discrete grid on which they are defined, and so do not move. We did not make a detailed investigation of the of the VPFC model with additional noise. Further issues arise as the noise renormalises the parameters of the continuum model.

There are state points in the PFC and VPFC phase diagram where all possible interpretations of ϕ break down: these are the state points where the equilibrium state is the stripe or the hole phase, such as those displayed in Fig. 6.9. Systems of spherical particles do not have an ensemble average density profile ρ nor a coarse-grained density profile $\tilde{\rho}$ with stripes/holes, unless the particles in the system interact via pair potentials containing competing attractive and repulsive parts [86, 129, 150]. We must conclude that for the parameter values corresponding to these state points, the gradient expansion that is implicit in the PFC and VPFC free energy functionals has broken down and that these order parameter profiles are unphysical.

The radial distribution functions for the one component model displayed in Fig. 6.6 (see also Fig. 5 of Ref. [118]) are very similar to those in real fluids. We observe static correlations which are very similar to what one observes in fluids. Increasing the value of $\bar{\phi}$ increases the number of bumps and close packing causes long range (crystalline) ordering of the bumps. Calculating the effective pair potential between isolated pairs of bumps, we find a pair potential having an

attractive minimum at a pair separation distance which is slightly larger than the diameter of the bumps. Thus, the interactions and correlations between bumps share certain features with some colloidal fluids [151]. We also extend the model to consider a two component mixture, with a simple repulsive coupling between the two order parameter profiles. At low values of $\bar{\phi}$ the bumps commonly appear in pairs and at intermediate values they tend to form chains. At higher values of $\bar{\phi}$ the system exhibits crystalline ordering. The appearance of these structures is somewhat reminiscent of the arrangement of the particles in a binary mixture of oppositely charged colloidal particles - see e.g., Ref. [139, 152] and references therein. The radial distribution functions and the effective pair potentials show there is a fairly strong attraction between bumps of the opposite species a and b. The minimum in the ab effective pair potential is at a shorter pair separation distance than the minimum in the aa and bb pair potentials and so we observe square ordering when the concentration $c \approx 1/2$ and $\bar{\phi}$ is high enough for the bumps to pack into a crystalline structure. However, when $c \approx 0$ or $c \approx 1$, we observe hexagonal ordering and so we observe a transition from hexagonal to square ordering as the concentration c is varied. We find that this transition occurs smoothly but can become skewed by changing the size of one of the species of bumps ($q_a \neq q_b$).

It would be interesting to further investigate the effect that varying the ratio q_a/q_b has on the structures which form. In particular, determining the range of values of q_a and q_b for which bump profiles form in the 2D system would allow one to determine the range of size ratios of particles (bumps) that can be modelled. The transition between hexagonal and square structures could then be studied for systems with very different sized bumps and if the VPFC in this regime continues to be able to model mixtures of charged colloidal particles, then a wide range of different crystal structures should be observed [139].

Note also that the localised structures that we observe are not a unique property of the VPFC model but are in fact also present in the regular PFC model for a small range of parameter values outside the limit of linear stability. This is something that should be focused on in future work.

Chapter 7

Summary and Conclusions

The topic for this thesis is the description of colloidal soft matter systems using microscopic continuum models. In particular, we have considered a DDFT model for evaporating thin films of colloidal suspensions and a modified PFC model which is employed to study fluids and crystals with defects.

We begin with the DDFT model. In chapter 2 we discussed some of the basic concepts and ideas of DFT which is the backbone of the model used in our case study in chapter 4. This was presented using two different approaches; we show how from thermodynamic reasoning we may arrive at the general DFT formalism in Sec. 2.1 and then in Sec. 2.2 we briefly describe how DFT may be derived more formally from the microscopic structure of materials. Most importantly we introduce the concept of the Helmholtz free energy equation $F[\rho]$ which is a functional of the one body density ρ and show how the free energy $F[\rho]$ may be split into three distinct parts; an ideal gas part $F_{\mathrm{id}}(\rho)$, an excess part $F_{\mathrm{ex}}(\rho)$ associated with the contribution from the interactions of the particles and a contribution from any external fields acting on the particles F_{ext} (c.f. Eq. (2.16)). We also define the minimisation principle in Eq. (2.11); which states that the equilibrium density profile ρ^* may be determined by minimising the grand potential with respect to the one body density ρ. In the final section of chapter 2 we derive the DDFT result in Eq. (2.47). We start with the stochastic equations of motion for Brownian particles in Eq. (2.33) and then derive an expression for the time evolution of the probability density f (shown in Eq. (2.35)), relating the probability density f with the one body density ρ we then determine a time evolution equation for ρ, which we write in a concise form in Eq. (2.47). This important result is used to determine the dynamics of the model presented in chapter 4 as well as the dynamics in the PFC models discussed in chapters 5 and 6.

The system which we model in chapter 4 is described in detail in chapter 3 and we show some key experimental results [28, 44, 47, 48, 50] and discuss some alternative modelling approaches [45, 48, 50, 51]. We are interested in the nanostructures which are formed during the evaporative dewetting of thin films of colloidal suspensions. The main motivation for this research comes from seeking to understand the mechanisms for the formation of the intricate patterns observed in experiments [51]; a fine labyrinth structure (as shown in Fig. 3.4 (a)), a network

structure (Fig. 3.4 (b)) and a branched flower-like pattern (Fig. 3.4 (c)). Two distinct dewetting processes are identified. At first there is a macroscopic receding front which leaves behind an ultra thin film of the colloidal solution and then this ultra thin film ruptures and undergoes a second dewetting stage, it is the latter process which interests us here. A brief overview is given of the KMC model which was used by Vancea et al. to describe such a system [51]. The simulation results obtained with the KMC model displayed a dependency of the branched structures on the mobility of the nanoparticles and the different strengths of the various interactions terms. One of the major shortcomings of the model was that it only considered solvent evaporation and assumed that the affect of solvent transportation was negligible, this issue was addressed by the DDFT model we introduced in chapter 4.

The free energy Eq. (4.8) used in the DDFT model is derived from the same Hamiltonian Eq. (4.1) as the KMC model, but we now consider a continuum model where we solve for the densities of the two components ρ_l and ρ_n (c.f. Eqs. (4.12) and (4.12)). The dynamics model the diffusion of the nanoparticles (Eq. (4.14)) and the diffusion and the evaporation of the liquid (Eq. (4.19)) and we introduce the three mobility coefficients; the nanoparticle mobility coefficient α (c.f. Eq. (4.17) and Fig. 4.2), the conserved liquid diffusion mobility coefficient M_c and the non-conserved liquid evaporation mobility coefficient M_{nc} (c.f. Eq. (4.19)). The equilibrium behaviour of the model is explored in Sec. 4.4, where we determine the affect of the nanoparticles on the coexistence curves as well as determining the linear stability of the two component model and identifying regions in parameter space where one should observe liquid-particle demixing. In Sec. 4.5 we go on to discuss the nonlinear dynamics of the model. We show how the three different types of patterns found in experiments may be formed, before switching the focus onto the formation of the branched structures. We investigate the dependence of the mean number of fingers $\langle f \rangle$ on the various mobility coefficients and discover a trend which is consistent with the experimental and KMC results. The effect of localised liquid-particle demixing at the receding front on the fingering mechanism is also investigated. In our conclusion of the chapter, we reflect on our results and hypothesise about possible mechanisms with regards to the transverse front instability.

The other main topic of this thesis is the PFC model. The PFC model is a theory which has a conserved dynamics with a free energy which may be minimised by periodic order parameter profiles and is primarily used for studying freezing and crystal formation. We present

the model equations for the regular PFC model (Eqs. (5.15), (5.17) and (5.18)) in Sec. 5.1 of chapter 5 and show how they may be derived from the DDFT described in chapter 2. The thermodynamics of the regular PFC model is discussed in detail in Sec. 5.3. In particular, we use a linear stability analysis to determine the limit of linear stability of the homogeneous phase and calculate the 1D coexistence curves using a two mode approximation in Fig. 5.3. We then present the more commonly studied two dimensional system phase diagram in Fig. 5.4, where the coexistence curves are determined numerically. With the model equations for the regular PFC model defined and having explored the basic equilibrium behaviour of the model we proceed to discuss the second major project of this thesis: a modified PFC model.

The model equations of the modified PFC model that we study are given by Eqs. (5.15), (6.1), (5.18) and (6.2). The model basically takes the form of the regular PFC model but with a 'vacancy' term appended onto the free energy [118, 119]. This extra term penalises negative values of the order parameter ϕ which results in some novel phase behaviour and the formation of localised structures for small values of ϕ when r is small. We consider this one component model in both one and two dimensions, calculating the phase diagram for each. The vacancy term breaks the symmetry of the phase diagrams, with modulated structures only observable for $\bar{\phi} \gtrsim 0$ and the coexistence lines being shifted to higher $\bar{\phi}$ values. However, the most fundamental change is the introduction of a large area in the phase diagram where localised structures form. For the 1D model we study the formation of the localised structures in detail using bifurcation analysis to find homoclnic snaking regions [130–133]. For the 2D model we run numerous time simulations in the localised section of the phase diagram and treating the individual bumps as particles/colloids, we calculate radial distribution functions and effective pair potentials. We introduce a two component model for two order parameter fields ϕ_a and ϕ_b. The free energy of this two component model is given by Eq. (6.7), which includes a coupling term $\eta\phi_a\phi_b$. This coupling term penalises structures in one order parameter field which overlap with structures in the other order parameter field. For the remainder of chapter 6 we now concentrate on the two component bump profiles which form. Repeating the analysis we performed for the one component model, we calculate the radial distribution functions and effective pair potentials for the two component model. It is noted that at low concentrations of one species we observe mainly hexagonally ordered crystalline structures, whilst at equal concentrations we observe square ordering. This transition is subsequently investigated in Sec. 6.3.3. Finally we conclude with a discussion on the interpretation of the order parameter in this VPFC model.

The two case studies are presented consecutively in the thesis and are linked in chapter 5 through the derivation of the PFC model equations using concepts from DFT and DDFT. Throughout this derivation process various approximations and assumptions are made and in particular, we approximate the excess free energy term with a gradient expansion and then the intrinsic free energy is approximated using a Taylor series expansion. The dynamics of the model are derived under the assumption that $M\rho_1$ is small, where M is the mobility coefficient and ρ_1 is a reference density (c.f. Eqs. (5.13)–(5.15)). Therefore, in many respects, the regular PFC model can be considered as a DDFT model with further assumptions and simplifications. Although, in this case, the application of these two models are very different, the basic form of the models is very similar. Both models have their roots in microscopic theory and, as discussed throughout the thesis, can be derived by averaging over different ensembles of microscopic configurations. Through this averaging process we lose some of the microscopic details of the system, but what we find is that these simple theories can still qualitatively describe the behaviour and capture the physics of real soft matter systems.

Appendix A

Alternative parameter values for the DDFT model of evaporating suspensions

In this appendix we present some additional results for the DDFT model of the evaporation of thin films of colloidal suspensions from a surface (c.f. chapter 4). These results were obtained before the in-depth investigation of the phase behaviour of the system (see Sec. 4.4 of chapter 4) was conducted. After studying the equilibrium behaviour of the fluid we realised that the parameter values used here should result in micro-phase separation. However, this was not observed in our simulations, due to the discretisation of the system. The resulting structures shown here are qualitatively very similar to those discussed in Sec. 4.5 of chapter 4 and are presented here to demonstrate the robustness of the model - i.e. similar structures are observed for a large range of parameter values.

A.1 Artificial cut off of wavenumbers induced by discretisation

For all the numerical results presented in this chapter we set the interaction energies as: $\epsilon_l = 1.25$, $\epsilon_n = 0$ and $\epsilon_{nl} = 0.6$. After performing the linear stability analysis on our model for these parameter values we realised that this set of parameter values should lead to micro-phase separation (i.e. $\epsilon_l\epsilon_n - \epsilon_{nl}^2 < 0$), as opposed to the bulk liquid-gas phase separation that we observe in our numerical simulations. This discrepancy occurs because a maximum wavenumber for density fluctuations is imposed when we discretise the system. By solving the dynamical equations on a grid with a grid spacing of Δx we impose an artificial cut off point which prevents the system exhibiting density modulations with a wavenumber larger than $\frac{\pi}{\Delta x}$. Fig. A.1 (a) shows that this prevents micro-phase separation when we set $\Delta x = 1$ [1]. However, if we reduce this step size to $\Delta x = 0.25$ then we observe micro-phase separation as predicted by the linear stability analysis. When we suppress micro-phase separation by setting $\Delta x = 1$, we allow the system to exhibit bulk phase separation. The $c = 0$ line shown in Fig. A.1 (b) and A.1 (c) is the spinodal line for the bulk phase separation, denoting the region where the system is linearly unstable. Inside the $c = 0$ curve we observe evaporation through spinodal

[1] Note that when we set $\Delta x = 1$ one may consider our discretised continuum model as simply being the original lattice model Eq. (4.1). However, because of Eq. (4.55) we have introduced next nearest neighbour interactions into the Hamiltonian.

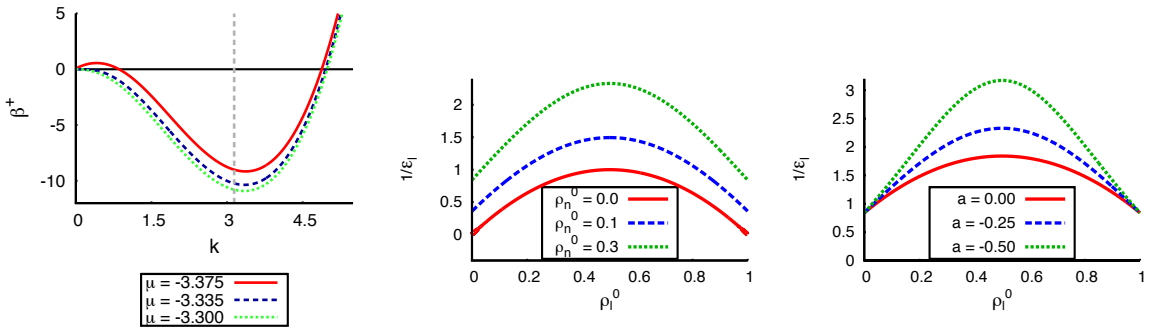

(a) Dispersion relations **(b)** Spinodal for varying ρ_n^0 **(c)** Spinodal for varying a

Figure A.1: In (a) we show how the discretisation limits the wavenumbers available and therefore prevents micro-phase separation. In (b) and (c) we display an effective spinodal for a system which doesn't exhibit micro-phase separation and how the spinodal varies depending on (b) the average nanoparticle density ρ_n^0 and (c) the value of a in Eq. (4.53).

decomposition. This appendix chapter follows the same layout as Secs. 4.5.2 and 4.5.3 and shows how similar structures and their dependencies on the mobility parameters in the model are also obtained for this alternative set of model parameter values when the artificial cut off of large-k density modulations is imposed.

A.2 Influence of the vapour chemical potential μ

Recall that as μ is decreased below its coexistence value μ_{coex}, the dewetting mechanism is at first via the nucleation of holes (when the metastable system is linearly stable) and then when μ is further decreased, via spinodal dewetting (when the system is linearly unstable). In this section we show the formation of labyrinth, network and branched structures which are somewhat similar to those described in Sec. 4.5.2.

Using the effective spinodal (c.f. A.1) for the parameter values used here, we find that the fluid should be unstable when $\beta\mu < -3.336$. The simulations agree very well with this value. The speed of the evaporation increases for decreasing $\beta\mu$. For very low values of $\beta\mu$ the evaporation of the liquid becomes so fast that the nanoparticles do not have time to rearrange by diffusion and we are simply left with a distribution of nanoparticles similar to the initial values $\rho_n(\mathbf{r}, t = 0)$. For the parameters $\epsilon_l = 1.25$, $\epsilon_n = 0$ and $\epsilon_{nl} = 0.6$, this occurs when $\beta\mu \lesssim -3.42$. In Fig. A.2 we show the particular case when $\beta\mu = -3.375$. The process shown here is very similar to the one described for Fig. 4.11 and the final nanoparticle structure is also similar. When there is an attraction between the nanoparticles (i.e. when $\epsilon_n > 0$) we observe small

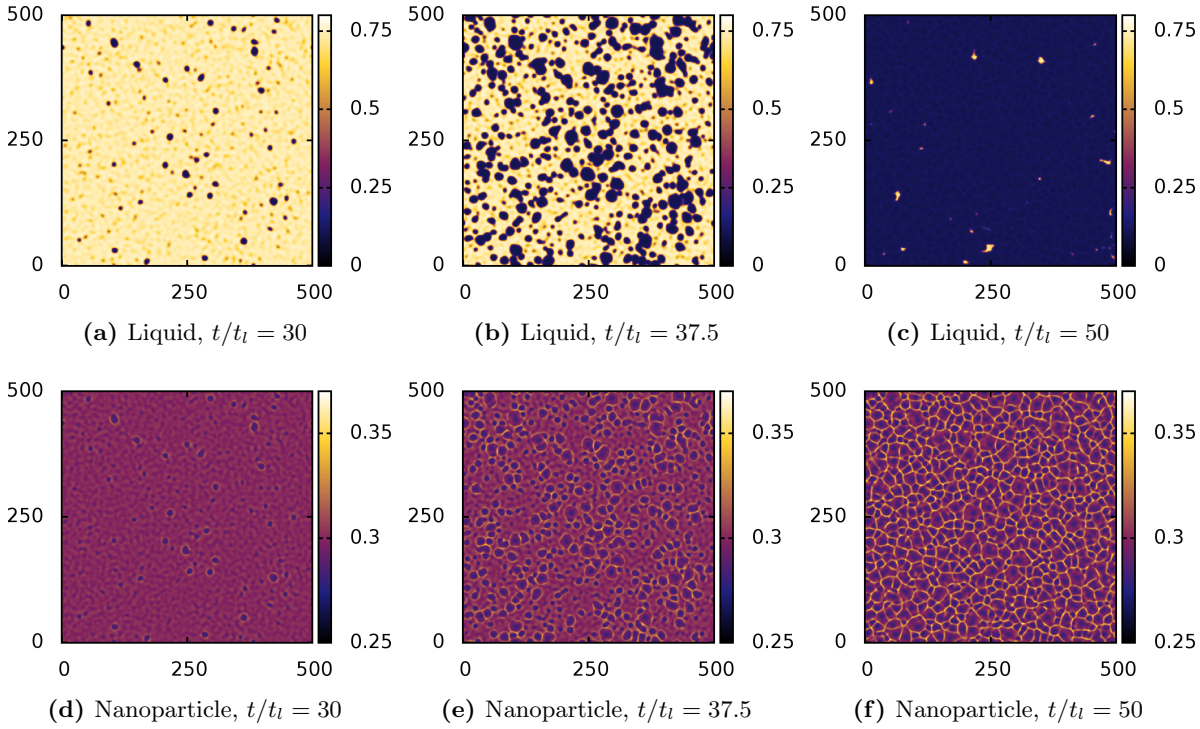

(a) Liquid, $t/t_l = 30$ **(b)** Liquid, $t/t_l = 37.5$ **(c)** Liquid, $t/t_l = 50$

(d) Nanoparticle, $t/t_l = 30$ **(e)** Nanoparticle, $t/t_l = 37.5$ **(f)** Nanoparticle, $t/t_l = 50$

Figure A.2: Density profiles displaying evaporation via spinodal decomposition. The top row shows the liquid density profiles and the bottom row shows the nanoparticle profiles at times $t/t_l = 30$ (left), $t/t_l = 37.5$ (centre) and $t/t_l = 50$ (right), where $t_l \equiv \frac{\beta}{M_l^{nc}}$. The system parameter values are: $k_B T = 1$, $\epsilon_l = 1.25$, $\epsilon_n = 0$, $\epsilon_{nl} = 0.6$, $M_l^c = 0$, $M_l^{nc} = 1$, $\alpha = 0.2$, $\beta\mu = -3.375$ and $\lambda = 0.1$.

heaps of nanoparticles form towards the end of the spinodal process, visible as white spots in Fig. 4.11 (f). However, in this case when $\epsilon_n = 0$, this mechanism is less conspicuous.

Increasing the chemical potential into the range $-3.336 < \beta\mu \lesssim -3.325$, the fluid becomes metastable and when the amplitude of the random modulations on the initial density profile are large enough with a sufficient level of noise (sufficient to create holes larger than the critical hole radius R^c) then one observes evaporation via the nucleation and growth of holes. Here we show two different cases from this metastable parameter region. First we show the case in Fig. A.3 where $\beta\mu = -3.335$ and the probability of nucleation is fairly high, hence, the initial noise nucleates many holes within a small space. As each of these holes becomes larger the receding fronts collects up the nanoparticles (due to the positive particle-liquid interactions $\epsilon_{nl} > 0$) and so high density nanoparticle rims begin to form. These rims then meet as the growing holes fill remaining space and form a seemingly random polygonal network. This process and resulting structures are very similar to the case displayed in Fig. 4.12. In Fig. A.4

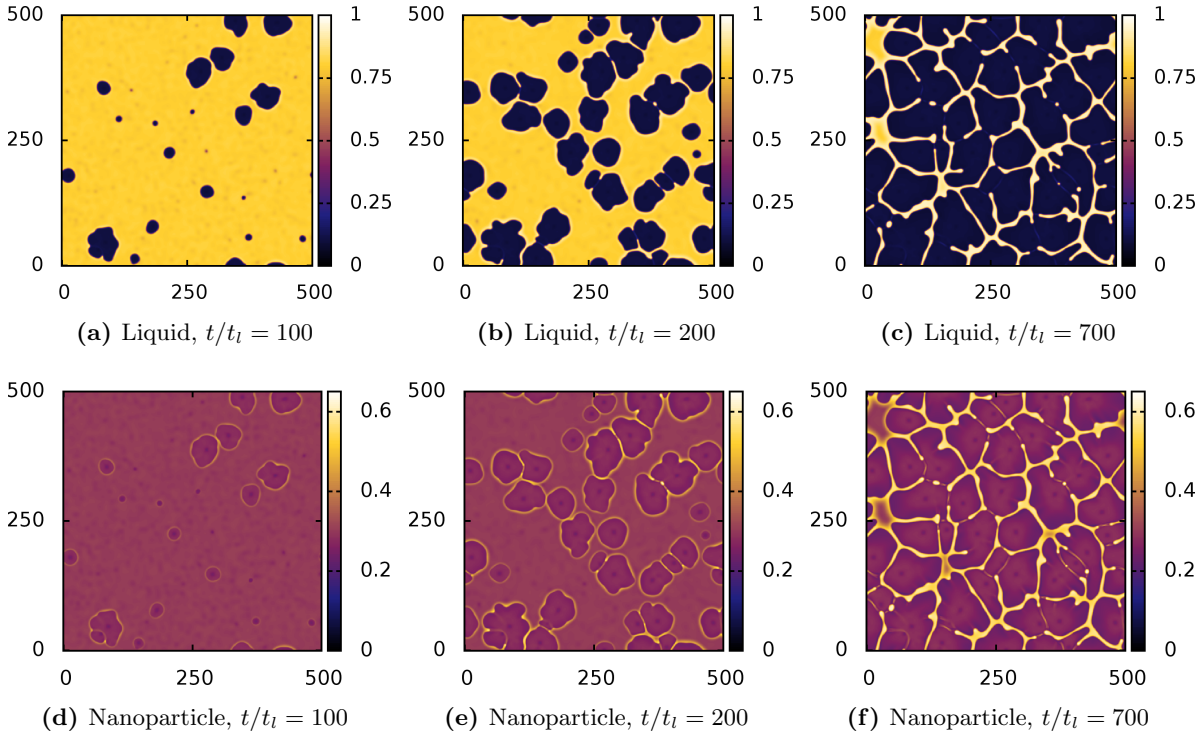

(a) Liquid, $t/t_l = 100$ **(b)** Liquid, $t/t_l = 200$ **(c)** Liquid, $t/t_l = 700$

(d) Nanoparticle, $t/t_l = 100$ **(e)** Nanoparticle, $t/t_l = 200$ **(f)** Nanoparticle, $t/t_l = 700$

Figure A.3: Density profiles displaying nucleation and growth of holes which leads to the development of a network pattern. The top row shows the liquid density profiles and the bottom row shows the nanoparticle profiles at times $t/t_l = 100$ (left), $t/t_l = 200$ (centre) and $t/t_l = 700$ (right). The system parameter values are: $k_BT = 1$, $\epsilon_l = 1.25$, $\epsilon_n = 0$, $\epsilon_{nl} = 0.6$, $M_l^c = 0$, $M_l^{nc} = 1$, $\alpha = 0.2$, $\beta\mu = -3.335$ and $\lambda = 0.2$.

we show the case when $\beta\mu = -3.3$, where the probability of nucleation is much smaller and in reality would usually occur at surface defects. In this case the initial noise is insufficient in size to produce holes large enough to grow and so to study the dewetting process we artificially nucleate a point in the centre by making $\rho_l = 0$ in the centre four lattice sites. The resulting hole then grows and high density nanoparticle rims form as in Fig. A.3. Now however, as there is ample space, the hole can grow much larger and a transverse front instability begins to develop (the initial stages of this front instability can be observed in the larger holes in Fig. A.3). This instability creates a wavy front. The bumps in this front are then left behind as the front continues to recede, eventually leaving a branched pattern of nanoparticles deposited on the surface. Once again the processes and resulting nanostructure are very similar to those discussed in Sec. 4.5, which shows that the same structures can be observed with different energetic parameter values. It is important to note that the difference in the overall shape of the hole is due to the Laplacian approximation used in the numerical scheme, in Fig. A.4 we used the following approximation: $\nabla^2\rho = \frac{1}{2(\Delta x)^2}\left(\sum \rho^{NN} + \frac{1}{2}\sum \rho^{NNN} - 6\rho\right)$, where as in Fig. 4.14

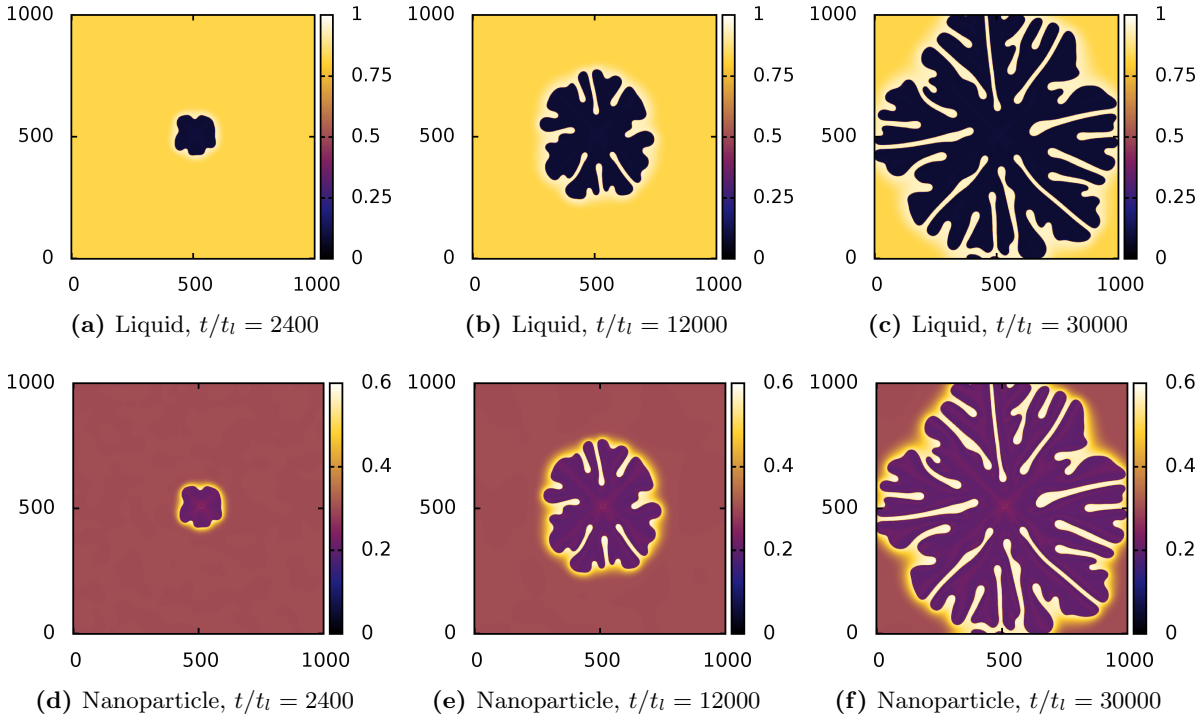

(a) Liquid, $t/t_l = 2400$ **(b)** Liquid, $t/t_l = 12000$ **(c)** Liquid, $t/t_l = 30000$

(d) Nanoparticle, $t/t_l = 2400$ **(e)** Nanoparticle, $t/t_l = 12000$ **(f)** Nanoparticle, $t/t_l = 30000$

Figure A.4: Density profiles displaying the growth of an artificially nucleated hole which develops branched structures. The top row shows the liquid density profiles and the bottom row shows the nanoparticle profiles at times $t/t_l = 2400$ (left), $t/t_l = 12000$ (centre) and $t/t_l = 30000$ (right). The system parameter values are: $k_BT = 1$, $\epsilon_l = 1.25$, $\epsilon_n = 0$, $\epsilon_{nl} = 0.6$, $M_l^c = 0$, $M_l^{nc} = 1$, $\alpha = 0.2$, $\beta\mu = -3.3$ and $\lambda = 0.1$.

$\nabla^2\rho = \frac{1}{6(\Delta x)^2}\left(\sum 4\rho^{NN} + \sum \rho^{NNN} - 20\rho\right)$ was used. These simulations are very sensitive to the Laplacian approximation used because we are modelling the growth of a circular hole and so the next nearest neighbour contributions are important. For further insight into the effect of the Laplacian approximation see appendix B.

A.3 Analysis of the fingering

We continue by conducting an investigation of the branched finger structures and how they depend on the various transport processes in the system. Switching to a planar geometry, we proceed by creating straight dewetting fronts by initiating a straight gas-liquid interface at the bottom of our simulation box and introducing no-flux boundary conditions at the top and bottom of the system. Setting the non-conserved liquid mobility $M_l^{nc} = 1$ we investigate how the branched structures change as the nanoparticle mobility coefficient α and the liquid diffusion mobility coefficient M_l^c are varied.

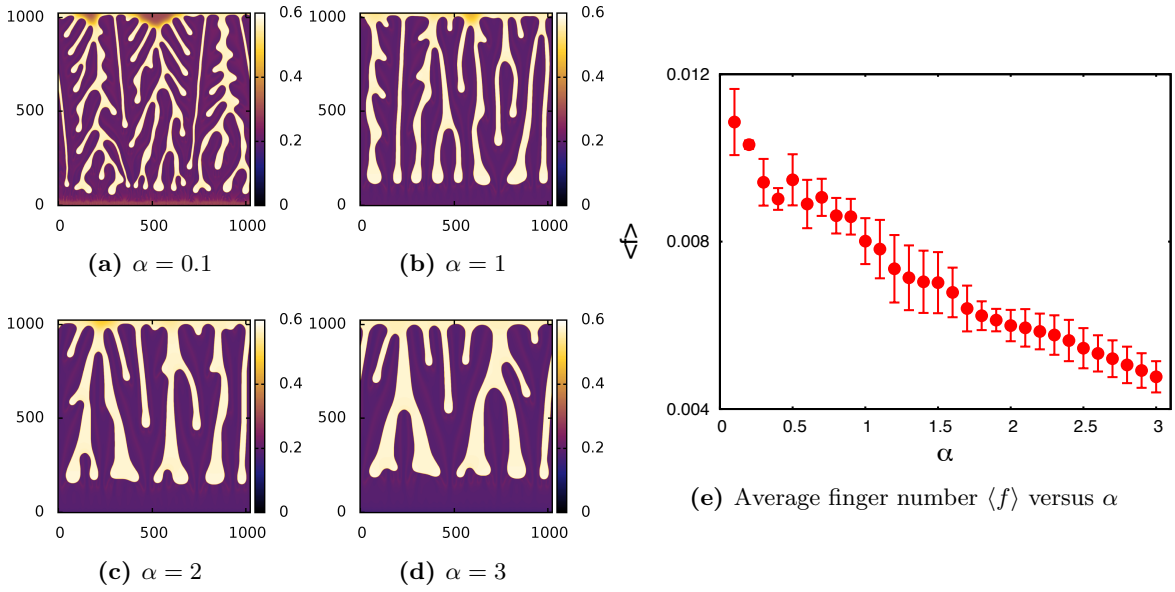

(a) $\alpha = 0.1$ **(b)** $\alpha = 1$ **(c)** $\alpha = 2$ **(d)** $\alpha = 3$

(e) Average finger number $\langle f \rangle$ versus α

Figure A.5: Nanoparticle density profiles for calculations with (a) $\alpha = 0.1$, (b) $\alpha = 1$, (c) $\alpha = 2$ and (d) $\alpha = 3$. In (e) we display a plot showing the dependence of the number of fingers on the parameter value α. The parameter values are: $k_BT = 1$, $\epsilon_l = 1.25$, $\epsilon_n = 0$, $\epsilon_{nl} = 0.6$, $M_l^c = 0$, $M_l^{nc} = 1$, $\beta\mu = -3.3$, $\Delta x = 1$ and $\lambda = 0.1$.

In Fig. A.5 we show how the average number of fingers $\langle f \rangle$ changes as the nanoparticle mobility coefficient α is varied from 0.1 to 3, for the case where $\epsilon_l = 1.25$, $\epsilon_n = 0$ and $\epsilon_{nl} = 0.6$. When comparing these results (Fig. A.5 (e)) with the results obtained with different energetic parameter values, displayed in Fig. 4.15 not only do we find the general trend is the same, but the two sets of results are quantitatively similar too. There is a significant increase in the average number of fingers as the value of α is decreased, suggesting that the nanoparticle diffusion plays a very important role in the development of the branched structures.

One of the major benefits of the DDFT model over the KMC model is the inclusion of the liquid diffusion process. As such, we also explore the influence of the liquid diffusion mobility coefficient M_l^c on the branched structures which are formed. In Fig. A.6 we show how the average number of fingers changes as the value of M_l^c is varied, for the case where $\epsilon_l = 1.25$, $\epsilon_n = 0$ and $\epsilon_{nl} = 0.6$. As with the corresponding results with different energetic parameter values (Fig. 4.16), the general trend shows that increasing the value of M_l^c increases the average number of fingers in the branched structures. However, we again observe that the change in the number of fingers is fairly small and the diffusion of the liquid seems far less important to the formation of the branched structures than the diffusion of the nanoparticles.

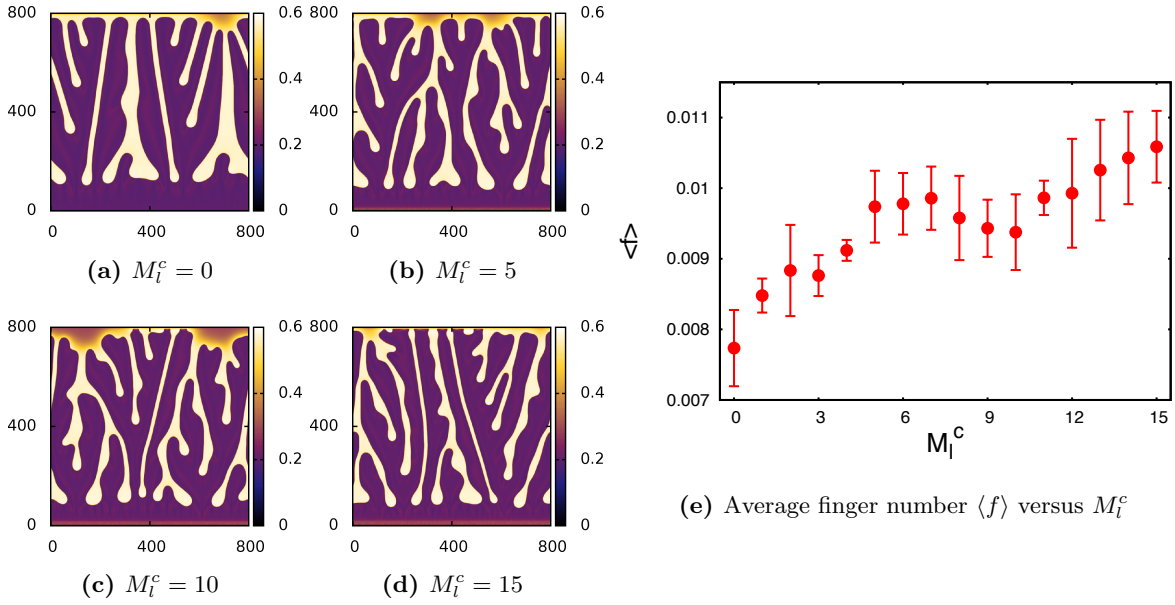

(a) $M_l^c = 0$ **(b)** $M_l^c = 5$

(c) $M_l^c = 10$ **(d)** $M_l^c = 15$

(e) Average finger number $\langle f \rangle$ versus M_l^c

Figure A.6: Nanoparticle density profiles for (a) $M_l^c = 0$, (b) $M_l^c = 5$, (c) $M_l^c = 10$ and (d) $M_l^c = 15$. In (e) we display a plot showing how the number of fingers $\langle f \rangle$ depends on the value of M_l^c. The parameter values are: $k_B T = 1$, $\epsilon_l = 1.25$, $\epsilon_n = 0$, $\epsilon_{nl} = 0.6$, $M_l^{nc} = 1$, $\alpha = 1$, $\beta\mu = -3.3$ and $\lambda = 0.1$.

Changing the energetics of the system affects the thermodynamics and the stability of the system. In this case, changing the parameters to $\epsilon_l = 1.25$, $\epsilon_n = 0$ and $\epsilon_{nl} = 0.6$ drastically changed the thermodynamics of the system and should have led to micro-phase separation. By discretising the system with the step size Δx we imposed an artificial cut-off which prevented the system from micro-phase separating. Reassuringly, the structures that were observed and their dependencies on the various mobility coefficients were qualitatively very similar to the results previously discussed in Sec. 4.5. We observe a difference in the nanoparticle density values between Figs. 4.12 and A.3, Figs. 4.14 and A.4, Figs. 4.15 and A.5 and Figs. 4.16 and A.6. In Sec. 4.5 when $\epsilon_n = 0.6$ we observe structures with higher density values, this is due to the attraction between nanoparticles increasing their tendency to gather together. This also explains why the network structure in Fig. 4.12 appears to be more well defined, having fewer broken 'links' than its counterpart in Fig. A.3.

Appendix B

Discretisation of the Laplacian term

In this appendix we briefly discuss some different numerical approximations for the Laplacian term $\nabla^2(f)$. We then show some examples from the two case studies presented in this thesis (chapters 4 and 6) to demonstrate how the various Laplacian approximations can affect the numerical solutions.

B.1 Laplacian approximations

In some systems, different approximations to the Laplacian term can result in major qualitative differences to the resulting solution, particularly when the next neighbour contributions are important. Therefore, it is important to be aware of the differences between these approximations and to make sure that any characteristics of the solutions obtained can be explained by the physical processes of the system being modelled and are not numerical artifacts. In both the dynamical density functional theory and the phase field crystal model we solve dynamical equations numerically using a finite difference scheme. These dynamical equations contain the Laplacian $\nabla^2(f)$ and Laplacian squared $\nabla^4(f)$ terms, for which we have to make a numerical approximation. Here we follow the discussion laid out in appendix b of Ref. [92]. Using a central difference scheme for a two dimensional grid (x, y) with equal grid spacing in both directions $\Delta x = \Delta y$, we obtain:

$$\begin{aligned}
\nabla^2(f) &= \frac{\partial^2 f}{\partial x^2} + \frac{\partial^2 f}{\partial y^2} \\
&= \frac{f(x-\Delta x, y) - 2f(x,y) + f(x+\Delta x, y)}{\Delta x^2} + \frac{f(x, y-\Delta y) - 2f(x,y) + f(x, y+\Delta y)}{\Delta y^2} \\
&= \frac{f(x-\Delta x, y) + f(x+\Delta x, y) + f(x, y-\Delta x) + f(x, y+\Delta x) - 4f(x,y)}{\Delta x^2}
\end{aligned} \tag{B.1}$$

For simplicity we can write this in the following form:

0	1	0
1	-4	1
0	1	0

(B.2)

where the central box denotes the lattice site at the point (x, y) and the others are the neighbouring sites. For example, the top right box is the lattice site at $(x + \Delta x, y + \Delta x)$. The matrix in B.2 tells us the contribution of each lattice site to the Laplacian calculation. The

simple formulation in Eq. (B.1) neglects the values of the next nearest neighbour lattice sites; $f(x-\Delta x, y-\Delta x)$, $f(x-\Delta x, y+\Delta x)$, $f(x+\Delta x, y-\Delta x)$ and $f(x+\Delta x, y+\Delta x)$. Hence, errors may occur in evaluating $\nabla^2 f$ when large gradient differences occur over lines which lie at approximately 45° to the orientation of the lattice.

We can obtain an improved discretised formula for $\nabla^2 f$ by including the next nearest neighbour values. To do this we can consider the effect of rotating the lattice by 45°.

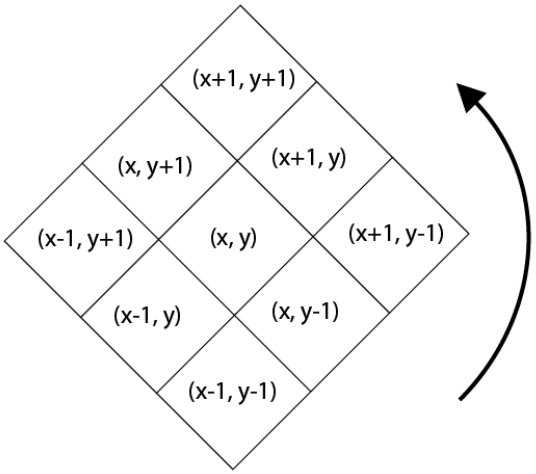

The distance between the centre of the middle and top lattice site is $\sqrt{2}\Delta x$. It is the same distance to the left, right and bottom, lattice sites. Note, this rotation is equivalent to the coordinate transform $x \to x - y$ and $y \to x + y$. If we now apply the central difference approximation we obtain:

$$\begin{aligned} \nabla^2(f) &= \frac{1}{(\sqrt{2}\Delta x)^2}[f(x-\Delta x, y+\Delta x) + f(x+\Delta x, y-\Delta x) \\ &\quad + f(x-\Delta x, y-\Delta x) + f(x+\Delta x, y+\Delta x) - 4f(x,y)] \qquad \text{(B.3)} \\ &\equiv \end{aligned}$$

$\frac{1}{2}$	0	$\frac{1}{2}$
0	-2	0
$\frac{1}{2}$	0	$\frac{1}{2}$

We now take a linear combination of Eqs. (B.1) and (B.3):

γ

0	1	0
1	-4	1
0	1	0

$+ \quad (1-\gamma)$

$\frac{1}{2}$	0	$\frac{1}{2}$
0	-2	0
$\frac{1}{2}$	0	$\frac{1}{2}$

Picking the value of $\gamma = 0.5$, we obtain the following formula (as used in Ref. [91]):

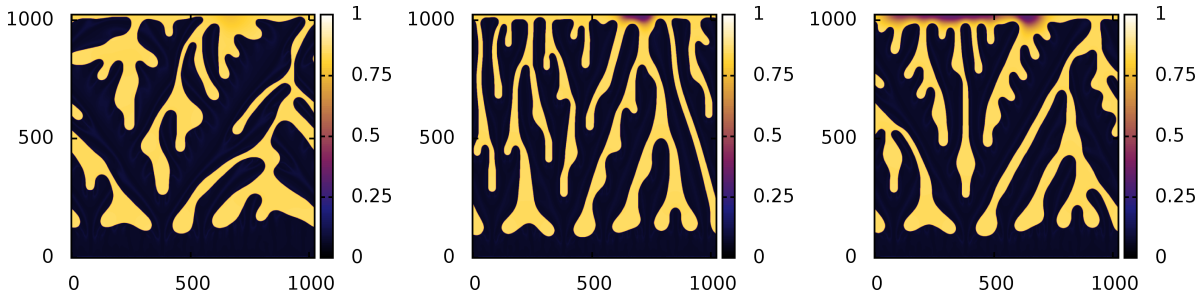

(a) $\nabla^2(f)$ term given by Eq. (B.2) **(b)** $\nabla^2(f)$ term given by Eq. (B.4) **(c)** $\nabla^2(f)$ term given by Eq. (B.5)

Figure B.1: Final nanoparticle density profiles for the DDFT model, when $k_BT = 1$, $\epsilon_l = 1.4$, $\epsilon_n = 0.6$, $\epsilon_{nl} = 0.8$, $M_l^c = 0$, $M_l^{nc} = 1$, $\alpha = 1$ and $\beta\mu = -3.8$. The Laplacian approximation used for the calculations are Eqs. (B.2) (left), (B.4) (centre) and (B.5) (right).

$\frac{1}{4}$	$\frac{1}{2}$	$\frac{1}{4}$
$\frac{1}{2}$	-3	$\frac{1}{2}$
$\frac{1}{4}$	$\frac{1}{2}$	$\frac{1}{4}$

(B.4)

which significantly reduces the errors in $\nabla^2 f$ compared to using the approximation in Eq. (B.1). Alternatively, we can choose the value $\gamma = \frac{2}{3}$, which gives the least error at very small wavenumbers (i.e. at length scales much larger than the grid spacing):

$\frac{1}{6}$	$\frac{2}{3}$	$\frac{1}{6}$
$\frac{2}{3}$	$\frac{-10}{3}$	$\frac{2}{3}$
$\frac{1}{6}$	$\frac{2}{3}$	$\frac{1}{6}$

(B.5)

B.2 Examples of how the different approximations affect numerical solutions

We now consider the effect of using the three different Laplacian approximations i) Eq. (B.2), ii) Eq. (B.4) and iii) Eq. (B.5) on the DDFT and PFC models studied in this thesis. We begin by investigating how the different Laplacian approximations affect the formation of branched finger structures in the DDFT model (c.f. chapter 4). The initial and boundary conditions are chosen such that we have a single straight dewetting front running from the bottom to the top of the simulation box (as this is the set up used to study these patterns in Sec. 4.5). In Fig. B.1 we show a typical case where we observe the formation of a branched structure where $k_BT = 1$, $\epsilon_l = 1.4$, $\epsilon_n = 0.6$, $\epsilon_{nl} = 0.8$, $M_l^c = 0$, $M_l^{nc} = 1$, $\alpha = 1$ and $\beta\mu = -3.8$. In

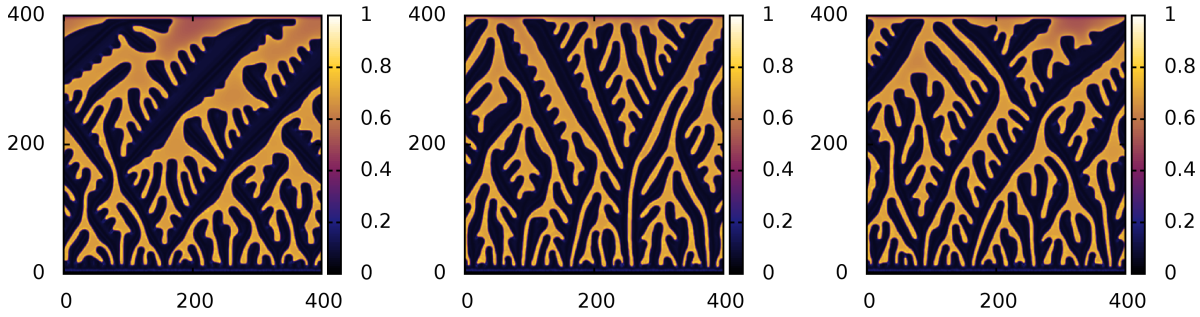

(a) $\nabla^2(f)$ term given by Eq. (B.2) **(b)** $\nabla^2(f)$ term given by Eq. (B.4) **(c)** $\nabla^2(f)$ term given by Eq. (B.5)

Figure B.2: Final nanoparticle density profiles for the DDFT model with the nanoparticle mobility function given by M_n^* as defined in Eq. 4.57. With the parameter values $k_BT = 1$, $\epsilon_l = 1.4$, $\epsilon_n = 0.6$, $\epsilon_{nl} = 0.8$, $M_l^c = 0$, $M_l^{nc} = 1$, $\alpha = 1$,$\beta\mu = -3.8$, $\rho_c = 0.7$ and $R = 2$. The Laplacian approximation used for the calculations are Eqs. (B.2) (left), (B.4) (centre) and (B.5) (right).

Fig. B.2 we display a case with the same parameter values but using a nanoparticle mobility function which causes the nanoparticles to jam when the local nanoparticle density is high - c.f. Sec. 4.5.5. For both of these cases (Figs. B.1 and B.2) we display three final density profiles where all the parameters and the initial density profiles are the same, but different Laplacian approximations were used. In both Figs. B.1 and B.2 we observe that using the approximation Eq. (B.2) (left profile images), which ignores the next nearest neighbour terms results in the branched structures forming at larger angles to the dewetting front. This diagonal orientation is also evident (to a lesser extent) when using approximation Eq. (B.5) (right profile images). When using Eq. (B.4) to approximate the Laplacian term (centre profile images) we observe that the branched structures tend to form at quite small angles to the dewetting front. However, both Eqs. (B.4) and (B.5) approximations appear to produce qualitatively similar results in these two cases. We also observe an increase in the average number of fingers $\langle f \rangle$ as the weight of the next nearest neighbour terms is increased.

We also consider the DDFT results where we have localised liquid-liquid demixing at the dewetting front, where $k_BT = 1$, $\epsilon_l = 1.7$, $\epsilon_n = 0.8$, $\epsilon_{nl} = 1$, $M_l^c = 0$, $M_l^{nc} = 1$, $\alpha = 0.5$ and $\beta\mu = -4$, shown in Fig. B.3. In this case the system is more sensitive to the approximation used. We observe a significant difference in the directional orientation of the branched structures when using the different approximations. We see the formation of alternating fingers and series of droplets (formed from doublons) when using Eq. (B.4) (centre) and Eq. (B.5) (right) to approximate the Laplacian terms. However, this pattern develops vertically when using Eq. (B.4)

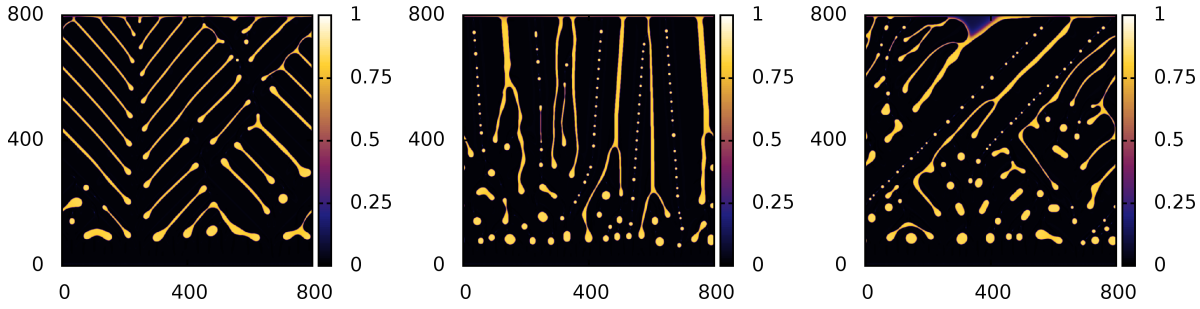

(a) $\nabla^2(f)$ term given by Eq. (B.2) **(b)** $\nabla^2(f)$ term given by Eq. (B.4) **(c)** $\nabla^2(f)$ term given by Eq. (B.5)

Figure B.3: Final nanoparticle density profiles for the DDFT model, when $k_BT = 1$, $\epsilon_l = 1.7$, $\epsilon_n = 0.8$, $\epsilon_{nl} = 1$, $M_l^c = 0$, $M_l^{nc} = 1$, $\alpha = 0.5$ and $\beta\mu = -4$. The Laplacian approximation used for the calculations are Eqs. (B.2) (left), (B.4) (centre) and (B.5) (right).

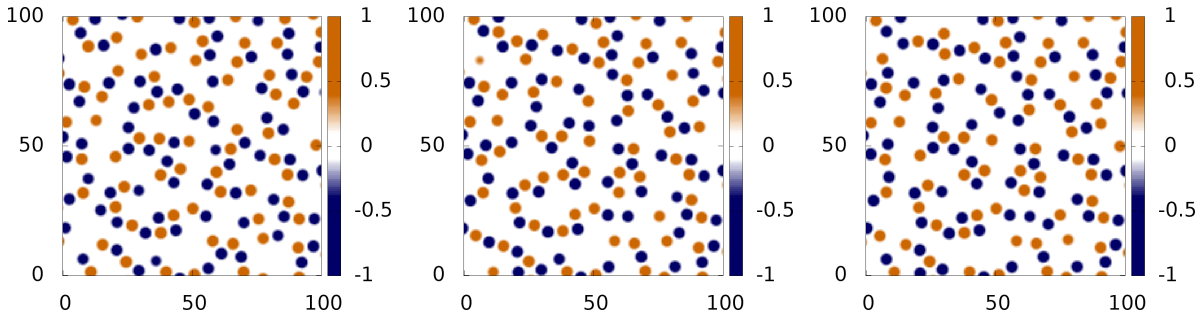

(a) $\nabla^2(f)$ term given by Eq. (B.2) **(b)** $\nabla^2(f)$ term given by Eq. (B.4) **(c)** $\nabla^2(f)$ term given by Eq. (B.5)

Figure B.4: Scaled order parameter $\Delta\hat{\phi}$ profiles for the two component VPFC model, when $\alpha_a = \alpha_b = 1$, $r = -0.9$, $\eta = 4$, $q_a = q_b = 1$ and $\bar{\phi_a} = \bar{\phi_b} = 0.02$. The Laplacian approximation used for the calculations are Eqs. (B.2) (left), (B.4) (centre) and (B.5) (right).

and diagonally when using Eq. (B.5).

Finally, we consider the influence of the different Laplacian approximations on the two component VPFC model (c.f. chapter 6), where $\alpha_a = \alpha_b = 1$, $r = -0.9$, $\eta = 4$, $q_a = q_b = 1$ and $\bar{\phi_a} = \bar{\phi_b} = 0.02$ shown in Fig. B.4. We observe that there is very little difference to the scaled order parameter profiles when using the three different approximations. The location of some of the bumps are different, but qualitatively the results are very similar. Clearly this shows the VPFC model is much less sensitive to the choice of Laplacian approximation.

In summary, approximating the Laplacian simply by using central different approximations can lead to large errors over long time scales. We therefore need to include next nearest neigh-

bour contributions to reduce these errors. Here we have discussed two such approximations Eqs. (B.4) and (B.5). In most cases the differences between the results when using the different approximations is fairly small (as in Figs. B.1 B.2 and B.4) and the difference to the qualitative behaviour of the system is negligible. However, Fig. B.3 clearly shows that in some circumstances the particular approximation can have a large impact on even the qualitative behaviour of the system.

Appendix C

Large network pattern

In this appendix we display a very large network pattern and some close ups which were produced for a project to create a large poster with a reasonable resolution.

The following images were created with the purpose of producing a $908mm^2$ poster with 300 DPI resolution. The purpose of the poster was to illustrate the aesthetically pleasing structures that may be observed in nature and reproduced with mathematical models. As such, the presentation here is very similar; we display the image and various close ups without description of the physical processes (the system is described in detail in chapters 3 and 4). The network pattern used is a nanoparticle profile calculated from a time simulation with a grid size of 10800×10800 and a grid spacing of $\Delta x = 1$. The parameters for this simulation were: $k_B T = 1$, $\epsilon_l = 1.4$, $\epsilon_n = 0.6$, $\epsilon_{nl} = 0.8$, $M_l^c = 0$, $M_l^{nc} = 1$, $\alpha = 0.5$, $\beta\mu = -3.9$ and $\lambda = 0.2$. Unfortunately, due to computational constraints it was not possible to use a smaller step size on such a large grid and as such, the length scale of the resulting structures is very small as compared to the size of the system. As such, we produced new images with larger length scales by taking samples of the original profile and interpolating new points to maintain the same resolution. Due to the very small typical length scale in the original density profile, we start by displaying the bottom left quarter of the calculated profile in Fig. C.1. In Fig. C.2 we show the bottom left sixteenth of the original profile and then in Fig. C.3 we show the bottom left 128^{th}. It is important to note that the images presented here can not be printed at their full resolution in this size with the printing resources available.

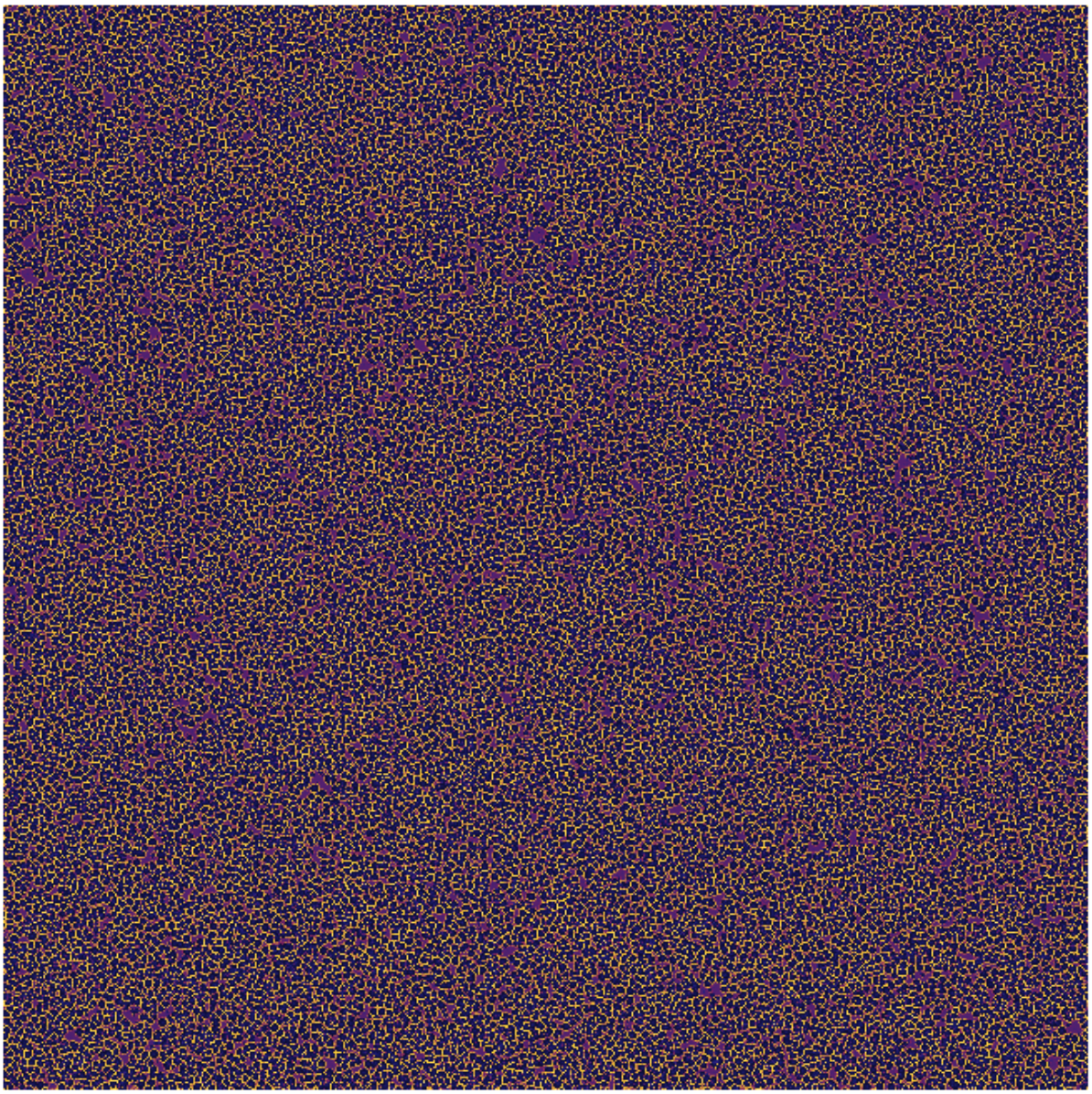

Figure C.1: Nanoparticle density profile displaying a network formation in a large system. Here we show the bottom left quarter of the original simulation and so the grid size is 5400×5400 and the grid spacing is $\Delta x = 1$ - i.e. we display an area of $5400\sigma^2$.

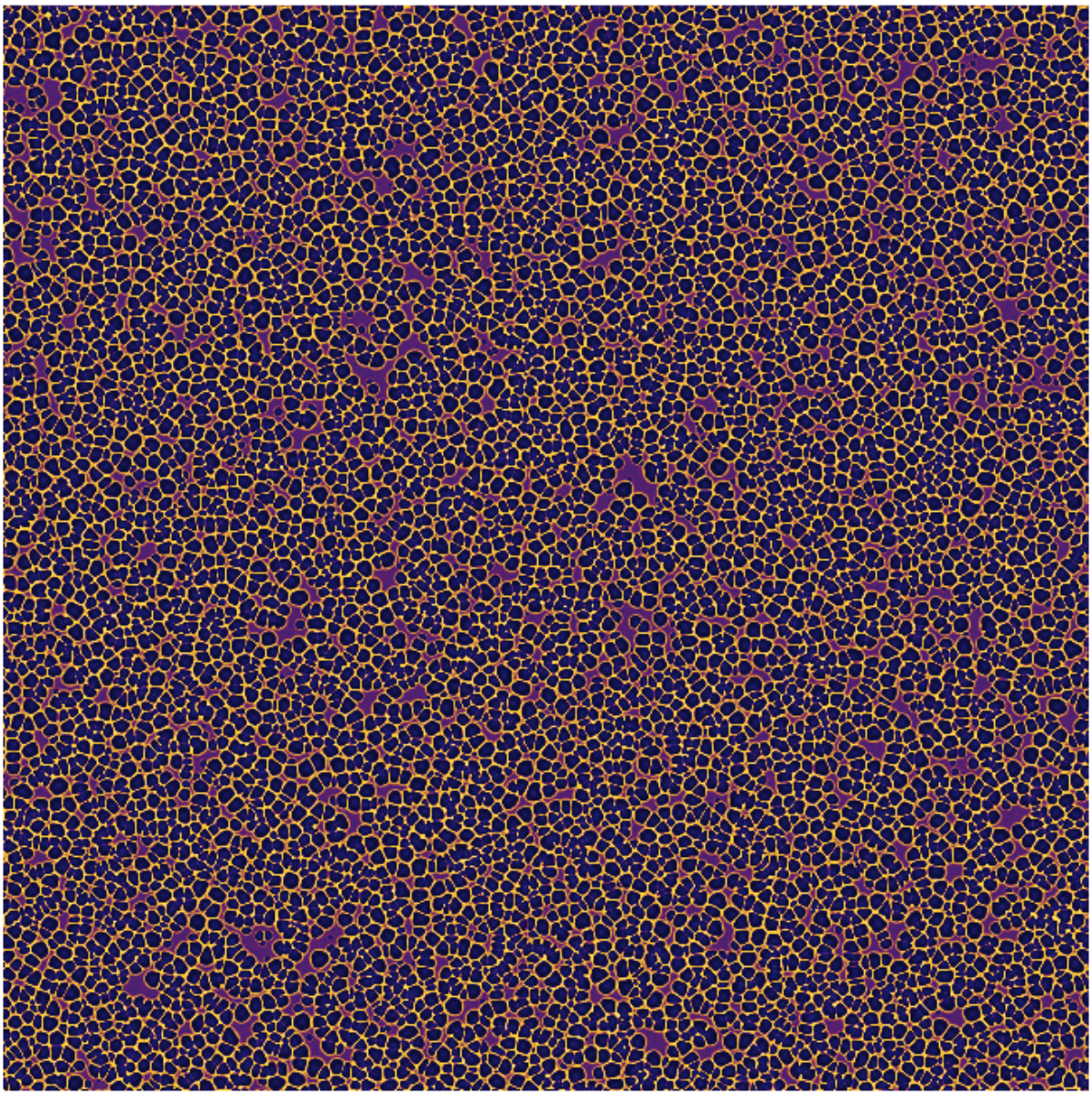

Figure C.2: Nanoparticle density profile displaying a network formation in a large system. Here we show the bottom left sixteenth of the original simulation and so the grid size is 5400×5400 and the grid spacing is $\Delta x = 0.5$ - i.e. we display an area of $2700\sigma^2$.

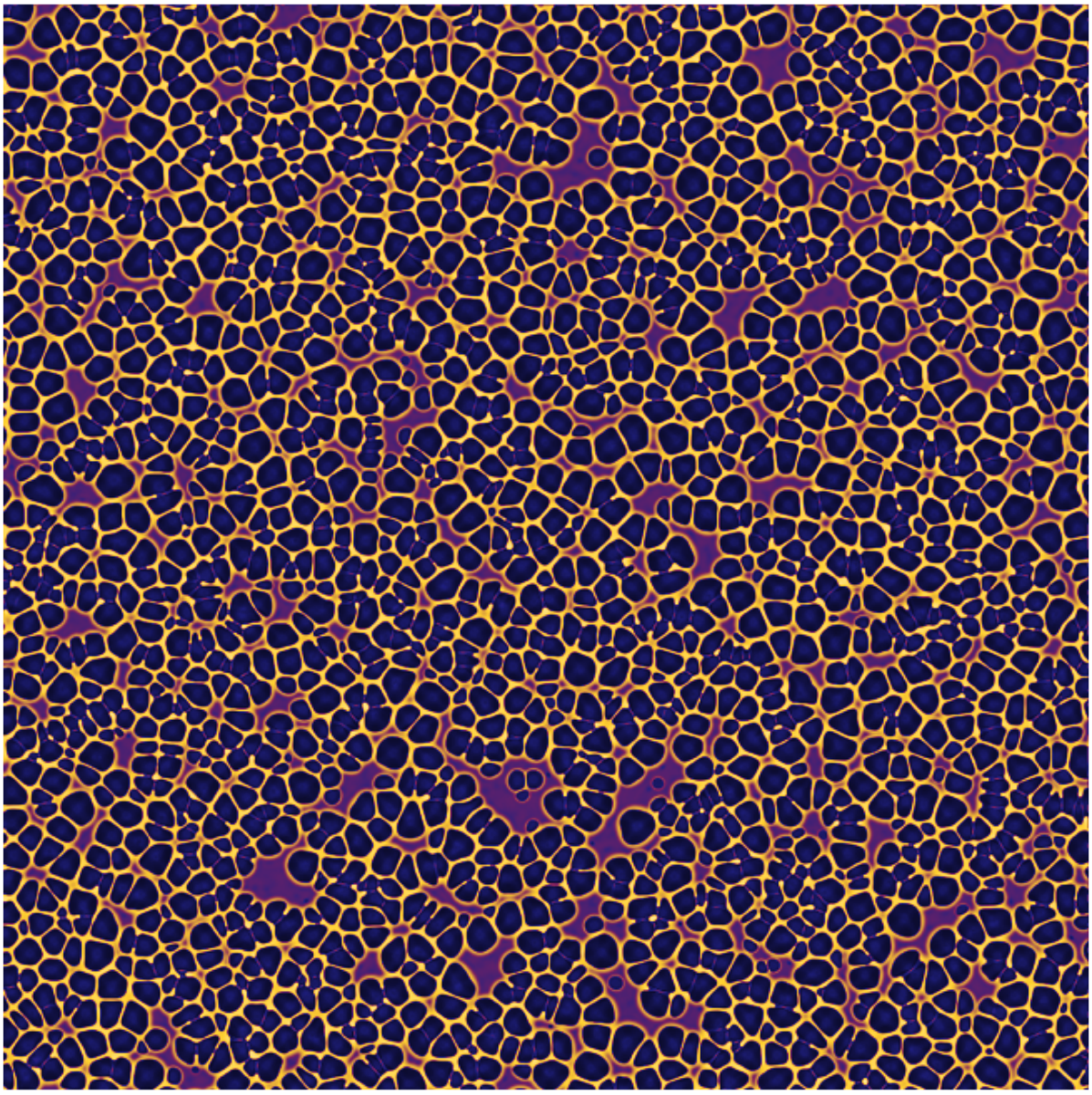

Figure C.3: Nanoparticle density profile displaying a network formation in a large system. Here we show the bottom left 128^{th} of the original simulation and so the grid size is 5400 $\times$ 5400 and the grid spacing is $\Delta x = 0.25$ - i.e. we display an area of $1350\sigma^2$.

Appendix D

Calculating the tricritical point analytically

In Sec. 5.3.2 of chapter 5 we show how the tricritical point in the 1D regular PFC model can be calculated geometrically. Here we present an alternative, analytic approach to calculating the tricritical point.

In Sec. 5.3.2 we use a two mode approximation for the order parameter ϕ in the periodic phase (5.25). Substituting this expression for ϕ into the free energy Eqs. (5.17) and (5.18) we obtain an expression for the free energy of the periodic phase Eq. (5.26) in terms of the average order parameter value in the periodic phase $\bar{\phi}_p$, the parameters r and q and the two amplitudes A and B. By minimising the free energy Eq. (5.26) with respect to the two amplitudes A and B we obtain two conditions Eqs. (5.27) and (5.28). Linearising the second of these expressions Eq. (5.28) in terms of B, we obtain the following:

$$0 = \frac{3}{2}\bar{\phi}_p A^2 + \left(\Delta_p + 9q^4 + \frac{3}{2}A^2\right)B,$$

which gives

$$B = -\frac{\bar{\phi}_p A^2}{6q^4} + O(\Delta_p A^2, A^4). \tag{D.1}$$

Inserting the amplitude of B Eq. (D.1) into the first condition Eq. (5.27) and solving for A, we find:

$$0 = \Delta_p + \left(\frac{3}{4} - \frac{\bar{\phi}_p^2}{2q^4}\right)A^2 + O(\Delta_p^2),$$

which gives the leading order dependence on Δ_p of the amplitude A:

$$A = 2\sqrt{-\frac{\Delta_p}{3}}\left(1 - \frac{2\bar{\phi}_p^2}{3q^4}\right)^{-\frac{1}{2}} + O(\Delta_p) \tag{D.2}$$

(c.f. Eq. (5.30)). Note that in the limit that $\bar{\phi}_p \to 0$ we recover the result that the amplitude A reduces to $A = 2/3\sqrt{-3\Delta_p}$. The free energy of a homogeneous flat film is given by Eq. (5.33). The chemical potential in the periodic phase is given by $\mu_p = \frac{\partial f_p}{\partial \phi_p}$ and in the homogeneous phase $\mu_h = \frac{\partial f_h}{\partial \bar{\phi}_h}$. We write the average value of ϕ in the periodic state $\bar{\phi}_p = \bar{\phi}_h + C$, where C is

the difference between the average value of the order parameter in the two coexisting phases, implying that the coexistence condition is

$$\mu_p(\bar{\phi}_h + C) - \mu_h(\bar{\phi}_h) = 0, \tag{D.3}$$

or equivalently:

$$(\Delta_h + q^4)C + \frac{3}{2}\bar{\phi}_h A^2 + O(A^4, CA^2, C^2) = 0, \tag{D.4}$$

where $\Delta_h = r + 3\bar{\phi}_h^2$. Assuming that $\Delta_h \ll 1$ and solving this expression for C we obtain:

$$C = -\frac{3\bar{\phi}_h A^2}{2q^4} + O(\Delta_h A^2, A^4). \tag{D.5}$$

The amplitude B in Eq. (D.1) becomes

$$B = -\frac{\bar{\phi}_h A^2}{6q^4} + O(A^2, \Delta_h A^2, A^4). \tag{D.6}$$

Inserting the two amplitudes Eqs. (D.6) and (D.5) into the first condition (5.27) we obtain

$$A = 2\sqrt{-\frac{\Delta_h}{3}}\left(1 - \frac{38\bar{\phi}_h^2}{3q^4}\right)^{-\frac{1}{2}} + O(\Delta_h) \tag{D.7}$$

Taking the limit $C \to 0$ now takes us to the tricritical point. At the tricritical point $\Delta_h = \Delta_p = 0$ and the chemical potentials $\mu_p(\bar{\phi}_h)$ and $\mu(\bar{\phi}_h)$ are identical. Thus from Eq, (D.7) we see that the tricritical point occurs at $\bar{\phi} = \sqrt{3/38}q^2$, $r = -(9/38)q^4$. This agrees exactly with the tricritical point calculated in Sec. 5.3.2 for $q = 1$.

Appendix E

Two component VPFC order parameter profiles for varying concentration

In this appendix, we show further results to augment those presented in Sec. 6.3.3. First of all in Sec. E.1 we show the $\Delta\hat{\phi}$ profiles for the intermediate values of c not shown in Sec. 6.3.3 and the angle probability distributions $p(\Theta)$ obtained from the Delaunay triangulation of these profiles. Then in Sec. E.2 we display some $\Delta\hat{\phi}$ profiles for varying concentrations c where $\bar{\phi}_a + \bar{\phi}_b = 0.15$. For this parameter range we find that when $c = 0$ or $c = 1$ we observe crystalline hexagonally ordered structures, but around $c = 0.5$ we lose the long range ordering and so we do not obtain strong squared ordering for any value of c.

E.1 Results for $\bar{\phi}_a + \bar{\phi}_b = 0.24$

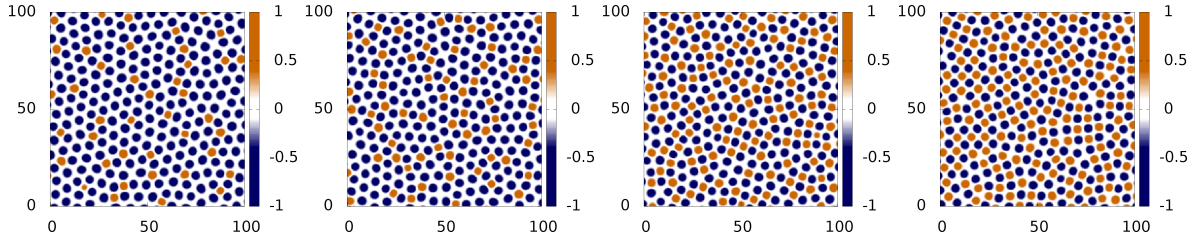

(a) $c = 0.08$ **(b)** $c = 0.17$ **(c)** $c = 0.33$ **(d)** $c = 0.42$

Figure E.1: Plots of the order parameter $\Delta\hat{\phi}$, in which bumps in species a appear in orange and bumps in species b appear in blue, for a constant total order parameter value $\bar{\phi}_a + \bar{\phi}_b = 0.24$. We show results from the symmetric mixture ($q_a = q_b = 1$) where the concentration of species a is (a) $c = 0.08$, (b) $c = 0.17$, (c) $c = 0.33$ and (d) $c = 0.42$. The parameter values are: $\eta = 4$ and $r = -0.9$.

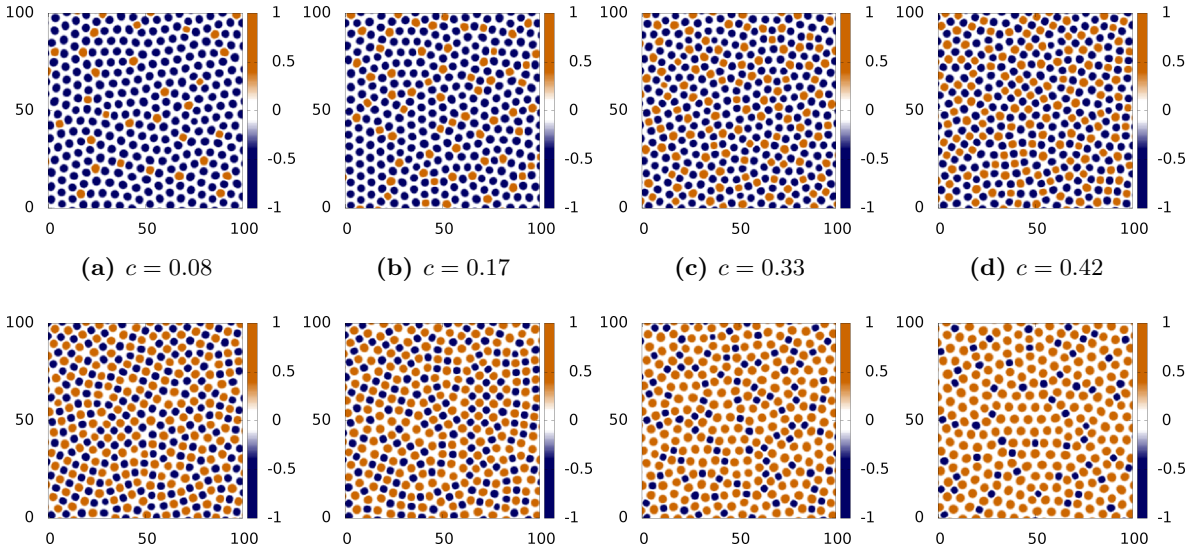

(a) $c = 0.08$ **(b)** $c = 0.17$ **(c)** $c = 0.33$ **(d)** $c = 0.42$

(e) $c = 0.58$ **(f)** $c = 0.67$ **(g)** $c = 0.83$ **(h)** $c = 0.92$

Figure E.2: Plots of the order parameter $\Delta\hat{\phi}$, in which bumps in species a appear in orange and bumps in species b appear in blue, for a constant total order parameter value $\bar{\phi_a} + \bar{\phi_b} = 0.24$. We show results from the asymmetric mixture ($q_a = 1, q_b = 1.1$) where the concentration of species a is (a) $c = 0.08$, (b) $c = 0.17$, (c) $c = 0.33$, (d) $c = 0.42$, (e) $c = 0.58$, (f) $c = 0.67$, (g) $c = 0.83$ and (h) $c = 0.92$. The parameter values are: $\eta = 4$ and $r = -0.9$.

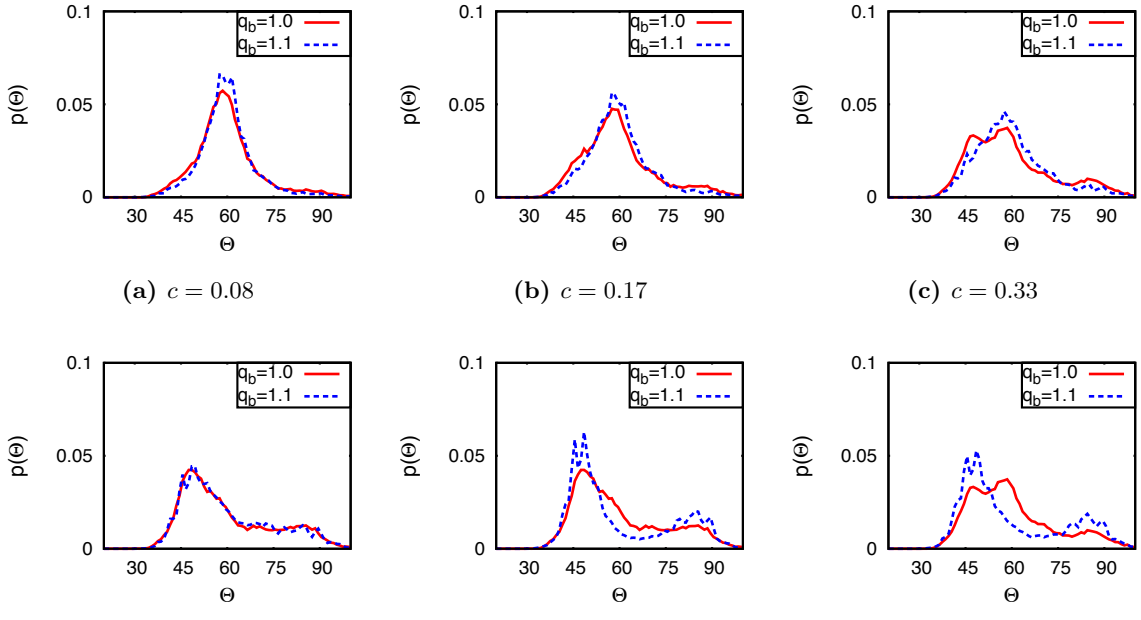

(a) $c = 0.08$ **(b)** $c = 0.17$ **(c)** $c = 0.33$

(d) $c = 0.42$ **(e)** $c = 0.58$ **(f)** $c = 0.67$

Figure E.3: Continues on the next page

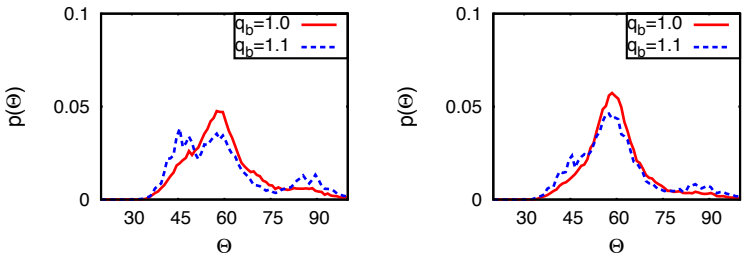

(g) $c = 0.83$ **(h)** $c = 0.92$

Figure E.3: Continued from the previous page: The angle distribution $p(\Theta)$ for a constant total order parameter value $\bar{\phi}_a + \bar{\phi}_b = 0.24$. The concentration of species a is (a) $c = 0.08$, (b) $c = 0.17$, (c) $c = 0.33$, (d) $c = 0.42$, (e) $c = 0.54$, (f) $c = 0.67$, (g) $c = 0.83$ and (h) $c = 0.92$ (corresponding to the simulation snapshots shown in Figs. E.1 and E.2). Results for the symmetric system are shown as the red solid lines and the asymmetric system results are shown as blue dashed lines. The parameter values are: $q_a = 1$, $\eta = 4$ and $r = -0.9$.

E.2 Results for $\bar{\phi}_a + \bar{\phi}_b = 0.15$

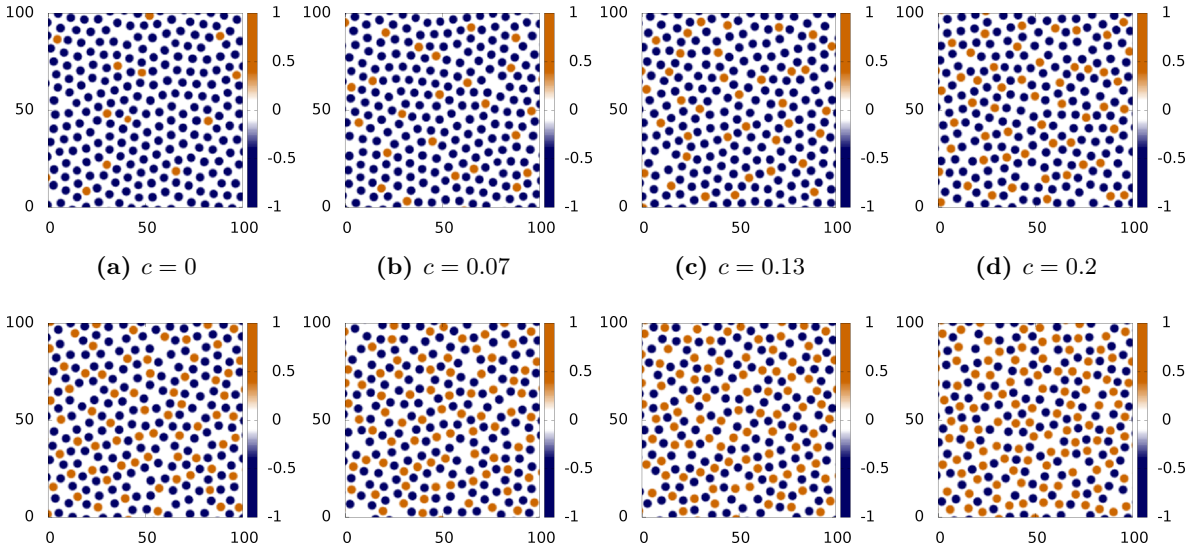

(a) $c = 0$ **(b)** $c = 0.07$ **(c)** $c = 0.13$ **(d)** $c = 0.2$

(e) $c = 0.27$ **(f)** $c = 0.33$ **(g)** $c = 0.4$ **(h)** $c = 0.47$

Figure E.4: Plots of the order parameter $\Delta\hat{\phi}$, in which bumps in species a appear in orange and bumps in species b appear in blue, for a constant total order parameter value $\bar{\phi}_a + \bar{\phi}_b = 0.15$. We show results from the symmetric mixture ($q_a = q_b = 1$) where the parameter values are: $\eta = 4$ and $r = -0.9$.

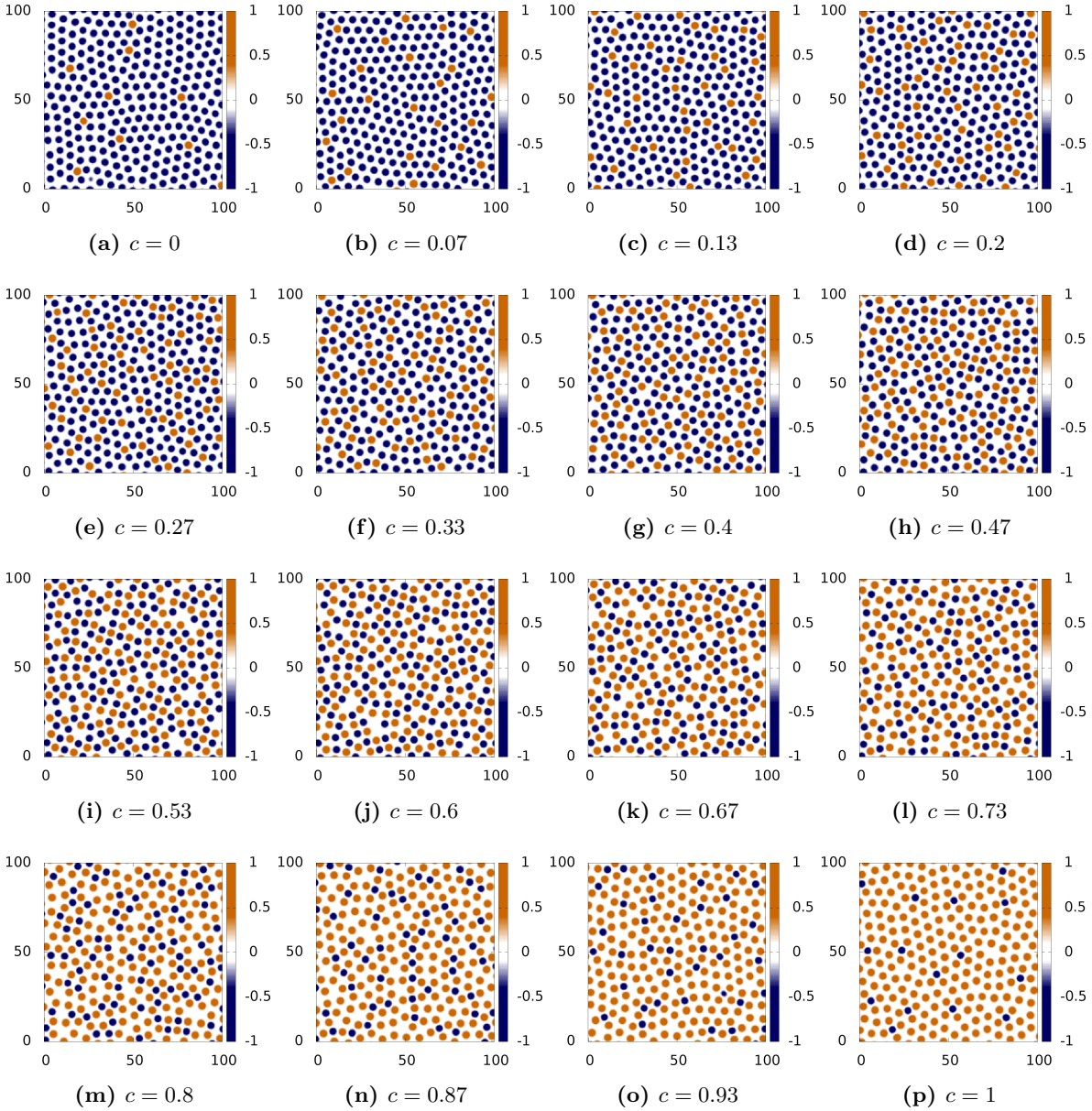

(a) $c = 0$ **(b)** $c = 0.07$ **(c)** $c = 0.13$ **(d)** $c = 0.2$

(e) $c = 0.27$ **(f)** $c = 0.33$ **(g)** $c = 0.4$ **(h)** $c = 0.47$

(i) $c = 0.53$ **(j)** $c = 0.6$ **(k)** $c = 0.67$ **(l)** $c = 0.73$

(m) $c = 0.8$ **(n)** $c = 0.87$ **(o)** $c = 0.93$ **(p)** $c = 1$

Figure E.5: Plots of the order parameter $\Delta\hat{\phi}$, in which bumps in species a appear in orange and bumps in species b appear in blue, for a constant total order parameter value $\bar{\phi_a} + \bar{\phi_b} = 0.15$. We show results from the asymmetric mixture ($q_a = 1, q_b = 1.1$) where the parameter values are: $\eta = 4$ and $r = -0.9$.

Bibliography

[1] J. P. Hansen and I. R. McDonald, *Theory of simple liquids* (Academic Press, London, 2006).

[2] F. Mandl, *Statistical Physics* (John Wiley & Sons, Chichester, 1971).

[3] R. Evans, Adv. Phys. **28**, 143 (1979).

[4] A. J. Archer and R. Evans, J. Chem. Phys. **121**, 4246 (2004).

[5] R. Evans, in *Fundamentals of inhomogeneous fluids*, edited by D. Henderson (Dekker, New York, 1992), Chap. 3.

[6] N. D. Mermin, Phys. Rev. **137**, A1441 (1965).

[7] U. M. B. Marconi and P Tarazona, J. Chem. Phys. **110**, 8032 (1999).

[8] U. M. B. Marconi and P Tarazona, J. Phys.: Condens. Matter **12**, A413 (2000).

[9] A. Giacometti, A. Maritan, and J. R. Banavar, Phys. Rev. Lett. **75**, 577 (1995).

[10] M. Mimura, H. Sakaguchi, and M. Matsushita, Physica A **282**, 283 (2000).

[11] A. Yochelis, Y. Tintut, L. L. Demer, and A. Garfinkel, New J. Phys. **10**, 055002 (2008).

[12] C. Tomlinson, Phil. Mag. Ser. 4 **39**, 32 (1870).

[13] C. G. Marangoni, Ann. Phys. **143**, 337 (1871).

[14] V. S. Mitlin, J. Colloid Interface Sci. **156**, 491 (1993).

[15] G. Reiter, Phys. Rev. Lett. **68**, 75 (1992).

[16] R. Xie *et al.*, Phys. Rev. Lett. **81**, 1251 (1998).

[17] R. Seemann, S. Herminghaus, and K. Jacobs, Phys. Rev. Lett. **86**, 5534 (2001).

[18] U. Thiele, M. G. Velarde, and K. Neuffer, Phys. Rev. Lett. **87**, 016104 (2001).

[19] U. Thiele, Eur. Phys. J. E. **12**, 409 (2003).

[20] J. Becker *et al.*, Nat. Mater. **2**, 59 (2003).

[21] P. Beltrame and U. Thiele, SIAM J. Appl. Dyn. Syst. **9**, 484 (2010).

[22] C. Redon, F. Brochard-Wyart, and F. Rondelez, Phys. Rev. Lett. **66**, 715 (1991).

[23] A. Sharma and G. Reiter, J Colloid Interface Sci. **178**, 383 (1996).

[24] A. Sharma and R. Khanna, Phys. Rev. Lett. **81**, 3463 (1998).

[25] M. Bestehorn and K. Neuffer, Phys. Rev. Lett. **87**, 046101 (2001).

[26] Available at `http://hydrosheds.cr.usgs.gov/images/hydrosheds_amazon_large.jpg`, as verified on 08/02/12.

[27] Available at `http://commons.wikimedia.org/wiki/File:Diplora_labyrinthiformis_(Grooved_Brain_Coral)_closeup.jpg`, as verified on 08/02/12.

[28] A. Stannard, J. Phys.: Condens. Matter **23**, 083001 (2011).

[29] Y. A. Vlasov, X-Z. Bo, J. C. Sturm, and D. J. Norris, Nature **414**, 289 (2001).

[30] T. P. Bigioni *et al.*, Nat. Mater. **5**, 265 (2006).

[31] J. Xu, J. F. Xia, and Z. Q. Lin, Angew. Chem.-Int. Edit. **46**, 1860 (2007).

[32] O. Karthaus, L. Grasjö, N. Maruyama, and M. Shimomura, Chaos **9**, 308 (1999).

[33] X. Gu, D. Raghavan, J. F. Douglas, and A. Karim, J. Polym. Sci. B **40**, 2825 (2002).

[34] S. W. Hong, J. Xia, and Z. Lin, Adv. Mater. **19**, 1413 (2007).

[35] Gang Liu, Cunfu Zhang, Jiang Zhao, and Yingxi Zhu, Langmuir **24**, 7923 (2008).

[36] M. Mertig *et al.*, Surf. Interface Anal. **25**, 514 (1997).

[37] M. Mertig *et al.*, Appl. Phys. A **66**, S565 (1998).

[38] U. Thiele, M. Mertig, and W. Pompe, Phys. Rev. Lett. **80**, 2869 (1998).

[39] H. Maeda, Langmuir **15**, 8505 (1999).

[40] I. I. Smalyukh *et al.*, Phys. Rev. Lett. **96**, 177801 (2006).

[41] L. Zhang, S. Maheshwari, H. Chang, and Y. Zhu, Langmuir **24**, 3911 (2008).

[42] M. Maillard, L. Motte, A. T. Ngo, and M. P. Pileni, J. Phys. Chem. B **104**, 11871 (2000).

[43] G. L. Ge and L. Brus, J. Phys. Chem. B **104**, 9573 (2000).

[44] P. Moriarty, M. D. R. Taylor, and M. Brust, Phys. Rev. Lett. **89**, 248303 (2002).

[45] E. Rabani, D. R. Reichman, P. L. Geissler, and L. E. Brus, Nature **426**, 271 (2003).

[46] L. V. Govor, G. Reiter, J. Parisi, and G. H. Bauer, Phys. Rev. E **69**, 061609 (2004).

[47] C. P. Martin, M. O. Blunt, and P. Moriarty, Nano Lett. **4**, 2389 (2004).

[48] C. P. Martin *et al.*, Phys. Rev. Lett. **99**, 116103 (2007).

[49] A. Stannard *et al.*, J. Chem. Phys. C **112**, 15195 (2008).

[50] E. Pauliac-Vaujour *et al.*, Phys. Rev. Lett. **100**, 176102 (2008).

[51] I. Vancea *et al.*, Phys. Rev. E **78**, 041601 (2008).

[52] H. Yabu and M. Shimomura, Adv. Funct. Mater. **15**, 575 (2005).

[53] R. D. Deegan *et al.*, Nature **389**, 827 (1997).

[54] E. Adachi, A. S. Dimitrov, and K. Nagayama, Langmuir **11**, 1057 (1995).

[55] R. D. Deegan, Phys. Rev. E **61**, 475 (2000).

[56] R. D. Deegan *et al.*, Phys. Rev. E. **62**, 756 (2000).

[57] L. Shmuylovich, A. Q. Shen, and H. A. Stone, Langmuir **18**, 3441 (2002).

[58] V. X. Nguyen and K. J. Stebe, Phys. Rev. Lett **88**, 164501 (2002).

[59] X. Gu, D. Raghavan, J. F. Douglas, and A. Karim, J. Polym. Sci. Pt. B-Polym. Phys. **40**, 2825 (2002).

[60] L. Xu, T. Shi, P. K. Dutta, and L. An, J. Chem. Phys. **127**, 144704 (2007).

[61] E. Pauliac-Vaujour and P. Moriarty, J. Phys. Chem. C **111**, 16255 (2007).

[62] A. Oron, S. H. Davis, and S. G. Bankoff, Rev. Mod. Phys. **69**, 931 (1997).

[63] L. Frastia, A.J. Archer, and U. Thiele, Phys. Rev. Lett. **106**, 077801 (2011).

[64] J. Xu *et al.*, Phys. Rev. Lett. **96**, 066104 (2006).

[65] H. Bodiguel, F. Doumenc, and B. Guerrier, Langmuir **26**, 10758 (2010).

[66] H. C. M. Fernandes, J. J. Arenzon, and Y. Levin, J. Chem. Phys. **126**, 114508 (2007).

[67] H. C. M. Fernandes, Y. Levin, and J. J. Arenzon, Phys. Rev. E **75**, 052101 (2007).

[68] J. F. Gouyet, M Plapp, W Dieterich, and P Maass, Adv. Phys. **52**, 523 (2003).

[69] P. M. Chaikin and T. C. Lubensky, *Principles of Condensed Matter Physics* (Cambridge University Press, Cambridge, 2000).

[70] R. C. Desai and R. Kapral, *Dynamics of Self-Organized and Self-Assembled Structures* (Cambridge University Press, Cambridge, 2009).

[71] Y. Levin, J. J. Arenzon, and M. Sellitto, Europhys. Lett. **55**, 767 (2001).

[72] U. Thiele, Eur. Phys. J. Special Topics **197**, 213 (2011).

[73] C. P. Royall, M. Dzubiella, J. Schmidt, and A. van Blaaderen, Phys. Rev. Lett. **98**, 188304 (2007).

[74] A. J. Archer and M. Rauscher, J. Phys. A. **37**, 9325 (2004).

[75] A. V. Lyushnin, A. A. Golovin, and L. M. Pismen, Phys. Rev. E **65**, 021602 (2002).

[76] U. Thiele, J. Phys.: Cond. Mat. **22**, 084019 (2010).

[77] J. W. Cahn and J. E. Hilliard, J. Chem. Phys. **28**, 258 (1958).

[78] J. W. Cahn, J. Chem. Phys. **42**, 93 (1965).

[79] J. S. Langer, in *Solids far from Equilibrium*, edited by C. Godreche (Cambridge University Press, Cambridge, 1992), Chap. 3, pp. 297–363.

[80] D. Woywod and Schoen M., Phys. Rev. E **73**, 011201 (2006).

[81] A. Pototsky, M. Bestehorn, D. Merkt, and U. Thiele, J. Chem. Phys. **122**, 224711 (2005).

[82] A. J. Archer and R. Evans, Phys. Rev. E. **64**, 041501 (2001).

[83] J. S. Rowlinson and F. L. Swinton, *Liquids and Liquid Mixtures*, 3rd ed. (Butterworth Scientific, London, 1982).

[84] L. Leibler, Macromolecules **13**, 1602 (1980).

[85] Y. Nishiura and I. Ohnishi, Phys. D **84**, 31 (1995).

[86] A. J. Archer and N. B. Wilding, Phys. Rev. E **76**, 031501 (2007).

[87] R. P. Sear *et al.*, Phys. Rev. E **59**, R6255 (1999).

[88] A. I. Campbell, V. J. Anderson, J. S. van Duijneveldt, and P. Bartlett, Phys. Rev. Lett. **94**, 208301 (2005).

[89] A. Stradner *et al.*, Nature **432**, 492 (2004).

[90] H. Sedgwick, S. U. Egelhaaf, and W. C. K Poon, J. Phys.: Condens. Matter **16**, S4913 (2004).

[91] G. Brown, P. A. Rikvold, M. Sutton, and M. Grant, Phys. Rev. E **56**, 6601 (1997).

[92] S. Fomel and J. F. Claerbout, Stanford Exploration Project **95**, 43 (1997).

[93] D. W. Oxtoby and R. Evans, J. Chem. Phys. **89**, 7521 (1988).

[94] S. Akamatsu, G. Faivre, and T. Ihle, Phys. Rev. E. **51**, 4751 (1995).

[95] G. Reiter and A. Sharma, Phys. Rev. Lett. **87**, 166103 (2001).

[96] U. Thiele *et al.*, J. Phys.: Condens. Matter **21**, 264016 (2009).

[97] B. Utter and E. Bodenschatz, Phys. Rev. E **72**, 011601 (2005).

[98] C. G. Sztrum, O. Hod, and E. Rabani, J. Phys. Chem. B **109**, 6741 (2005).

[99] G. Yosef and E. Rabani, J. Phys. Chem. B **110**, 20965 (2006).

[100] D. Bonn *et al.*, Rev. Mod. Phys. **81**, 739 (2009).

[101] S. van Teeffelen, R. Backofen, A. Voigt, and H. Löwen, Phys. Rev. E. **79**, 051404 (2009).

[102] H. Löwen *et al.*, Philosophical Magazine Letters **87**, 847 (2007).

[103] S. van Teeffelen, C. N. Likos, and H. Löwen, Phys. Rev. Lett. **100**, 108302 (2008).

[104] T. V. Ramakrishnan and M. Yussouff, Phys. Rev. B **19**, 2775 (1979).

[105] K. R. Elder *et al.*, Phys. Rev. B. **75**, 064107 (2007).

[106] P. C. Hohenberg and B. I. Halperin, Rev. Mod. Phys. **49**, 435 (1977).

[107] Elder K.R., M. Katakowski, Haataja M., and M. Grant, Phys. Rev. Lett. **88**, 245701 (2002).

[108] K.R. Elder and M. Grant, Phys. Rev. E **70**, 051605 (2004).

[109] G. Tegze *et al.*, Soft Matter **7**, 1789 (2011).

[110] P. Stefanovic, M. Haataja, and N. Provatas, Phys. Rev. Lett. **96**, 225504 (2006).

[111] J. Mellenthin, A. Karma, and M. Plapp, Phys. Rev. B. **78**, 184110 (2008).

[112] H. Ohnogi and Y. Shiwa, Physica D **237**, 3046 (2008).

[113] A. Jaatinen and T. Ala-Nissila, J. Phys.: Condens. Matter **22**, 205402 (2010).

[114] P. K. Galenko and K. R. Elder, Phys. Rev. B **83**, 064113 (2011).

[115] G. I. Tóth *et al.*, J. Phys.: Condens. Matter **22**, 364101 (2010).

[116] L. Gránásy, G. Tegze, G. I. Tóth, and T. Pusztai, Phil. Mag. **91**, 123 (2011).

[117] K.-A. Wu, M. Plapp, and P.W. Voorhees, J. Phys.: Condens. Matter **22**, 364102 (2010).

[118] P. Chan, N. Goldenfeld, and J. Dantzig, Phys. Rev. E. **79**, 035701 (2009).

[119] J. Berry and M. Grant, Phys. Rev. Lett. **106**, 175702 (2011).

[120] S. Muralidharan and M. Haataja, Phys. Rev. Lett. **105**, 126101 (2010).

[121] Z.-F. Huang, K. R. Elder, and N. Provatas, Phys. Rev. E. **82**, 021605 (2010).

[122] J. Swift and P.C. Hohenberg, Phys. Rev. A. **15**, 319 (1977).

[123] E. Knobloch, Phys. Rev. A **40**, 1549 (1989).

[124] P. C. Matthews and S. M. Cox, Nonlinearity **13**, 1293 (2000).

[125] T. Pusztai *et al.*, J. Phys.: Condens. Matter **20**, 404205 (2008).

[126] G. Stell, J. Stat. Phys. **78**, 197 (1995).

[127] A. Ciach, W. T. Gòżdż, and R. Evans, J. Chem. Phys. **118**, 3702 (2003).

[128] A. J. Archer, C. N. Likos, and R. Evans, J. Phys.: Condens. Matter **16**, L297 (2004).

[129] A. J. Archer, D. Pini, R. Evans, and L. Reatto, J. Chem. Phys. **126**, 014104 (2007).

[130] J. Burke and E. Knobloch, Phys. Rev. E **73**, 056211 (2006).

[131] J. Burke and E. Knobloch, Chaos **17**, 037102 (2007).

[132] J. Burke and E. Knobloch, Phys. Lett. A **360**, 681 (2007).

[133] E. Knobloch, Nonlinearity **21**, T45 (2008).

[134] E. Doedel *et al.*, Technical report, Caltech (2011) (unpublished).

[135] J. Burke and E. Knobloch, in *Dynamical Systems, Differential Equations and Applications*, *Discrete and Continuous Dynamical Systems-Suppl. September*, edited by X.-J. Hou *et al.* (AIMS, Springfield, 2009), pp. 109–117.

[136] J. H. P. Dawes, SIAM J. Appl. Dyn. Syst. **7**, 186 (2008).

[137] D. Lo Jacono, A. Bergeon, and E. Knobloch, J. Fluid Mech. **687**, 595 (2011).

[138] M.P. Allen and D.J. Tildesley, *Computer simulation of liquids* (Clarendon Press, Oxford, 1999).

[139] M. E. Leunissen *et al.*, Nature **437**, 235 (2005).

[140] A. P. Hynninen *et al.*, Phys. Rev. Lett. **96**, 138308 (2006).

[141] A. P. Hynninen, M. E. Leunissen, A. van Blaaderen, and M. Dijkstra, Phys. Rev. Lett. **96**, 018303 (2006).

[142] Mark de Berg, Marc van Kreveld, Mark Overmars, and Otfried Schwarzkopf, *Computational Geometry: Algorithms and Applications* (Springer, Berlin, 1997).

[143] Ø. Hjelle and M. Dæhlen, *Triangulations and Applications* (Springer, Berlin, 2006).

[144] D. Stoyan, W. S. Kendall, and J. Mecke, *Stochastic Geometry and Its Applications*, 2nd ed. (Wiley, West Sussex, 1995).

[145] U. Thiele and K. Eckert, Phys. Rev. E **58**, 3458 (1998).

[146] A. Bowyer, The Computer Journal **24**, 162 (1981).

[147] U. Bortolozzo, M. G. Clerc, and S. Residori, New J. Phys **11**, 093037 (2009).

[148] L. Berthier and G. Biroli, Rev. Mod. Phys. **83**, 587 (2011).

[149] A. Cavagna, Phys. Rep. **476**, 51 (2009).

[150] A. J. Archer, Phys. Rev. E **78**, 031402 (2008).

[151] J.-L. Barrat and J. P. Hansen, *Basic Concepts for Simple and Complex Liquids* (Cambridge University Press, Cambridge, 2003).

[152] P. Bartlett and A. I. Campbell, Phys. Rev. Lett. **95**, 128302 (2005).